

# **Electrochemical and Microstructural Study of Copper in Aqueous and Soil Environments**

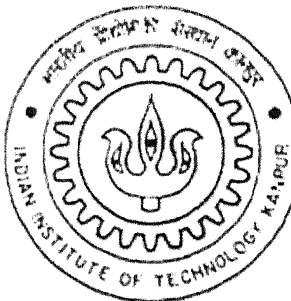
A Thesis submitted

In partial Fulfillment of the Requirements  
For the degree of

**MASTER OF TECHNOLOGY**

by

**Ashish Srivastava**  
(Y220605)



*to the*

**DEPARTMENT OF MATERIALS AND METALLURGICAL ENGINEERING**

**INDIAN INSTITUTE OF TECHNOLOGY, KANPUR**  
**INDIA 208016**

**January 2005**

**Dedicated to My Parents...**

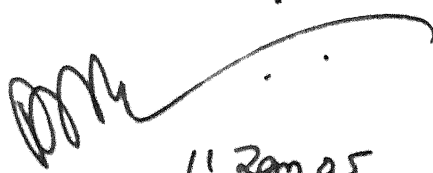
१८ JUL 2005 /MME  
प्राचीन लेखन कार्यक्रम  
भारतीय प्राचीनगिकी संस्थान कानपुर  
वर्षाचि दृ० ▲... 152132



A152132

# CERTIFICATE

This is to certify that the present thesis work entitled "**“Electrochemical and Microstructural Study of Copper in Aqueous and Soil Environments”**", has been carried out by Ashish Srivastava (Y220605), under our supervision and to the best of our knowledge it has not been submitted elsewhere for the award of a degree.



11 Ram 05

**Dr. R Balasubramaniam**

Professor

Dept. of Materials and Metallurgical Engg.

IIT Kanpur, India.

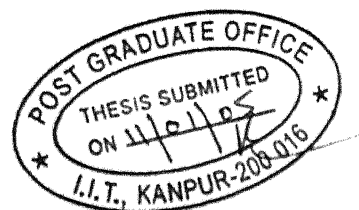


**Dr. K. N. Rai**

Professor

Dept. of Materials and Metallurgical Engg.

IIT Kanpur, India.



## ACKNOWLEDGEMENTS

---

I wish to express my deep sense of gratitude and sincere thanks to Dr. R. Balasubramaniam and Dr. K. N. Rai for their able guidance, remarkable patience and constant encouragement throughout the course of my M.Tech programme at IIT Kanpur. I consider it my privilege that I got the opportunity to work under them.

I would like to thank Dr. M.N. Mungole, Senior Research Engineer, Department of MME, IIT Kanpur for his useful comments and suggestions.

I am immensely thankful to Harish ji and Santosh, Lab assistants, for helping me in many ways during my experimental work.

I find myself quite lucky that I got such a nice environment in corrosion lab, IIT Kanpur. I would like to thank Ajit, Anand, Anoop, Shruti, Surender, Deepika, Bijayani, Dr. Valli, Sahoo, Mukesh, Dr. Delphine and all other friends who have helped me in various capacities throughout my thesis at IIT Kanpur. I will never forget the nice time I spent with my colleagues in the laboratory.

I could not have reached this stage in my life without the sacrifice, constant encouragement and unfailing emotional support from my loving parents, Mr. V. B. Srivastava and Mrs. Saroj Srivastava.

I am indebted to IIT Kanpur for providing me the best environment to stay and do research in the most fruitful way.

Ashish Srivastava  
IIT Kanpur  
January 2005

# **CONTENTS**

---

	<b>Page number</b>
<b>Certificate</b>	<b>i</b>
<b>Acknowledgements</b>	<b>ii</b>
<b>Abstract</b>	<b>vii</b>
<b>List of Figures</b>	<b>x</b>
<b>List of Tables</b>	<b>xix</b>
<b>Chapter 1      Introduction</b>	
1.1. Copper	1
1.2. Applications	2
1.3. Objectives of the present study	4
1.4. Plan of work	4
<b>Chapter 2      Literature Review</b>	
2.1 Corrosion in Soil	6
2.1.1 Introduction to soil corrosion	6
2.1.2 Soil parameters affecting corrosivity	7
2.1.2.1 Water	7
2.1.2.2 Degree of aeration	9
2.1.2.3 pH	9
2.1.2.4 Soil resistivity	9
2.1.2.5 Chlorides	10
2.1.2.6 Sulfates	10
2.1.2.7 Microbiologically influenced corrosion	10
2.2 Corrosion of Copper in Soil	10
2.3 Effect on copper corrosion	13
2.3.1 Chloride ions	13
2.3.2 Sulfide ions	16

2.3.3	Ammonium ions	19
2.3.4	Moisture	21
2.3.5	Oxygen	21
2.3.6	Localized corrosion	22
2.4	Electrochemical Corrosion	23
2.4.1	Polarization	26
2.4.2	Linear polarization	29
2.5	Electrochemical Impedance Spectroscopy	31
2.5.1	Introduction	31
2.5.2	Electric circuit representation	32
2.5.3	Data presentation	34
2.5.4	Physical Electrochemistry and Equivalent Circuit Elements	38
2.5.5	Physical Significance	42
2.6	Archaeological analogues	50
<b>Chapter 3 Experimental Procedure</b>		
3.1	Raw material	54
3.2	Soil Characterization	54
3.2.1	Chloride content	54
3.2.2	Moisture content	55
3.2.3	Particle size distribution	55
3.3	Electrochemical Characterization	58
3.3.1	Sample preparation	58
3.3.2	Apparatus for linear polarization and electrochemical impedance spectroscopy studies	58
3.3.3	Electrolytes	62
3.3.4	Test procedure for electrochemical studies	64
3.3.5	Potential stabilization	64
3.3.6	Linear polarization	65
3.3.7	Electrochemical impedance spectroscopy	65
3.4	Surface analysis by scanning electron microscopy (SEM)	66

3.5 Archaeological analogue analysis	66
3.5.1 Chalcolithic chisel	67
3.5.2 Chalcolithic axe	70
<b>Chapter 4     Results and Discussion</b>	
4.1     Archaeological analogue study	72
4.1.1 Chalcolithic chisel	72
4.1.2 Chalcolithic axe	77
4.2     Scanning electron microscopy	80
4.2.1   Aqueous Solution	80
4.2.2   Soil Environment	114
4.2.3   Comparison	156
4.3     Free corrosion potential	158
4.3.1   Aqueous Solution	158
4.3.2   Soil Environment	161
4.3.3   Comparison	164
4.4     Linear polarization	168
4.4.1   Aqueous Solution	168
4.4.2   Soil Environment	175
4.4.3   Comparison	175
4.5     Electrochemical Impedance Spectroscopy	177
4.5.1   Aqueous Solution	177
4.5.1.1 Damage function	204
4.5.2   Soil Environment	206
4.5.3   Comparison	218
<b>Chapter 5     Summary</b>	
5.1     Conclusions	232
5.2     Suggestions for future work	236
5.3     Sources of error	237

**References**

238

**Appendix A**

**Appendix B**

## **ABSTRACT**

---

The nature of corrosion products on two Chalcolithic archaeological copper samples have been characterized using XRD. The outer regions of the surface film on these coppers were composed primarily of sulphate while the inner region (near the metal-scale interface) was composed of cuprite. As the electrochemical behavior of ancient copper is similar to that of modern copper, an important result of the study of ancient Indian copper is the serious consideration of selecting copper as the material of construction of long-term underground storage of nuclear wastes. Characterization of surface patina on archaeological copper objects sheds light on understanding long-term corrosion mechanisms and validation of theoretical models for predicting long-term corrosion.

The electrochemical behavior of pure copper for long term immersion has been studied in aqueous and soil environments using free corrosion potential (FCP), linear polarization and electrochemical impedance spectroscopy (EIS) techniques. Different environment compositions were selected, to understand the effect of pollutants (chloride, sulfide and ammonium ions) on corrosion properties of copper. Surface films after long term immersion (432 hours) in various exposure environments were analyzed using SEM and EDAX. Wherever chloride ion<sup>-</sup> was present in the environment, it resulted in breakage of the surface layer after long term immersion. When there was no Cl<sup>-</sup> or when present in very low concentration, the surface layer was thin and moreover not adherent to substrate in aqueous solutions. The penetration during corrosive attack was not deep in absence of chloride in soil and aqueous environments. SEM studies further suggested that morphology and growth of surface films obtained in aqueous solutions was different than soil environments in most of the cases. The corrosive attack in the soil environments was not homogeneous as it was found in aqueous solutions. The damaging effect of chloride ions was more pronounced in case of aqueous solutions than soil environments. EDAX analysis confirmed that in most of the cases, there was a copper oxide film formed on the surface, which was porous in nature. Copper chloride was present locally at some places on the surface.

Free corrosion potentials were recorded after 2, 24, 48, 72, 96, 168, 240, 312 and 432 hours of immersion in soil and aqueous environments. FCP stabilized at more active potentials for environments containing chloride ions. The chloride ions from NaCl

destabilized the surface film and rendered the surface more active. FCP of aqueous solution containing only sulfide ions stabilized at the noblest potential with immersion time as compared to other environments. Linear polarization experiments were conducted after 2 hours and 432 hours of immersion. Linear polarization results brought out the damaging role of chloride ions while the relatively less severe effect of sulfide ions could also be noted. On increasing the chloride content, the polarization resistance was lowered after long term immersion both in aqueous and soil environments. The polarization resistance was lowest for aqueous solution possessing NaCl and NH<sub>4</sub>Cl, after long term immersion.

Electrochemical impedance spectroscopy (EIS) measurements are particularly useful in understanding the nature and evolution of surface films as a function of immersion time because they do not perturb the system dramatically. EIS data were recorded after 2, 24, 48, 72, 96, 168, 240, 312 and 432 hours of immersion in soil and aqueous environments at free corrosion potential. The experimentally obtained EIS data was analyzed and a relative comparison could be made for different environments. Some important features regarding the protective nature of the surface films could be discerned from the experimental EIS data itself. The decrease in diameter of Nyquist plots (obtained from chloride containing solutions) indicated a decrease in corrosion resistance after long term immersion, which was attributed to the damaging effect of chloride. The nature of Bode phase plots indicated the porous nature of the film, which was characterized by large phase shift towards zero degrees and very narrow medium frequency capacitive region. In chloride containing aqueous solutions, film formation occurs readily after immersion as compared to other solutions, but long term exposure to chloride environment can be deleterious for copper, as it was evident from Bode phase plots. The phase angles were shifted towards 90° after 2 hours of immersion, but after long term immersion (432 hours) phase angles were decreased in chloride solutions. The film formed in chloride solutions were relatively compact and adherent as compared to other solutions. Bode magnitude plots revealed the maximum decrease in total impedance for the solution possessing highest chloride content among all aqueous solutions.

The theoretically estimated impedance spectra was modeled by using R(Q(R(QR))) circuit. The logic for fitting the EIS data to R(Q(R(QR))) circuit was based on microstructural observation of the surfaces. Variation of circuit parameters for aqueous

solutions with time suggested that among all aqueous solutions, capacitive nature of surface film formed in aqueous solution containing NaCl and NH<sub>4</sub>Cl, was highest and fairly constant with time. In NaCl containing aqueous solutions, film thickness did not change significantly with time. The film resistance was lowest for the surface film obtained in aqueous solution possessing NaCl and NH<sub>4</sub>Cl throughout the immersion period. Capacitive behavior of double layer decreased sharply for most of the cases after 432 hours of immersion. This is attributed to the surface roughness of the exposed metal and it also indicated that due to localized attack, exposed metal surface was very rough. Double layer capacitance was lower in chloride containing solutions. It indicated that metal surface was relatively rough in presence of chloride. Charge transfer resistance was low for chloride solutions, and among them it was lowest for solution containing NaCl and NH<sub>4</sub>Cl. The variation of Damage Function with time suggested the benign role of sulfide ions and the damaging role of chloride ions in different aqueous solutions.

---

## LIST OF FIGURES

---

Fig. 1	Relationship of variables affecting the rate of corrosion in soil is presented. For simplicity, only the MIC effects of sulfate-reducing bacteria are shown.	8
Fig. 2	Pourbaix diagram for water at 25 <sup>0</sup> C with [Cu] = 10 <sup>-6</sup> mol kg <sup>-1</sup> and [CO <sub>3</sub> <sup>2-</sup> ] = 2mmol kg <sup>-1</sup> and [Cl <sup>-</sup> ] = 1.7 mol kg.	14
Fig. 3	Various types of polarization methods.	28
Fig. 4	Example linear polarization curve.	30
Fig. 5	Sinusoidal Current Response in a Linear System.	33
Fig. 6	Nyquist Plot with Impedance Vector.	35
Fig. 7	Simple Equivalent Circuit with One Time Constant.	36
Fig. 8	Bode plot with one time constant.	37
Fig. 9	Equivalent circuits used for modeling experimental EIS data, when a porous layer is present.	43
Fig. 10	Equivalent circuits used for modeling experimental EIS data, when a porous layer is present and also diffusion processes are dominating for determining the corrosion rate of reaction.	43
Fig. 11	Schematic of an idealized corrosion product deposit on a corroding surface. The whole metal surface is not covered with deposit. Pores are showing the exposed metal.	44
Fig. 12	Schematic Bode plots from EIS measurements and equivalent circuits that could be used to fit them for various possible corrosion product deposit structures.	49
Fig. 13	Weight loss measured as a function of time during drying of 10 gm of soil at 110 <sup>0</sup> C.	56
Fig. 14	Particle size distribution curve for Bentonite clay.	57
Fig. 15	Schematic diagram showing the connections in the potentiostat.	59
Fig. 16	Electrochemical cell used for conducting long term electrochemical experiments.	61
Fig. 17	A picture of copper chisel excavated from Balathal.	68

Fig. 18	A picture of copper axe excavated from Balathal.	71
Fig. 19	SEM micrograph photographed from one of the edges of a Chalcolithic copper chisel.	73
Fig. 20	X-ray diffraction pattern from the surface of the chalcolithic Cu chisel (a) before and (b) after slightly polishing the surface of the sample.	75
Fig. 21	Potentiodynamic polarization curves for modern and chalcolithic coppers (chisel) in aerated 3.5 wt% NaCl solution.	76
Fig. 22	XRD patterns obtained from chalcolithic copper axe as a function of corrosion product thickness	78
Fig. 23	A typical SEM micrograph of copper surface obtained after immersion of 432 hours in aqueous solution A1.	81
Fig. 24	SEM micrograph of copper surface obtained after immersion of 432 hours in aqueous solution A1, showing agglomerated particles.	82
Fig. 25	SEM micrograph of copper surface obtained after immersion of 432 hours in aqueous solution A1, showing bright Copper Chloride region.	83
Fig. 26	EDS analysis done at point A in Fig. 25.	84
Fig. 27	EDS analysis done at point B in Fig. 25.	85
Fig. 28	SEM micrograph of copper surface obtained after immersion of 432 hours in aqueous solution A1. A porous surface layer is present.	86
Fig. 29	SEM micrograph of copper surface obtained after immersion of 432 hours in aqueous solution A1, showing that the surface layer is cracked at some places.	87
Fig. 30	SEM micrograph of copper surface obtained after immersion of 432 hours in aqueous solution A1, showing breakage and cracks in the surface layer.	89
Fig. 31	SEM magnified view of the broken surface layer obtained after 432 hours of immersion in aqueous solution A1.	90
Fig. 32	SEM micrograph of copper surface obtained after immersion of 432 hours in aqueous solution A1, showing the magnified view inside	91

	the broken surface layer.	
Fig. 33	SEM micrograph of copper surface obtained after immersion of 432 hours in aqueous solution A1, showing the needle like structure beneath the surface layer.	92
Fig. 34	SEM micrograph of copper surface obtained after immersion of 432 hours in aqueous solution A1, showing a region from where the layer was peeled off.	93
Fig. 35	EDS analysis done at point A in Fig. 34.	94
Fig. 36	EDS analysis done at point B in Fig. 34.	95
Fig. 37	EDS analysis done at point C in Fig. 34.	96
Fig. 38	A typical SEM micrograph of copper surface obtained after immersion of 432 hours in aqueous solution A3.	98
Fig. 39	SEM micrograph of copper surface obtained after immersion of 432 hours in aqueous solution A3, showing the portion of the layer which was peeling off.	99
Fig. 40	SEM micrograph of copper surface obtained after immersion of 432 hours in aqueous solution A3, showing a region of the surface, from where the layer has peeled off.	100
Fig. 41	A typical SEM micrograph of copper surface obtained after immersion of 432 hours in aqueous solution A4.	102
Fig. 42	SEM micrograph of copper surface obtained after immersion of 432 hours in aqueous solution A4, showing that at locations where the surface film had been removed the underlying grain boundaries were etched by the corrosive solution.	103
Fig. 43	SEM micrograph of copper surface obtained after immersion of 432 hours in aqueous solution A4, showing that attack occurred at certain preferential crystallographic directions.	104
Fig. 44	SEM micrograph of copper surface obtained after immersion of 432 hours in aqueous solution A5, showing the overall picture of the surface at lower magnification.	106
Fig. 45	SEM micrograph of copper surface obtained after immersion of 432	107

hours in aqueous solution A5, showing the severe attack by the corrosive solution.	
Fig. 46 EDS analysis done at point C in Fig. 45.	108
Fig. 47 EDS analysis done at point B in Fig. 45.	109
Fig. 48 SEM micrograph of copper surface obtained after immersion of 432 hours in aqueous solution A5, showing rough surface.	110
Fig. 49 EDS analysis done at point A in Fig. 48.	111
Fig. 50 EDS analysis done at point B in Fig. 48.	112
Fig. 51 Region of oxide layer surrounding point B in Fig. 48 is presented here at higher magnification. Some cracks are also visible.	113
Fig. 52 SEM micrograph of copper surface obtained after 432 hours of immersion in soil environment S6, showing nucleated oxide particles. The surface was not homogeneous.	115
Fig. 53 SEM micrograph of copper surface obtained after 432 hours of immersion in soil environment S6, showing that Copper Oxide layer was composed of very small nucleated particles.	116
Fig. 54 A magnified SEM view of copper surface obtained after 432 hours of immersion in soil environment S6, showing that Copper Oxide layer was composed of very small nucleated particles.	117
Fig. 55 SEM micrograph of copper surface obtained after 432 hours of immersion in soil environment S6, suggested that small nucleated particles constitute a surface layer, which was not broken, although cracks were present in the layer.	118
Fig. 56 SEM micrograph of copper surface obtained after 432 hours of immersion in soil environment S6, showing that green corrosion products were distributed throughout the surface.	119
Fig. 57 SEM micrograph of copper surface obtained after 432 hours of immersion in soil environment S6. At some places on the surface, the porous nature of the surface film could be discerned.	120
Fig. 58 SEM micrograph of copper surface obtained after 432 hours of immersion in soil environment S8. The surface layer appeared to	122

	peel off from the surface	
Fig. 59	A magnified SEM view of copper surface obtained after 432 hours of immersion in soil environment S8. It is shown that attack took place along some preferred orientation within the grains.	123
Fig. 60	SEM micrograph of copper surface obtained after 432 hours of immersion in soil environment S8, showing white corrosion products.	124
Fig. 61	SEM micrograph of copper surface obtained after 432 hours of immersion in soil environment S8, showing a high magnification view of the region near white corrosion product in Fig. 60.	125
Fig. 62	EDS analysis done at point A in Fig. 61.	126
Fig. 63	EDS analysis done at point B in Fig. 61.	127
Fig. 64	SEM micrograph of copper surface obtained after 432 hours of immersion in soil environment S8, showing a location from where the layer had peeled off from the surface.	128
Fig. 65	EDS analysis done at point A in Fig. 64.	129
Fig. 66	EDS analysis done at point B in Fig. 64.	130
Fig. 67	SEM micrograph of copper surface obtained after 432 hours of immersion in soil environment S8, showing that some chloride contamination due to KCl was present on Copper Oxide layer.	131
Fig. 68	EDS analysis done at point A in Fig. 67.	132
Fig. 69	SEM micrograph of copper surface obtained after 432 hours of immersion in soil environment S8, showing that the surface layer was composed of Copper Oxide particles nucleating and agglomerating on the surface.	133
Fig. 70	EDS analysis done at point A in Fig. 69.	134
Fig. 71	EDS analysis done at point B in Fig. 69.	135
Fig. 72	SEM micrograph of copper surface obtained after 432 hours of immersion in soil environment S9, showing some bright Copper Oxide particles.	137
Fig. 73	EDS analysis done at point A in Fig. 72.	138

Fig. 74	SEM micrograph of copper surface obtained after 432 hours of immersion in soil environment S9, shows a location where the underlying metal has been exposed	139
Fig. 75	EDS analysis done at point A in Fig. 74.	140
Fig. 76	A typical SEM micrograph of copper surface obtained after 432 hours of immersion in soil environment S10.	142
Fig. 77	SEM micrograph of copper surface obtained after 432 hours of immersion in soil environment S10. Bright Copper Oxide scales are peeling off from the surface.	143
Fig. 78	EDS analysis done at point A in Fig. 77.	144
Fig. 79	EDS analysis from the dark region of Fig. 77.	145
Fig. 80	SEM micrograph of copper surface obtained after 432 hours of immersion in soil environment S10. Copper Oxide scale was peeling off and cracks were present on the scale.	146
Fig. 81	SEM micrograph of copper surface obtained after 432 hours of immersion in soil environment S10. A bright copper Oxide scale at higher magnifications is shown.	147
Fig. 82	SEM micrograph of copper surface obtained after 432 hours of immersion in soil environment S10. A bright copper Oxide scale at higher magnifications is shown. The region surrounding the scale is composed of Copper Oxide.	148
Fig. 83	EDS analysis done at point A in Fig. 82.	149
Fig. 84	SEM micrograph of copper surface obtained after 432 hours of immersion in soil environment S10. Some fibrous structure was visible at bottom right corner which appeared to be incorporated into the peeled off layer.	150
Fig. 85	SEM micrograph of copper surface obtained after 432 hours of immersion in soil environment S10, showing fibrous Copper Oxide.	151
Fig. 86	EDS analysis done at point A in Fig. 85.	152
Fig. 87	SEM micrograph of copper surface obtained after 432 hours of immersion in soil environment S10, showing exposed base metal.	153

Fig. 88	SEM micrograph of copper surface obtained after 432 hours of immersion in soil environment S10, showing some Copper Oxide crystals..	154
Fig. 89	EDS analysis done at point A in Fig. 88.	155
Fig. 90	Variation of free corrosion potential of copper as a function of time for immersion in aqueous solutions of different compositions.	159
Fig. 91	Variation of free corrosion potential of copper as a function of time for immersion in soil environment (Set 1).	162
Fig. 92	Variation of free corrosion potential of copper as a function of time for immersion in soil environment (Set 2).	163
Fig. 93	Comparison of linear polarization curves obtained in aqueous solutions after 2 hours of immersion	169
Fig. 94	Comparison of linear polarization curves obtained in aqueous solutions after 432 hours of immersion.	170
Fig. 95	Comparison of linear polarization curves obtained in soil environments (Set 2) after 2 hours of immersion.	171
Fig. 96	Comparison of linear polarization curves obtained in soil environments (Set 2) after 432 hours of immersion.	172
Fig. 97	Nyquist plots obtained in aqueous solutions after 2 hours of immersion.	178
Fig. 98	Bode phase plots obtained in aqueous solutions after 2 hours of immersion.	179
Fig. 99	Bode magnitude plots obtained in aqueous solutions after 2 hours of immersion.	180
Fig. 100	Nyquist plots obtained in aqueous solutions after 432 hours of immersion.	181
Fig. 101	Bode phase plots obtained in aqueous solutions after 432 hours of immersion.	182
Fig. 102	Bode magnitude plots obtained in aqueous solutions after 432 hours of immersion.	183
Fig. 103	Equivalent circuit used for fitting experimental EIS data obtained in	188

	aqueous solutions.	
Fig. 104	Equivalent circuit used for fitting experimental EIS data obtained in aqueous solution A3, when Warburg impedance was also present.	188
Fig. 105	Solution resistance ( $R_s$ ) plotted as a function of time obtained after fitting the experimental data in aqueous solutions with the circuits shown in Figs. 103 and 104.	193
Fig. 106	' $n_1$ ' (for film) plotted as a function of time obtained after fitting the experimental data in aqueous solutions with the circuits shown in Figs. 103 and 104.	194
Fig. 107	Constant phase element ( $Q_1$ ) for surface film plotted as a function of time obtained after fitting the experimental data in aqueous solutions with the circuits shown in Figs. 103 and 104.	196
Fig. 108	Film resistance ( $R_1$ ) plotted as a function of time obtained after fitting the experimental data in aqueous solutions with the circuits shown in Figs. 103 and 104.	198
Fig. 109	' $n_{EDL}$ ' (for double layer) plotted as a function of time obtained after fitting the experimental data in aqueous solutions with the circuits shown in Figs. 103 and 104.	200
Fig. 110	Constant phase element ( $Q_{EDL}$ ) for double layer plotted as a function of time obtained after fitting the experimental data in aqueous solutions with the circuits shown in Figs. 103 and 104.	201
Fig. 111	Charge transfer resistance ( $R_{CT}$ ) plotted as a function of time obtained after fitting the experimental EIS data in aqueous solutions with the circuits shown in Figure 103 and Figure 104.	203
Fig. 112	Damage function plotted as a function of time for all aqueous solutions	205
Fig. 113	Nyquist plots obtained in soil environments after 2 hours of immersion.	207
Fig. 114	Bode phase plots obtained in soil environments after 2 hours of immersion.	208
Fig. 115	Bode magnitude plots obtained in soil environments after 2 hours of	209

	immersion.	
Fig. 116	Nyquist plots obtained in soil environments after 432 hours of immersion.	210
Fig. 117	Bode phase plots obtained in soil environments after 432 hours of immersion.	211
Fig. 118	Bode magnitude plots obtained in soil environments after 432 hours of immersion.	212
Fig. 119	Comparison of Nyquist plots obtained after immersion in aqueous solution A3 and soil environment S8.	219
Fig. 120	Comparison of Nyquist plots obtained after immersion in aqueous solution A1 and soil environment S6.	220
Fig. 121	Comparison of Nyquist plots obtained after immersion in aqueous solution A2 and soil environment S7.	221
Fig. 122	Comparison of Nyquist plots obtained after immersion in aqueous solution A5 and soil environment S10.	222
Fig. 123	Comparison of Bode Phase plots obtained after immersion in aqueous solution A1 and soil environment S6.	224
Fig. 124	Comparison of Bode Phase plots obtained after immersion in aqueous solution A2 and soil environment S7.	225
Fig. 125	Comparison of Bode Phase plots obtained after immersion in aqueous solution A5 and soil environment S10.	226
Fig. 126	Comparison of Bode Phase plots obtained after immersion in aqueous solution A3 and soil environment S8.	227
Fig. 127	Comparison of Bode magnitude plots obtained after immersion in aqueous solution A5 and soil environment S10.	228
Fig. 128	Comparison of Bode magnitude plots obtained after immersion in aqueous solution A1 and soil environment S6.	229
Fig. 129	Comparison of Bode magnitude plots obtained after immersion in aqueous solution A2 and soil environment S7.	230

## LIST OF TABLES

---

Table 1	Standard reference electrode potentials.	25
Table 2	Compositions of different environments	63
Table 3	Free corrosion potential (FCP) values in aqueous solutions obtained at different times.	160
Table 4	Free corrosion potential (FCP) values in soil environments (Set 1) obtained at different times.	165
Table 5	Free corrosion potential (FCP) values in soil environments (Set 2) obtained at different times.	166
Table 6	Polarization resistances ( $R_p$ ) calculated from the linear polarization curves obtained after 2 hours and 432 hours of immersion in the aqueous solutions	173
Table 7	Polarization resistances ( $R_p$ ) calculated from the linear polarization curves obtained after 2 hours and 432 hours of immersion in the soil environments (Set 2)	174
Table 8	Values of fitting parameters modeled from EIS data obtained in aqueous solution.	190
Table 9	Values of fitting parameters modeled from EIS data obtained in soil environments.	215

## INTRODUCTION

### 1.1 Copper

Copper is mankind's oldest metal, dating back to some 10,000 years. All of the great civilizations of the past, including the Sumerian, Egyptian, Greek, roman, and Chinese, used copper and copper alloys (principally and later brass) for both decorative and utilitarian purposes. From antiquity through the Middle Ages and the renaissance, copper was used for military purposes, artistic applications such as church bells and statuary, tools, and numerous other functional objects. However, it was the industrial revolution that brought about a tremendous change in the production and consumption of copper and copper alloys. The industrial importance of copper in the 20<sup>th</sup> and 21<sup>st</sup> centuries has been extended by the ease with which it combines with other metals. Tin and Zinc are always have been the principal alloying elements, but many others-Al, Ni, Be, Cr, Cd, Mn, etc.-form alloys with unique combinations of mechanical and physical properties and excellent corrosion and wear resistance. These attributes have contributed toward copper and its alloys being the material of choice for building construction (e.g., plumbing, wiring, and roofing), but have also led to the use of copper in many demanding engineering applications in the marine, automotive, chemical, and electronics industries. Continuing developments in superconductors, electric vehicles, solar heating, and large-scale desalination of water should ensure that copper remains an essential material in future [1].

Copper, with atomic number 29 and atomic weight 63.546, occupies the first position of subgroup 1B in the periodic table. The single outer shell 4s electron is responsible for many important physical properties of copper, including its high electrical conductivity, its chemical stability and its reddish color. Copper exhibits the face-centered cubic (fcc) structure at all temperatures below the melting point. The density of copper varies from 8.90 to 8.95 g/cm<sup>3</sup>, depending on the metal's thermo mechanical history. Pure copper has a melting point of 1084°C [1]. Copper alloys range in color from

the reddish pink of pure copper to golden yellow and silvery white, depending on alloy composition. Copper, particularly when in the annealed state, is considered a soft and ductile metal. Along with strength, fatigue resistance, and ability to take a good finish, the primary selection criteria for copper and copper alloys are; electrical conductivity, thermal conductivity, corrosion resistance, color, and ease of fabrication.

Copper and copper alloys are widely used in many environments and applications because of their excellent corrosion resistance, which is combination of other desirable properties, such as superior electrical and thermal conductivity, ease of fabricating and joining, wide range of attainable mechanical properties, and resistance to biofouling. Copper corrodes at negligible rates in unpolluted air, water, and deaerated nonoxidizing acids. Copper alloy artifacts have been found in nearly pristine condition after having been buried in the earth for thousands of years, and copper roofing in rural atmospheres has been found to corrode at rates of less than 0.4 mm (15 mils) in 200 years [1]. One thousand mils equals one inch [2]. Copper resists many saline solutions, alkaline solutions, and organic chemicals. However, copper is susceptible to more rapid attack in oxidizing acids, oxidizing heavy metal salts, sulfur, ammonia ( $\text{NH}_3$ ), and some sulfur and  $\text{NH}_3$  compounds. Resistance to acid solution depends mainly on the severity of oxidizing conditions in the solution. Reaction of copper with sulfur and sulfides to form copper sulfide ( $\text{CuS}$  or  $\text{Cu}_2\text{S}$ ) usually precludes the use of copper and copper alloys in environments known to contain certain sulfur species.

## 1.2 Applications

Copper and copper alloys provide superior service in many applications included in the following general classifications [1]:

- Applications requiring resistance to atmospheric exposure, such as roofing and other architectural uses, hardware, building fronts, grille work, hand rails, lock bodies, door-knobs, and kick plates.
- Freshwater supply lines and plumbing fittings, for which superior resistance to corrosion by various types of waters and soils is important.
- Marine applications-most often freshwater and seawater supply lines, heat exchangers, condensers, shafting valve stems, and marine hardware-in which

resistance to seawater, hydrated salt deposits, and biofouling from marine organisms is important.

- Heat exchangers and condensers in marine service, steam power plants, and chemical process applications, as well as liquid-to-gas or gas-to-gas heat exchangers in which either process stream may contain a corrosive contaminant.
- Industrial and chemical plant process equipment involving exposure to a wide variety of organic and inorganic chemicals.
- Electrical wiring, hardware, and connectors; printed circuit boards; and electronic applications that require demanding combinations of electrical, thermal, and mechanical properties, such as semiconductor packages, lead frames, and connectors.
- Underground applications such as electric cables and nuclear waste storage canisters (This is addressed in greater detail below).

The possibility of disposing of nuclear waste in copper containers buried deep underground has been investigated [3-6]. Except for the mining and oil industries, underground construction is usually limited to the first few tens of meters from the surface. However, an underground waste vault would be located at a depth of 500 to 1000 m (1640-3280 ft) in stable bedrock. At these depths, the environment differs in several respects from that nearer the surface. With increasing depth, the natural groundwater tends to become more saline and less oxidizing. In addition, the pressures exerted by hydrostatic and lithostatic forces become greater. These aspects affect the design and corrosion behavior of any metallic structure buried at such great depths.

A copper nuclear waste disposal container would be surrounded by a compacted clay like material. This serves a dual purpose: first it acts as physical barrier, reducing the rate of transport of species to and from the container, and second it provides some chemical buffering effects and effectively increases the pH of the environment. Both of these properties are beneficial in terms of the corrosion resistance of copper.

The clay most likely to be used is a montmorillonite clay, such as sodium bentonite. In the compacted form, this clay swells when wet and would effectively seal all cracks in the surrounding rock. The low permeability of the clay ensures that there would be no mass flow of groundwater and that transport of dissolved species would

occur by diffusion only. The rate of diffusion in the clay is perhaps 100 times slower than in free solution. This slow rate of diffusion applies not only to the transport of oxidants, such as dissolved oxygen ( $O^{2-}$ ) or sulfide ions ( $S^{2-}$ ), to the copper surface but also to the diffusion of soluble corrosion products away from the surface. The net effect is reduction in the corrosion rate of copper compared with that in free solution. One study suggests that under such conditions uniform corrosion of oxygen-free electronic copper would only amount to 1.1 mm (43.4 mils) in  $10^6$  years [5]. Experimental results indicate that the clay may reduce the corrosion rate by about a factor of ten over that in bulk solution, although these results suggest a corrosion rate of about 1  $\mu\text{m}/\text{yr}$  (0.04 mils/yr) [6].

### **1.3 Objectives of the present study**

The corrosion of copper has been investigated extensively both in field studies and in laboratory studies [7-44]. One reason for this is its importance in microelectronic devices, circuit boards, and contacts, while another reason is its extensive use in, e.g. artistic, structural, and architectural applications. Many of the laboratory corrosion testing deals with aqueous solutions. Limited literature is available concerning the corrosion of copper and its alloys in soil environmental conditions. The aim of the present study was to understand the electrochemical behavior (especially passivation) of copper in simulated aqueous and soil environmental conditions containing pollutants (e.g. chloride, sulfide, ammonium ions). Specific attention was focused on understanding the ability of pure copper to form protective surface films and the stability of surface films with time. As a pre-cursor to understanding the corrosion of copper, the long-term corrosion behavior of two archaeological copper samples have also been studied.

### **1.4 Plan of work**

The following plan of work has been adopted for the thesis.

1. Selection of materials for study and preparing the experimental arrangement.
2. Linear polarization behavior of the samples in aqueous and soil environments of different composition.

3. Time dependent electrochemical impedance spectroscopy study of the samples in aqueous and soil environments.
4. Microstructural characterization of the sample surfaces after exposing the samples to aqueous and soil environments.
5. Analysis and interpretation of data.

## **CHAPTER 2**

---

### **LITERATURE REVIEW**

In the present chapter the literature on corrosion of copper in burial environments and atmosphere has been presented. Most of the earlier studies on copper corrosion were done in aqueous solutions. Only limited literature is available for copper corrosion in soil environments under laboratory testing conditions. Some insights on copper corrosion in soil environment have been provided. Copper is a candidate material for nuclear waste storage canisters for geologic disposal of nuclear fuel. The effect of pollutants such as chloride, sulfide and ammonium ions is discussed. A review of various electrochemical techniques used to characterize the electrochemical behavior of copper is also presented. The chapter ends with description of some archaeological analogue studies done on copper.

#### **2.1 Corrosion in Soil**

##### **2.1.1 Introduction to soil corrosion**

Corrosion of metallic materials in soil environment is a major concern, especially as much of the buried infrastructure is aging. Increasingly stringent environmental protection requirements are also placing a focus on corrosion issues. Topical examples of soil corrosion are related to oil, gas, and water pipelines; buried storage tanks (a vast number are used by petrol/diesel stations); electrical communication cables and conduits; anchoring systems etc. Such systems are expected to function reliably and continuously over several decades.

Soil corrosion is a complex phenomenon, with a multitude of variables involved. Chemical reactions involving almost each of the existing elements are known to occur in soils, many of which are not yet fully understood. Soil is an aggregate of minerals, organic matters, water, and gasses (mostly air). It is formed by the combined weathering action of wind and water, and also organic decay. The proportions of the basic

constituents vary greatly in different soil types. Variations in soil properties and characteristics across three dimensions can have a major impact on corrosion of buried structures. For example, the response of carbon steel to soil corrosion depends primarily on the nature of the soil and certain other environmental factors, such as the availability to moisture and oxygen. These factors can lead to extreme variations in the rate of corrosion attack. Under worst conditions, a buried vessel may perforate in less than one year, although archaeological digs in arid desert regions have uncovered iron tools that are hundreds of years old [7].

Some general rules can be formulated. Soils with high moisture content, high electrical conductivity, high acidity, and high dissolved salts will be most corrosive. The effect of aeration on soils is somewhat different from the effect of aeration in water because poorly aerated conditions in water can lead to accelerated attack by sulfate-reducing anaerobic bacteria [7].

## **2.1.2 Soil parameters affecting corrosivity**

Several important variables have been identified that have an influence on corrosion rates in soil. These include water, degree of aeration, pH, redox potential, resistivity, soluble ionic species (salts), and microbiological activity [45]. The complex nature of selected variables is presented graphically in Fig 1.

### **2.1.2.1 Water**

Water in liquid form represents the essential electrolyte required for electrochemical corrosion reactions. A distinction is made between saturated and unsaturated water flow in soils. The latter represents movement of water from wet areas toward dry soil areas. Saturated water flow is dependent on pore size and distribution, texture, structure, and organic matter. Water movement in soil can occur by the following mechanisms: gravity, capillary action, osmotic pressure (from dissolved species), and electrostatic interaction with soil particles. The water-holding capacity of a soil is strongly dependent on its texture. Coarse sands retain very little water, while fine clay soils store water to a high degree.

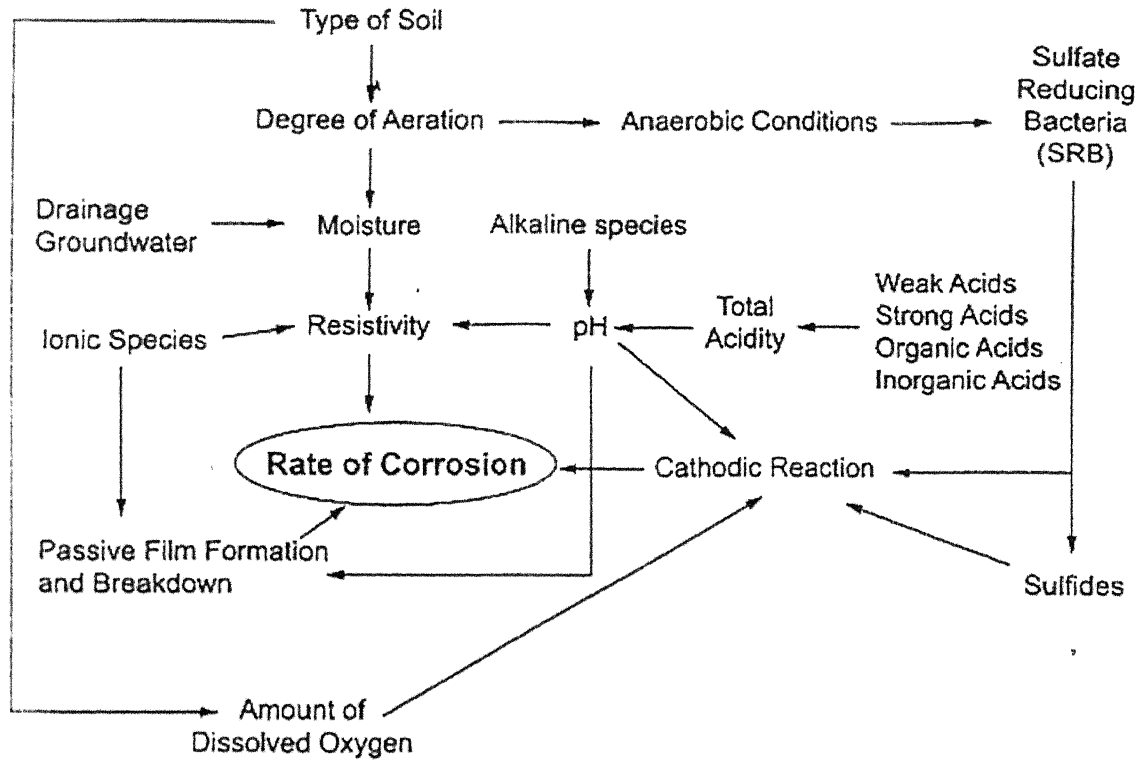


**Fig. 1** Relationship of variables affecting the rate of corrosion in soil is presented. For simplicity, only the MIC effects of sulfate-reducing bacteria are shown [45].

#### **2.1.2.2 Degree of aeration**

The oxygen concentration decreases with increasing depth of soil. In neutral or alkaline soils, the oxygen concentration obviously has an important effect on corrosion rate as a result of its participation in the cathodic reaction. However, in the presence of certain microbes (such as sulfate reducing bacteria), corrosion rates can be very high, even under anaerobic conditions. Excavation can obviously increase the degree of aeration in soil, compared with the undisturbed state. It is generally accepted that corrosion rates in disturbed soil with greater oxygen availability are significantly higher than in undisturbed state.

#### **2.1.2.3 pH**

Soils usually have a pH range of 5 to 8. in this range, pH is generally not considered to be the dominant variable affecting corrosion rates. More acidic soils obviously represent a serious corrosion risk to common construction materials such as steel, cast iron, and zinc coatings. Soil acidity is produced by mineral leaching, decomposition of acidic plants, industrial wastes, acid rain, and certain forms of microbiological activity. Alkaline soils tend to have high sodium, potassium, magnesium, and calcium contents. The latter two elements tend to form calcareous deposits on buried structures, and these have protective properties against corrosion. The pH level can affect the solubility of corrosion products and also the nature of microbiological activity.

#### **2.1.2.4 Soil resistivity**

Resistivity has historically often been used as a broad indicator of soil corrosivity. Since ionic current flow is associated with soil corrosion reactions, high soil resistivity will arguably slow down corrosion reactions. Soil resistivity generally decreases with increasing water content and the concentration of ionic species. Soil resistivity is by no means the only parameter affecting the risk of corrosion damage. A high soil resistivity alone will not guarantee absence of serious corrosion.

#### **2.1.2.5 Chlorides**

Chloride ions are generally harmful, as they precipitate directly in anodic dissolution reactions of metals. Furthermore, their presence tends to decrease the soil resistivity. They may be found naturally in soils as a result of brackish groundwater and historical geological sea beds or come from external sources such as deicing salts applied to roadways. The chloride ion concentration in the corrosive aqueous soil electrolyte will vary as soil conditions alternate between wet and dry.

#### **2.1.2.6 Sulfates**

Compared to the corrosive effect of chloride ions, sulfates are generally considered to be more benign in their corrosive action toward metallic materials. The presence of sulfates does pose a major risk for metallic materials in the sense that sulfates can be converted to highly corrosive sulfides by anaerobic sulfate reducing bacteria.

#### **2.1.2.7 Microbiologically influenced corrosion**

Microbiologically influenced corrosion (MIC) refers to corrosion that is influenced by the presence and activities of microorganisms and/or their metabolites (the products produced through their metabolism). Bacteria, fungi, and other microorganisms can play a major part in soil corrosion. Spectacularly rapid corrosion failures have been observed in soil as a result of microbial action, and it is becoming increasingly apparent that most metallic alloys are susceptible to some form of MIC.

### **2.2 Corrosion of Copper in soil**

Copper has been one of the corrosion barriers proposed as the canister in the disposal of nuclear wastes. The material selection must be based on the analysis of the geochemical conditions at depth in soil, the interaction between the groundwater and the components in the engineered barrier system and on the analysis of the mechanical situation at the repository level. The design goal has been to isolate the spent nuclear fuel in a canister that would withstand known corrosion processes for at least 100000 years [3].

Copper possesses a very wide thermodynamic stability domain in water (absence of corrosion), particularly in a reducing environment. This special characteristic is dependent upon the absence of complex-forming agents (chloride, sulfur or ammonia species in particular):

- In an oxidizing environment, copper corrodes at low generalized corrosion rates (less than one micrometer per year).
- The risk of localised corrosion by pitting or crevice corrosion cannot be excluded. The mechanical resistance of copper is low in comparison with that of steel: the design of a copper container must be associated with an internal structure in steel, which guarantees the mechanical strength function (for example, the Swedish insert [3] for spent fuel containers)

Werme [3] has reviewed the background to the choice of copper for nuclear waste storage canisters. His experiments include design of a reference waste canister, which has an outer 50 mm thick corrosion barrier of copper and an inner load-bearing nodular cast iron insert. This canister was buried at a depth of 500-700 m in the Swedish bedrock in deposition holes, bored from the floor of access tunnels, surrounded by a 35 cm thick buffer layer of compacted sodium bentonite. After burial the canister was subjected to conditions that will vary from initially oxygenated conditions to oxygen-free, reducing conditions to study its corrosion behavior under repository conditions [3].

The geochemical conditions at the repository play a major role in predicting the corrosion behavior of copper canisters. During the period, ground water chemistry changes as the result of climate change, which is further affecting the pore water composition. As a consequence, the corrosion behavior of the canister will also change with time. However the environment and the corrosion behavior will attain a steady state. The microbial activities at the repository horizon will have a large effect on the geochemical conditions. Puigdomenech *et al* have shown that microbes in hard rock aquifers and tunnels have a dominating role in reducing oxygen [4]. The microbial activity will, therefore be of importance in rapidly re-establishing the reducing conditions. Under oxygen-free conditions, copper will corrode in sulfide-containing groundwater. The worst case scenario for corrosion of the copper canister would be if sulfate-reducing bacteria formed biofilms on the canisters or grew intensively in the

buffer close to the canister. The corrosion process would be controlled by transport of sulfate to the canister, if enough hydrogen or degradable organic carbon were available for such growth. This could lead to considerably accelerated corrosion since the transport of sulfate is expected to be much faster than the transport of sulfide [3].

High levels of oxygen will be present initially during the saturation phase of the repository. During this time the canister surface may become covered with a duplex corrosion product layer. The inner layer will be Cu<sub>2</sub>O and the outer layer will consist of basic Cu<sup>+2</sup> salts, most likely either malachite (Cu<sub>2</sub>CO<sub>3</sub>(OH)<sub>2</sub>) or atacamite (CuCl<sub>2</sub>.3Cu(OH)<sub>2</sub>), depending on the relative concentrations of carbonate and chloride in the water [3].

Once the section of the repository, in which the canister is placed, is closed the remaining oxygen will control the redox potential [3]. The redox potential will drop as the oxygen is depleted from the system especially in the presence of sulfide. When this happens, the thermodynamically stable solids will change from CuO, or CuCl<sub>2</sub>.3Cu(OH)<sub>2</sub>, depending on the pH and Cl<sup>-</sup> activity, to first Cu<sub>2</sub>O and then Cu, or copper sulfides if sulfides are present. In a sealed repository (or a sealed laboratory test setup) the extent of general corrosion is limited by the general lack of oxidants [3].

In order to assess the extent of canister corrosion in the repository, the effects of moisture, oxygen, chloride and sulfide must be considered. Not much work has been done to study the effect of these pollutants in soil environment for copper corrosion. Most of the studies are related to corrosion of Cu-Ni alloys in aqueous solutions, as it is widely used in marine applications. In the present literature review, studies conducted using these pollutants for copper and its alloys in aqueous solutions are described.

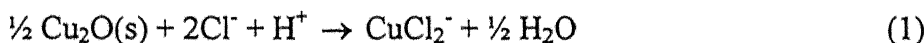
## 2.3 Effect on copper corrosion

### 2.3.1 Chloride ions

A great deal of evidence is available concerning the effect of  $\text{Cl}^-$  on the corrosion of Cu. As can be seen in Fig. 2, chloride ions stabilize dissolved copper as complex anions, such as  $\text{CuCl}_2^-$  and  $\text{CuCl}_3^{2-}$  depending on the  $\text{Cl}^-$  concentration [3]. At sufficiently low pH, Cu corrosion is accompanied by the evolution of  $\text{H}_2$  in  $\text{Cl}^-$  containing solutions. In the presence of oxygen, the thermodynamic stability of  $\text{CuCl}_2 \cdot 3\text{Cu}(\text{OH})_2$  with respect to  $\text{Cu}_2\text{O}$  and  $\text{CuO}$  increases [3]. Kruger [8], demonstrated that not only did the presence of water increase the oxidation rate of Cu (to  $\text{Cu}_2\text{O}$ ) but also that  $\text{Cl}^-$  have an additional pronounced accelerating effect.

Chloride ions will also affect the properties and stability of the surface films. The presence of chloride ions rapidly can reduce the stability of the oxide layer ( $\text{Cu}_2\text{O}$  and  $\text{CuO}$ ) on the copper surface [9]. By incorporation of  $\text{CuCl}$  'islands' in the surface  $\text{Cu}_2\text{O}$  film, defects are created, which are believed to initiation points for pitting. Substitution of monovalent  $\text{Cl}^-$  ions for divalent  $\text{O}^{2-}$  in the  $\text{Cu}_2\text{O}$  lattice enhances the semi conducting properties of the surface film [3]. The  $\text{Cu}_2\text{O}$  film formed in  $\text{Cl}^-$  solutions may, therefore, support  $\text{O}_2$  reduction and the anodic Cu dissolution and, therefore, be less protective than  $\text{Cu}_2\text{O}$  films formed in the absence of  $\text{Cl}^-$ . It should be borne in mind, however that the extent of copper corrosion by oxygen in soil, with or without the presence of high levels  $\text{Cl}^-$  would be limited by the availability of oxygen in the nearby surroundings.

Strandberg and Johansson [10] have shown that chloride induced corrosion starts with the breakdown of the  $\text{Cu}_2\text{O}$  layer that forms in air. Without knowing the detailed mechanism for the chloride-induced breakdown, the overall reaction can be written as:



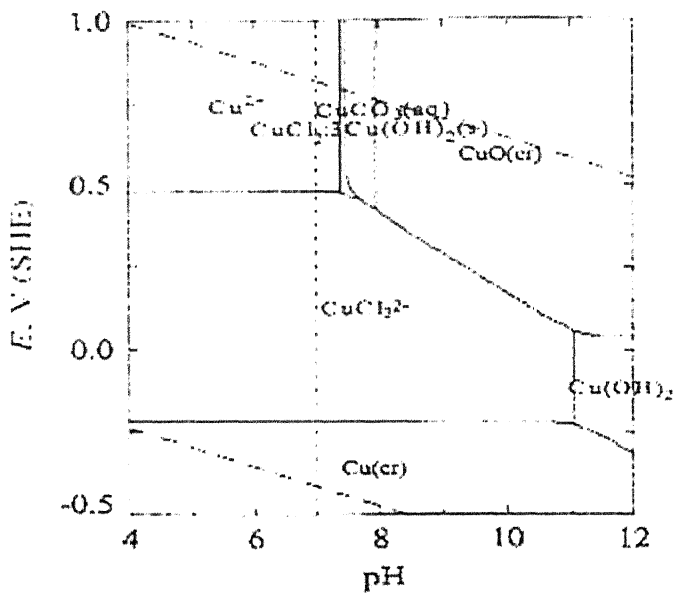
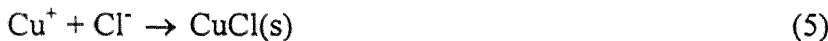
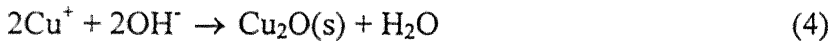


**Fig. 2** Pourbaix diagram for water at 25° C with  $[\text{Cu}] = 10^{-6} \text{ mol kg}^{-1}$  and  $[\text{CO}_3^{2-}] = 2 \text{ mmol kg}^{-1}$  and  $[\text{Cl}^-] = 1.7 \text{ mol kg}^{-1}$  [3].

The corrosion is electrochemical in nature and proceeds by the usual anode and cathode reactions as follows:



Two possible reaction routes can result in the formation of either  $\text{Cu}_2\text{O}$  or nantokite ( $\text{CuCl}$ ), depending on chemical conditions in the aqueous adlayer:



$\text{CuCl}$  was detected on the copper surface if sufficiently large amount of chloride was present during electrochemical exposure [9, 10].

It has been reported in the literature that  $\text{Cu}_2\text{O}$  should be the primary corrosion product in nearly neutral  $\text{Cl}^-$  solutions [12]. It is also suggested that ataconite (cupric hydroxychloride) tended to occur as a specific corrosion product around pitted areas [12].

The films formed on copper in chloride containing solutions are compact and somewhat smoother than the  $\text{Cu}_2\text{O}$  films formed in distilled water [8]. North *et al* have suggested that films formed on copper surface in air are essentially featureless as compared to films formed in 3.4%  $\text{NaCl}$  solution [12]. The epitaxial formation of  $\text{Cu}_2\text{O}$  films in distilled water [8], and the variation of thickness of the films formed in the  $\text{Cl}^-$  solution as a function of substrate structure again indicate that these films are formed directly on the metal by anodic reaction [12].

The accelerating effect of  $\text{Cl}^-$  ions on the oxidation behavior of Cu in solution must again be related to a modification of the defect structure of  $\text{Cu}_2\text{O}$  in such a fashion as to make it even less protective than film formed in distilled water [12]. It is suggested that  $\text{Cl}^-$  from solution replace some  $\text{O}^{2-}$  in the oxide lattice. The charge imbalance so created can be neutralized by one  $\text{Cu}^+$  ion passing into solution for each  $\text{Cl}^-$  substitution, thereby creating an additional neutral cation vacancy. The additional cation vacancies further reduce the barrier presented by the  $\text{Cu}_2\text{O}$  to outward diffusion of  $\text{Cu}^+$  ions. The introduction of  $\text{Cl}^-$  ions into the  $\text{Cu}_2\text{O}$  lattice appears to create some distortion. Also the  $\text{Cl}^-$  degrades the protective nature of  $\text{Cu}_2\text{O}$  films on Cu more effectively than  $\text{OH}^-$  [12].

### **2.3.2 Sulfide ions**

Sulfide is usually introduced in environment in many ways, such as from rotting vegetation and from industrial waste discharge. The mechanism of formation of sulfide in seawater has been discussed by many researchers, among them Richards [13] in 1965. The deleterious effect on the behavior of copper and its alloys in sea water environment has been reported by many investigators (e.g. Refs. 14-16). Most data indicate, acceleration of corrosion of Cu-Ni alloys in sulfide polluted natural water, and similar effects were observed in synthetic seawater and even in aqueous solution of sodium chloride [17]. According to Syrett [18], sulfide interferes with the normal growth of the protective oxide film that forms on the surface of Cu-Ni alloys when exposed to seawater. Normally a thick black layer of scales is formed on copper surface when exposed to sulfide polluted environment

In 1940, Glasstone [19] pointed out that cupric ions in concentrations of  $10^{-9}$  moles  $\text{L}^{-1}$  appreciably increase the rate of oxidation of aqueous sulfide by dissolved oxygen [20]. The oxidation product of sulfide ( $\text{S}^{2-}$ ) is sulfur with oxidation states of 0, 2, 2.5, 4 and 6 [21]. Some of these oxidation products are shown to be corrosive to Cu alloys. Ostlund and Alexander [22] confirmed that the half-life of sulfide at a concentration level of 3.8 ppm in air-saturated sea water is about 20 min. Thus in long term experiments, the concentration of sulfide must be monitored as a function of time. Bates and Popplewell [23] investigated the corrosion of Cu- Ni alloy in aerated, flowing and polluted (10 ppm sulfide) seawater. They showed that 90 Cu-10 Ni suffered slight attack while the attack on 70 Cu-30 Ni was very severe and that the 10 ppm sulfide decayed to 0.1 ppm in 1 day. It has also been reported that free corrosion potential for Cu alloys was shifted gradually in the negative direction as the sulfide concentration was increased [24]. Because of the thermodynamic stability of cuprous sulfide ( $\text{Cu}_2\text{S}$ ) and because of the presence of sulfide minerals in many types of soil, Cu may be subject to corrosion in the presence of sulfide under the long term reducing conditions expected to develop around the copper canisters in the repository [3].

Various scientists have studied the electrochemical and corrosion behavior of Cu alloys in sulfide environments. The majority of these studies are associated with

corrosion of Cu alloys in polluted sea water. Care should be taken in applying the results of these studies to the corrosion of Cu in soil environment (Cu canisters), however because most of them involved Cu-Ni alloys (commonly used in marine heat exchangers) and because the particularly aggressive forms of corrosion observed in these applications are associated with alternating oxidizing and reducing conditions [3].

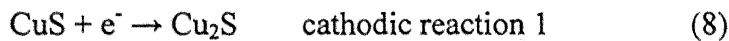
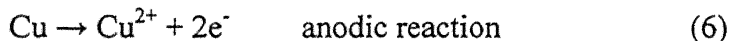
Several electrochemical studies of the early stages of film formation on Cu in sulfide environments have been published. As commonly observed in other environments, Cu forms a duplex corrosion product film in sulfide solutions. It consists of an inner layer of  $\text{Cu}_2\text{S}$  (variously reported to be between 0.4 nm [3] and 25-30 nm thick [3] and a thicker outer layer of CuS. Non-stoichiometric sulfides,  $\text{Cu}_{2-x}\text{S}$ , may form during the conversion of  $\text{Cu}_2\text{S}$  to CuS. The rate of growth of the CuS layer is believed to be controlled by the rate of transport of sulfide to the surface, which would be a particularly slow process in the compacted bentonite to be used in a repository.

Sanchez et al had studied the corrosion mechanism of copper alloys in sulphide contaminated sea water. They had emphasized the specific kinetic effects of the sulphide species, which is the  $\text{SH}^-$  ion at the pH of sea water [25]. The main effect of the pollutant is to accelerate dramatically the rate of oxygen reduction, whereas the anodic process remains practically unaltered; this effect occurred with the alloys studied under most of the experimental conditions. Copper corrosion in presence of sulfide resulted in an increase in the  $\text{O}_2$  reduction current with the corresponding increase in corrosion rate, studied by Sanchez and Schiffrian [25] and also explained in a simple way the reason for the repeatedly reported damaging effect of both sulphide and dissolved oxygen in sea water [26-30]. It has also been found out that either  $\text{CO}_2$  or  $\text{H}_2\text{S}$  in sea water caused otherwise protective cuprite scales upon brass to become non-adherent and non-protective [12].

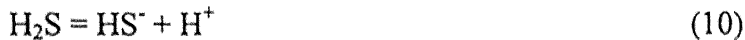
In sulfide-polluted environments all investigators are in basic agreement that the corrosion product is a film of  $\text{Cu}_2\text{S}$ . Many investigators proposed various mechanisms for Cu alloys corrosion in sulfide polluted seawater [18, 31, 32]. By examining the solubility of the various corrosion products, i.e.  $\text{Cu}_2\text{S}$  ( $\text{pK}_{\text{sp}} = 23.7$ ), CuS ( $\text{pK}_{\text{sp}} = 44.07$ ), FeS ( $\text{pK}_{\text{sp}} = 17.1$ ), NiS ( $\text{pK}_{\text{sp}} = 20$ ),  $\text{Ni(OH)}_2$  ( $\text{pK}_{\text{sp}} = 17.19$ ),  $\text{Fe(OH)}_2$  ( $\text{pK}_{\text{sp}} = 13.8$ ) and  $\text{Fe(OH)}_3$

( $pK_{sp} = 38.7$ ), a mechanism can be postulated here to explain the accelerated corrosion in sulfide polluted environment [24].

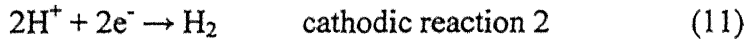
It begins with the dissolution of all the elements in the alloys (Cu-Ni), i.e. Cu, Ni and Fe. The rate of dissolution depends on the exchange current density for each anodic reaction. This means that Cu will dissolve as  $Cu^{+2}$ , Ni as  $Ni^{+2}$ , and Fe as  $Fe^{+2}$  and  $Fe^{+3}$ . due to corrosion product solubility considerations,  $CuS$  will precipitate first. After a period of time, the residual oxygen is consumed and there will be deficiency in the reaction zone. Thus,  $CuS$  conversion to  $Cu_2S$  (metal reduction) will be the cathodic reaction and the corrosion rate will continue, thus:



The violation of the electroneutrality will induce the following equilibrium to the right:



Thus, near the interface (reaction zone) the hydrogen ions concentration will rise inducing another simultaneous cathodic reaction, i.e.



Bolmer [33] suggested that the reduction of hydrogen overvoltage in the presence of dissolved  $S^{2-}$  is related to the easier discharge of hydrogen from hydrogen sulfide molecules, but he suggested a somewhat different discharge scheme:



Kaesche [34] suggested that the discharge of hydrogen ions from  $H_2S$  molecules is energetically more advantageous than the discharge of hydronium ions, due to the lower dissociation energy of HS-H bond. In this case, the reduction of  $H_2S$  molecules can proceed according to the equation:

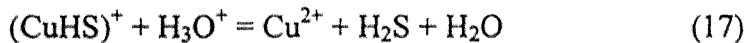
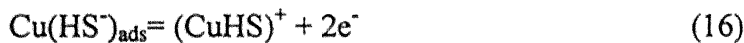
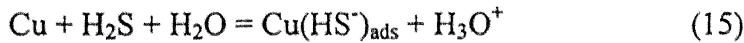


In a similar fashion to  $HS^-$ ,  $S^{2-}$  will regenerate  $H_2S$  molecules, so that a negligible concentration of  $H_2S$  is enough to greatly speed the cathodic reaction.

For the case of aerated and stirred solution, another cathodic reaction accompanies the anodic reaction, which is oxygen reduction. Thus in sulfide polluted seawater under aerated and stirred conditions; the corrosion rate is very high. It is possible to explain the effect of sulfide on the corrosion rate of Cu-Ni alloy from a different point of view.

(1) The catalytic mechanism of the sulfide action, which consists of the formation of an intermediate compound of copper and sulfur, which in the opinion of Hackermann and Makridas [35] is characterized by lower transfer energy across the phase boundary than that of copper ions. This compound dissociates in seawater near the interface, and in this manner the sulfide ions are regenerated. Thus, even small H<sub>2</sub>S concentrations are apt to accelerate the corrosion process appreciably.

(2) According to the mechanism proposed by Iofa [36], the intensification of the anodic reaction of copper ionization by hydrogen sulfide has the following pattern:



Thus, H<sub>2</sub>S acts as a catalyst for the above reaction.

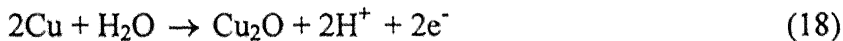
(3) A rather different point of view is put forward by Panasenko [37]. He attributes the acceleration of the anodic reaction to the formation of an intermediate complex (Cu[H<sub>2</sub>S])<sub>ads</sub>. The strong bonding of the metal atoms with sulfur leads to weakening of the bonds between the metal atoms, and this facilitates their passage into solution. The resultant complex decomposes and hydrogen sulfide is regenerated.

### 2.3.3 Ammonium ions

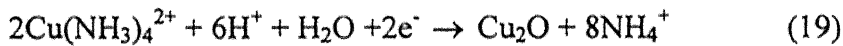
Copper based alloys are susceptible to corrosive attack by ammonia in the environment. Small amounts of ammonia are present as a pollutant in many coastal and estuarine waters used for cooling condensers or other heat exchangers. It is known that ammonia can sometimes give rise to stress corrosion cracking in brass or aluminum brass tubes, and it is becoming recognized that traces of ammonia can also produce abnormal corrosion of copper alloys. Polluted seawater contains ammonia resulting from

decaying organic matter. Ammonia might be present from other sources such as effluent from ammonia plants and from sewage plants. Seawater polluted with ammonia affects the corrosion of copper based alloys in two ways under crevice conditions with heat-transfer; it causes severe pitting and has been reported in one case to induce SCC. Second, ammonia and ammonium salts enhance general attack by dissolving and complexing with the copper ion [38].

Hoar *et al* have studied the effect of ammonia on corrosion of brasses and Cu exposed to solutions containing ammonium and Cu sulphates at various pH values [39]. Their analysis suggested that the bright black film formed on brasses, was associated with rapid intergranular SCC that occurs only on brasses and not on pure Cu. The bright black film formed on brasses was produced by  $\text{Cu}_2\text{O}$ , contaminated by Zn. On isolated Cu in near-neutral solutions containing  $\text{Cu}^{+2}$  and  $\text{NH}_3$ ,  $\text{Cu}_2\text{O}$  can be produced by the local anodic reaction.



which may take place by initial oxidation to  $\text{Cu}(\text{NH}_3)^+$  followed by precipitation to  $\text{Cu}_2\text{O}$ , and by the local cathodic reaction



which may take place by initial reduction to  $\text{Cu}(\text{NH}_3)^+$  followed by precipitation to  $\text{Cu}_2\text{O}$ . The reddish-brown layers found on anodically polarized Cu, in solutions with or without  $\text{Cu}^{2+}$ , undoubtedly arise from Eq. (18).

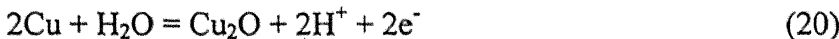
In pure water, copper ions are surrounded by polar water molecules, which form coordination bonds with the copper ion. The solubility of copper in pure water is determined by the ability of the water molecules to shield the copper ion from other copper ions in solution. Complexing of copper occurs with  $\text{NH}_3$ , because the polar  $\text{NH}_3$  molecules replace the water molecules that surround the copper ions in solution. The  $\text{NH}_3$  molecules are more effective at shielding the charge of a copper ion from other copper ions in solution, thereby lowering the activity of the copper ion, and allowing more ions in solution, increasing the solubility [40].

### **2.3.4 Moisture**

Previous studies of copper corrosion in distilled water shows that at low O<sub>2</sub> concentrations only Cu<sub>2</sub>O was formed. The outer surfaces of the cuprite films were relatively rough. It was found that the rate of oxidation of copper in distilled water was greater than that measured in oxygen on similar crystal planes by Rhodin [41]. Comparison of studies on copper corrosion in water and in air shows that water accelerates the growth of Cu<sub>2</sub>O on Cu [12]. The reason for the accelerating effect water lies in a defect structural change in the Cu<sub>2</sub>O film. This effect has been studied previously by Heine *et al* [42] for oxide films on Al. Here it was proposed that OH<sup>-</sup> adsorbed from neutral solutions on the oxide surface, replace some O<sup>2-</sup> in the oxide lattice. The same model has been applied to Cu<sub>2</sub>O formed in distilled water by North and Pryor [12]. Since each OH<sup>-</sup>-O<sup>2-</sup> substitution creates a charge imbalance; electrical neutrality can be restored in one of the two fashions:

- (a) A positive hole could be eliminated from the oxide;
- (b) A Cu<sup>+</sup> ion could pass from the oxide into solution thereby creating an additional neutral cation vacancy.

Kruger [8, 43] showed that Cu<sub>2</sub>O formed epitaxially, in distilled water. The fact that the Cu<sub>2</sub>O forms epitaxially implies that it is direct anodic corrosion product rather than being precipitated from solution. Accordingly, the primary anodic reaction appears to be



Doubtless a minor part of the anodic current is carried by,



### **2.3.5 Oxygen**

Initially, the corrosion will be controlled by the reduction of O<sub>2</sub> to OH<sup>-</sup> according to the reaction



In addition to this reduction process, the corrosion reaction is characterized by such factors as oxide surface films and the concentration of O<sub>2</sub>. The rate of O<sub>2</sub> reduction on the surface will be slower on oxide-covered surfaces than on film-free Cu. The nature of the surface film on the copper will also affect the rate of O<sub>2</sub> reduction. The Cu<sup>+2</sup> salts are electrically insulating and if a continuous layer of these species is formed, the reduction rate of O<sub>2</sub> will be reduced significantly [3]. Generally, the outer layer of the duplex corrosion products will be non-continuous, so that O<sub>2</sub> reduction can proceed on the inner semi conducting Cu<sub>2</sub>O layer.

In a repository, where the copper canister is placed, the rate of reduction is likely to be controlled by the supply of O<sub>2</sub> rather than by the rate of the surface reaction. A consequence of the presence of electrically insulating Cu<sup>+2</sup> salts is the possible spatial separation of anodic and cathodic surface reactions.

### **2.3.6 Localized corrosion**

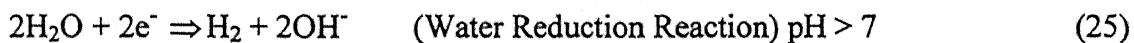
For pure Cu, which does not undergo dealloying, the most important form of localized corrosion is pitting. Pitting of copper water pipes has been studied extensively [33]. Pit initiation involves formation of CuCl pocket in an otherwise protective Cu<sub>2</sub>O film. Dissolution of Cu as CuCl<sub>2</sub><sup>-</sup> occurs at the defect produced by the CuCl pocket. The dissolved Cu<sup>+</sup> is oxidized to Cu<sup>2+</sup> by O<sub>2</sub> and precipitates forming a crust of CuCO<sub>3</sub>.Cu(OH)<sub>2</sub> and CaCO<sub>3</sub>. The crust forms an occluded region in which localized dissolution continues. Water flowing in the pipe of study was containing dissolved ions such as HCO<sub>3</sub><sup>-</sup>, SO<sub>4</sub><sup>-2</sup>, Cl<sup>-</sup> and Ca<sup>+2</sup> etc. [44].

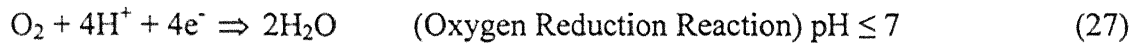
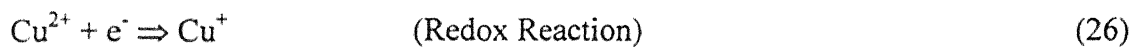
O<sub>2</sub> is a prerequisite for pit propagation. This would not be the case for pits on Cu canisters (or systems with limited amount of oxygen), both because of the limited amount of O<sub>2</sub> available and because of the restricted mass transport conditions, which will limit the supply of O<sub>2</sub> to the corrosion sites. Therefore, pits on Cu canisters will be far likely to die than pits on Cu water pipes as discussed earlier [3].

## 2.4 Electrochemical Corrosion

Corrosion can be defined as the degradation of a metal by an electrochemical reaction with its environment [46]. All metals are found in their low energy state ores, in the form of their oxides, sulfides, carbonates or more complex compounds. Large amount of energy is required in order to extract a pure metal from its ore. This pure metal is a high-energy state of the metal and hence they tend to come back to the low energy state by recombining with the environment. This process is called corrosion. The thermodynamic aspects of corrosion will be briefly discussed. All the interactions between elements and compounds are governed by the free energy changes ( $\Delta G$ ). Any reaction is said to be spontaneous when  $\Delta G$  for the reaction is negative. At room temperature most of the chemical compounds of metals have lower free energy than the pure metals and hence most of the metals have an inherent tendency to corrode.

In all kinds of aqueous corrosion, there are two reactions occurring at the metal/liquid interface; an electron producing reaction (anodic or oxidation reaction) and an electron consuming reaction (cathodic or reduction reaction). The corrosion reaction for the creation of a wet electrochemical cell requires four basic requirements, the cathode on which the reduction reaction occurs, an anode on which oxidation occurs, an electrolyte to act as the conducting medium for ions and a electrical connection for electron to flow between the anode and cathode. The anodic reaction is invariably corrosion of the metal as shown in Eq. 23. Several cathodic reactions can occur during corrosion [47]. The simplest of them is reduction of hydrogen ions as in Eq. 24. In the absence of any of these reactions water reduction will occur as in Eq. 25. Another is reduction of an oxidized ion in solution (redox reaction) as in Eq. 26. And yet another reaction is reduction of dissolved oxygen as in Equations 27 and 28.





The potential difference between the anode and the cathode could be measured by using a high impedance voltmeter in the circuit. This provides only the potential difference between the electrodes and in order to measure the absolute potential we need a third electrode. This third electrode is called as the standard electrode against which all the measurements can be made. Reference electrodes like standard hydrogen electrode (SHE), saturated calomel electrode (SCE), etc. are usually used as the standard electrodes. Table 1 lists some commonly used standard electrodes and their potentials.

**Table 1** Standard reference electrode potentials [48].

Electrode	Electrolyte	Potential (V)
Calomel (SCE)	Saturated KCl	+0.2420
Calomel (NCE)	1.0 M KCl	+0.2810
Calomel	0.1 M KCl	+0.3335
Silver/Silver Chloride (SSC)	1.0M KCl	+0.2224
SSC	Sea water	+0.25 (approx)
Copper/Copper sulfate (CSE)	Sea water	+0.30 (approx)
Zinc	Sea water	-0.79

## 2.4.1 Polarization

When a metal is not in equilibrium with the solution of ions, the electrode potential differs from the standard electrode potential by an amount known as the polarization.

FOLCROFT PA 19  
PO BOX 243  
INTL SUBS AGC  
SCHENKER INTL  
INDIAN INST OF  
\*\*\*\*\*  
014159031205780

.....

Being internal candidate no such  
time is required.

Yes., Protection of basic pay is requested.

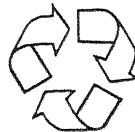
American Chemical Society Member & Subscriber Services  
P.O. Box 3337 Columbus, OH 43210

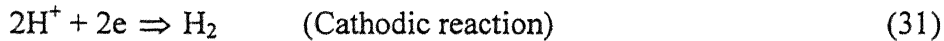
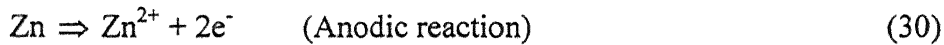
Essential Resources for the Chemical Sciences

ACS PUBLICATIONS

REG. U.S. PAT. & T. OFF. RECYCLING TRADE ASSOCIATION  
MINIMUM 30% POST-INDUSTRIAL CONSUMER CONTENT

RECYCLED  
TM  
PLASTIC





These reactions are called as the half-cell reactions and the potential corresponding to them are called cell potential. The potentials cannot coexist separately on an electrically conducting surface. The potentials will polarize to an intermediate value called as the corrosion potential or mixed potential ( $E_{corr}$ ). When there is no external current flowing into the system, then the equilibrium potential attained is called free corrosion potential ( $E_{corr}$ ).

As the reactions polarize on the same surface the change in potentials is given by,

$$\eta_a = \beta_a \log (i_a/i_o) \quad (32)$$

$$\eta_c = \beta_c \log (i_c/i_o) \quad (33)$$

where  $\eta_a$  and  $\eta_c$  are anodic and cathodic polarization,  $\beta_a$  and  $\beta_c$  are the Tafel constants,  $i_a$  and  $i_c$  are the anodic and cathodic currents respectively. At  $E_{corr}$ , the rates of anodic and cathodic reactions are equal and are equal to the current density,  $i_{corr}$ .

The various polarization techniques that are commonly used are linear polarization, Tafel extrapolation, potentiodynamic polarization and cyclic polarization. These polarization techniques are summarized in the Fig. 3.

The cyclic polarization curve in Fig. 3 will be used for a brief overview on the DC polarization corrosion measurement methods. Applied potentials in Fig. 3 are plotted on the Y-axis against log values of their corresponding electrical current densities on the X-axis. The linear polarization method uses the smallest potential spectrum of all the DC corrosion measurement methods. The circled area in Fig. 3 depicts the location of the linear polarization curve. Linear polarization measurements begin at approximately -20 mV from OCP and end around +20 mV from OCP [2]. Unlike other DC methods, linear polarization data are plotted on a linear graphical scale and the data typically fall on a straight line. The potential spectrum for the Tafel plot method is labeled in Fig. 3 with double arrows next to the potential axis. Tafel plot spectra begin at approximately -250 mV from OCP and end at approximately +250 mV from OCP. Tafel plot data are plotted as potential versus log values of current density as shown in Fig. 3. A Tafel plot has anodic and cathodic branches corresponding to anodic (oxidation) and cathodic

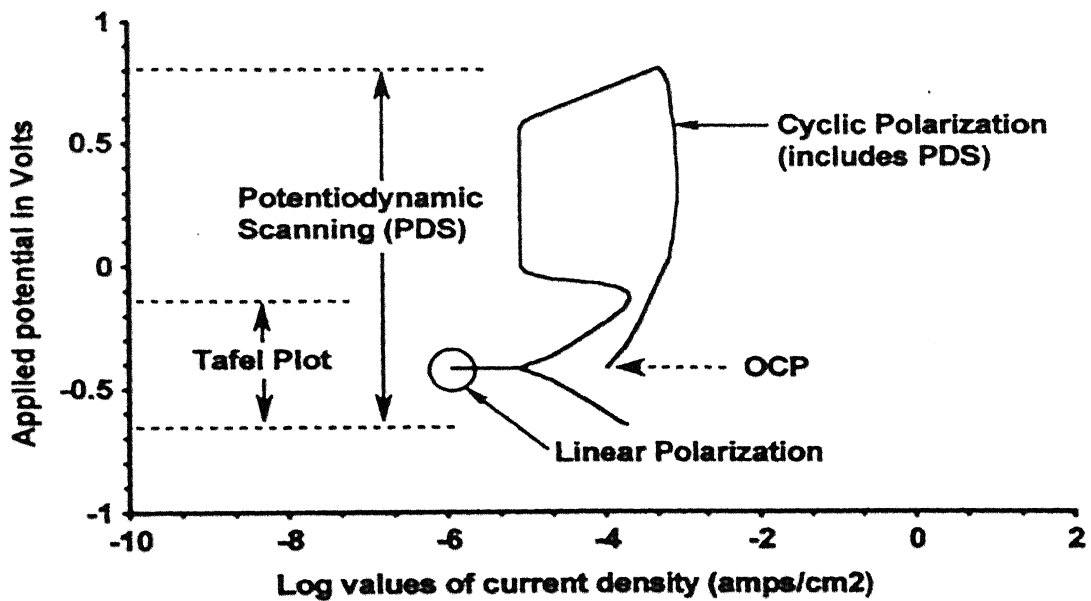


Fig. 3 Various types of polarization methods [2].

(reduction) corrosion half reactions for a metal [2]. The potentiodynamic scanning method uses a potential spectrum that begins around -250 mV from OCP and ends at approximately +1000 mV from OCP [2]. The cyclic polarization method incorporates the potentiodynamic scan potential spectrum, plus potentials from a reverse scan that is initiated from the end of the potentiodynamic scan back to OCP as shown in Fig. 3 [2].

Each method has advantages and disadvantages and one method may be more suitable for a given application than the others, or a combination of several methods may be needed for certain situations.

#### 2.4.2 Linear Polarization

Linear polarization measurements begin at approximately -20 mV from OCP and end around +20 mV from OCP [2]. Figure 4 contains linear polarization data collected with an approximately 20 mV wide potential spectrum. Test electrode electrical; current is zero at OCP, as shown in Fig. 4, and electrode potential polarity switches from cathodic to anodic as the scan proceeds past OCP. The main advantage linear polarization has over other DC corrosion measurement methods is its potential spectrum is so small, that it is essentially a non-destructive test. Consequently, linear polarization measurements can be repeatedly made on the same test electrode, allowing it to be used for applications like long term corrosion monitoring.

The slope of a line is the change in its Y-values divided by the change in its X-values. Hence the slope for a linear polarization curve is the change in potential divided by the corresponding change in current density. This relationship is written mathematically as:

$$\text{Slope} = \Delta E / \Delta i \quad (34)$$

The slope in equation (13) has resistance units in ohm-cm<sup>2</sup> and is referred to as corrosion or polarization resistance,  $R_p$ . The polarization resistance  $R_p$  is derived from the slope of the linear polarization curve when  $i$  tends to zero and is used in calculating the corrosion rates of the alloys using Eq. 35.

$$R_p = \beta a \beta c / 2.3 i_{corr}(\beta a + \beta c) \quad (35)$$

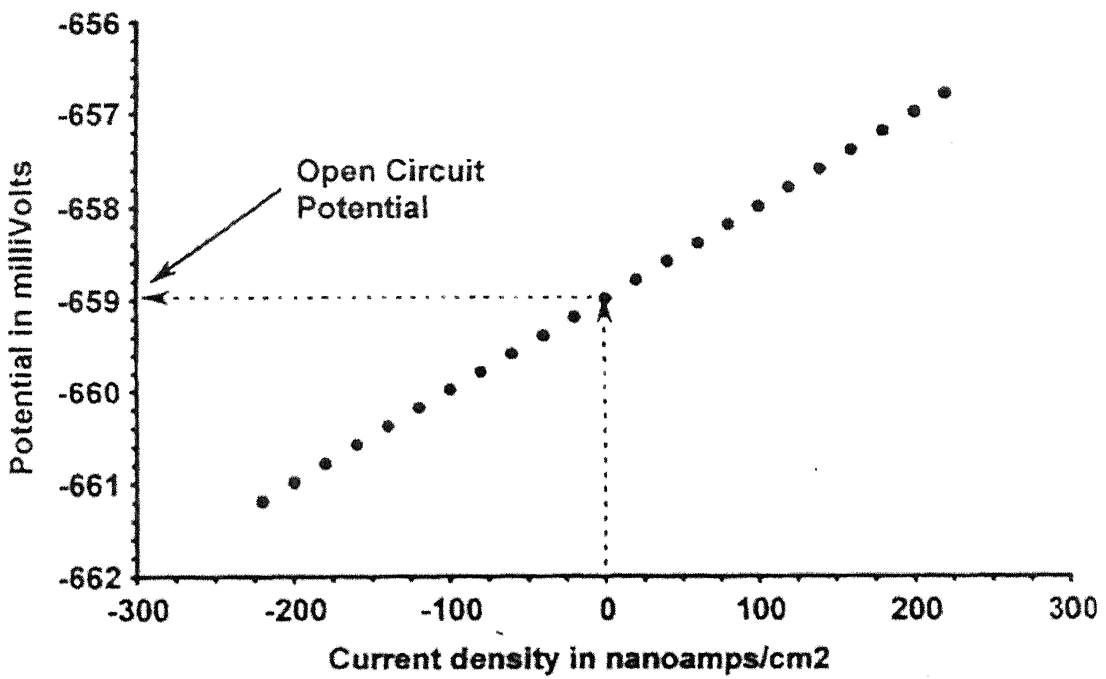


Fig. 4 Example linear polarization curve

where  $\beta_a$  and  $\beta_c$  are the anodic and cathodic Tafel constants [2] and  $i_{corr}$  is the corrosion current density. The main advantage of these methods is that the time taken for conducting experiments is relatively short, whereas the conventional weight loss methods require several days. The polarization methods are highly sensitive, and accelerating factors such as elevated temperature, to increase rates, is generally not necessary.

## 2.5 Electrochemical Impedance Spectroscopy

### 2.5.1 Introduction

Electrochemical systems can be studied with the methods based on impedance measurements. These methods involve the application of a small voltage perturbation, whereas in the methods based on linear sweep or potential step the system is perturbed far from equilibrium. EIS voltages cycle from peak anodic to cathodic magnitudes (and vice versa) using a spectrum of alternating current (AC) voltage frequencies, instead of a range of single magnitude and polarity direct current (DC) voltages. Resistance and capacitance values are obtained from each frequency, and these quantities can provide information on corrosion behavior and rates, diffusion and coating properties. The passive films formed and the electrical double layer is supposed to offer resistance and capacitance to the circuit, whose values are determined from the EIS data. The corrosion rate of a metal in an electrolyte can be determined by AC techniques. These techniques are more or less explicitly based on the hypothesis that the impedance of the metal-electrolyte interface is equivalent to the polarization resistance,  $R_p$ , i.e. the slope of the steady-state current potential curve ( $R_p = dV/di$ )  $E=E_{corr}$ .  $R_p$  is inversely proportional to corrosion current density,  $i_{corr}$ , i.e. the current density which is proportional to the corrosion rate. For determination of  $R_p$ , a sinusoidal current or potential perturbation of very small amplitude (to ensure that the measurement is performed in the linear region of the system) is applied as a function of frequency.

## 2.5.2 Electric circuit representation

Like resistance, impedance is a measure of the ability of a circuit to resist the flow of electrical current. Electrochemical impedance is usually measured by applying an AC potential to an electrochemical cell and measuring the current through the cell. The response to a sinusoidal potential excitation potential is an AC current signal, containing the excitation frequency and its harmonics. Electrochemical impedance is normally measured using a small excitation signal [49]. This is done so that the cell's response is pseudo-linear. In a linear (or pseudo-linear) system, the current response to a sinusoidal potential is a sinusoid at the same frequency but shifted in phase (Fig. 5). The excitation signal, expressed as a function of time, has the form:

$$E(t) = E_0 \cos(\omega t) \quad (36)$$

$E(t)$  is the potential at time  $t$ ,  $E_0$  is the amplitude of the signal, and  $\omega$  is the radial frequency [50]. The relationship between radial frequency  $\omega$  (expressed in radians/second) and frequency  $f$  (expressed in hertz) is:

$$\omega = 2\pi f \quad (37)$$

In a linear system, the response signal,  $I_t$ , is shifted in phase and has different amplitude,  $I_0$ :

$$I(t) = I_0 \cos(\omega t - \phi) \quad (38)$$

An expression analogous to Ohm's Law allows us to calculate the impedance of the system as:

$$Z = \frac{E(t)}{I(t)} = \frac{E_0 \cos(\omega t)}{I_0 \cos(\omega t - \phi)} = Z_0 \frac{\cos(\omega t)}{\cos(\omega t - \phi)} \quad (39)$$

The impedance is therefore expressed in terms of a magnitude,  $Z_0$ , and a phase shift,  $\phi$ .

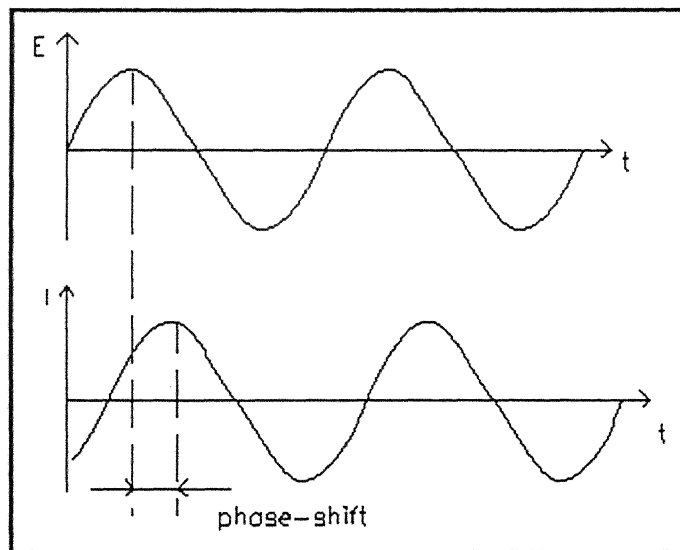


**Fig. 5** Sinusoidal Current Response in a Linear System.

### 2.5.3 Data Presentation

The expression for impedance ( $Z$ ) is composed of a real and an imaginary part. If the real part is plotted on the Y-axis and the imaginary part on the X-axis of a chart, we get a "Nyquist plot" (Fig. 6). It can be noted, that in this plot the y-axis is negative and that each point on the Nyquist plot is the impedance at one frequency. Fig. 6 is annotated to show that low frequency data are on the right side of the plot and higher frequencies are on the left [51]. On the Nyquist plot, the impedance can be represented as a vector of length  $|Z|$ . The angle between this vector and the x-axis is phase shift. However, Nyquist plots have one major shortcoming. It does not give the information about the frequency at which a data point is obtained. The Nyquist plot in Fig. 6, results from the electrical circuit of Fig. 7. The semicircle is characteristic of a single "time constant". Electrochemical impedance plots often contain several time constants. Often only a portion of one or more of their semicircles is seen. Another popular presentation method is the Bode plot (Fig. 8). The X-axis of a Bode magnitude plot contains log values of frequencies (base 10) and the Y-axis contains log values of the total impedance for each frequency. Plot slope is zero when polarization is through resistances, and slope is less than zero when capacitive reactance becomes part of the circuit response to a polarization. Bode phase plot contains log of frequency on the X-axis and the absolute value of the impedance ( $|Z| = Z_0$ ) on the Y-axis [51, 52,].

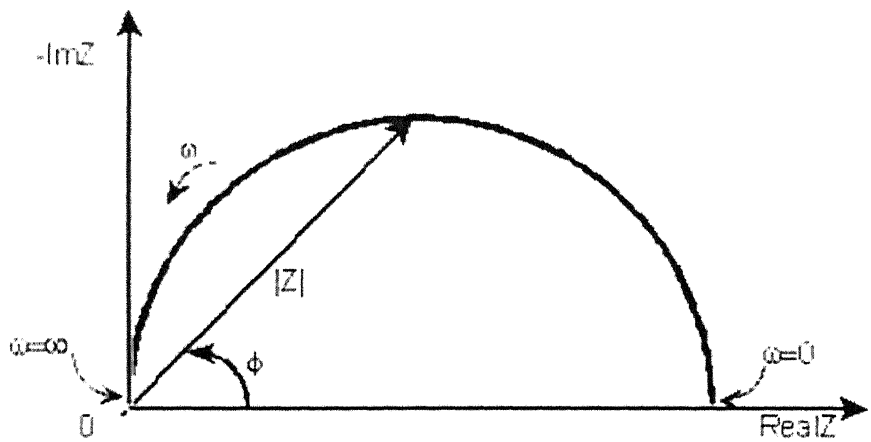
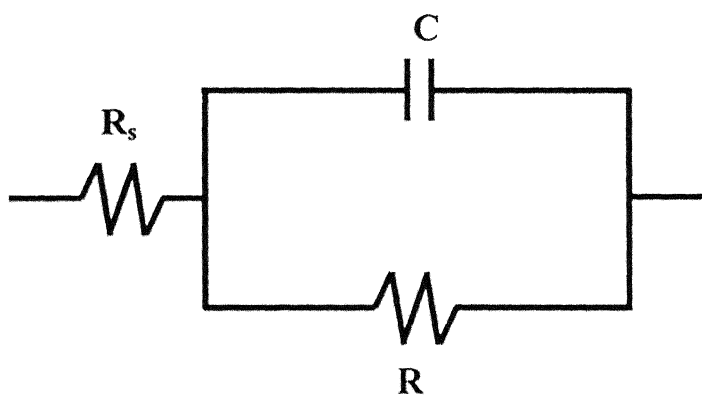
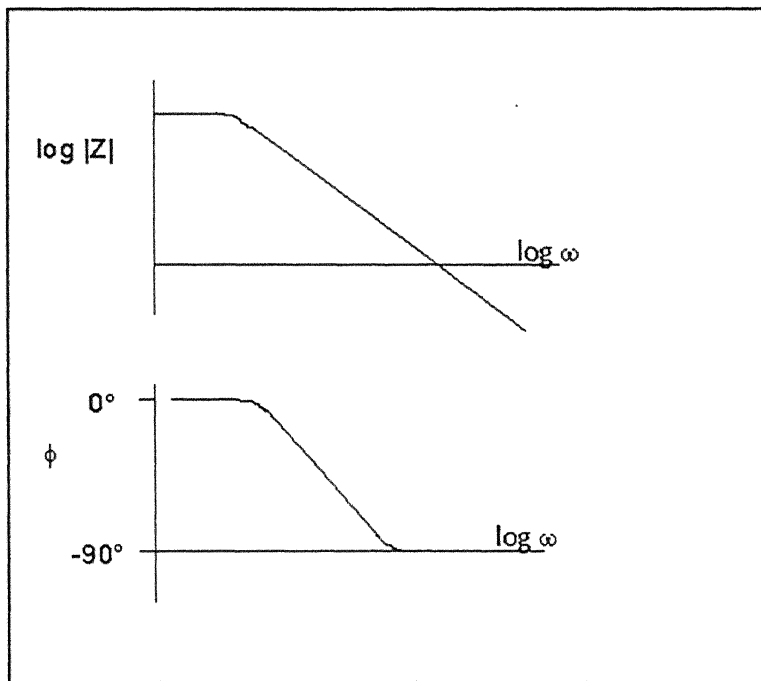


Fig. 6 Nyquist Plot with Impedance Vector.



**Fig. 7** Simple Equivalent Circuit with One Time Constant.



**Fig. 8** Bode plot with one time constant.

## 2.5.4 Physical Electrochemistry and Equivalent Circuit Elements

### Electrolyte Resistance

Solution resistance is often a significant factor in the impedance of an electrochemical cell. A modern 3 electrode potentiostat compensates for the solution resistance between the counter and reference electrodes. However, any solution resistance between the reference electrode and the working electrode must be considered when the cell is modeled. The resistance of an ionic solution depends on the ionic concentration, type of ions, temperature and the geometry of the area in which current is carried. In a bounded area with area  $A$  and length  $l$  carrying a uniform current the resistance is defined as:

$$R = \rho \frac{l}{A} \quad (40)$$

where,  $\rho$  is the solution resistivity [53]. The conductivity of the solution ( $\kappa$ ) is more commonly used in solution resistance calculations. Its relationship with solution resistance is:

$$R = \frac{1}{\kappa} \frac{l}{A} \Rightarrow \kappa = \frac{l}{RA} \quad (41)$$

Unfortunately, most electrochemical cells do not have uniform current distribution through a definite electrolyte area. The major problem in calculating solution resistance therefore concerns determination of the current flow path and the geometry of the electrolyte that carries the current fortunately; solution resistance is not usually calculated from ionic conductance [53]. Instead, it is found when you fit a model to experimental EIS data.

### Double Layer Capacitance

An electrical double layer exists at the interface between an electrode and its surrounding electrolyte. This double layer is formed as ions from the solution "stick on" the electrode

surface. Charges in the electrode are separated from the charges of these ions. The separation is very small, on the order of angstroms. Charges separated by an insulator form a capacitor. The value of the double layer capacitance depends on many variables including electrode potential, temperature, ionic concentrations, types of ions, oxide layers, electrode roughness, impurity adsorption, etc.

## Polarization Resistance

Whenever the potential of an electrode is forced away from its value at open circuit, that is referred to as polarizing the electrode. When an electrode is polarized, it can cause current to flow via electrochemical reactions that occur at the electrode surface. The amount of current is controlled by the kinetics of the reactions and the diffusion of reactants both towards and away from the electrode. In cells where an electrode undergoes uniform corrosion at open circuit, the open circuit potential is controlled by the equilibrium between two different electrochemical reactions. One of the reactions generates cathodic current and the other anodic current. The open circuit potential ends up at the potential where the cathodic and anodic currents are equal. It is referred to as a mixed potential. The value of the current for either of the reactions is known as the corrosion current.

When there are two simple, kinetically controlled reactions occurring, the potential of the cell is related to the current by the following (known as the Butler-Volmer equation).

$$I = I_{corr} \left( 10^{\frac{2.303(E-E_{oc})}{\beta_a}} - 10^{\frac{-2.303(E-E_{oc})}{\beta_c}} \right) \quad (42)$$

where,

I is the measured cell current in amps,

$I_{corr}$  is the corrosion current in amps,

$E_{oc}$  is the open circuit potential in volts,

$\beta_a$  is the anodic Beta coefficient in volts/decade,

$\beta_c$  is the cathodic Beta coefficient in volts/decade.

If a small signal approximation ( $E - E_{oc}$  is small) is applied to then following expression for  $I_{corr}$ , which is indicative of corrosion rate, is obtained:

$$I_{corr} = \frac{\alpha_a \alpha_c}{2.303 (\alpha_a + \alpha_c)} \left( \frac{1}{R_p} \right) \quad (43)$$

This introduces a new parameter,  $R_p$ , the polarization resistance. The polarization resistance behaves like a resistor. From the above equation it is visible that  $I_{corr}$  is inversely proportional to  $R_p$ .

### Charge Transfer Resistance

A similar resistance is formed by a single kinetically controlled electrochemical reaction. In this case we do not have a mixed potential, but rather a single reaction at equilibrium. Consider a metal substrate in contact with an electrolyte. The metal molecules can electrolytically dissolve into the electrolyte, according to:



or more generally:



In the forward reaction in the first equation, electrons enter the metal and metal ions diffuse into the electrolyte. Charge is being transferred. This charge transfer reaction has a certain speed. The speed depends on the kind of reaction, the temperature, the concentration of the reaction products and the potential. The general relation between the potential and the current is:

$$i = i_0 \left[ \frac{C_o}{C_o^*} e^{\left(\frac{\alpha n F \eta}{RT}\right)} - \frac{C_R}{C_R^*} e^{\left(\frac{-(1-\alpha)n F \eta}{RT}\right)} \right] \quad (46)$$

with,

$i_0$  = exchange current density

$C_o$  = concentration of oxidant at the electrode surface

$C_o^*$  = concentration of oxidant in the bulk

$C_R$  = concentration of reductant at the electrode surface

$F$  = Faradays constant

$T$  = temperature

$R$  = gas constant

$\alpha$  = reaction order

$n$  = number of electrons involved

$\eta$  = overpotential ( $E - E_0$ )

The overpotential,  $\eta$ , measures the degree of polarization. It is the electrode potential minus the equilibrium potential for the reaction. When the concentration in the bulk is the same as at the electrode surface,  $C_o=C_o^*$  and  $C_R=C_R^*$ . This simplifies the above equation into:

$$i = i_0 \left[ e^{\alpha \frac{nF}{RT} \eta} - e^{-(1-\alpha) \frac{nF}{RT} \eta} \right] \quad (47)$$

This equation is called the Butler-Volmer equation. It is applicable when the polarization depends only on the charge transfer kinetics. Stirring will minimize diffusion effects and keep the assumptions of  $C_o=C_o^*$  and  $C_R=C_R^*$  valid. When the over potential,  $\eta$ , is very small and the electrochemical system is at equilibrium, the expression for the charge transfer resistance changes into:

$$R_{ct} = \frac{RT}{nFi_0} \quad (48)$$

From this equation the exchange current density can be calculated when  $R_{ct}$  is known.

## Diffusion

Diffusion can create impedance known as the Warburg impedance. This impedance depends on the frequency of the potential perturbation. At high frequencies the Warburg impedance is small since diffusing reactants don't have to move very far. At low frequencies the reactants have to diffuse farther, thereby increasing the Warburg impedance. On a Nyquist plot the Warburg impedance appears as a diagonal line with a slope of 0.5. On a Bode plot, the Warburg impedance exhibits a phase shift of 45°.

## Coating Capacitance

A capacitor is formed when two conducting plates are separated by a non-conducting media, called the dielectric. The value of the capacitance depends on the size of the plates, the distance between the plates and the properties of the dielectric [54]. The relationship is:

$$C = \frac{\epsilon_0 \epsilon_r A}{d} \quad (49)$$

With,

$\epsilon_0$  = electrical permittivity

$\epsilon_r$  = relative electrical permittivity

A = surface of one plate

d = distances between two plates

### 2.5.5 Physical Significance

In order to obtain information about physical parameters such as polarization resistance, double layer capacitance etc, AC equivalent circuits presented in Figs. 9 and 10 are fitted to the experimental EIS data. A physical significance of the circuit used is presented in Fig. 11. A porous layer was formed on the base material in Fig. 11. At the locations where base metal was exposed, an electrical double layer would form. These sites were susceptible for localized corrosion. Circuits and their typical impedance response, used in Chapter 4 to fit the experimental data of various electrolyte compositions used in the AC-impedance study, will be discussed in this section.

The interpretation of EIS data using equivalent circuits can yield a substantial amount of information on the properties of evolving films. It should be noted that before preceding that, as with many electrochemical techniques, EIS records only a general surface response and not yield site-specific information. For the present application this means that EIS may successfully detect low-impedance path-ways associated with pores but cannot differentiate easily between a large number of narrow pores and a small

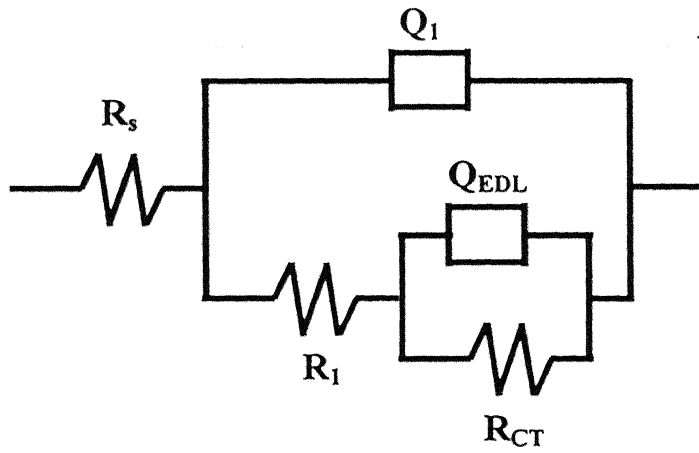


**Fig. 9** Equivalent circuits used for modeling experimental EIS data, when a porous layer is present.

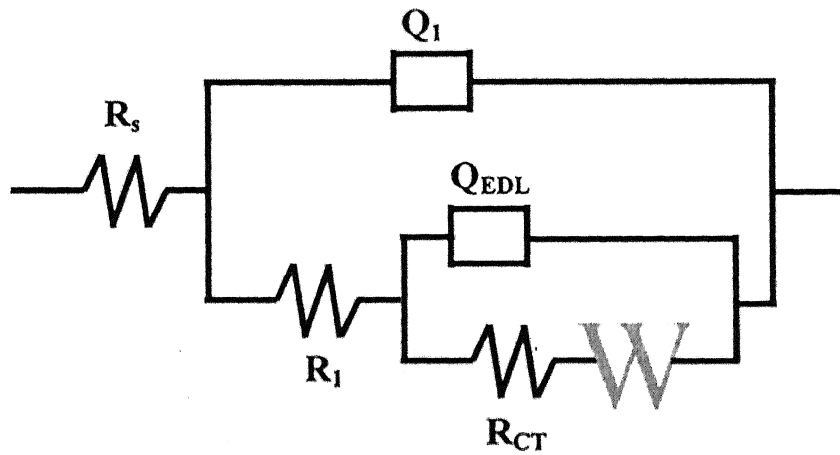


**Fig. 10** Equivalent circuits used for modeling experimental EIS data, when a porous layer is present and also diffusion processes are dominating for determining the corrosion rate of reaction.

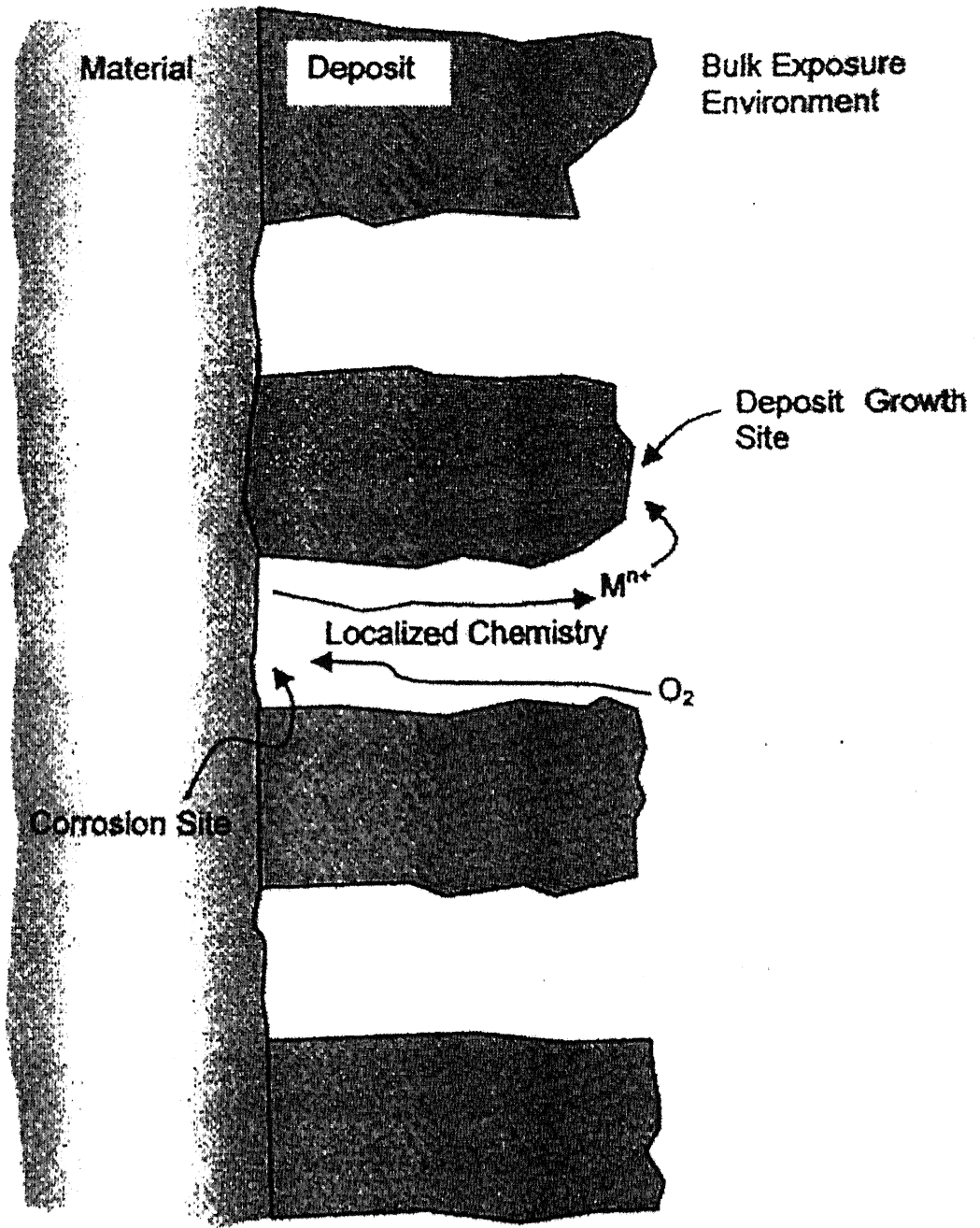


**Fig. 11** Schematic of an idealized corrosion product deposit on a corroding surface. The whole metal surface is not covered with deposit. Pores are showing the exposed metal [56].

number of larger ones; i.e., it cannot on its own provide an accurate measure of deposit porosity. Microscope and metallographic measurements are necessary complements.

For the circuits shown in Figs. 9 and 10, the meaning of various symbols is as follows:

$R_s$	Solution Resistance
$Q_1$	CPE due to porous product layer
$R_1$	Resistance due to porous product layer
$Q_{EDL}$	CPE due to electric doublet layer
$R_{CT}$	Charge transfer resistance
W	Warburg impedance

The CPE considers the fact that experimentally, the barrier film never exhibits the theoretically expected phase shift of  $-90^\circ$  and a slope of -1 for an ideal dielectric. The fitting procedure revealed that better agreement between theoretical and experimental data was obtained if a frequency dependent constant-phase element (CPE) was used instead of pure capacitance. The impedance of a constant phase element is defined in as [52, 55]:

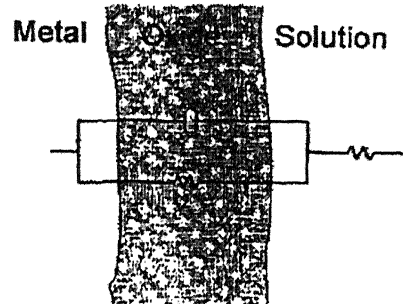
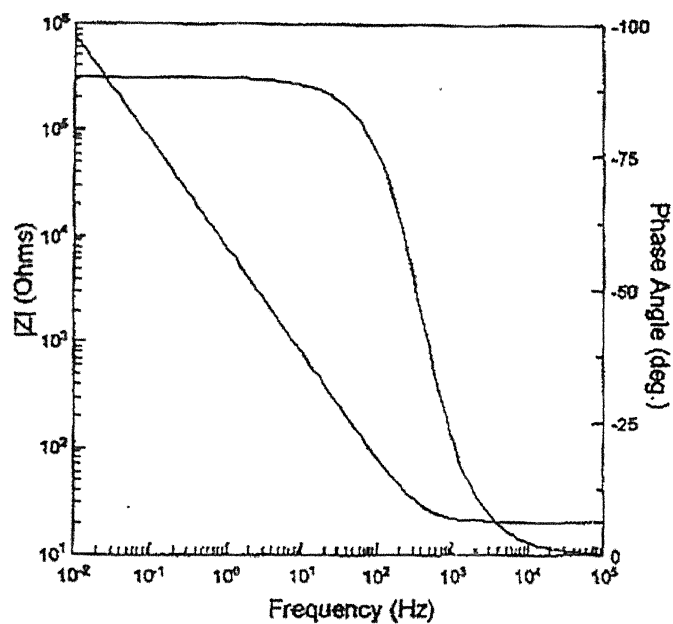
$$Z_{CPE} = [Q(j\omega)^n]^{-1} \quad (50)$$

where  $Q$  and  $n$  are frequency independent parameters, which usually depend on temperature and  $-1 \leq n \leq 1$  [52]. CPE describes an ideal capacitor for  $n = 1$  and an ideal resistor for  $n = 0$ . Generally the appearance of a CPE is due to the presence of inhomogeneities in the electrode-material system or due to surface roughness.

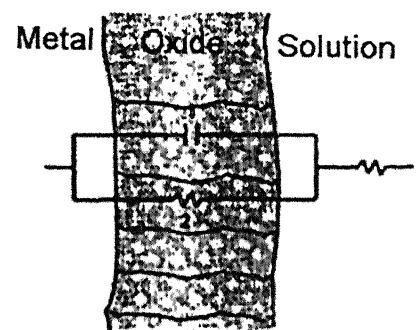
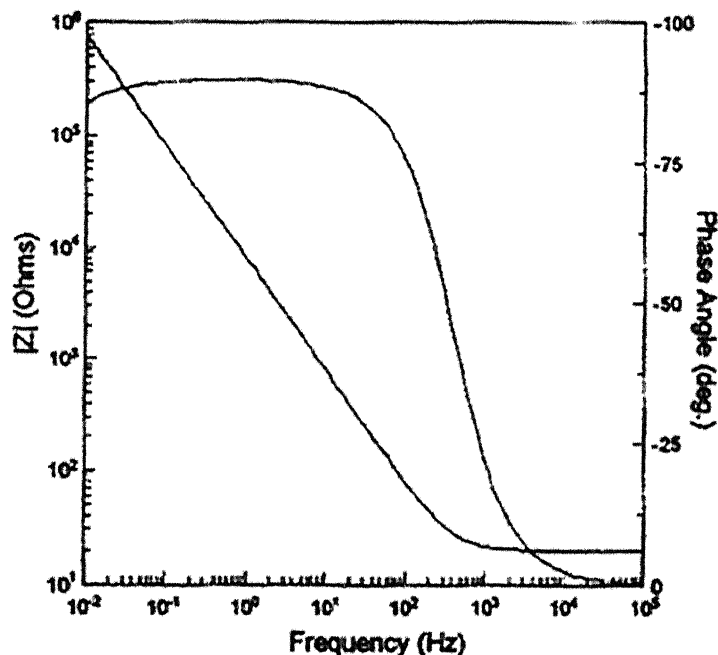
Figure 12 shows a collection of potential EIS responses and possible equivalent circuits that could be used to interpret them in terms of deposit porosities. The key features in the spectra illustrating the influence of the deposit on the corrosion process are to be found at the low frequency ends of the spectra. For a nonporous deposit, the response and simple parallel circuit shown in Fig. 12a would be expected. Here the deposit effectively acts a capacitor. Such a deposit is unlikely, and a system yielding this kind of response can be considered passive, since corrosion at the material/deposit interface could only be sustained by film dissolution/corrosion at the oxide/solution interface.

Deposits with extremely low porosities or an interconnected network of fine crystalline grain boundaries would be expected to show some loss of phase shift at low frequencies (i.e., a less than fully capacitive response) as the real resistance of the flaws become detectable (Fig. 12b). The value of resistance in Fig. 12b is inversely proportional to the corrosion rate.

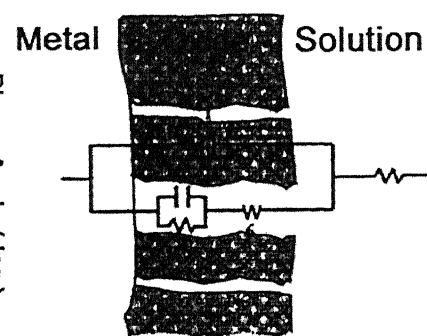
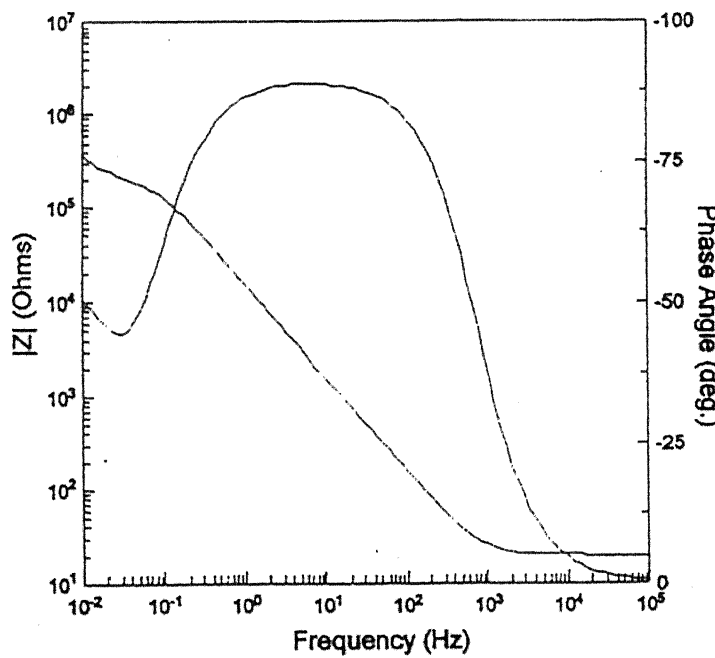
Eventually as pores increase in size, additional circuit elements are required to account for the detection of these pores as discrete time constants in the low frequency end of the spectrum (Fig. 12c). As frequencies are scanned to lower values in recording the EIS spectrum, the frequency at which the decrease in phase shift (i.e. a decrease in the absolute value of the phase angle) commences provides an indication of either the number density of fine pores or the dimensions of a smaller number of larger pores. The value of the pore resistance ( $R_{PORE}$ ) is a more direct indication of pore dimension. The interfacial capacitance ( $C_1$ ) approaches values anticipated for the double-layer capacitance at the material/solution interface but could be significantly increased if adsorbed intermediates are involved in the interfacial corrosion process. The interfacial resistance,  $R_1$ , is the system polarization resistance and it is inversely related to the corrosion rate. Since both anodic and cathodic reactions occur at the base of pores in the deposit,  $R_1$  cannot distinguish which of these two reactions is of overriding importance in determining the corrosion rate.



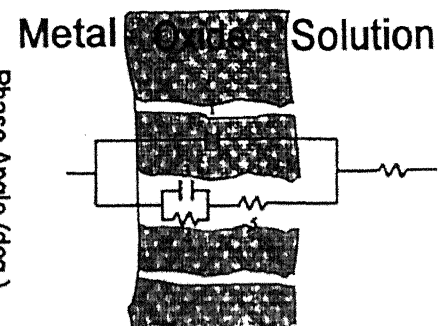
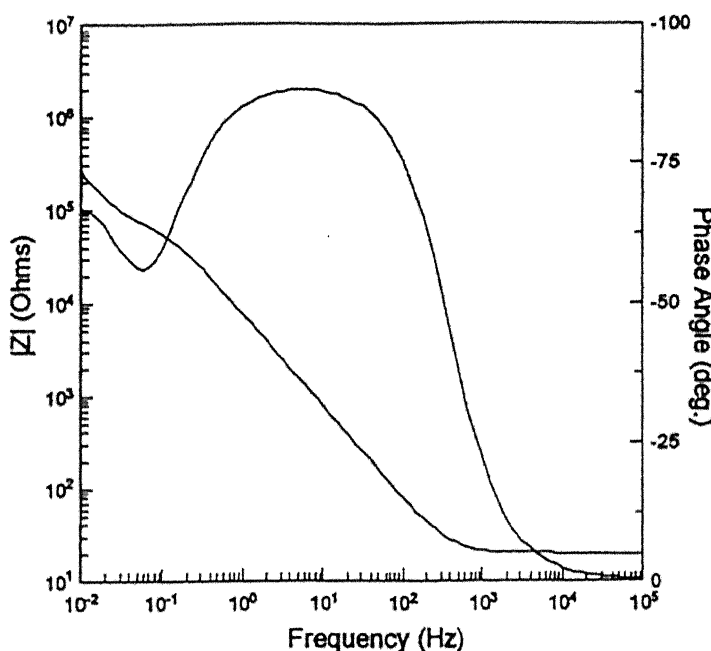
(a)



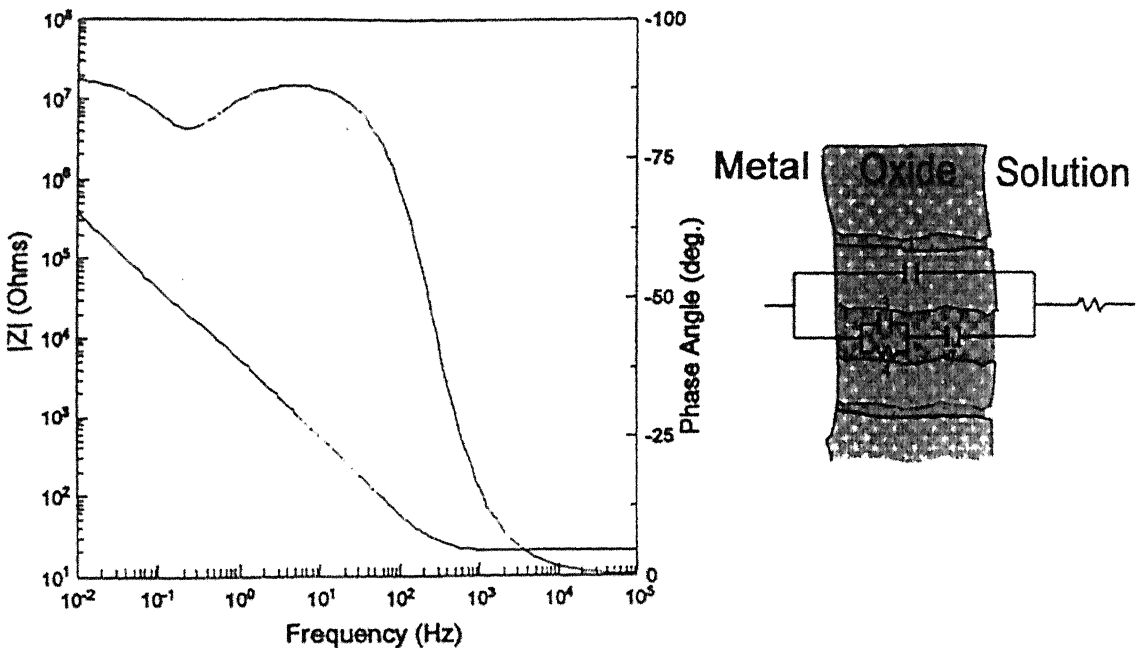
(b)



(c)



(d)



(e)

**Fig. 12** Schematic Bode plots from EIS measurements and equivalent circuits that could be used to fit them for various possible corrosion product deposit structures: (a) nonporous deposit (passive film); (b) deposit with minor narrow faults such as grain boundaries or minor fractures; (c) deposit with discrete narrow pores; (d) deposit with discrete pores wide enough to support a diffusive response (to the a c perturbation) within the deposit; (e) deposit with partial pore blockage by a hydrated deposit [56].

When diffusion is the rate controlling step, the use of the Warburg impedance ( $Z_w$ ) is required to fit the data, where

$$Z_w = \sigma\omega^{-1/2}(1-j) \quad (51)$$

and  $\sigma$  ( $\text{ohm s}^{1/2}$ ) is the Warburg impedance coefficient. In this case, the  $\log |Z|$  vs.  $\log f$  (frequency) plot will approach a slope of -0.5 and a phase angle ( $\theta$ ) of -45 degrees as  $\omega \rightarrow 0$ . Inevitably, diffusion is not totally dominant, and control of the corrosion process at the base of the pore will be partially controlled by interfacial kinetics. For this situation, the slope of  $\log |Z|$  against  $\log f$  will change with frequency in the range 0 to -0.5, and  $\theta$  will change with frequency over the range 0 to -45 degrees as illustrated in Fig. 12d [56].

The final section of Fig. 12e shows the EIS response anticipated if the accumulation of hydrated deposits were to partially reseal the pores. These deposits tend to act like a capacitor,  $C_H$ . Such an EIS response would be anticipated in complex environments (e.g., ones containing a number of anions) or in pores with complex chemistry (e.g., containing large gradients in pH and/or metal cation complexants). It is clear from the Bode plots in Fig. 12 that distinguishing between possible behavior is not simple.

## 2.6 Archaeological analogues

The development of nuclear energy, as many of other industrial activities, leads to the production of numerous types and quantities of wastes. These have the peculiarity of being radioactive for periods varying from some hours to millenia. The nuclear industry is not the only source of these wastes: other industries, as well as medicine, also generate waste. Most countries which have opted to dispose of their longer-lived products are exploring the possibilities of burial in suitable geological formations. In this way they are able to minimize the surveillance constraints for following generations.

A study conducted in France suggested that the amount of radioactive waste annually produced in France represents about  $28000 \text{ m}^3$ . The major part (90%) is of weak activity, with a half life of less than 30 years. The remaining 10% have a longer half life upto several thousand years [57]. In the case of underground disposal these radionuclides will be locked into metallic canisters, which will confine them for a few centuries.

resistance. A good example of archaeological analogue providing supporting validation is the example of the 1600 year old corrosion resistant Delhi Iron pillar [59], a classic example of phosphoric iron construction due to the formation of a protective passive film on the surface.

In contrast to short-term storage, a long-term nuclear waste storage must essentially involve storage in deep underground repositories because the time frame involved is much longer [58]. The design life is a minimum  $10^5$  years. The environment to which the long-term nuclear waste storage canisters will be exposed to will depend upon the storage philosophy adopted by the respective nuclear waste producing countries. For example, the American plan consists of storing the long-term wastes encased finally with a 20 mm thick canister constructed out of a Ni-based alloy (56Ni-22Cr-13.5Mo-3W-3Fe). A 50 mm thick type 316NG stainless steel inner container will provide the necessary structural integrity. These canisters will be stored in depository caves dug into the Yucca Mountain in Utah [60]. On the other hand, the Finnish and Swedish design of spent nuclear fuel package calls for packing the spent fuel in a canister made of spheroidal graphite cast iron, with an outer shield made of copper. The copper shield is responsible for the corrosion protection of the canister [3, 61, 62].

The design thickness of the wall of the storage canister is an important design parameter and this will be primarily based on the maximum corrosion allowance of the selected material in disposal conditions [58]. Considering copper as candidate canister material for long-term storage, the corrosion rates measured in weight loss coupon tests of relatively short duration (7 days), in bentonite clay environment, are of the order of 2 mm/year [61, 62]. This corrosion rate would indicate a lifetime of roughly 2500 years for a designed wall thickness of the copper shield of about 50 mm. This is clearly lower than that required for a life of more than  $10^5$  years. A far bigger problem is that the actual condition of the material after long-term exposure is not known and neither it is possible to obtain such data by laboratory testing alone.

It is in this regard that archaeological copper analogues can be very useful in understanding and validating theoretical models for long-term corrosion of copper in burial conditions. For example, the ancient Indian copper samples discussed here as examples, are very old samples, of conservative age of more than 3000 years old. It

would be beneficial in the current context to explore some information about long-term corrosion processes from these samples.

The archaeological samples that have been analyzed here belong to the chalcolithic period and were excavated at Balathal. Balathal is one among several chalcolithic sites discovered in the Mewar region of south Rajasthan. Recent excavations at Balathal in Udaipur District have revealed that it could be the oldest known village outside the domain of the Indus (Harappan) civilization [63, 64]. Radiocarbon dating has provided firm dates between 2350 BC and 1800 BC, thereby firmly placing it as a chalcolithic site [63]. The characteristic features of this culture are a variety of ceramics, beads of semi-precious stones and terracotta and animal figurines, copper technology, absence of stone blades and microliths, and an economy based on plant cultivation, animal husbandry, and limited hunting and fishing [63]. One of the main applications of Cu-based alloys in these cultures was for the manufacture of sharp-edge cutting tools, as copper based tools perform better than stone tools. The word *chalcolithic* itself implies “copper -stone”, thereby indicating that copper and stone tools were simultaneously utilized in this cultural phase of Indian history [58]. The Harappan influence was noted in the copper implements (barbed arrowheads, knives, chisel, chopper, nail) discovered at Balathal as they were similar to those found in association with Harappans. The Balathal site is close to Ahar (~ 35 km) from where the inhabitants could have obtained copper implements [63, 64]. It has also been suggested that, as the site is close to copper ore deposits, the chalcolithic people could have exploited the same [63].

### **EXPERIMENTAL PROCEDURE**

The experimental procedure adopted in the present work to understand the corrosion behavior of copper in aqueous solutions and in soil environments containing different corrodents has been described in this chapter. As a pre-cursor to understanding the corrosion of copper, the long-term corrosion behavior of some archaeological copper samples have been studied and the experimental procedure for archaeological analogue studies is also presented in this chapter.

#### **3.1 Raw material**

Pure copper samples were used for simulated soil and aqueous environments. Copper samples were cut out from copper sheet of thickness 3.24 mm. The composition of the copper sample was not determined and its microstructure confirmed that it was pure Cu. The corrosion behavior of Cu was understood in soil and aqueous environments.

#### **3.2 Soil Characterization**

Bentonite clay was used for testing in soil environments. Its characteristics were first understood. The supplier of the clay was Shree Cement Ltd, Beawar, Rajasthan, India.

##### **3.2.1 Chloride content**

The bentonite clay was chemically tested for determining the chloride content. The chemical testing was performed at FEAT (Facility for Ecological and Analytical Testing) Laboratory, IIT Kanpur. The chloride content was determined by titrating it against  $\text{AgNO}_3$  [65]. Two grams of solid clay sample was dissolved in 100 ml distilled water. After 3 hours of stirring it was filtered and the filtrate was later titrated against  $\text{AgNO}_3$  solution with  $\text{K}_2\text{CrO}_4$  indicator [66]. The amount of filtrate used in titration was a

measure of chloride content present in the bentonite clay. The chloride content was determined to be 3540 ppm.

### **3.2.2 Moisture content**

The Moisture content of the soil was determined by drying 10 grams of soil in a crucible for 8 hours at  $110^0$  C in a microwave oven. Weight loss measurements were determined at intermediate times (Fig. 13). After 2 hours, the weight loss of the dried soil was almost constant, indicating that after 2 hours the loosely locked water content present in the soil could be mostly removed. Therefore, it was decided to dry the soil for 2 hours at  $110^0$  C in, in further experiments.

### **3.2.3 Particle size and Distribution**

A Laser Scattering particle Analyzer (model: Economy, Laser Klasse 1; supplier Fritsch, Germany) was used for analyzing the particle size of bentonite clay. Low angle Fraunhofer light scattering using monochromatic (laser) light and dispersed particles were used in this case. The particles were suspended in a suspension made using 2 to 3 g of powder dissolved in approximately 60 ml of distilled water with 10% sodium metaphosphate. The particles were passed through a laser beam in a circulating water stream. The light scattered after interaction with the particles were measured by detectors, which were placed strategically. The size of the particles affects both the intensity and angular extent of scattering. With coherent light, scattering angle varies inversely with the particle diameter. The scattering depends on the refractive index of the particle in the suspension medium, wavelength of light and particle size and shape. The particle size distribution curve is shown in Fig. 14. After analysis of the particles size distribution, it was found that most of the particles were less than 20  $\mu\text{m}$ . Very few of them ( $\sim 1\%$ ) were greater than 10  $\mu\text{m}$  in size. The average particle size was 3.54  $\mu\text{m}$ . Only 7.34% of the particles were less than 1  $\mu\text{m}$  in size, while most of the particles were in 3-7  $\mu\text{m}$  range.

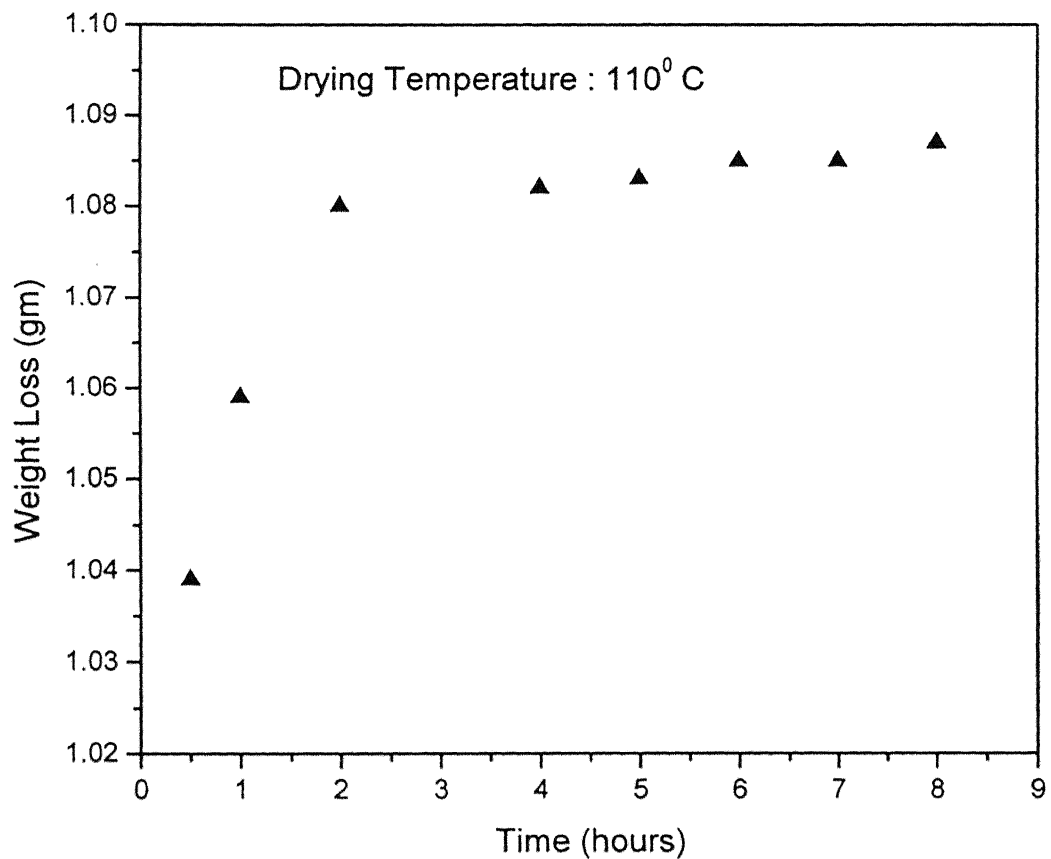


**Fig. 13** Weight loss measured as a function of time during drying of 10 gm of soil at  $110^0$ C.

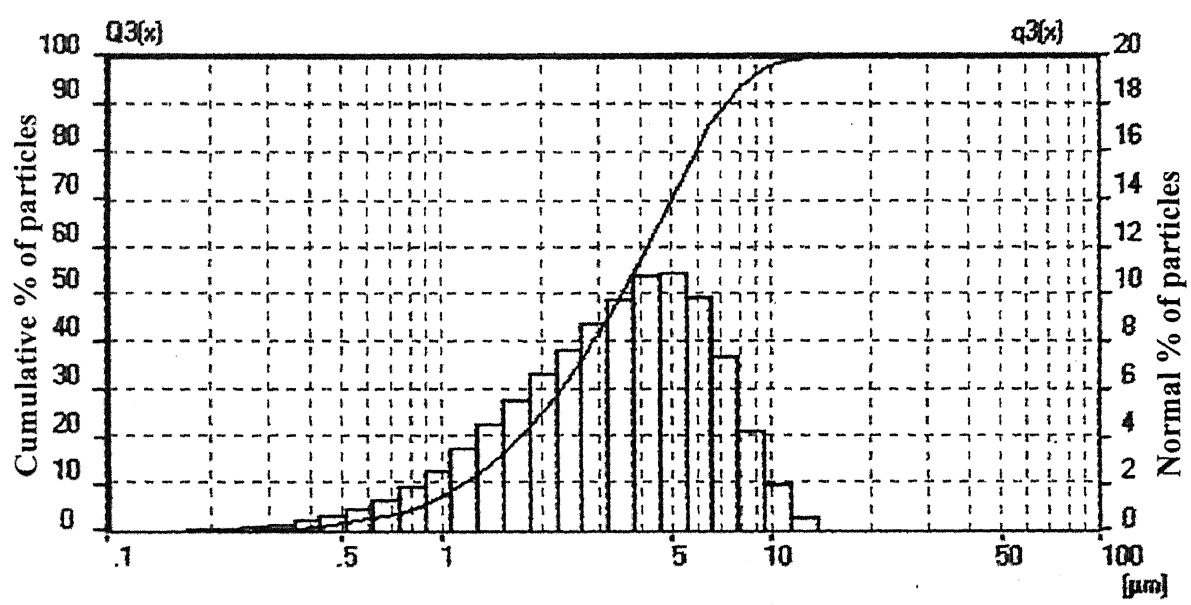


Fig. 14 Particle size distribution curve for bentonite clay.

### **3.3 Electrochemical characterization.**

#### **3.3.1 Sample preparation**

Standard metallographic techniques were used for preparation of the samples: sectioning, mounting, grinding and polishing. Rectangular specimens of area 1 cm by 1 cm were cut from the as received copper plate by using an abrasive cutter (Buehler, Germany). An electrical wire was soldered before mounting in order to provide electrical contact to the sample. The sample with the soldered wire was cold mounted using epoxy resin, so as to expose only the material surface. An exposed area of 1 cm<sup>2</sup> was maintained for all the samples. All the surfaces of the specimens, were mechanically polished down to fine emery paper (starting form grit number 320 to 800, ANSI) and then degreased using acetone before being used for each electrochemical experiment

The procedure of preparing the samples for soil and aqueous solutions experiment was same. Total fifteen different copper samples were prepared by using the above mentioned procedure, of which ten samples were used for soil experiments and five other for aqueous solutions.

#### **3.3.2 Apparatus for linear polarization and electrochemical impedance spectroscopy studies.**

The main apparatus used for the electrochemical experiments were a polarization cell and a potentiostat interfaced to a personal computer. The potentiostat, used in the present study was Parstat 2263, supplied by, Princeton Applied Research, USA. The potentiostat was capable of performing wide variety of potentio and galvano functions required for basic and applied studies in the field of corrosion. The schematic of a potentiostat connected with the electrochemical cell is shown in Fig. 15. The potentiostat consists of an ammeter, an electrometer and a power supply. Three probes from the potentiostat were connected to the working electrode (green), reference electrode (white) and counter electrode (red). The fourth probe (black) was grounded.

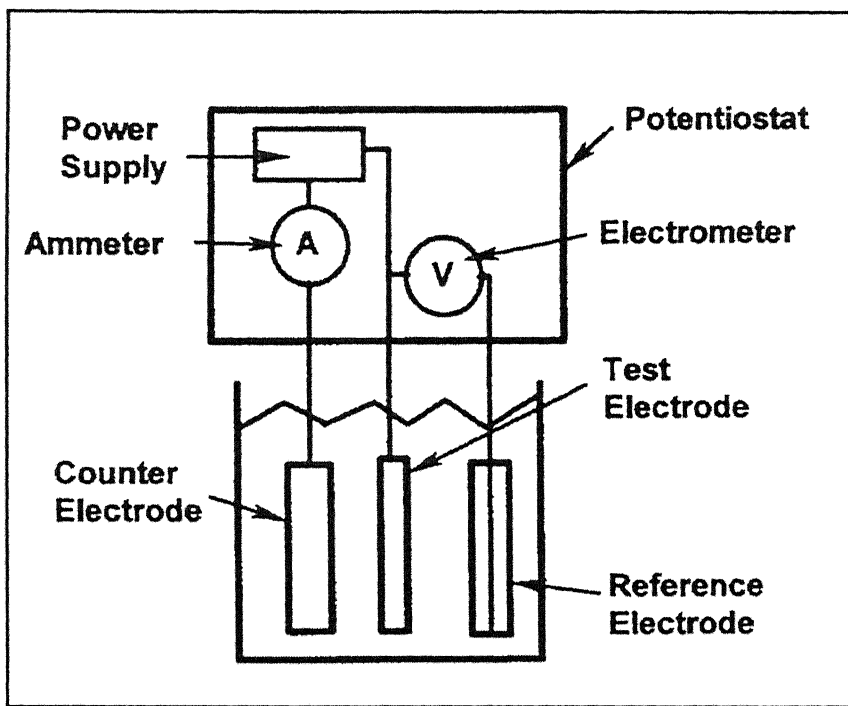


**Fig. 15** Schematic diagram showing the connections in the potentiostat.

Linear polarization and EIS experiments were carried out in a specifically designed electrochemical cell. The aim was to understand long term corrosion behavior and this electrochemical cell was convenient for these studies. A total of fifteen different cells were used simultaneously to obtain data from fifteen different experiments conducted simultaneously. This cell consisted of a cylindrical flask with a plastic cover on top, which had provisions in the form of circular openings of different sizes to permit the introduction of various electrodes. All the flasks were of 500 ml capacity. The distance between the openings on the cover plate was maintained in such a way that a very small gap was obtained on putting the different electrodes through these openings. The schematic representation of the cell is shown in Fig. 16. Standard calomel electrode (SCE) was used as the reference electrode and the counter electrode was a high purity graphite rod. Reference electrode was placed in a Luggin capillary filled with agar-agar gel. The Luggin capillary was fixed in the electrochemical cell, so that the electrolyte and the working electrode were not disturbed while doing experiments during the immersion period. The potential of the reference electrode was + 0.242 V with respect to standard hydrogen electrode (SHE). The Luggin probe connected with agar-agar salt bridge separated the bulk solution from the saturated calomel reference electrode (SCE). The probe tip could be easily adjusted to bring in close proximity with the working electrode in the specially designed electrochemical cell.

The three electrodes used were the working electrode (mounted specimen connected with a wire), the counter electrode (high purity graphite rod) and the reference electrode. (A saturated calomel electrode with  $E^{\circ} = + 0.242$  V vs. standard hydrogen electrode), as per the ASTM recommendations [67]. The potential of the calomel electrode was checked at periodic intervals to ensure the accuracy of the potential of the electrode.

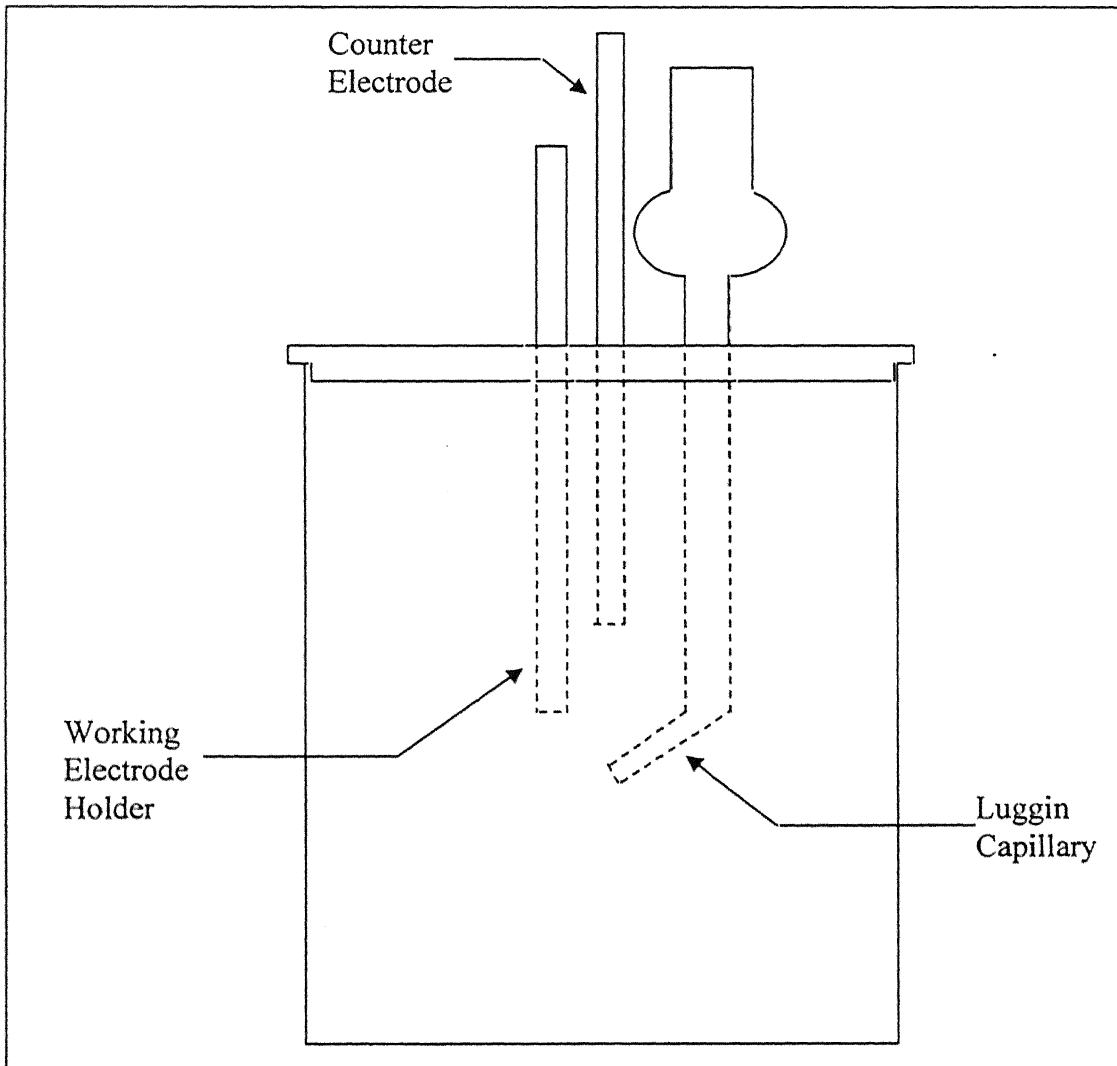


**Fig. 16** Electrochemical cell used for conducting long term electrochemical experiments.

### **3.3.3 Electrolytes**

The environments used in the present study to understand the electrochemical behavior of copper are tabulated in Table 2. Two different kinds of environments, aqueous and soil were used. The soil electrolytes are abbreviated as S1-S5 (Set 1) and S6-S7 (Set 2). The aqueous electrolytes are abbreviated from A1-A5.

In the preparation of aqueous solutions, 300 ml of distilled water was used and for soil environments, 300 grams of dried soil was utilized. Other additives were added according to the composition presented in Table 2. The chloride concentration in soil and aqueous solutions was adjusted by the addition of NaCl. Other pollutants such as ammonium and sulphide ions in the electrolytes were introduced by adding NH<sub>4</sub>Cl and Na<sub>2</sub>S respectively. Bentonite clay was used to produce soil environment. Soil environments were prepared by adding the constituents and then mixing soil thoroughly. Homogeneous mixing of soil could not be perfectly obtained due to agglomeration of soil particles. The aqueous solutions were thoroughly stirred before using them in the experiments. Although ASTM recommends 40 ml of test solution to every 1 cm<sup>2</sup> area of the test surface [67], it is also recommended to keep the ratio of the solution volume to specimen surface area high in order to avoid any appreciable change in the corrosivity of the solution during the test, especially since the solution would not be recirculated [67]. Only test solutions that were freshly prepared were used for each experiment in order to minimize contamination of the electrolyte. Additional care was taken to stir the solution thoroughly before starting each test. The temperature of the electrolytes was not controlled. The variation in temperature (20° -25° C) was minimum during the period in which the experiments were carried out. All the electrochemical cell outlets were sealed with Teflon tape in order to prevent evaporation of moisture during the course of the experiments.

**Table 2 (a): Aqueous Environments**

S. No.	Composition of Solutions	Solution Abbreviation
1.	3.5 wt% NaCl + 100 ppm Na <sub>2</sub> S + water	A1
2.	5 wt% NaCl + 100 ppm Na <sub>2</sub> S + water	A2
3.	100 ppm Na <sub>2</sub> S + Water	A3
4.	1000 ppm NH <sub>4</sub> Cl + Water	A4
5.	3.5 wt% NaCl + 1000 ppm NH <sub>4</sub> Cl + water	A5

**Table 2 (b): Soil Environments (Set 1)**

S. No.	Composition of Solutions	Solution Abbreviation
1.	10 wt % water + dry soil	S1
2.	15 wt % water + dry soil	S2
3.	20 wt % water + dry soil	S3
4.	3.5 wt % NaCl + 20 wt % water + dry Soil	S4
5.	5 wt % NaCl + 20 wt % water + dry Soil	S5

**Table 2 (c): Soil Environments (Set 2)**

S. No.	Composition of Solutions	Solution Abbreviation
1.	3.5 wt % NaCl + 20 wt % water + 100 ppm Na <sub>2</sub> S + dry Soil	S6
2.	5 wt % NaCl + 20 wt % water + 100 ppm Na <sub>2</sub> S + dry Soil	S7
3.	100 ppm Na <sub>2</sub> S + 20 wt % water + dry Soil	S8
4.	1000 ppm NH <sub>4</sub> Cl + 20 wt % water + dry Soil	S9
5.	3.5 wt % NaCl + 20 wt % water + 1000 ppm NH <sub>4</sub> Cl + dry Soil	S10

### **3.3.4 Test procedure for electrochemical studies**

Before each experiment in soil and aqueous environments, the working electrode was ground with 800 grit size (ANSI) emery paper. After this surface finishing operation, the sample surfaces were degreased with acetone. The electrolyte was transferred to the electrochemical cell. The electrodes were immersed in the electrolyte and secured in a place using a retort stand. Precaution was taken that the specimens were dipped to the same depth and the Luggin probe was adjusted so that its tip was consistently as close to the working electrode as possible. It is well known that the portion of the electrolyte between the working electrode and the capillary tip of the reference electrode also contributes towards the electrical resistance. Since resistance is a function of the distance between the electrodes, better reproducibility for the measured values was achieved by maintaining the gap as small as possible in order to minimize the extra resistance.

### **3.3.5 Potential stabilization**

The variation of free corrosion potential (FCP) with time was monitored after immersion of the samples in the environment until a steady potential was obtained. These stabilized FCP were used to define the range of experimental potentials in the electrochemical experiments. All potentials were measured with respect to the SCE. Proper care was ensured so that the specimens were immersed in electrolytic solution for a minimum specified duration. Precautions were also taken to avoid any delay in starting the experiment immediately after immersing the specimen and providing the connections. The corrosion potential of the working electrode was continuously recorded starting immediately after immersion until a constant potential was obtained. The period for stabilization depended upon the specimen, its surface finish, and the electrolyte.

### **3.3.6 Linear polarization**

Linear polarization experiments were performed in the potential range of -20 mV to +20 mV with respect to FCP for all the samples. All the experiments were conducted after stabilization of free corrosion potential (FCP). Linear polarization experiments were performed immediately after immersion (after stabilizing the free corrosion potential) and also after 432 hours of immersion in aqueous and soil environments (set 2). In soil environment S9, linear polarization experiment could not be performed after 432 hours of immersion as the working electrode lost electrical contact. All linear polarization experiments were carried out at a scan rate of 0.166 mV/sec. The results obtained using a scan rate of 0.166 mV/sec (as per the recommendation of ASTM standards [67]) was found suitable for the reliable measurement of equilibrium electrochemical characteristics for copper. Generally, the total duration of each test was around 4 minutes. The data was processed by the computer and stored digitally. The specimen area for all the samples was taken into account during the processing of data.

### **3.3.7 Electrochemical impedance spectroscopy**

Electrochemical impedance spectroscopy (EIS) measurements were performed by applying a sinusoidal potential perturbation of 10 mV at the open circuit potentials. The impedance spectra were measured with frequency sweep from 100 kHz to 10 mHz in logarithmic increment. A total number of 36 points was recorded for each experiment. Generally, the total duration of the experiment was around 10 minutes. EIS experiments were started after stabilization of free corrosion potential for all the specimens. After completing the EIS experiment on first immersion, the electrochemical cell was disconnected from the potentiostat and the reference electrodes were removed from the luggin capillary. However, the specimen was allowed to remain immersed in the solution. Reference electrode was placed separately in saturated KCl solution. The EIS experiments were repeated after 2, 24, 48, 72, 96, 168, 240, 312 and 432 hours in aqueous and soil environments (Set 2). The reference electrode was placed back into the solution through the Luggin capillary in the cell after the required time duration before

beginning a fresh experiment. The free corrosion potential was also measured each time prior to any EIS experiment.

The total time duration of long term immersion experiments were same for aqueous and soil environments (Set 2). In soil environment Set 1, no EIS experiment was performed, however FCP was recorded after same interval of time as was done for other cases. Set 1 soil experiments were basically trial experiments, conducted to study the effect of moisture and chloride ions in soil. Soil environment S1, S2 and S9 could not run for specified amount of time, due to loss of electrical contact in soil after some days.

Linear polarization and electrochemical impedance spectroscopy experiments were conducted using the same potentiostat (Parstat 2263). All the experiments were controlled using a computer and the data was collected using PowerSuite version 2.33.0 software. The EIS data was analyzed by ZsimpWin Version 3.00 software.

### **3.4 Surface analysis by scanning electron microscopy (SEM)**

Scanning electron microscopy (SEM) was utilized to study the nature of surface films formed on copper samples after immersion in different electrolytes for 432 hours. The scanning electron microscope (SEM) used was FEI Quanta 200 equipped with the EDX (compositional analysis) facility. Surface microstructures were obtained at different locations in the samples. Spot analysis was also performed to understand the composition of different features on the surface. SEM helped in understanding the physical nature of the surface films and surface, which further helped in fitting the appropriate equivalent circuit for modeling of EIS data.

### **3.5 Archaeological analogue analysis**

Several copper tools and weapons were discovered during recent excavations at Balathal in Udaipur District of Rajasthan. Radiocarbon dating suggested that these artifacts belong to Chalcolithic period of human civilization. The word *chalcolithic* itself implies “copper-stone”, thereby indicating that copper and stone tools were simultaneously utilized in this cultural phase of Indian history [58]. In the present

investigation, a copper chisel from Balathal was addressed by a detailed metallurgical investigation. Also the surface patina formed on a copper axe of the same period would be analyzed. Metallurgical investigations on ancient copper provide valuable insights on the long-term corrosion and degradation behaviour of copper. These valuable archaeological analogues assist in the selection and design of materials for long-term corrosion resistance, like those required for long-term underground storage of nuclear wastes. Copper is one of the natural materials of choice and investigations on archaeological copper would provide valuable inputs in material selection for canisters for long-term nuclear waste storage.

### **3.5.1 Chalcolithic chisel**

The copper chisel that was utilized in the present study was of square cross-section at one end, tapering down to a smaller flatter cross-section at another end. A picture of the chisel is presented in Fig. 17. Its total length was 9 cm and cross-section at the square section was  $0.86 \times 0.86$  cm. It was covered with an adherent surface patina, which appeared light green in color. A small section was made at the square cross-section end using a diamond cutter. Samples of pure modern copper were also prepared for comparison purposes. Three samples were prepared from this section. The first sample was utilized for metallographic studies. The second sample was specifically maintained for careful X-ray diffraction (XRD) analysis. The third sample was mounted for electrochemical analysis. While cutting the samples, special care was taken to ensure that the surface scales (i.e. the corrosion products) were not disturbed, especially in the sample utilized for XRD analysis. The specimen for metallographic observations was mounted. Special care was taken during mounting to maintain the flatness of the sample and the mount. The cross-section of the chisel was the section observed on the microscope. The sample was ground and polished very carefully to avoid the reappearance of new scratches. The final polishing was performed with  $1\text{ }\mu\text{m}$  diamond paste. The specimen was etched in ferric chloride solution for revealing the microstructure. The microstructures were observed in a JEOL 840A scanning electron microscope (SEM).

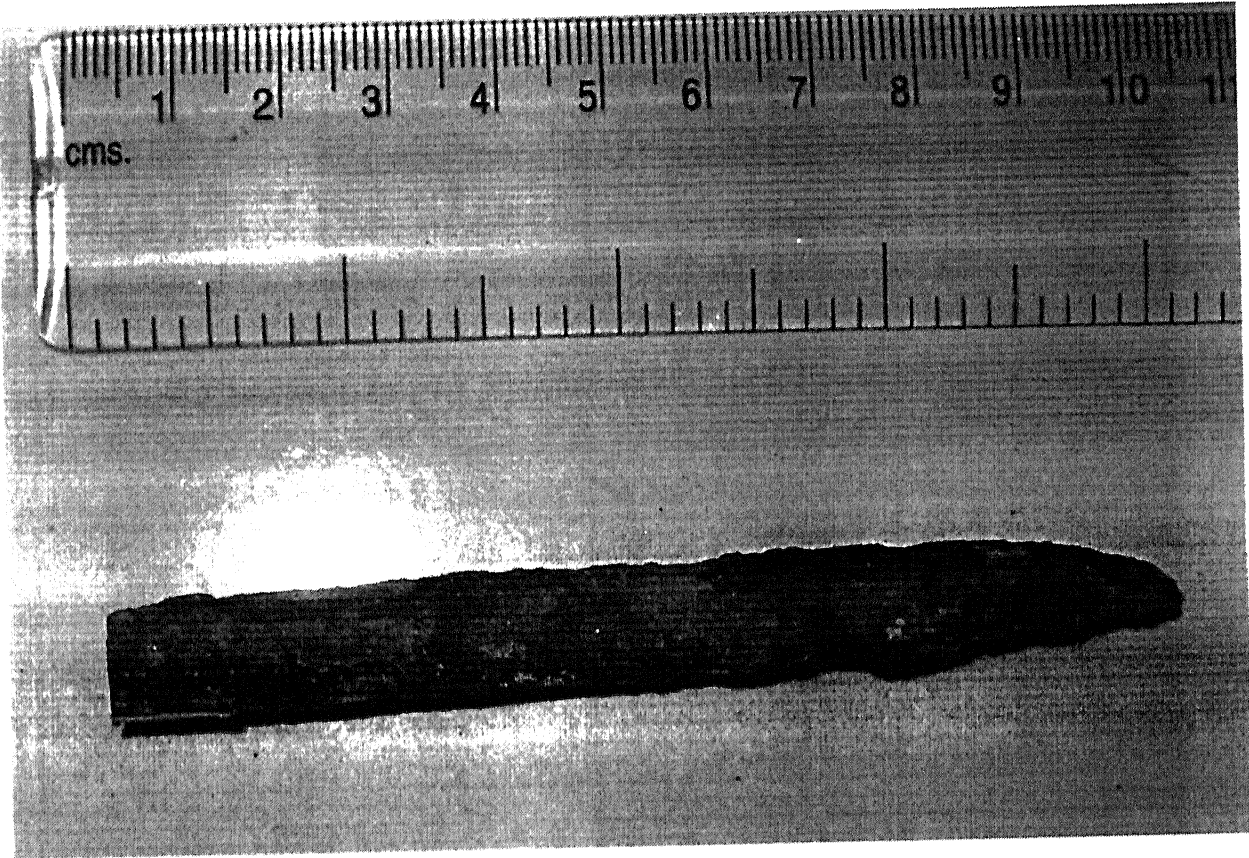


**Fig. 17** Copper chisel excavated from Balathal. The left end was of square cross section, whereas the right end was tapering down to a smaller flatter cross section.

The sample for electrochemical analysis was mounted in a cold setting epoxy, after soldering a conductive wire to it. Electrochemical polarization experiments were conducted utilizing a potentiostat (263A Perkin Elmer, USA). Polarization studies were carried out in 3.5 wt% NaCl solution. The samples were polished to 4/0 grade emery paper finish and the surfaces were cleaned using distilled water and acetone before the start of each experiment. A round-bottom polarization cell, with graphite counter electrodes and saturated calomel electrode (SCE) (+ 241 mV vs standard hydrogen electrode) reference electrode, was used in the electrochemical study. Potentiodynamic polarization experiments were conducted after stabilization of free corrosion potentials. Both chalcolithic Cu and modern Cu samples were tested. Corrosion rates were determined by the Tafel extrapolation and linear polarization methods. A scan rate of 1 mV/s was used for potentiodynamic polarization experiments and 0.166 mV/s for Tafel extrapolation, as per ASTM standards (ASTM 1987).

The X-ray diffraction (XRD) experiments were conducted in a Rich-Seifert X-ray Diffractometer, taking special care to maintain the same conditions for all the experiments (constant current of 20 mA and voltage of the X-ray tube, 30 kV). The wavelength of the radiation used was CuK $\alpha$  (1.54184 Å). The XRD patterns were analyzed by using DIFFRACplus Software (Bruker Advanced X-ray Solutions) and JCPDF database (JCPDF 2001). XRD patterns were first obtained from all the surfaces, and later, were again determined after slightly polishing off the surface layers using fine emery paper. It was not easy to identify the peaks due to high amount of noise and texturing and in this regard the DIFFRACplus software was very useful in removing some noise and texturing effects.

### **3.5.2 Chalcolithic axe**

The as-received copper axe surface was covered with some soil. Figure 18 shows the copper axe. It was 12 cm in length and the width was 4 cm at one end, which tapered down to 5 cm at the other end. The corrosion products were relatively undisturbed. One small piece was cut from the blunt end of the axe. While cutting, special care was maintained to avoid destruction or spalling of corrosion products. Two samples were obtained from the cut sample. One was utilized for metallographic observations, while the other for understanding corrosion product nature by X-ray diffraction (XRD) experiments. The cross section of the sample was mounted for metallographic observation. Special care was taken during mounting to maintain the flatness of the sample and the mount. The sample was ground and polished very carefully to avoid reappearance of new scratches. The final polishing was performed with 1  $\mu\text{m}$  diamond paste. The specimen was etched in 4.34 wt% ferric chloride solution ( $\text{FeCl}_3$  5gm, HCl 10gm,  $\text{H}_2\text{O}$  100ml) for 4 seconds to observe the microstructure after several trial for optimum etching.

In order to understand the nature of the corrosion product layer as a function of thickness, the surface of the sample was ground with standard SiC paper (Grit Number P180, Size 78  $\mu\text{m}$ ) to obtain powdered corrosion product as a function of thickness of the sample. In this way, ten different powdered samples were collected and each powder sample was analyzed by XRD. Similar grinding procedure was adopted in all cases so that the thickness of layer removed was similar. Each powder corrosion product sample was mixed with acetone and spread on glass slide to ensure random orientation of particles. XRD experiments were conducted in a Rich-Seifert X-ray diffractometer, taking special care to maintain the same conditions for all the experiments (constant current of 20 mA and voltage of the X-ray tube, 30 kV). The wavelength of the radiation used was  $\text{CuK}\alpha$  (1.54184 Å). The individual crystalline phases were identified in the XRD patterns using the DIFFRAC<sup>PLUS</sup> Software (Bruker Advanced X-ray Solutions) and JCPDF database (JCPDF 2001).

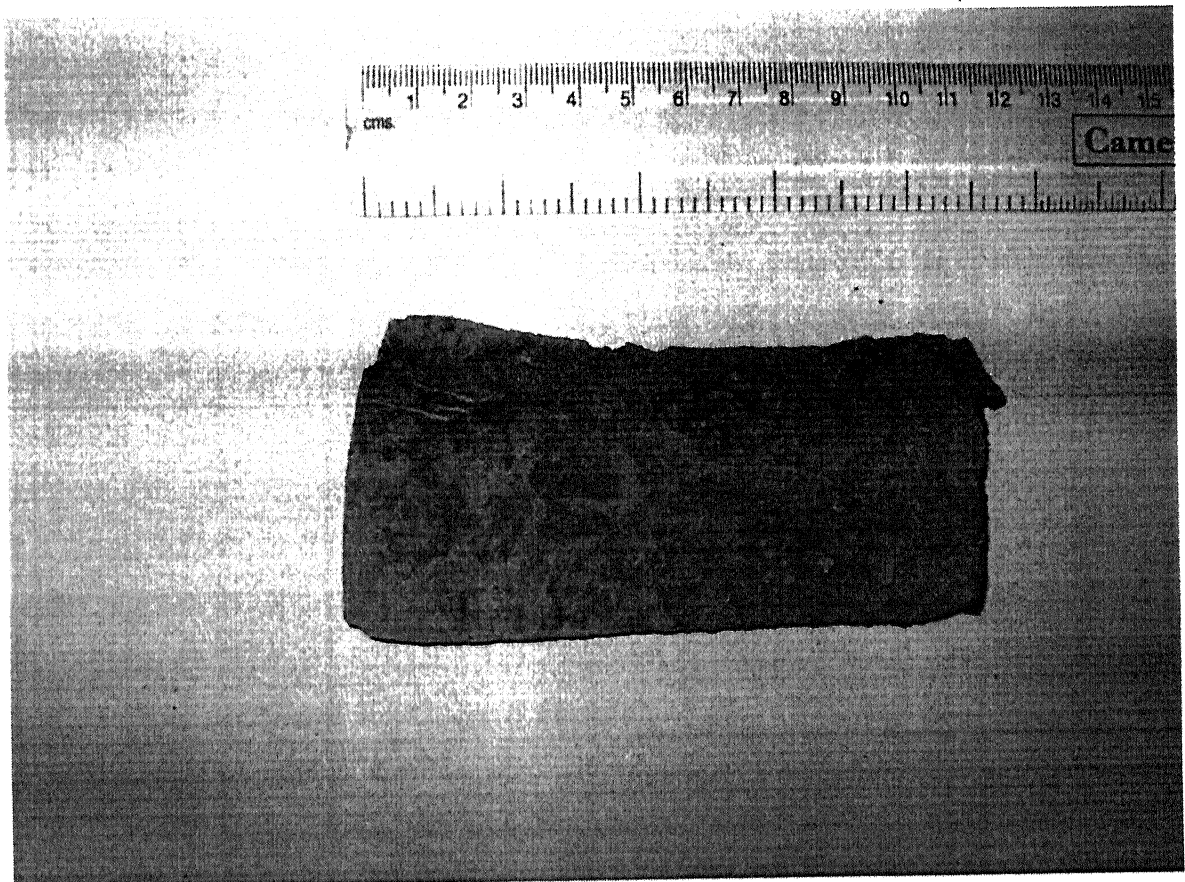


**Fig. 18** Copper axe excavated from Balathal. The cutting edge is to the left side while the blunt edge to the right. Samples for analysis were obtained from the blunt side.

## RESULTS AND DISCUSSION

The chapter starts with a discussion on two Chalcolithic archaeological copper samples. The nature of corrosion products on both archaeological copper samples have been characterized using XRD. The results of scanning electron microscopy (SEM), electrochemical polarization and electrochemical impedance spectroscopy studies conducted on pure copper in different corrosive solutions and soils will also be presented and discussed in this chapter. The aim of the study was to understand the behavior of copper in aqueous solutions and in soil environments containing different corrodents.

### 4.1 Archaeological analogue study

Several copper tools and weapons were discovered in the chalcolithic site of Balathal. The corrosion products deposited on two archaeological copper objects from Balathal namely, chisel and axe have been addressed below. Detailed metallurgical observations have been published elsewhere [68, 69].

#### 4.1.1 Chalcolithic chisel

The microstructure of the metal indicated essentially pure Cu matrix with sulfide inclusions randomly distributed. Microstructural analysis also indicated that the degree of corrosion was not severe and moreover, stress corrosion cracking was not evident from the surfaces of the samples. The corrosion layer was adherent on the surface (Fig. 19). The incursion of corrosion products into the matrix appears to occur along grain boundaries of the underlying copper matrix (Fig. 19). The intergranular nature of corrosion attack is understandable because of the higher-energy state of material at these locations. Nevertheless, it is also important to note that the incursion of corrosion products along the grain boundaries was not deep enough to warrant the use of the term

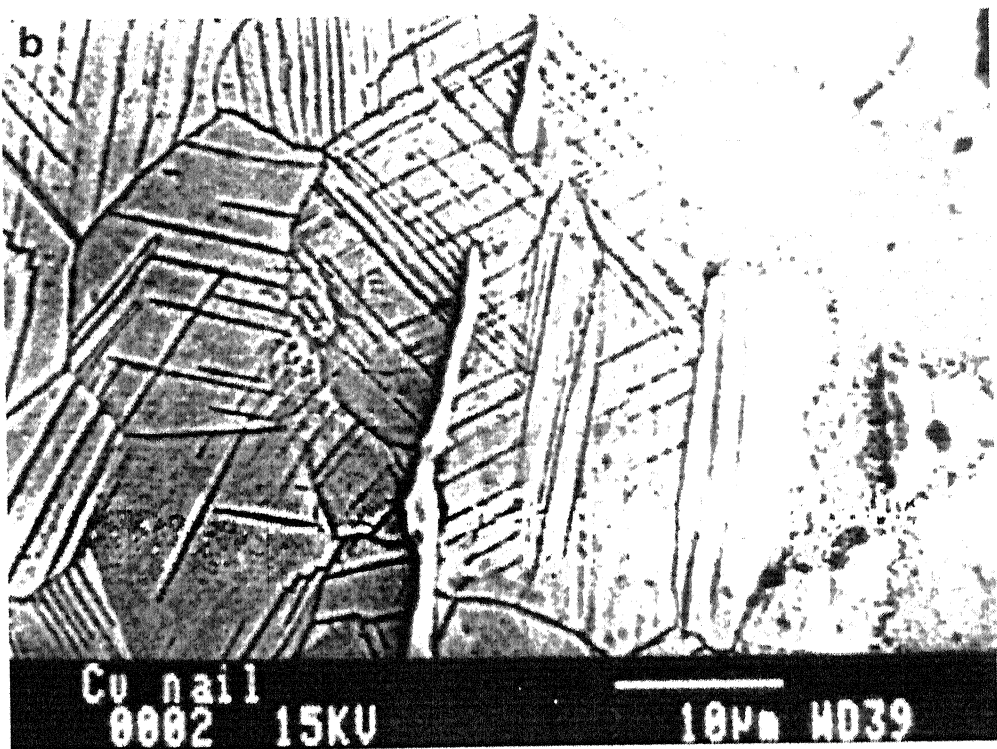


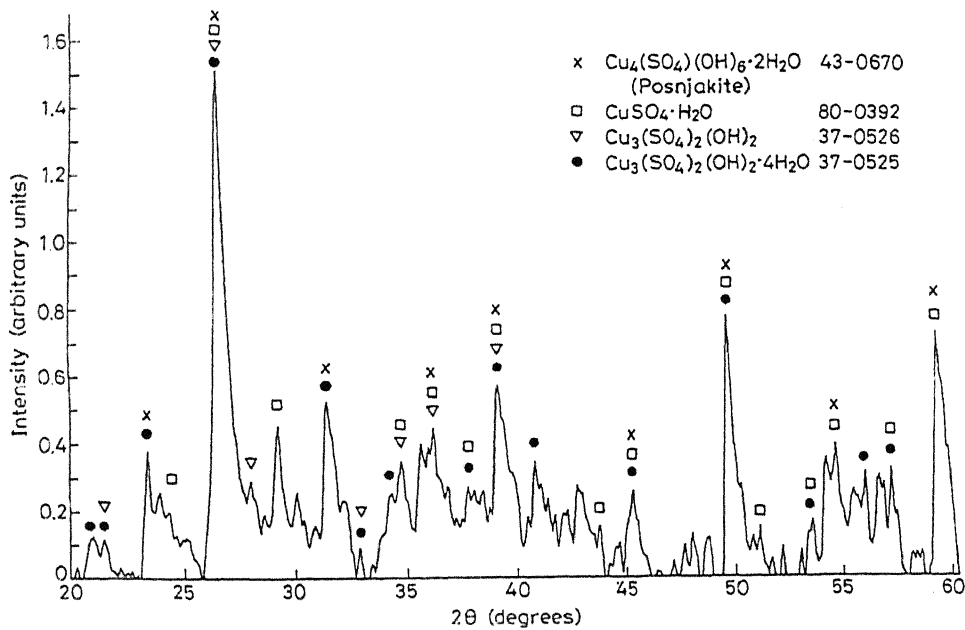
**Fig. 19** SEM micrograph photographed from one of the edges of a Chalcolithic copper chisel, showing deformed grains and incursion of corrosion products along grain boundaries. Corrosion layer is on the right side of the photograph.

pitting to describe this kind of environmental corrosion. A complementary conclusion is the lack of any environmentally induced cracking in the material. This is understandable because dangerous chloride ions were not present in the soil environment to which the chisel was exposed. This was also verified by the absence of chlorides in the X-ray diffraction patterns (Fig. 20) obtained from the surface patina. Therefore in the environments where chloride ions are not present, microstructural investigation on archaeological Indian copper confirm that there is no danger of stress corrosion cracking.

Information about long-term corrosion processes can be also obtained from characterization of surface patina from ancient Indian copper samples. The nature of surface patina will help in validating long-term corrosion models. For example, X-Ray diffraction (XRD) patterns, before polishing and after polishing of the sample surface, help in understanding the sequence of formation of corrosion products. X-Ray diffraction (XRD) patterns of the Chalcolithic copper sample were obtained as a function of patina thickness, by a simple polishing procedure using emery paper. The major corrosion products on the surface of the sample were hydrated copper sulfates and oxysulfates, like  $\text{Cu}_4(\text{SO}_4)(\text{OH})_6 \cdot 2\text{H}_2\text{O}$  (posnjakite),  $\text{CuSO}_4 \cdot \text{H}_2\text{O}$ ,  $\text{Cu}_3(\text{SO}_4)_2(\text{OH})_2$  and  $\text{Cu}_3(\text{SO}_4)_2(\text{OH})_2 \cdot 4\text{H}_2\text{O}$ . Analysis of XRD patterns obtained from the inner regions of the patina, close to the metal-scale interface, revealed that the phases were primarily copper oxide phases. The results of the analysis agree with the known general behavior for corrosion of copper in soil environment [70]. In the corrosion of copper in soil (and also atmospheric environments), the first product to form is cuprite. In the presence of S in the environment, the formation of sulfates and oxysulfates is favored and these phases are generally found above the copper oxide layer.

Now it should be investigated whether data obtained for ancient Indian copper would apply for modern copper. Electrochemical polarization studies conducted on ancient Indian copper samples clearly established that the coppers were electrochemically similar (Fig. 21). The major difference between the samples was the presence of second phase inclusions in the case of archeological Cu samples. Against the anticipation that the presence of second phase inclusions would deleteriously affect corrosion rates, electrochemically measured corrosion rates of Chalcolithic Cu sample (175 mm/y) and

(a)



(b)

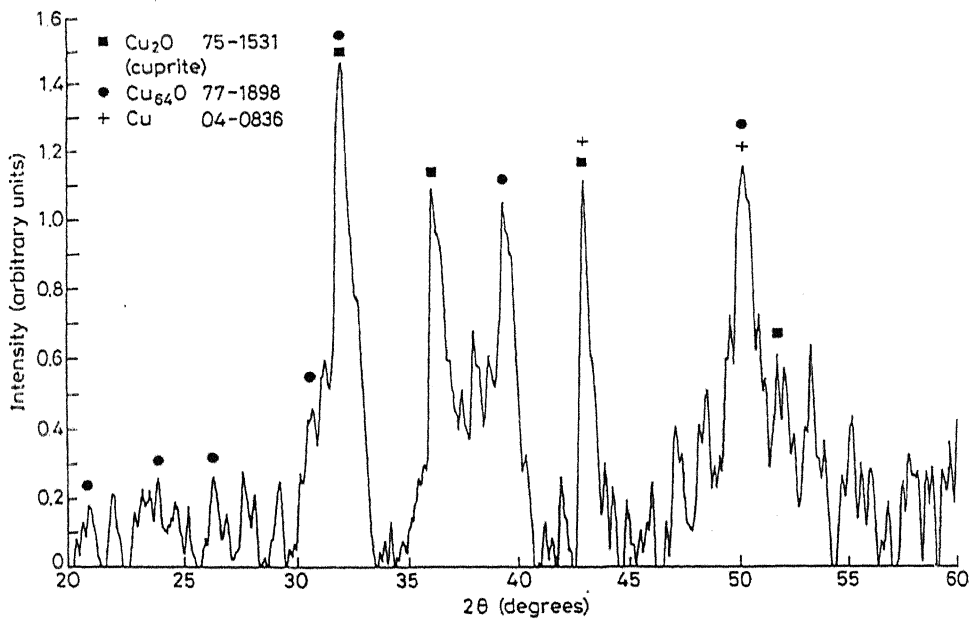


**Fig. 20** X-ray diffraction pattern from the surface of the chalcolithic Cu (chisel) sample (a) before and (b) after slightly polishing the surface of the sample. The peaks corresponding to the identified phases have been marked in both the patterns.

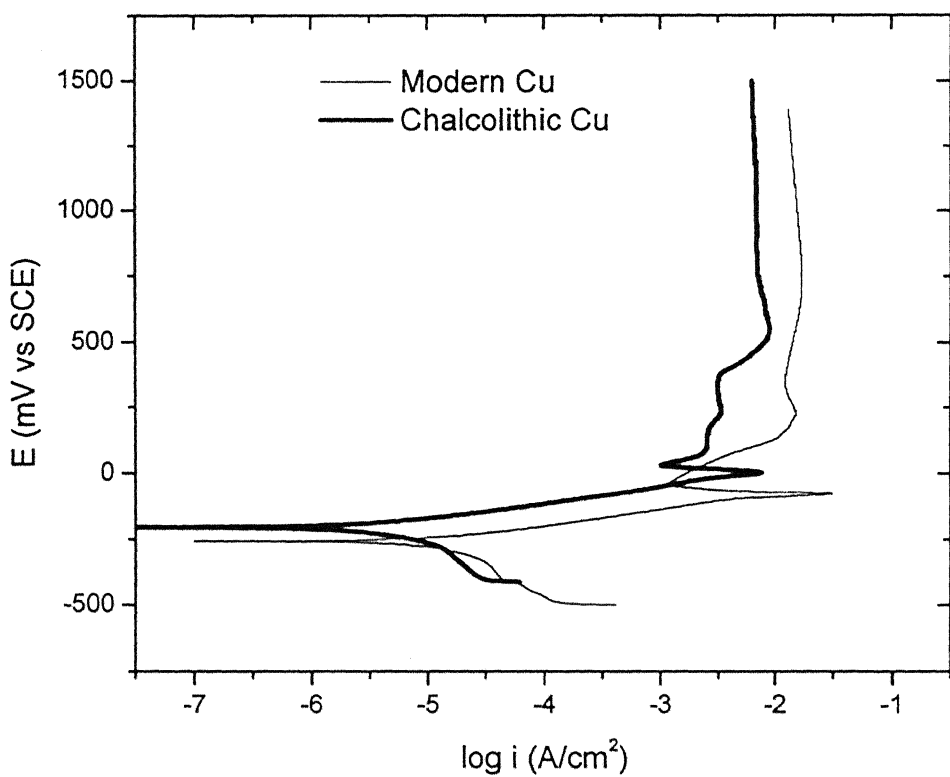


**Fig. 21** Potentiodynamic polarization curves for modern and chalcolithic coppers (chisel) in aerated 3.5 wt% NaCl solution.

OCP Cu sample (185 mm/y) were only marginally higher than that of modern Cu (55 mm/y) [68]. These data co-relate well with the published corrosion rate for Cu in seawater (25-127 mm/y) [71]. In the case of both archaeological coppers, the second phase slag particles appear to have slightly enhanced the dissolution tendencies, which could probably be due to galvanic coupling action of the Cu matrix with the sulfide slag inclusions. It is to be noted that the sulfides are electrically conducting and they aid in the establishment of local galvanic cells [72]. The effect of the inclusions was not significant because the volume fraction of inclusions was relatively low and, moreover, they were not interconnected but widely dispersed [68].

As the electrochemical behavior of ancient coppers is almost similar to that of modern copper, it implies that ancient and modern copper samples are almost similar chemically. As the ancient Indian copper samples have successfully withstood corrosion under unplanned soil burial conditions for such a long time, it indicates that modern-day planned burial of copper must also behave similarly. The corrosion of copper exposed to the soil environment will be the critical factor. As ancient Indian copper has proved that it can withstand corrosion in Indian soil conditions over a long period of time, it must be seriously considered as the material of construction of outer canisters for long-term underground storage of nuclear wastes.

#### **4.1.2 Chalcolithic axe**

The XRD patterns obtained from chalcolithic copper axe as a function of corrosion product thickness are presented in Fig. 22. In this figure, layer 1 denotes the outermost layer while layer 10 is the one closest to the metal-scale interface. The specific phases identified were  $\text{CuSO}_4 \cdot \text{H}_2\text{O}$  (JCPDF 80-0392) and  $\text{Cu}_2\text{O}$  (JCPDF 75-1531) in most of the layers. Outer layers revealed only faint cuprite peaks. Some interesting observations regarding the relative abundance of  $\text{CuSO}_4 \cdot \text{H}_2\text{O}$  and  $\text{Cu}_2\text{O}$  as a function of scale thickness can be noted. On progressing from layer 1 to layer 7, the major phase was copper sulfate and the intensity of its XRD peaks progressively decreased.

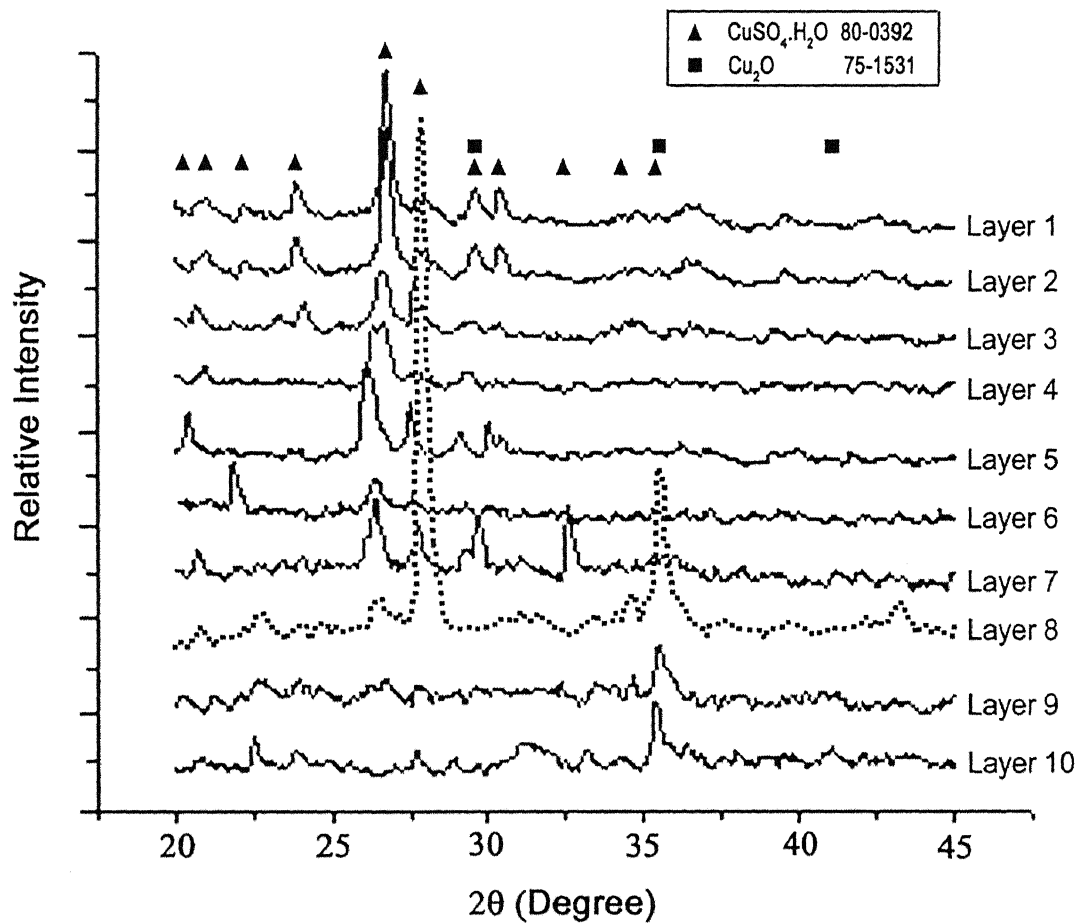


**Fig. 22** XRD patterns obtained from chalcolithic copper axe as a function of corrosion product thickness

At the same time, some cuprite peaks could be identified but their XRD peak intensity was very low. On layer 8, the intensity of the sulfate phase as well as cuprite was very high and this could be due to random experimental error because although random distribution was ensured and similar XRD condition was maintained, this particular sample must have been recorded with slightly different condition. It is known that intensity of the XRD peaks corresponds to volume fraction of that particular phase [73].

It is clear from the present analysis that the outer layers possess higher concentration of sulfate and inner layers higher concentration of oxide. This is in tune with the corrosion chemistry of copper metal. Within the first few hours of exposure of copper in rural and urban environments a thin cuprite layer could be detected and after that depending on time and exposure different sulfate compounds of copper can be observed in the copper patina [70].

The nature of different layers of corrosion product on the sample surface helps in understanding the sequence of formation of corrosion products. Corrosion product layers 9 and 10, which revealed large intensity cuprite peaks, were very near to the metal-scale interface. This observation suggests that the primary corrosion product formed on the copper axe was cuprite. On the other hand, rest of the layers mainly consisted of major  $\text{CuSO}_4 \cdot \text{H}_2\text{O}$ . The sulfate phase forms over the cuprite. This sulphate-rich layer is thicker than the cuprite-rich layer. In considering the development of the natural patinated layer on copper, it is clear that sulphate is the key substance that needs to be characterized, since it is almost universally found to be the major component of aged copper patinas and since it represents the terminal stage of the patination process. In the corrosion of copper in soil (and also atmospheric environments), the first product to form is cuprite. In the presence of S in the environment, the formation of sulfates and oxysulfates is favoured and these phases are generally found above the copper oxide layer. This behavior has also been observed in the present case of the chalcolithic copper axe.

As ancient Indian coppers are fairly well preserved in soil conditions for the above samples, a beneficial effect of studying ancient copper will be the serious consideration of selecting copper as the material of construction of canisters for long-term underground storage of nuclear wastes.

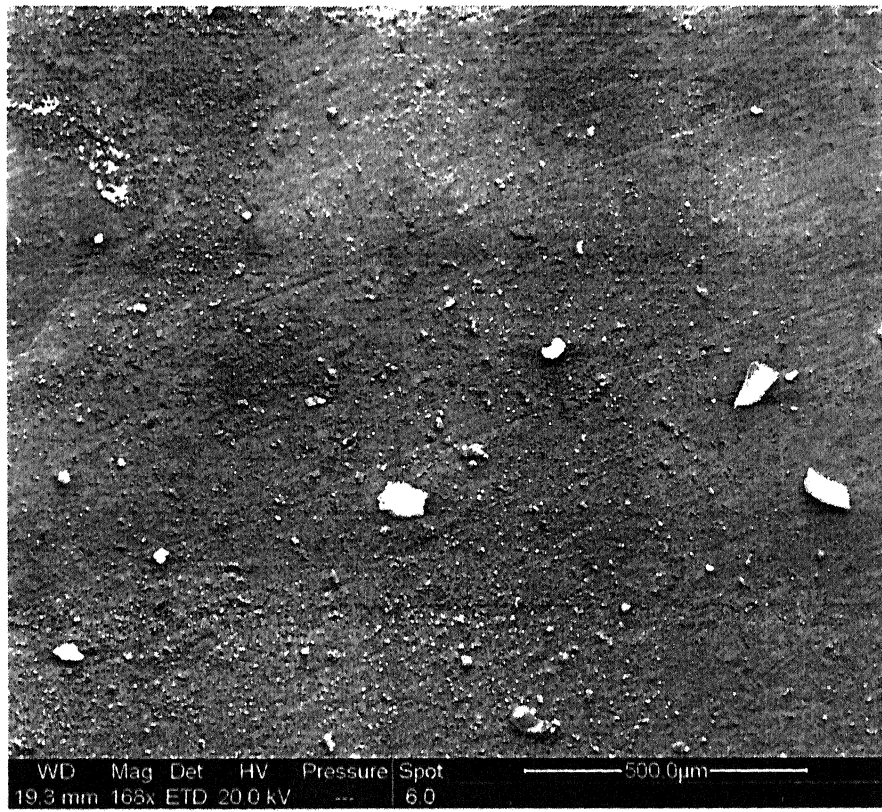
## **4.2 Scanning electron microscopy**

Surface films formed on copper after immersion of 432 hours in different environments were studied using scanning electron microscopy (SEM). Different environments consist of different atmospheric pollutants that affect copper corrosion.

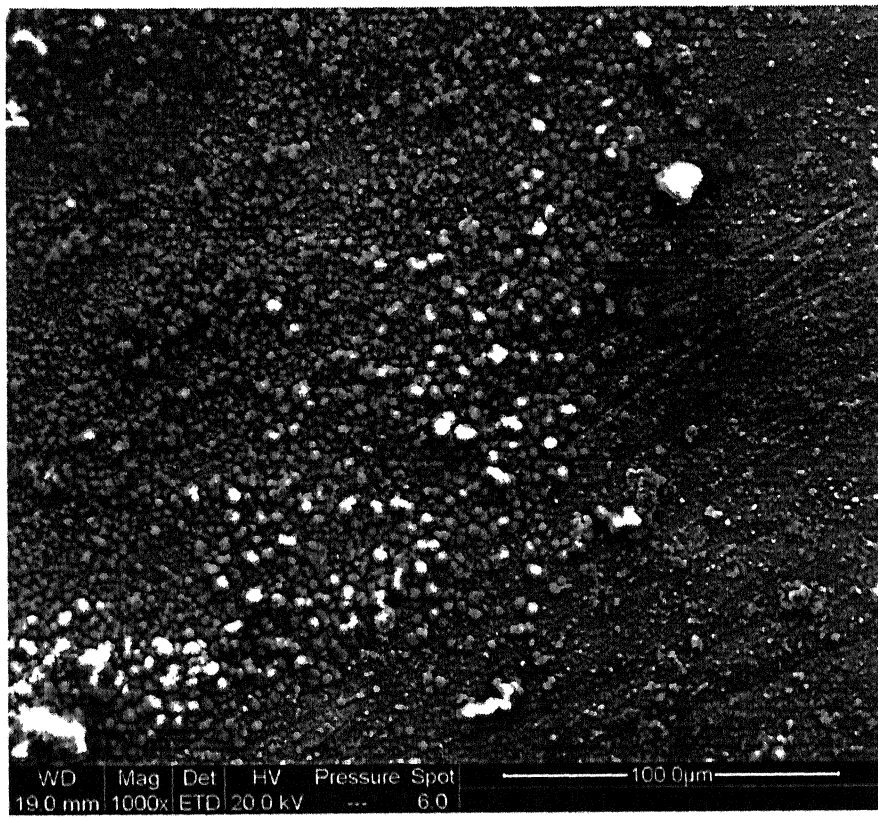
### **4.2.1 Aqueous Solution**

#### **3.5 wt% NaCl + 100 ppm Na<sub>2</sub>S + Water (A1)**

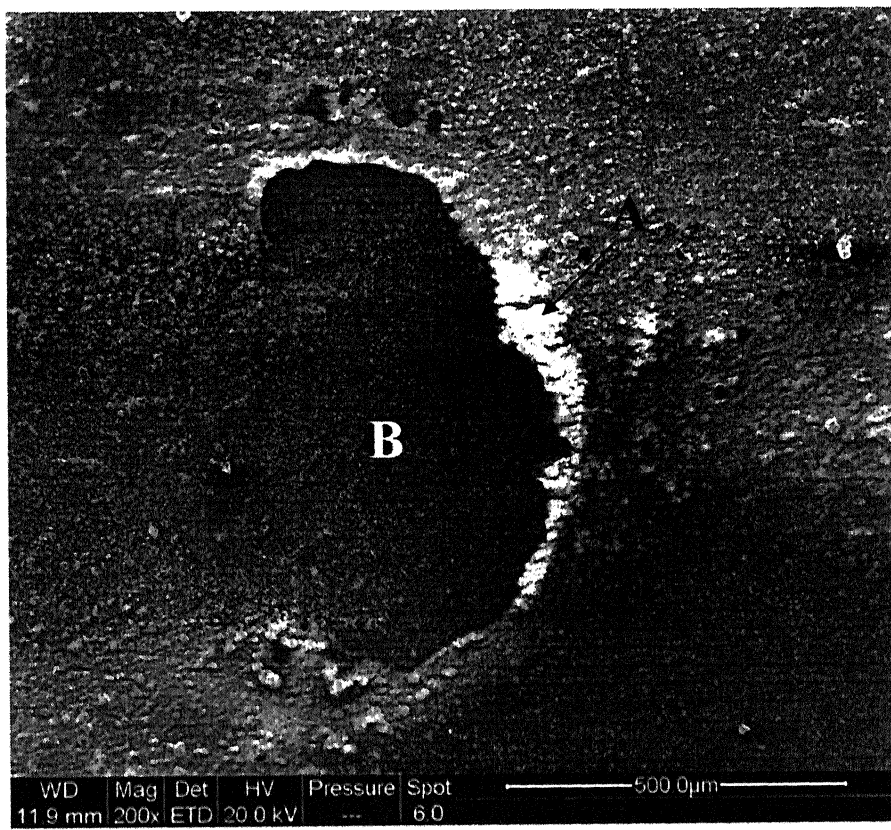
The surface did not present a smooth appearance. A typical SEM micrograph of the surface has been presented in Fig. 23. The entire surface was covered with very small agglomerated particles (Fig. 24). Essentially the entire surface was covered with oxide particles but at some locations islands of chlorides are found on the surface, which were confirmed later. Fig. 25 shows a region of the microstructure showing bright contrast. EDS analysis of one of these bright particles confirmed it to be a Copper Chloride particle (Fig. 26). EDS analysis also confirmed that the substrate below was of Copper oxide (Fig. 27). The presence of a surface layer could be distinguished (Fig. 28). It was more compact as compared to the layer formed in other testing solutions (e.g. A3). There were several locations where the surface layer was cracked (Fig. 29).



**Fig. 23** A typical SEM micrograph of copper surface obtained after immersion of 432 hours in aqueous solution A1.

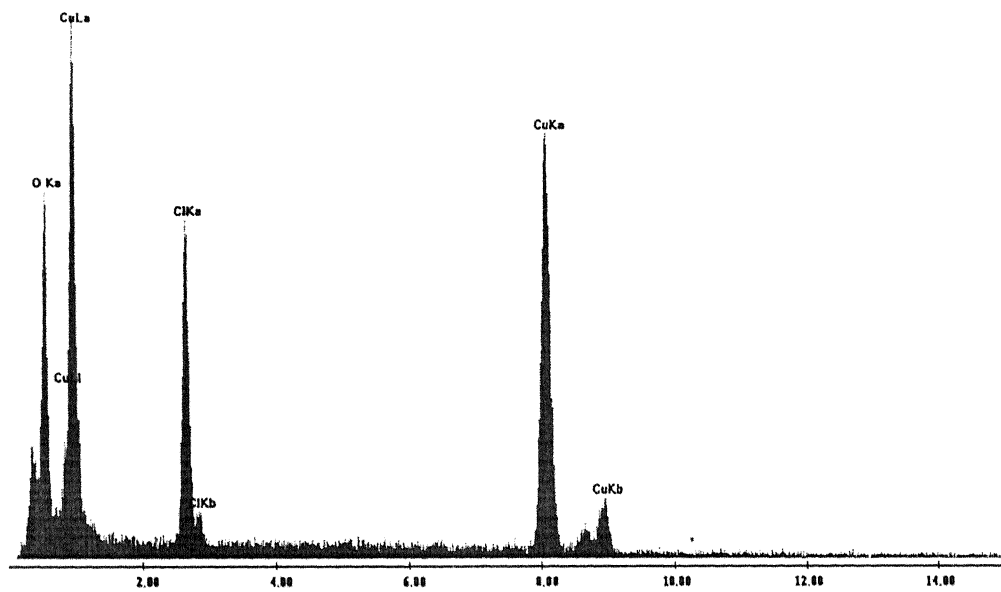


**Fig. 24** SEM micrograph of copper surface obtained after immersion of 432 hours in aqueous solution A1, showing agglomerated particles.



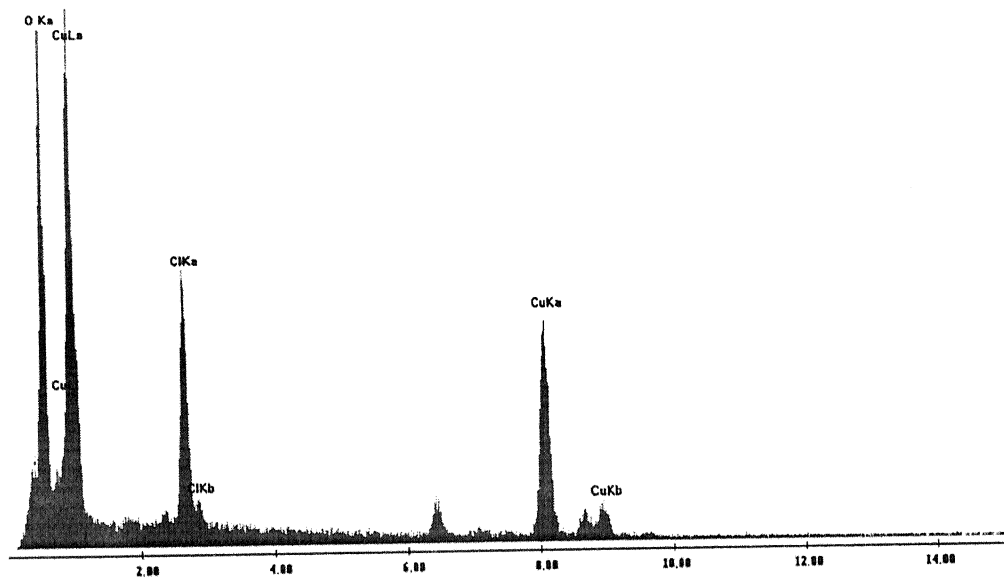
**Fig. 25** SEM micrograph of copper surface obtained after immersion of 432 hours in aqueous solution A1, showing bright Copper Chloride region.

Table A: AOT



**Fig. 26** EDS analysis at one of these bright particles (point A in Fig. 25) confirmed it to be a Copper Chloride particle.

Label A: AG1



**Fig. 27** EDS at point B in Fig. 25 confirmed that the substrate below was of Copper Oxide.

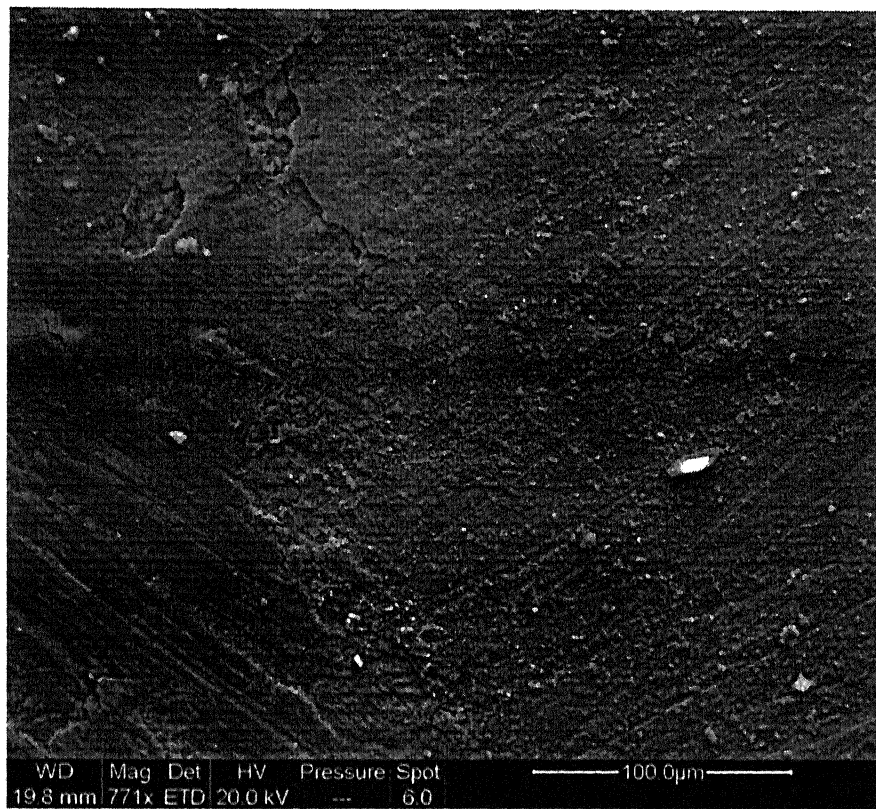


**Fig. 28** SEM micrograph of copper surface obtained after immersion of 432 hours in aqueous solution A1. A porous surface layer is present.

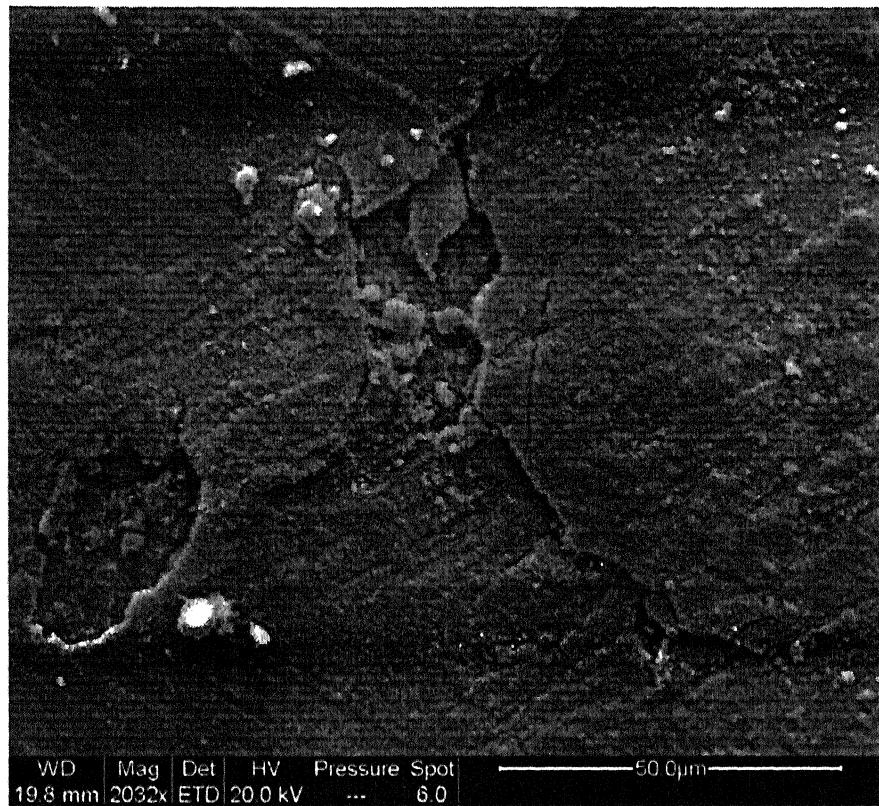


**Fig. 29** SEM micrograph of copper surface obtained after immersion of 432 hours in aqueous solution A1, showing that the surface layer is cracked at some places.

Cracks were also present near the locations where breakage occurred in the layer and not on the complete surface film (Figs. 30 and 31). The structure inside the location where the layer had peeled off (Fig. 30) was observed at higher magnification in Figs. 31 and 32. Fine needle-like structure was observed at these locations. EDS analysis of these fine needle indicated that they were Cu<sub>2</sub>O. This indicates that at any local break in the film, Cu<sub>2</sub>O forms with time. The needle-like morphology indicates the nature of the Cu<sub>2</sub>O when it first nucleates and grows. Fig. 33 shows a magnified view of this needle-like structure present at one location of break in film. Fig. 34 shows a region of the microstructure, from where the top surface layer (scale) has peeled off. EDS analysis (Fig. 35) obtained at point A on Fig. 34 shows that Copper Oxide was the scale on the metal surface. EDS analysis (Fig. 36) was also done from point B in Fig. 34, located, where the Copper Oxide layer was peeled off, indicated lower amount of Cu<sub>2</sub>O and therefore less amount of oxygen was present in the EDS spectra. Analysis (Fig 37) was also performed on a point C (a bright particle) and the EDS results indicated it to be Copper Chloride particle.

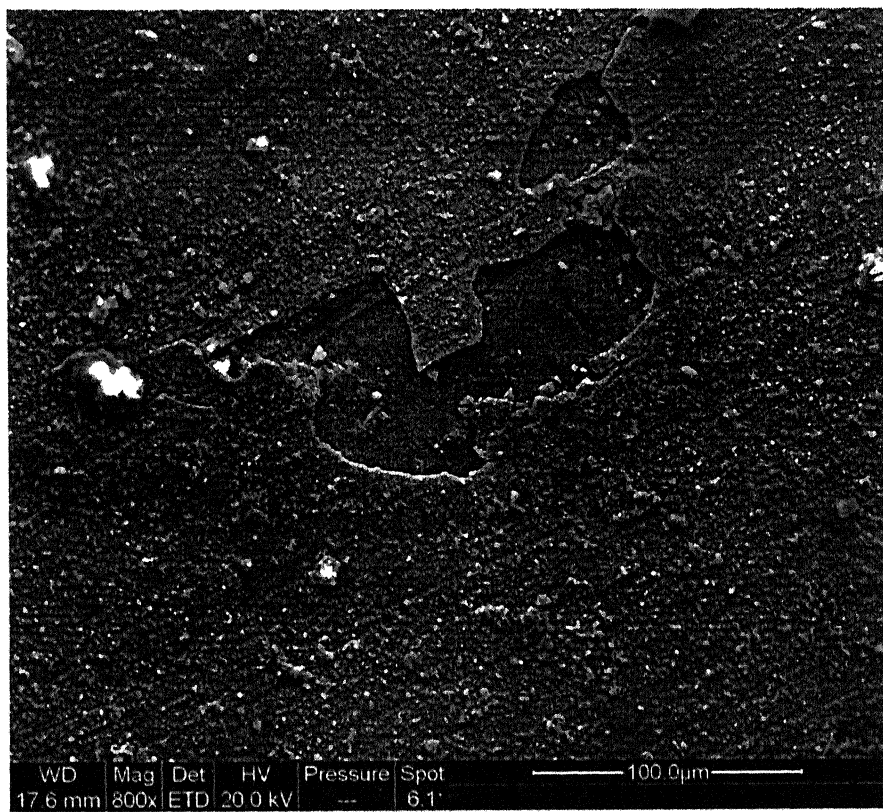


**Fig. 30** SEM micrograph of copper surface obtained after immersion of 432 hours in aqueous solution A1, showing breakage and cracks in the surface layer.

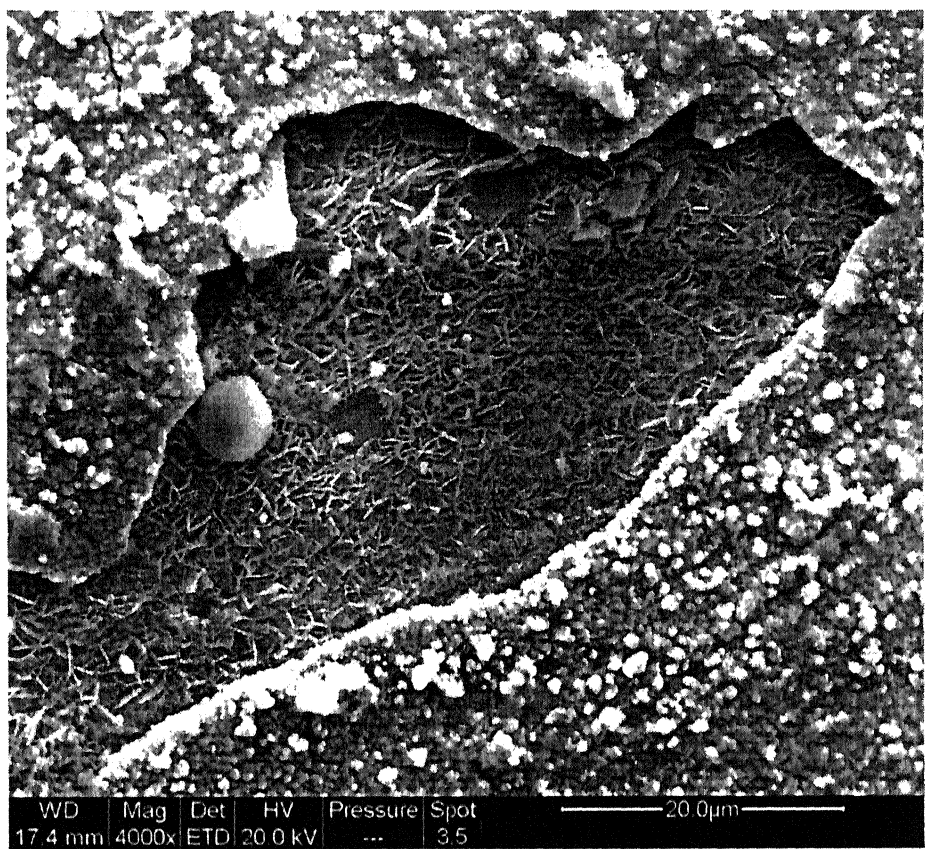


**Fig. 31** SEM magnified view of the broken surface layer obtained after 432 hours of immersion in aqueous solution A1.

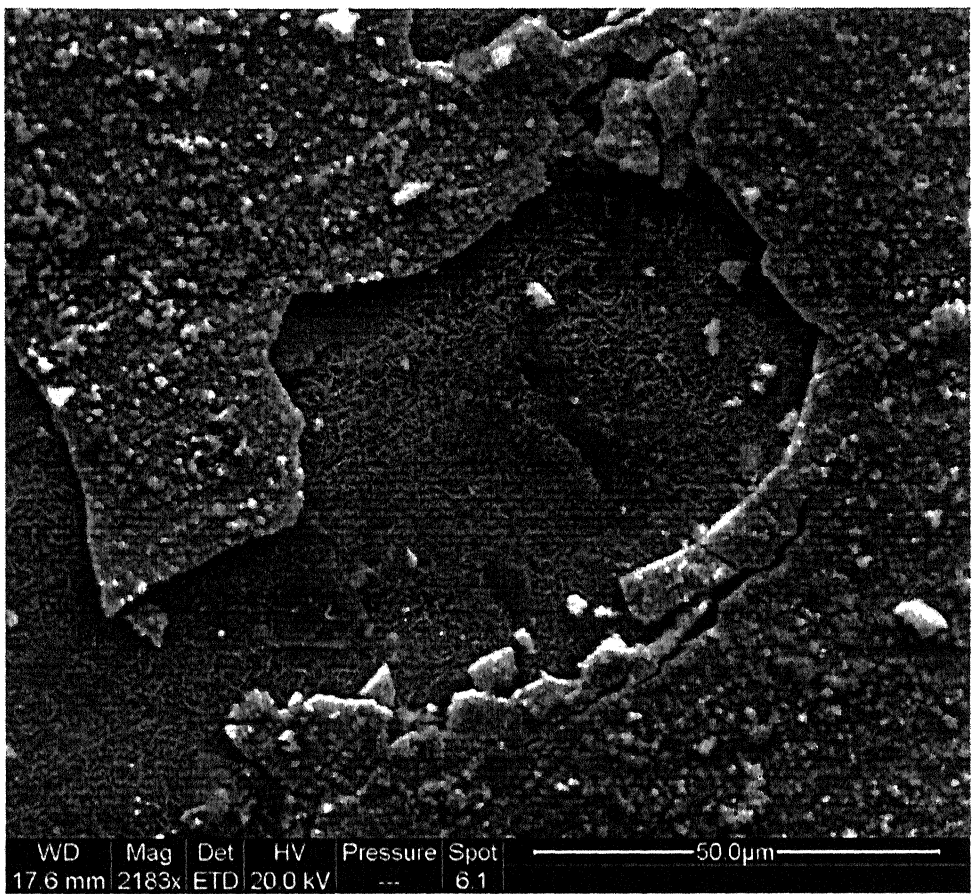


**Fig. 32** SEM micrograph of copper surface obtained after immersion of 432 hours in aqueous solution A1, showing the magnified view inside the broken surface layer.

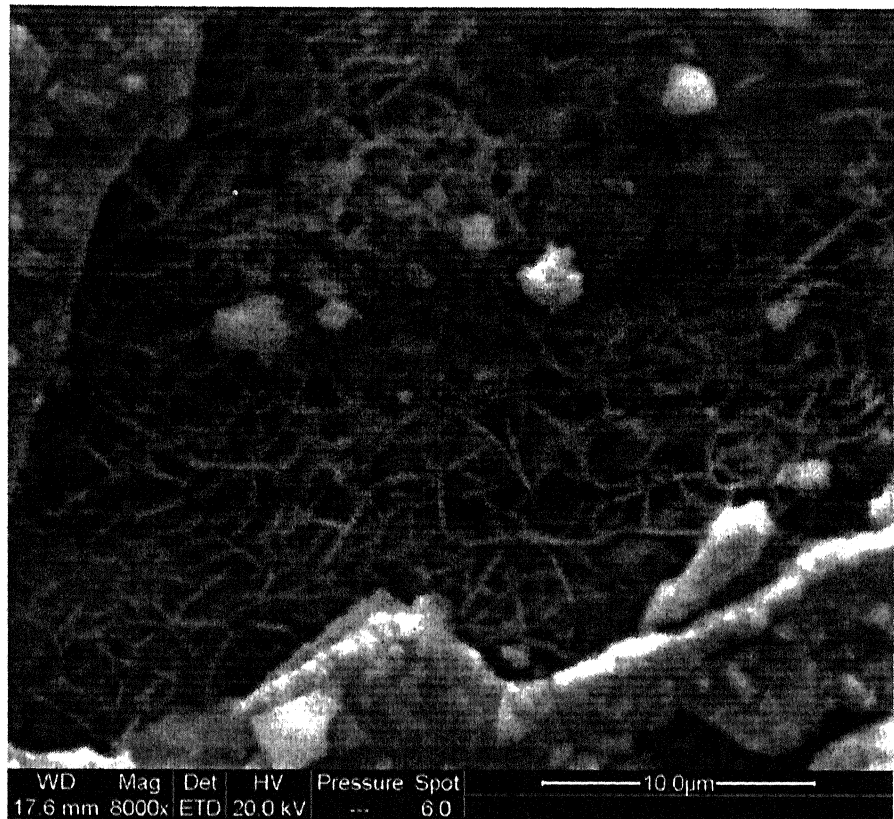
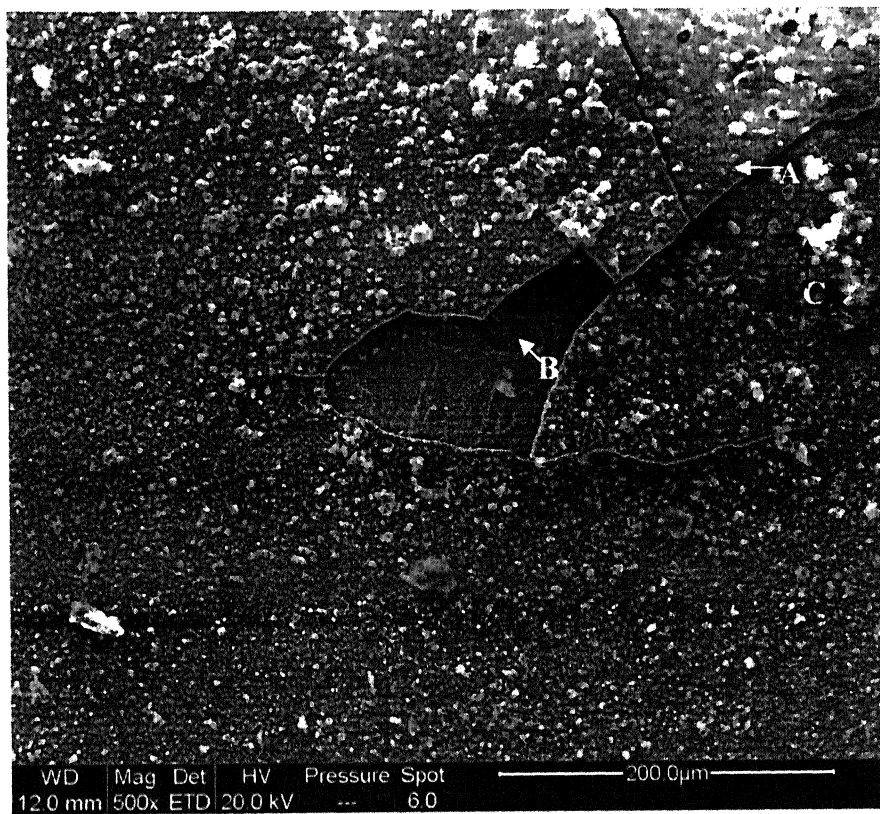
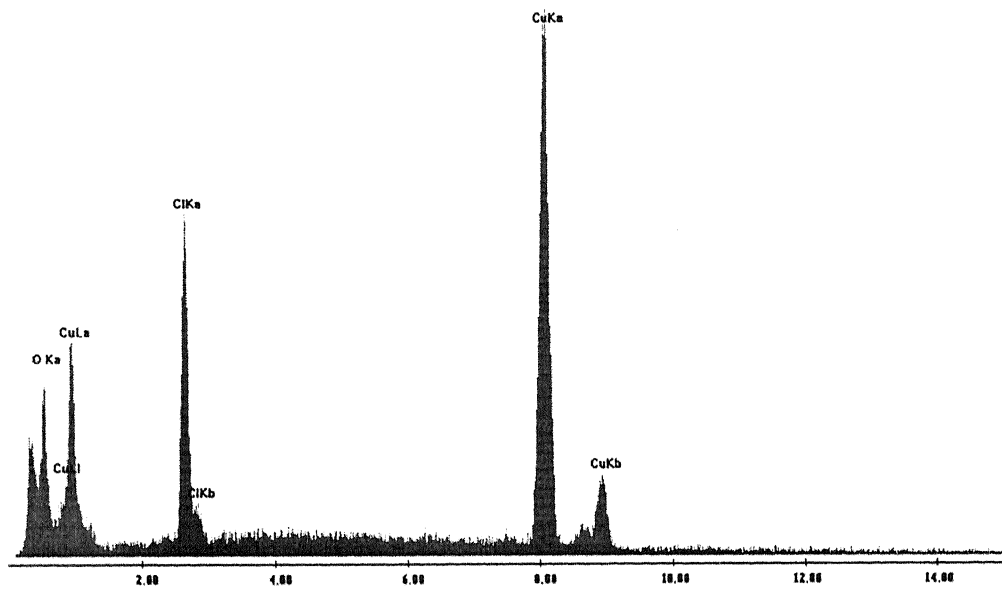


Fig. 33 SEM micrograph of copper surface obtained after immersion of 432 hours in aqueous solution A1, showing the needle like structure beneath the surface layer.



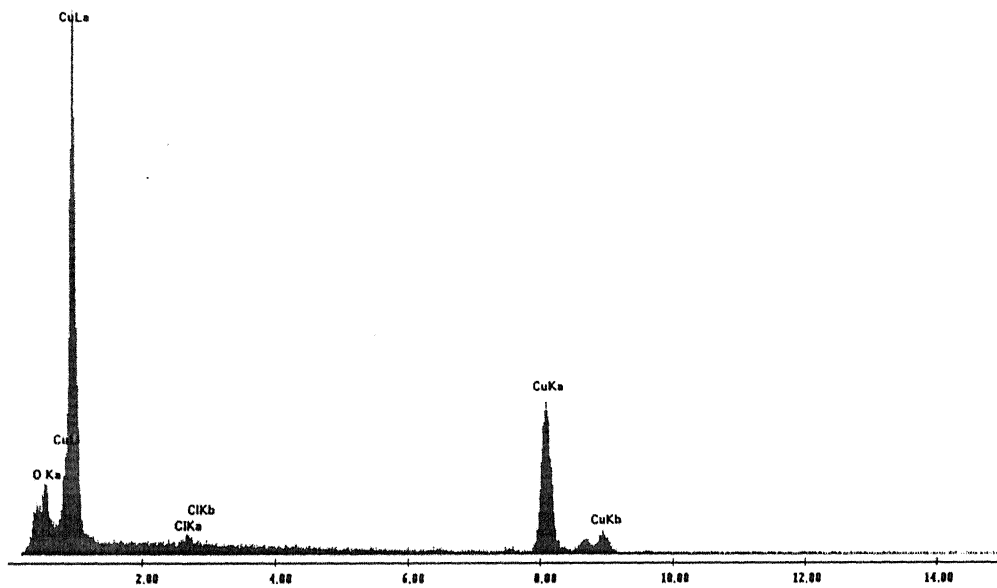
**Fig. 34** SEM micrograph of copper surface obtained after immersion of 432 hours in aqueous solution A1, showing a region from where the layer was peeled off.

Table A: AGI



**Fig. 35** Results of EDS done at point A in Fig. 34. EDS analysis confirmed that point A is located on Copper Oxide scale.

Label A: AO1



**Fig. 36** EDS at point B in Fig. 34 confirmed that point B is located in pure Copper region.

label A: AG1

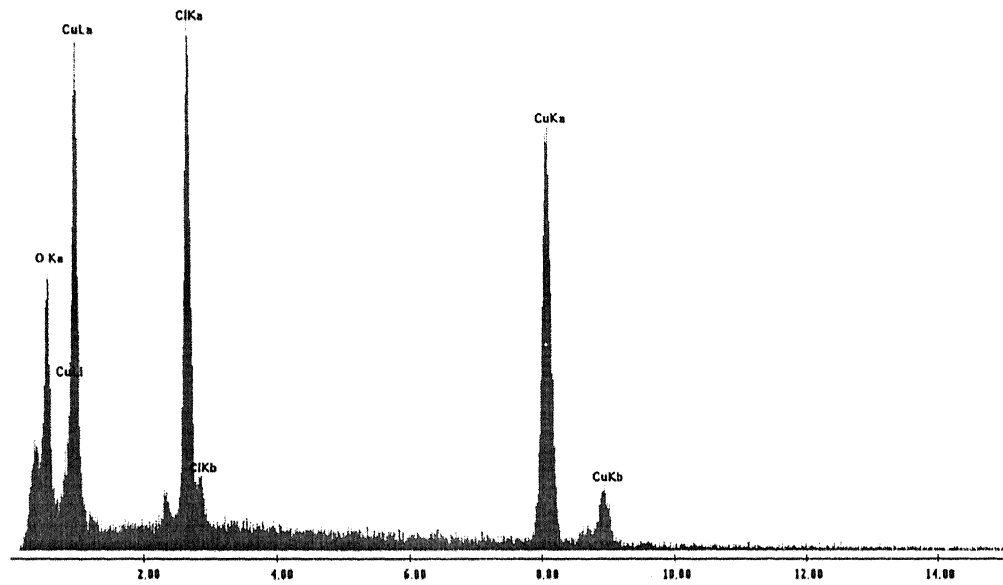


**Fig. 37** EDS at point C in Fig. 34 confirmed that point C is located on Copper Chloride particle.

## **100 ppm Na<sub>2</sub>S + Water (A3)**

Surface film formed on pure copper in this solution was studied in SEM. A film covered the surface. This was blackish brown in color as seen with the naked eye. A typical SEM micrograph from the surface is presented in Fig. 38. In Fig: 38, a part of the surface film has been disturbed and the underneath exposed metal can be noticed from where the layer has peeled off. The relatively darker region in Fig. 38 was clearly composed of surface film, and the rest of the area was of exposed base material, from where the surface layer had peeled off. The surface layer in this sample was relatively thin, and at several locations the edges of the scale were folded up (Figs. 39 & 40). The edges do not touch the base metal. It appears that the surface layer had slowly lost contact with the base metal and after that, it peeled off from the surface. The film does not appear to be protective, as it is not adherent to the surface. Cracks in the scale (Fig. 39) also indicate the non-protective nature of film. Most of the surface film from the middle of the sample was peeled off. Therefore, throughout the sample, the surface layer was present only in form of patches (Fig. 40). This physical picture of the surface provided the necessary background and justification for the use of a two time constant circuit, R(Q(R(QR))) for EIS analysis. The results indicate that the surface films formed in this environment are not protective.

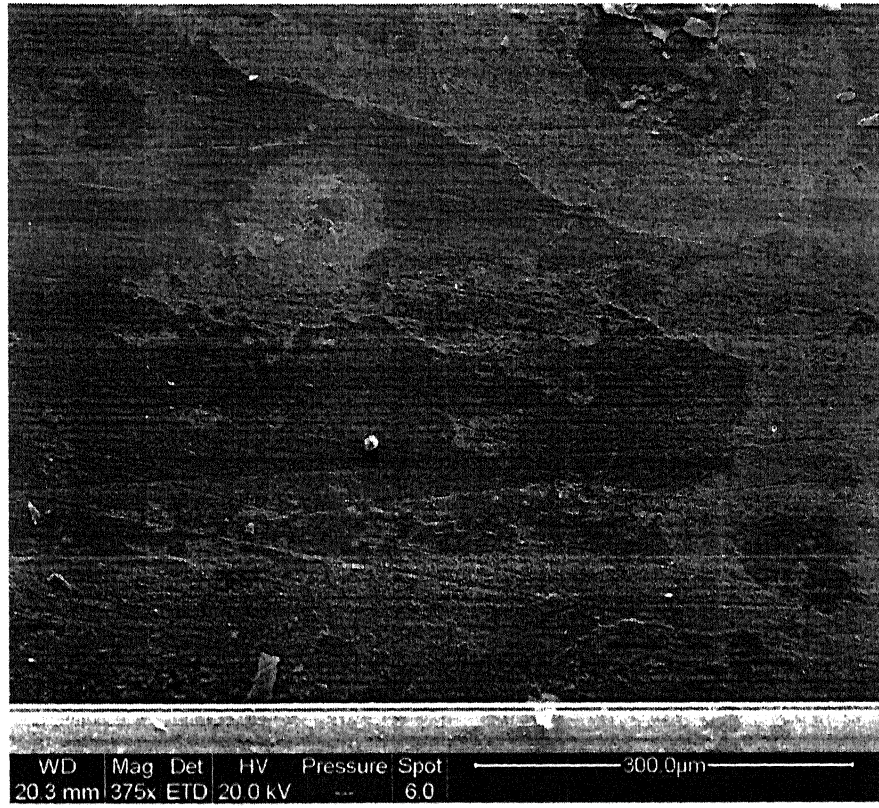


**Fig. 38** A typical SEM micrograph of copper surface obtained after immersion of 432 hours in aqueous solution A3.

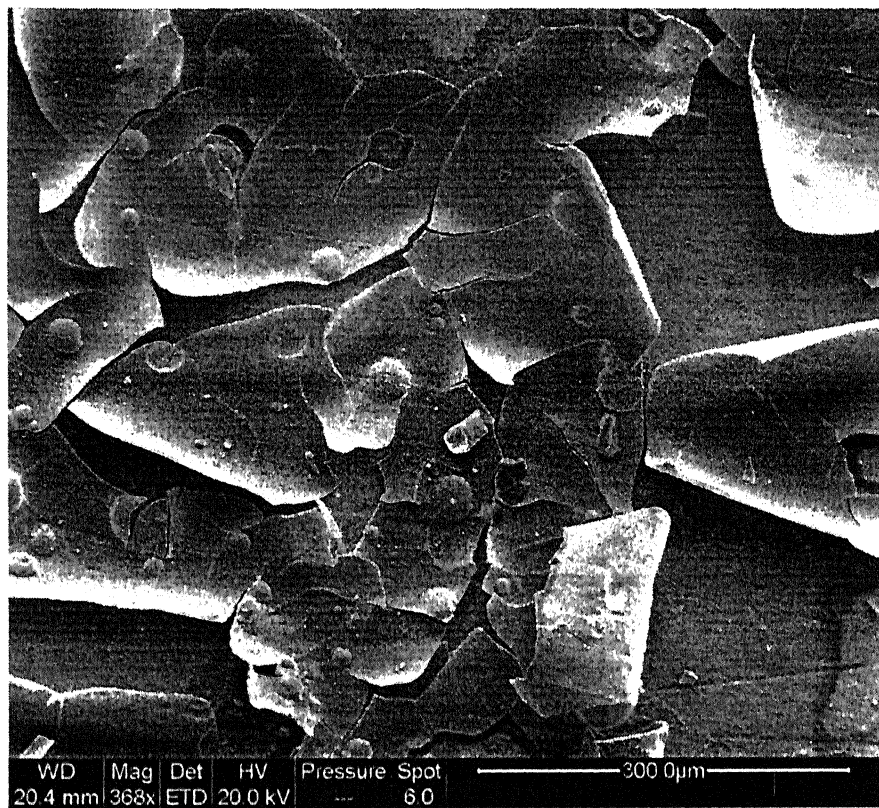
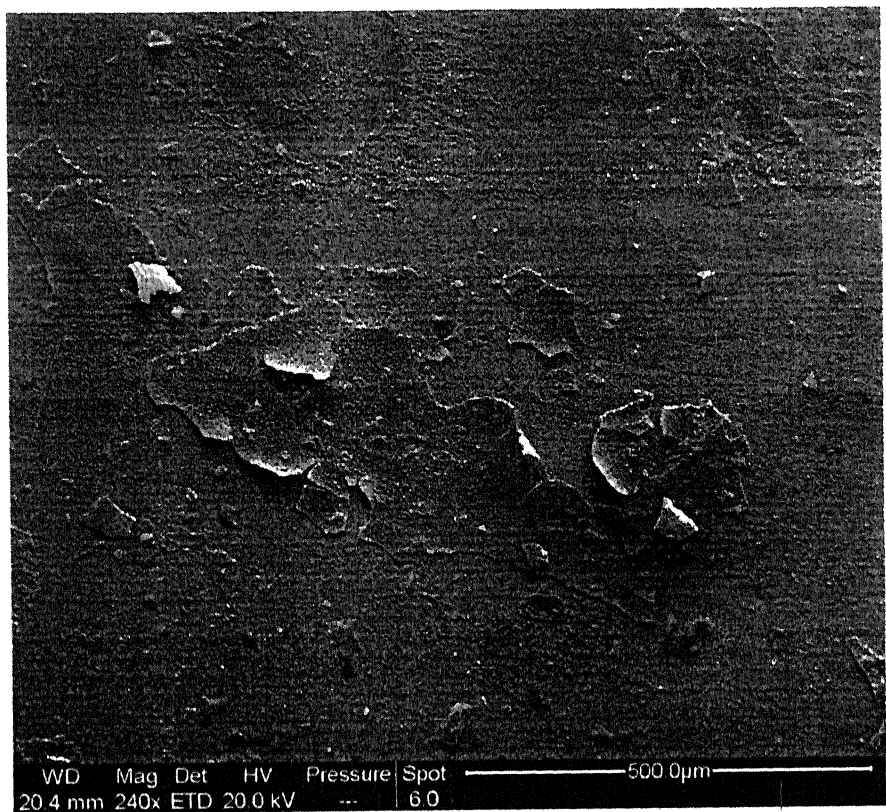


Fig. 39 SEM micrograph of copper surface obtained after immersion of 432 hours in aqueous solution A3, showing the portion of the layer which was peeling off.



**Fig. 40** SEM micrograph of copper surface obtained after immersion of 432 hours in aqueous solution A3, showing a region of the surface , from where the layer has peeled off.

## **1000 ppm NH<sub>4</sub>Cl + Water (A4)**

In this case, the surface film was brownish yellow in color as seen by the naked eye. The surface morphology of this film appeared to be similar to that after exposure to solution A1. There are some breakages in the top surface layer (Fig. 41). The film was thicker than the film obtained in solution A3 and moreover did not appear to peel off from the surface. Due to the discontinuous nature of the film, a two time constant circuit model,  $R(Q(R(QR)))$  would be used to fit EIS data. At locations where the surface film had been removed the underlying grain boundaries were etched by the corrosive solution (Fig. 42). The attack occurred at certain preferential crystallographic directions (Fig. 43).

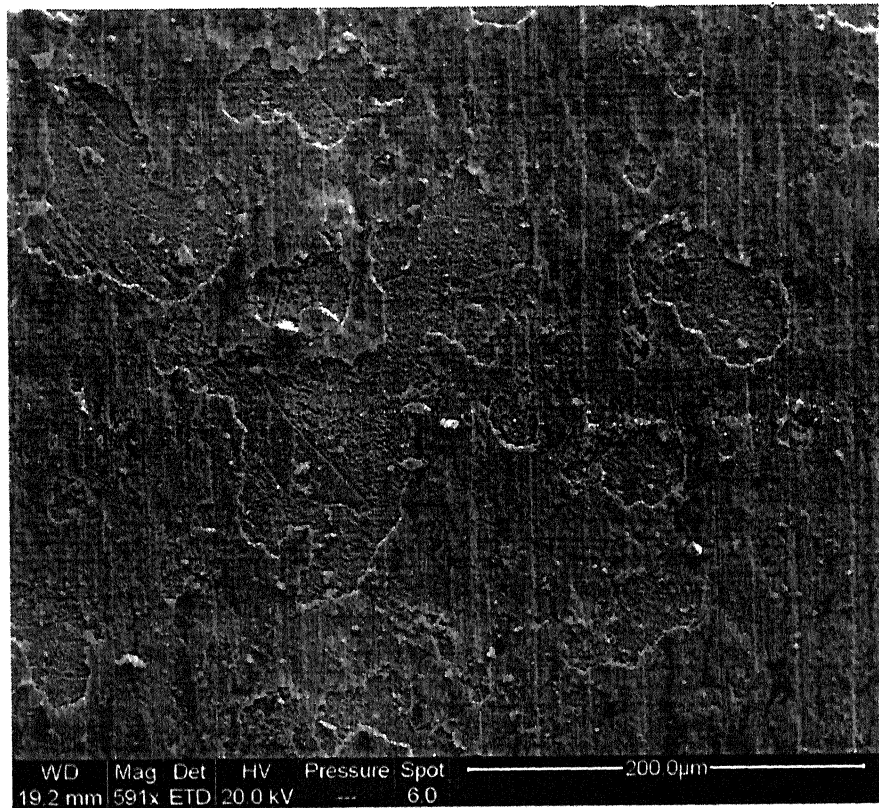


**Fig. 41** A typical SEM micrograph of copper surface obtained after immersion of 432 hours in aqueous solution A4.

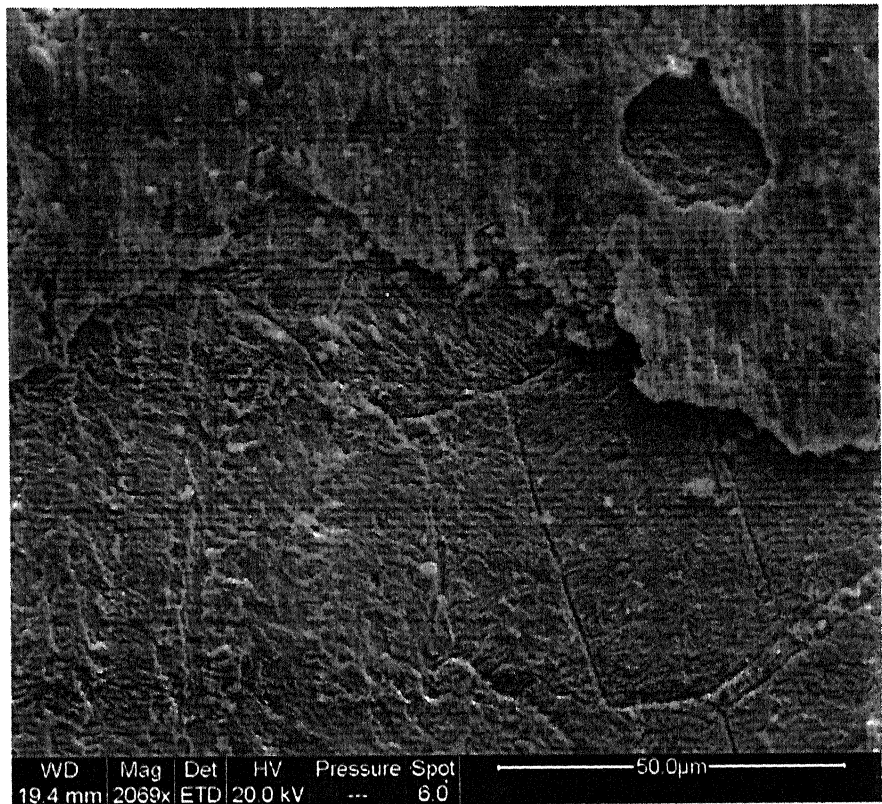
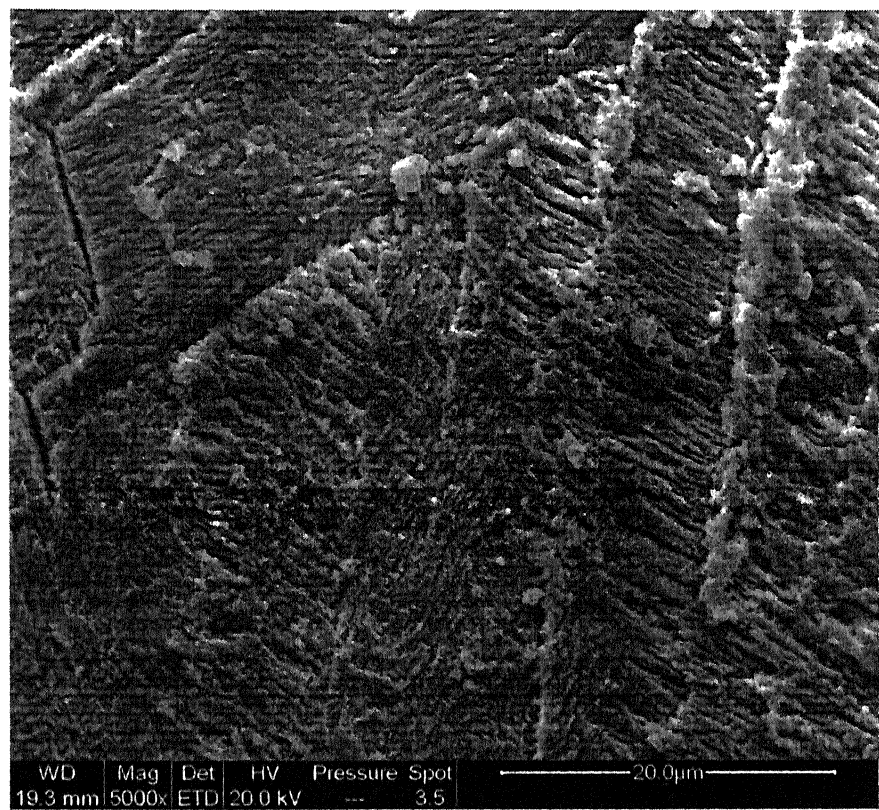


Fig. 42 SEM micrograph of copper surface obtained after immersion of 432 hours in aqueous solution A4, showing that at locations where the surface film had been removed the underlying grain boundaries were etched by the corrosive solution.



**Fig. 43** SEM micrograph of copper surface obtained after immersion of 432 hours in aqueous solution A4, showing that attack occurred at certain preferential crystallographic directions.

### **3.5 wt% NaCl + 1000 ppm NH<sub>4</sub>Cl + Water (A5)**

Figure 44 shows the surface of the sample at lower magnification. The large bright particles, dispersed on the surface, were copper chloride particles. The surface was relatively rough and the surface appeared to have been attacked severely by the corrosive solution (Fig. 45). The uneven surface appeared to be due to non-uniform rate of attack. There were locations which were more deeply attacked than the adjoining region (Fig. 45). EDS analysis was also performed to understand the nature of the surface. EDS analysis (Fig. 46) at point C confirmed that this was Copper Oxide layer. Some chloride could also be identified. Analysis (Fig. 47) from another point B in Fig. 45 indicated Copper Chloride predominantly. The copper oxide layer is composed of fine granular particles and copper chloride is present locally at some of the locations on the surface scale. The surface features indicate that the EIS data could be fit to R(Q(R(QR))) model. Point A in Fig. 48 again shows the exposed base metal (EDS graph shown in Fig. 49) and point B is located on the surface layer. The region near point B (EDS analysis is shown in Fig. 50) of Fig. 48, i.e. the copper oxide layer is shown at high magnification in Fig. 51. The microstructure is indicative of the layer growth by precipitation process. Cracks are also visible in the layer in Fig. 51.

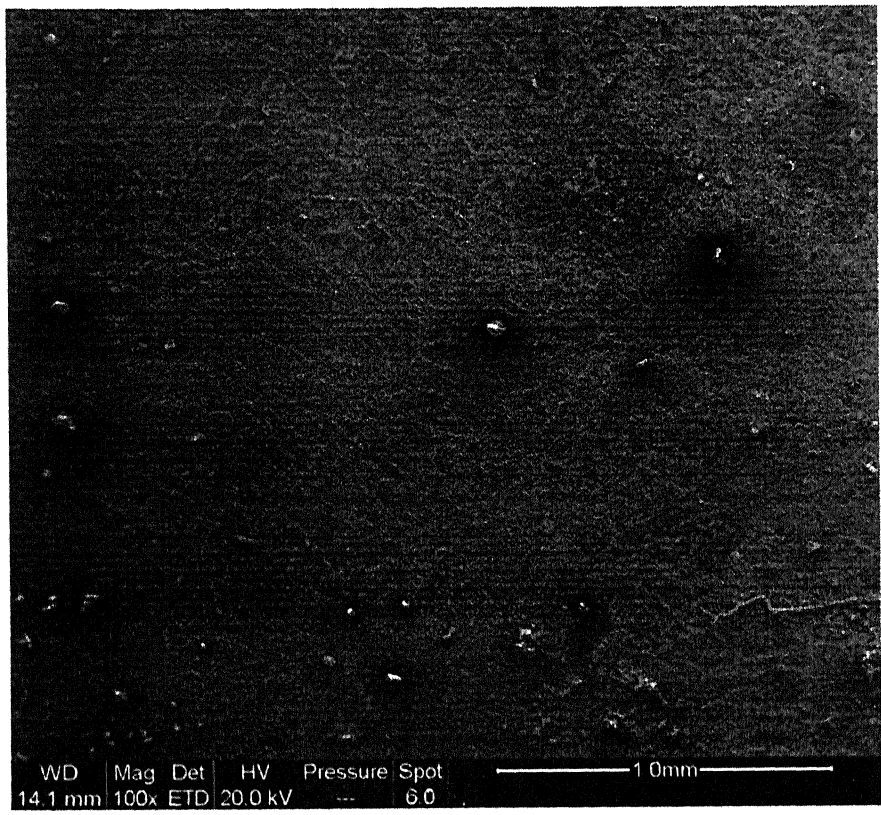


**Fig. 44** SEM micrograph of copper surface obtained after immersion of 432 hours in aqueous solution A5, showing the overall picture of the surface at lower magnification.

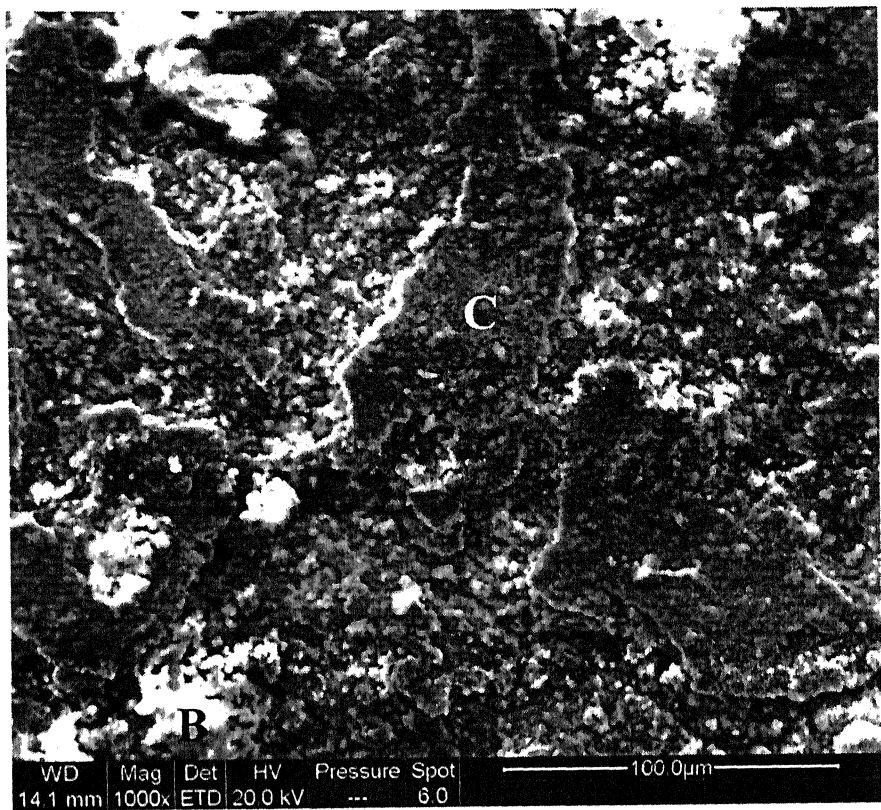
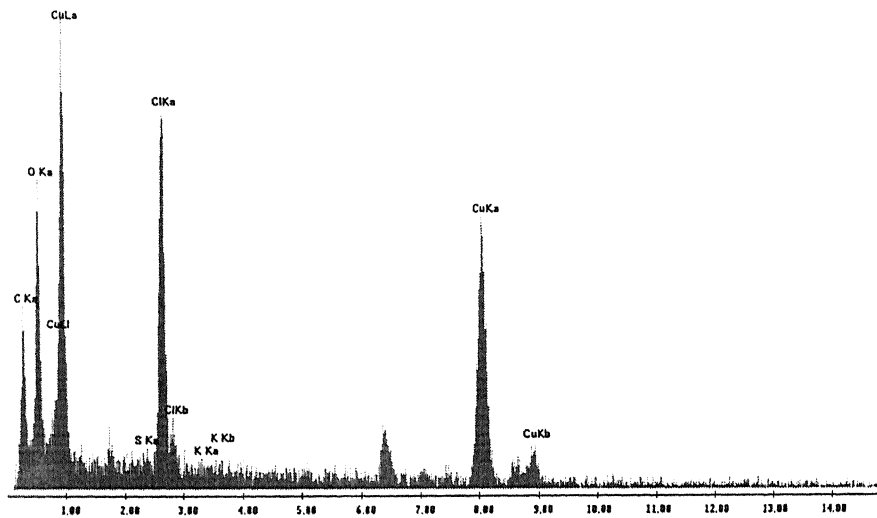


Fig. 45 SEM micrograph of copper surface obtained after immersion of 432 hours in aqueous solution A5, showing the severe attack by the corrosive solution.



**Fig. 46** EDS analysis done at point C in Fig. 45, confirmed that point C is located on copper oxide layer. Some chloride particles could also be identified on the oxide layer.

EDS ANALYSIS

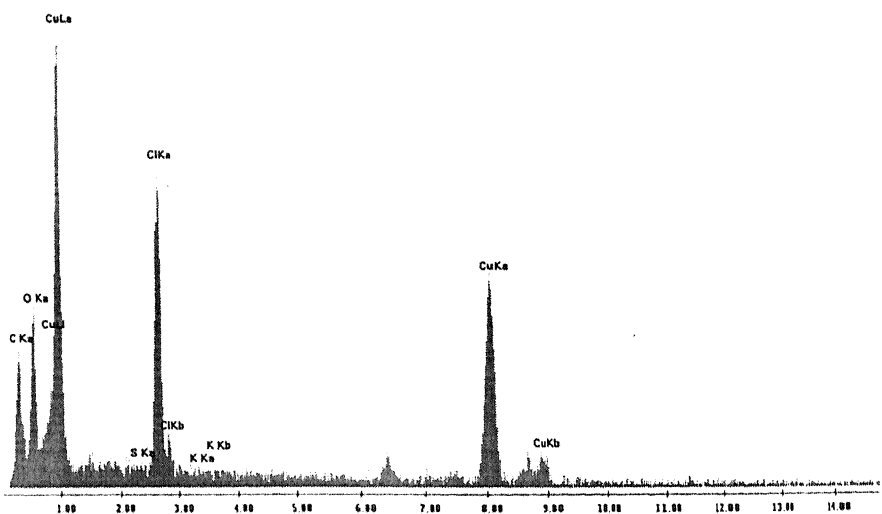
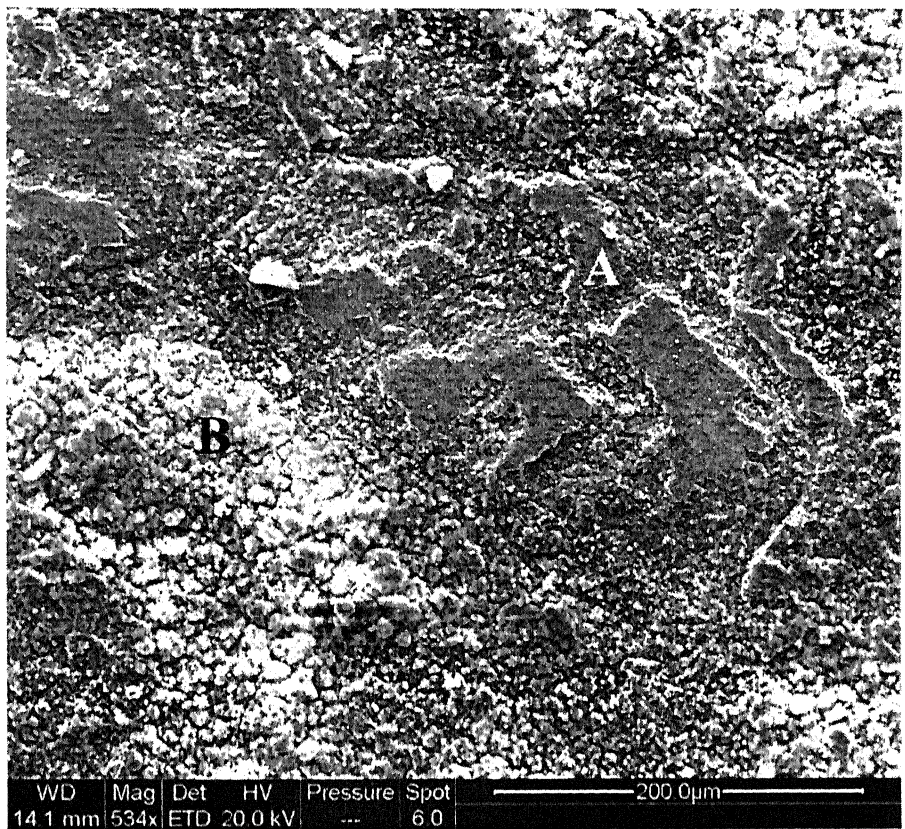
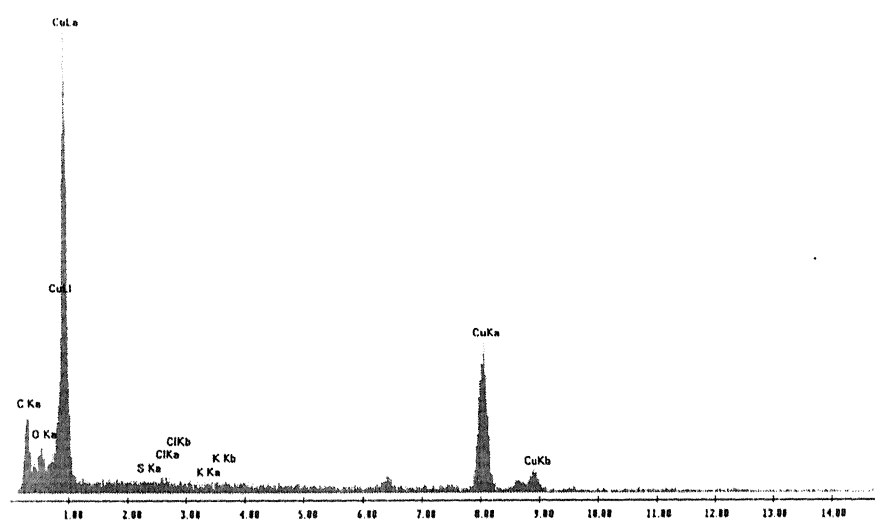


Fig. 47 EDS analysis from another point B in Fig. 45 indicated Copper Chloride predominantly.



**Fig. 48** SEM micrograph of copper surface obtained after immersion of 432 hours in aqueous solution A5, showing rough surface.



**Fig. 49** EDS analysis at point A in Fig. 48, confirmed that point A was located on exposed base metal.

Table 6. EDS

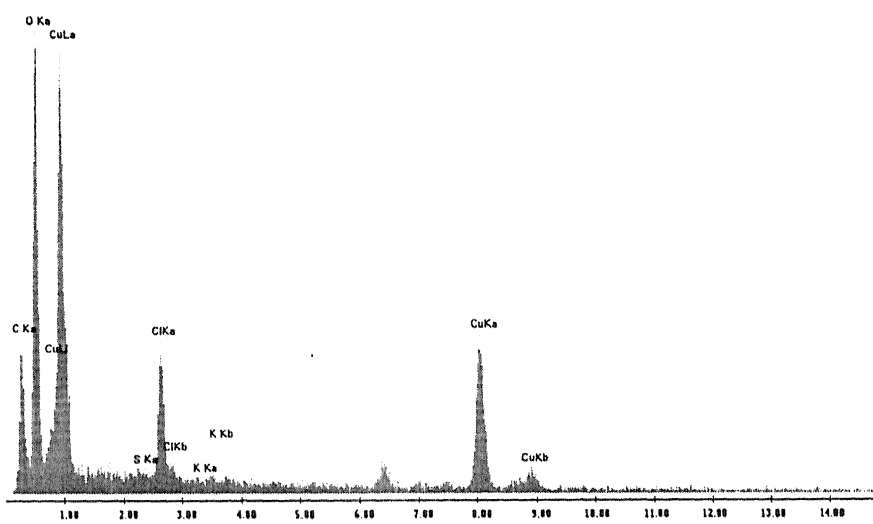


**Fig. 50** EDS at point B in Fig. 48 confirmed that point B was located on Copper Oxide layer.

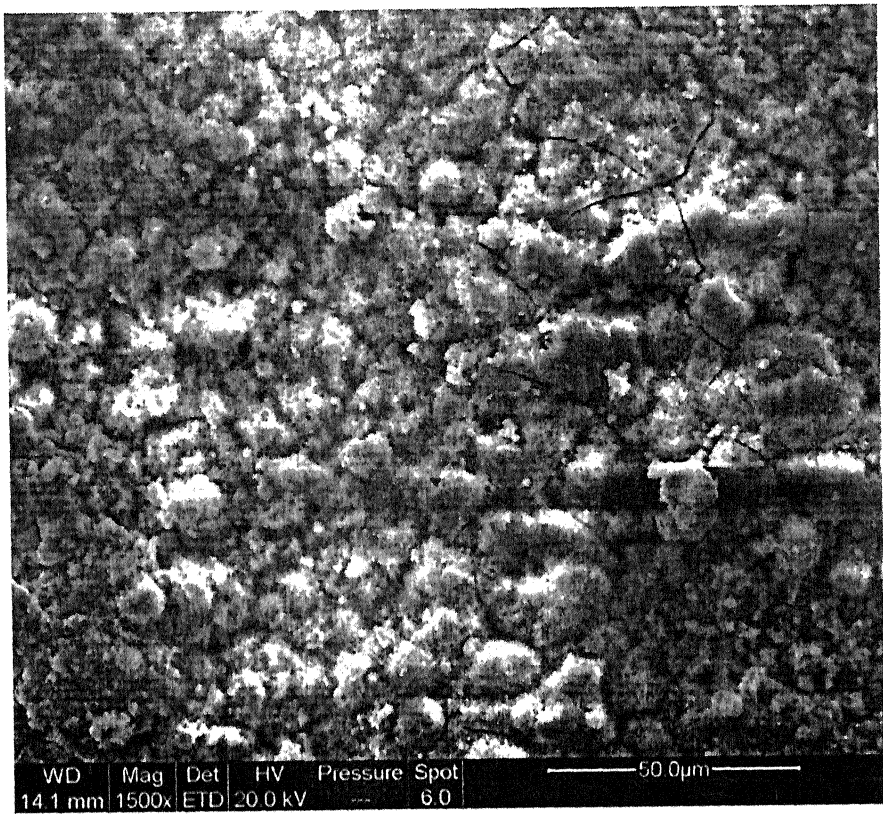


**Fig. 51** Region of oxide layer surrounding point B in Fig. 48 is presented here at higher magnification. Some cracks are also visible.

#### **4.2.2 Soil Environment**

The corrosive attack in the soil environments was not homogeneous, like in the case of aqueous solutions. One possible reason for the same was that after mixing the pollutants such as sodium sulfide and ammonium chloride in soil, some agglomeration of soil particles could be discerned. The metal surface was not uniformly exposed in the soil environments due to the very nature of the environment. This problem was realized later, when all the experiments were completed. The attack would have been uniform if the soil experiments would had been conducted in soil slurry or a better mixing mechanism was used.

#### **3.5 wt% NaCl + 100 ppm Na<sub>2</sub>S + 20 wt% water + dry soil (S6)**

The surface of the metal exposed in the soil condition S6 appeared bluish-green in color, in patches, on the surface. At some places, the surface was brown. Some particles were present on the surface that appeared to have been nucleated on the surface (Fig. 52). The surface was not homogeneous (Fig. 52). At higher magnification, it was found that the white particles of the previous figure (Fig. 52) were composed of smaller particles (Fig. 53). It appears that oxide layer precipitated in form of agglomerated particles. Cracks were also visible on these agglomerated particles (Fig. 54). Figure 55 suggests that these particles constitute a surface layer, which was not broken, although cracks were present in the layer. Green corrosion products were distributed throughout the surface (Fig. 56). Also at some places on the surface, the porous nature of the upper film could be discerned (Fig. 57). In Figure 57, the darker region is the central portion of the figure is lower in elevation as compared to the rest of the region. The surface layer was adherent on the surface, similar to the behavior noticed in chloride containing aqueous solutions.

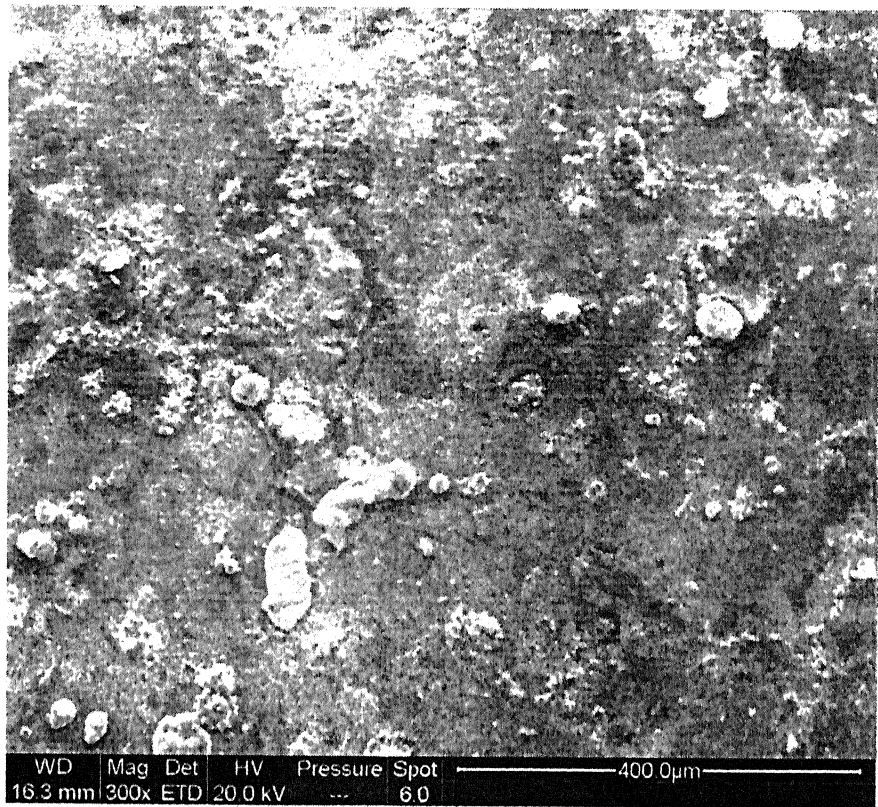


**Fig. 52** SEM micrograph of copper surface obtained after 432 hours of immersion in soil environment S6, showing nucleated oxide particles. The surface was not homogeneous.

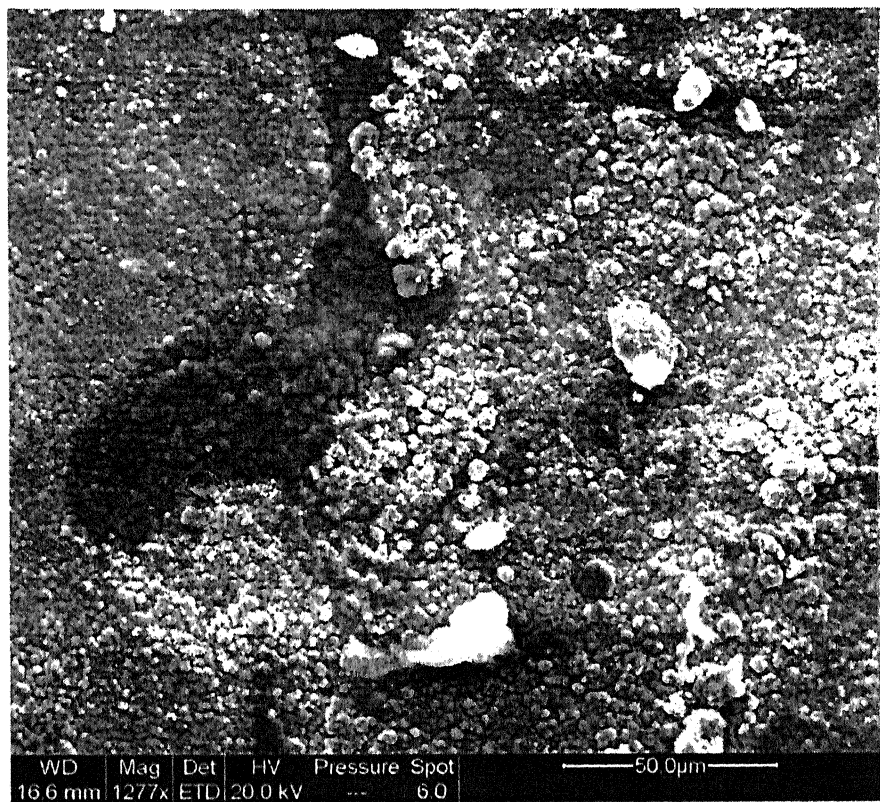


**Fig. 53** SEM micrograph of copper surface obtained after 432 hours of immersion in soil environment S6, showing that Copper Oxide layer was composed of very small nucleated particles.

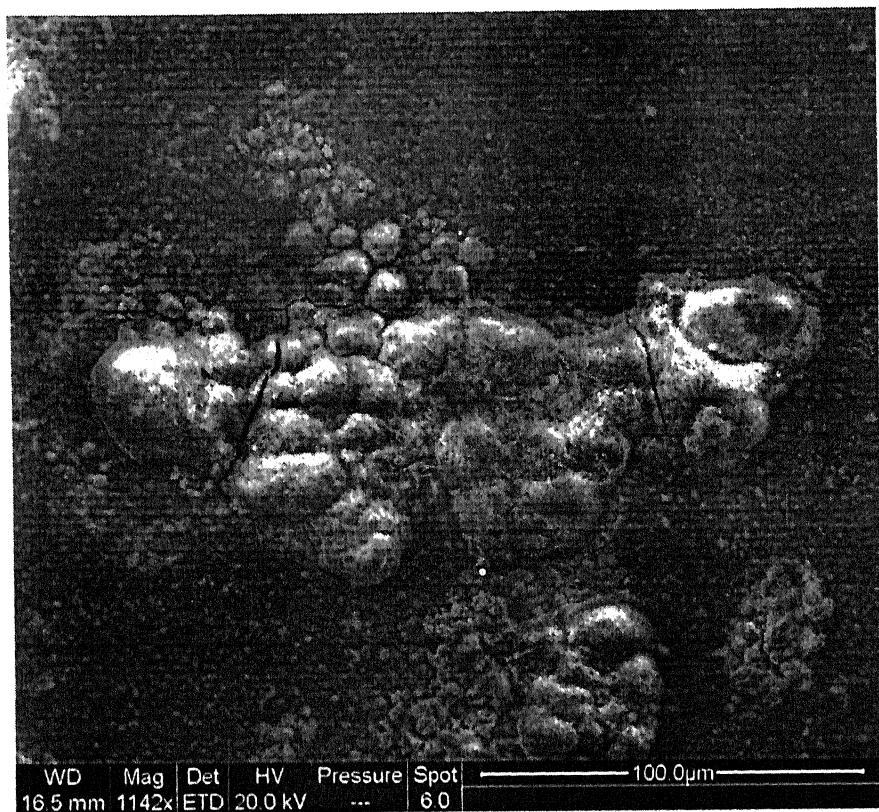


**Fig. 54** A magnified SEM view of copper surface obtained after 432 hours of immersion in soil environment S6, showing that Copper Oxide layer was composed of very small nucleated particles.

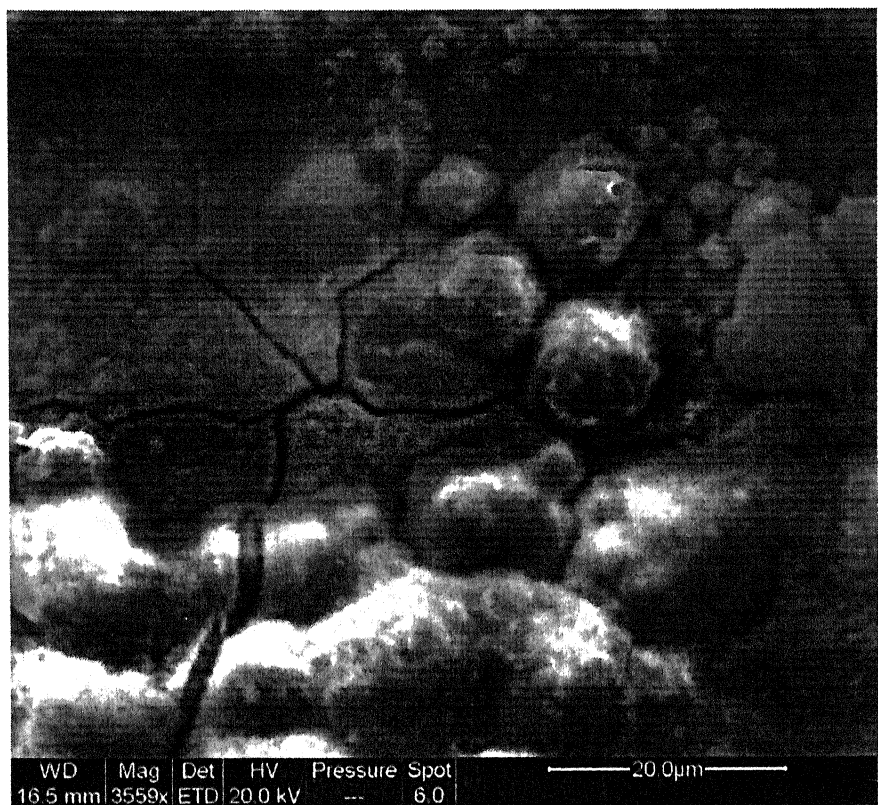


**Fig. 55** SEM micrograph of copper surface obtained after 432 hours of immersion in soil environment S6, suggested that small nucleated particles constitute a surface layer, which was not broken, although cracks were present in the layer.

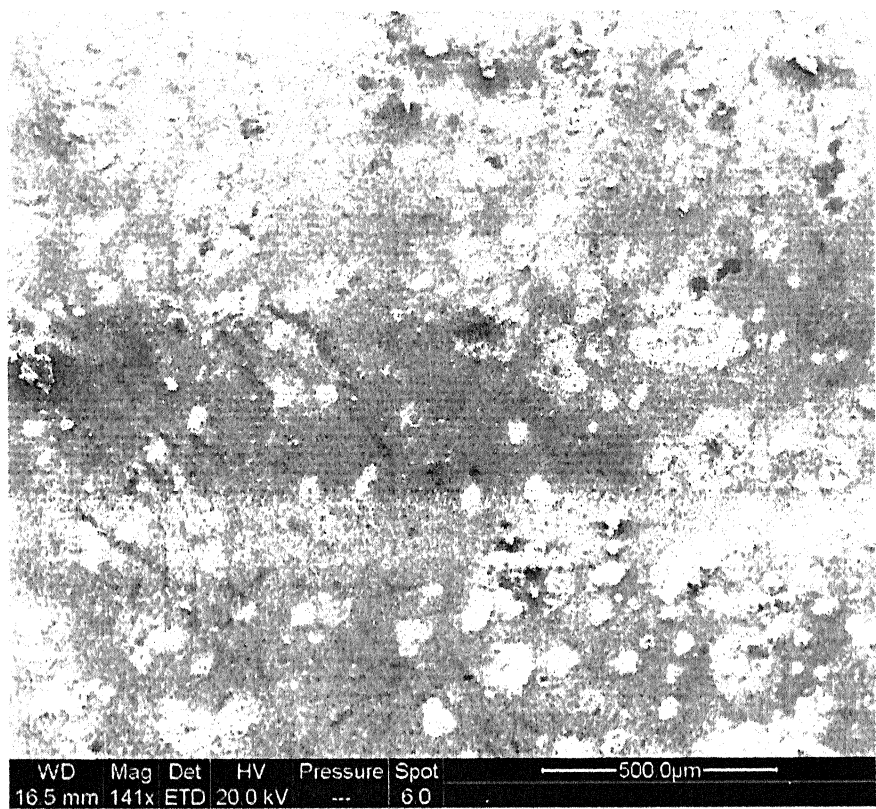


**Fig. 56** SEM micrograph of copper surface obtained after 432 hours of immersion in soil environment S6, showing that green corrosion products (which appeared bright in the microstructure) were distributed throughout the surface.

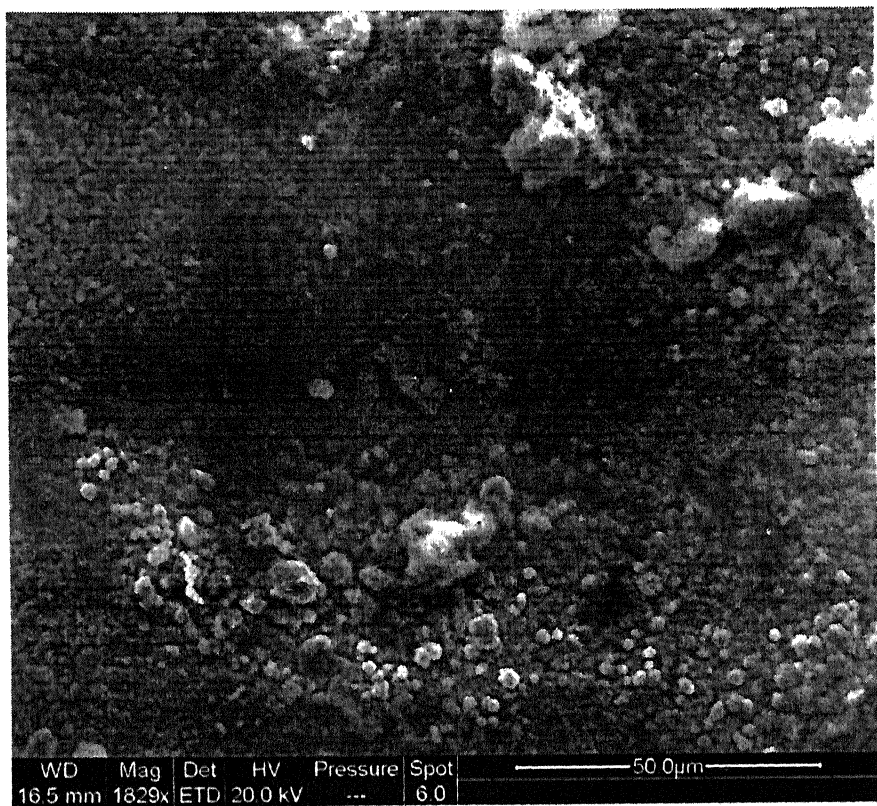
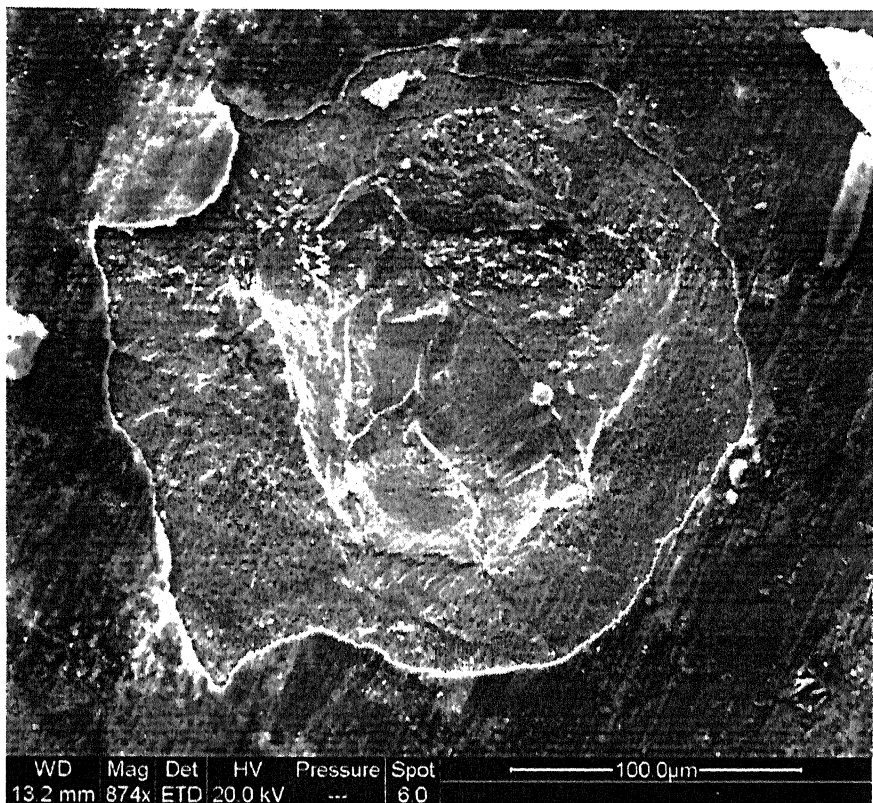


Fig. 57 SEM micrograph of copper surface obtained after 432 hours of immersion in soil environment S6. At some places on the surface, the porous nature of the surface film could be discerned.

## **100 ppm Na<sub>2</sub>S + 20 wt% water + dry soil (S8)**

The surface layer obtained in soil S8 appeared blackish-brown in color, although this discoloration was not homogeneous. At some places, some yellow soil particles were also present on the surface. The surface layer appeared to peel off from the surface (Fig. 58). In Fig. 58, the surface layer can be easily distinguished. Moreover, the layer appeared to peel off and this was similar to the surface obtained on immersion in solution A3. At higher magnification of the region that had peeled off in Fig. 58, it was found that attack took place along some preferred orientation within the grains (Fig. 59). Some white corrosion product was also seen on the surface (Fig. 60). A high magnification view of the region near white corrosion product is shown in Fig. 61. The darker portion of Fig. 61 was essentially pure Cu, which was present beneath the Copper Oxide layer (white portion). EDS analysis at points A and B to the darker and white portions of the microstructure are shown in Figs. 62 & 63. Figure 64 shows a location from where the layer was peeled off from the surface. Point A and B were analyzed by spot analysis (EDS graph shown in Figs. 65 & 66). The region from where the layer has been removed (point A) was essentially pure Cu and the layer was of Copper Oxide. Some chloride contamination due to KCl present in the salt bridge could be identified (Figure 67). The surface layer was composed of copper oxide particles nucleating and agglomerating on the surface (Fig. 69), which was later confirmed by EDS shown in Figs. 70 and 71. In between the agglomerated particles, pores were present.



**Fig. 58** SEM micrograph of copper surface obtained after 432 hours of immersion in soil environment S8. The surface layer appeared to peel off from the surface

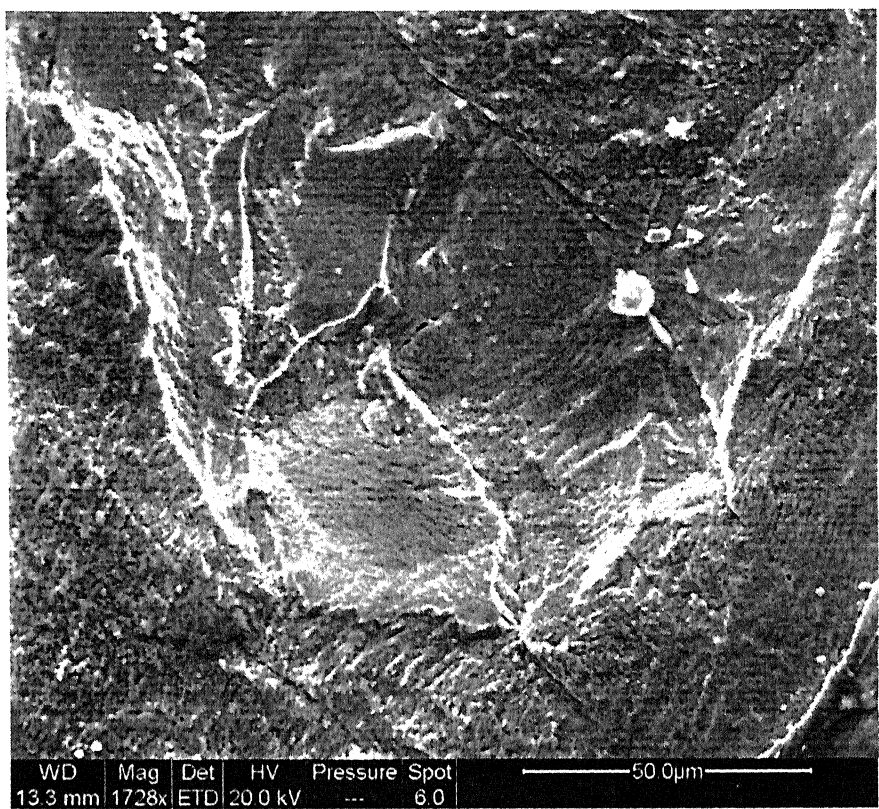


**Fig. 59** A magnified SEM view of copper surface obtained after 432 hours of immersion in soil environment S8. It is shown that attack took place along some preferred orientation within the grains.

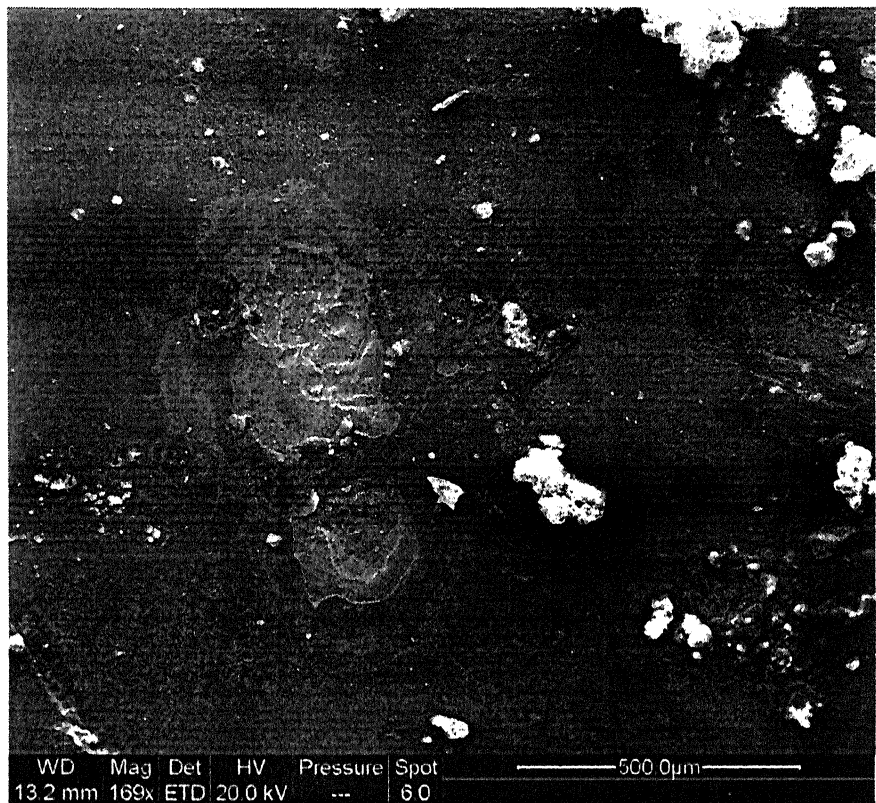


**Fig. 60** SEM micrograph of copper surface obtained after 432 hours of immersion in soil environment S8, showing some white corrosion product.

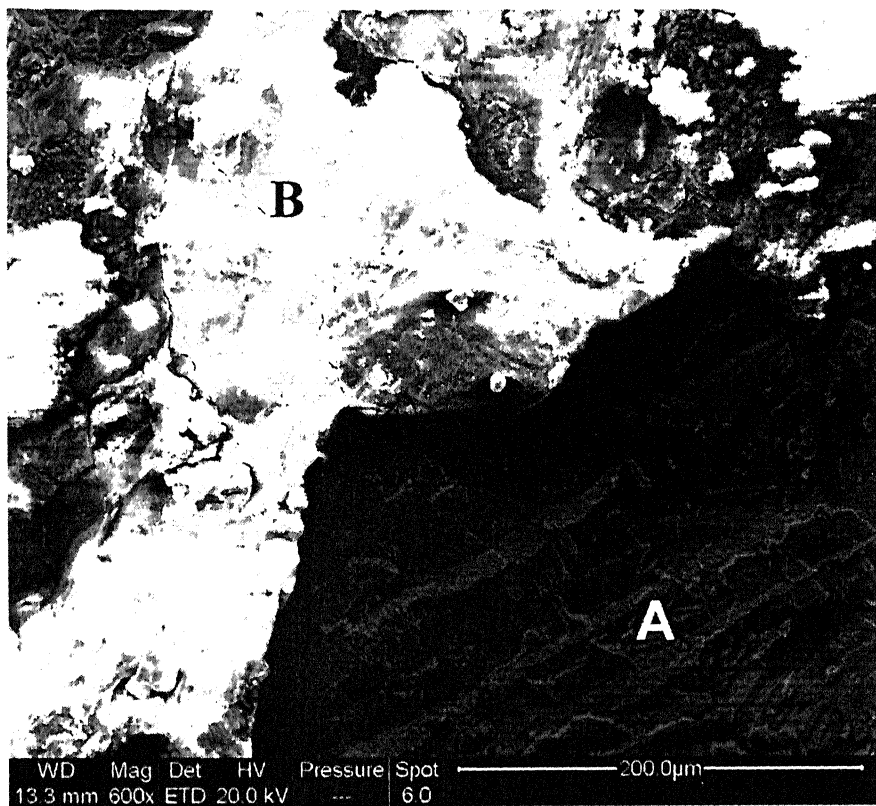


**Fig. 61** SEM micrograph of copper surface obtained after 432 hours of immersion in soil environment S8, showing a high magnification view of the region near white corrosion product in Fig. 60.

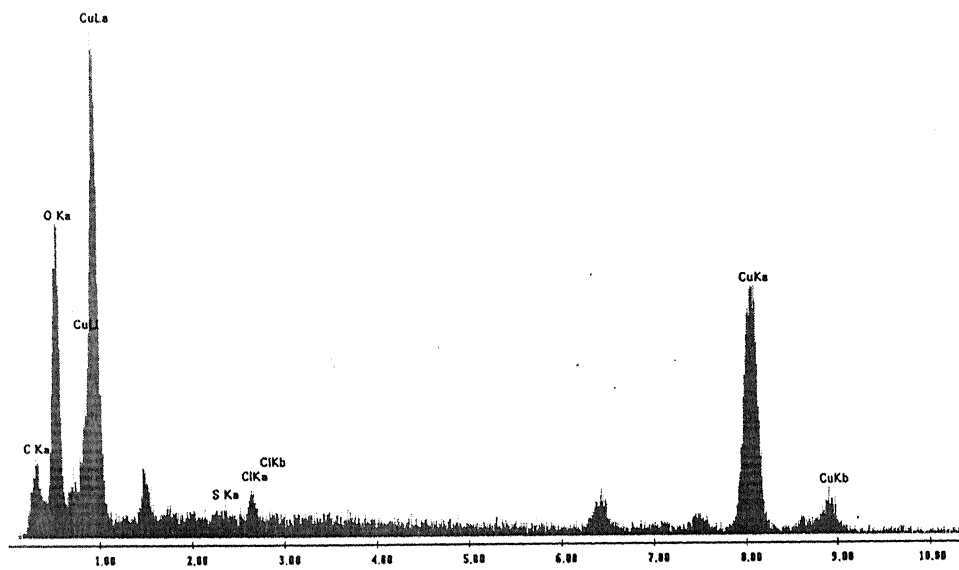


**Fig. 63** EDS analysis done at point B in Fig. 61 suggested that white corrosion product was Copper Oxide.

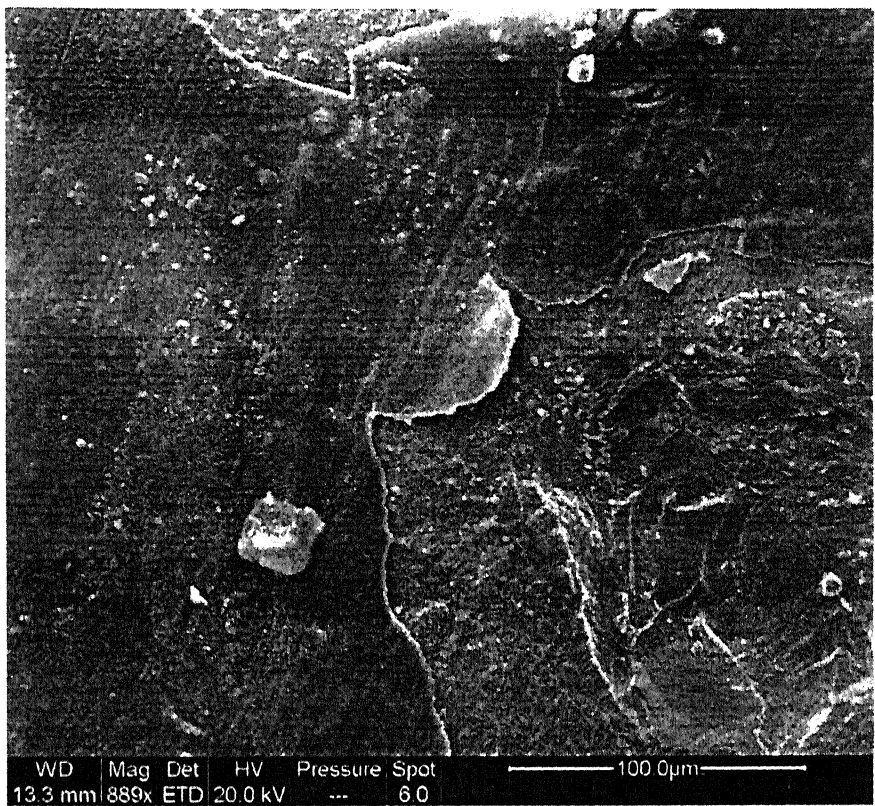


**Fig. 64** SEM micrograph of copper surface obtained after 432 hours of immersion in soil environment S8, showing a location from where the layer had peeled off from the surface.

Soil2\_A.soil2\_002

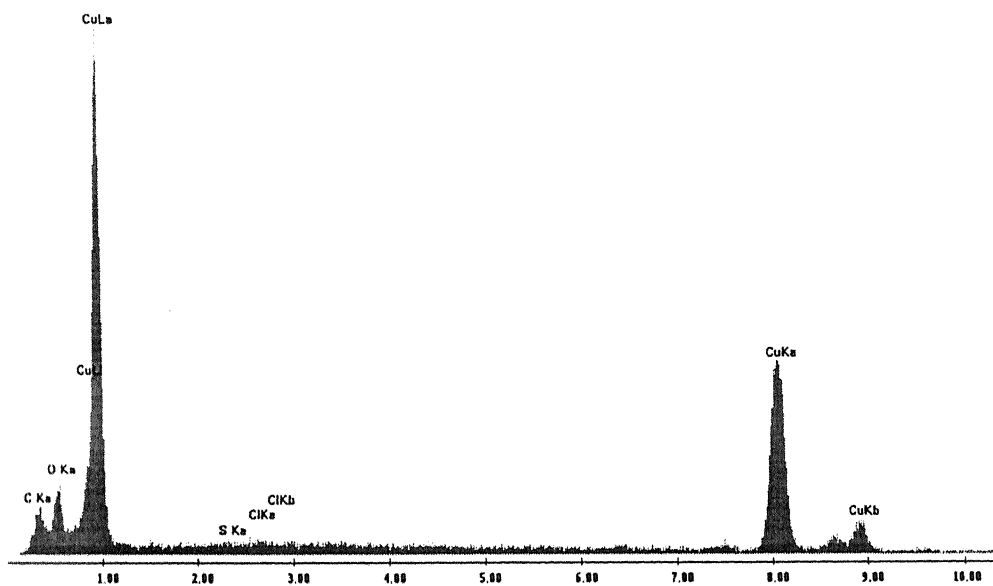


**Fig. 65** EDS analysis done at point A in Fig. 64 confirmed that point A is located on the pure Copper .region.

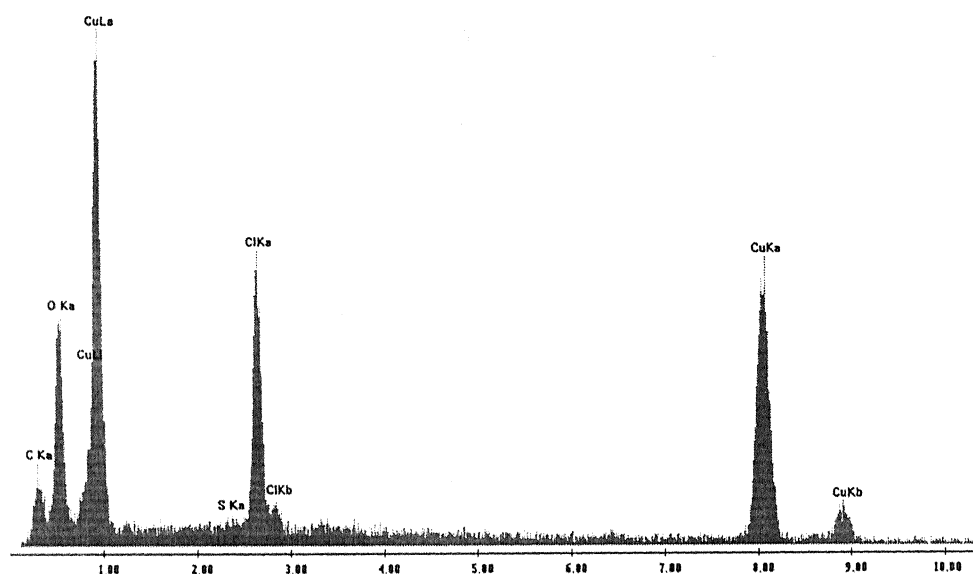


**Fig. 66** EDS analysis done at point B in Fig. 64 confirmed that point B was located on the Copper Oxide layer. Some chloride could also be identified on the layer.

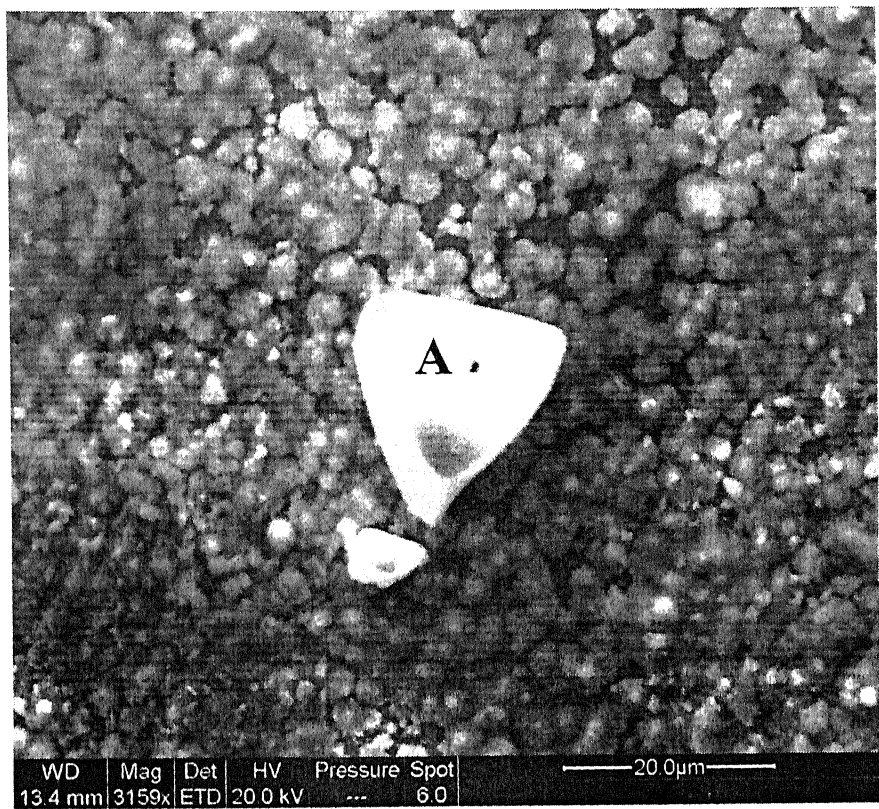


**Fig. 67** SEM micrograph of copper surface obtained after 432 hours of immersion in soil environment S8, showing that some chloride contamination due to KCl was present on Copper Oxide layer.

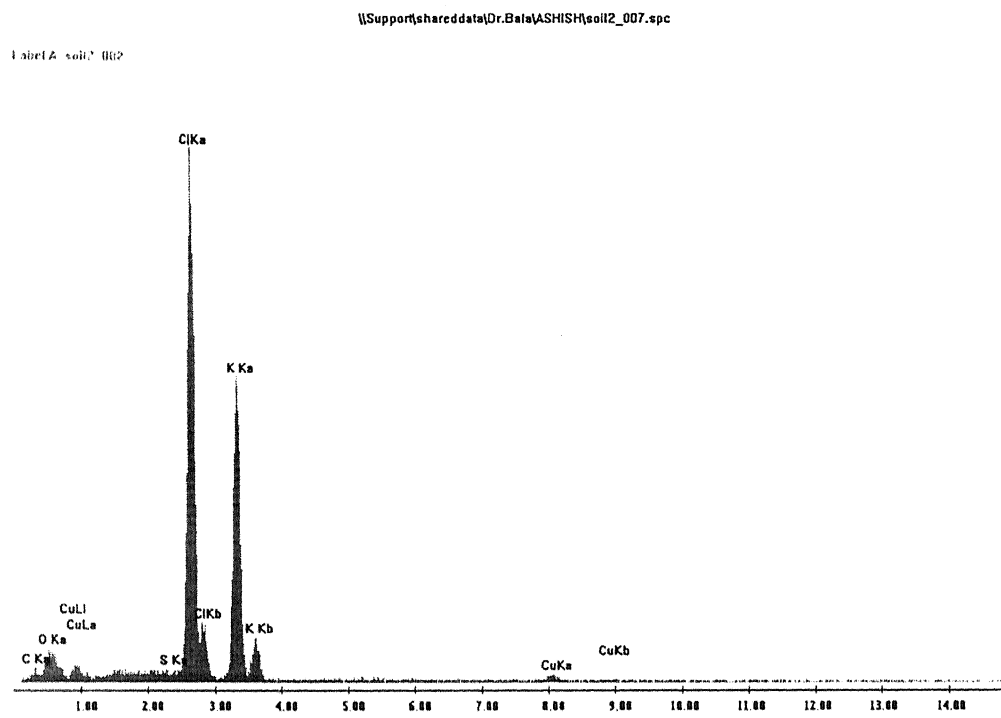
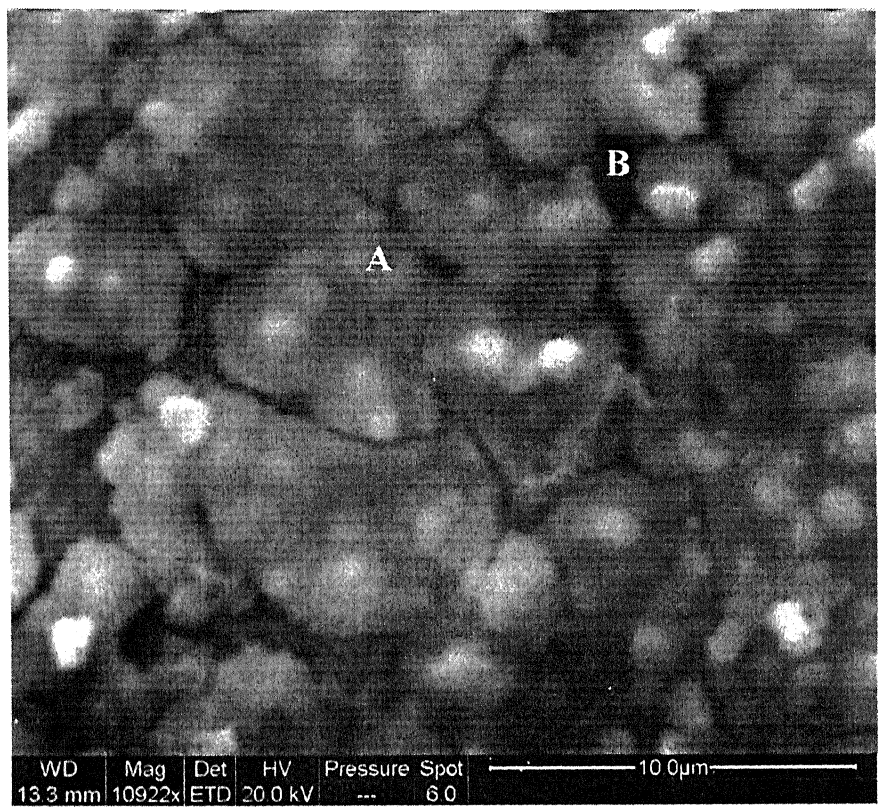
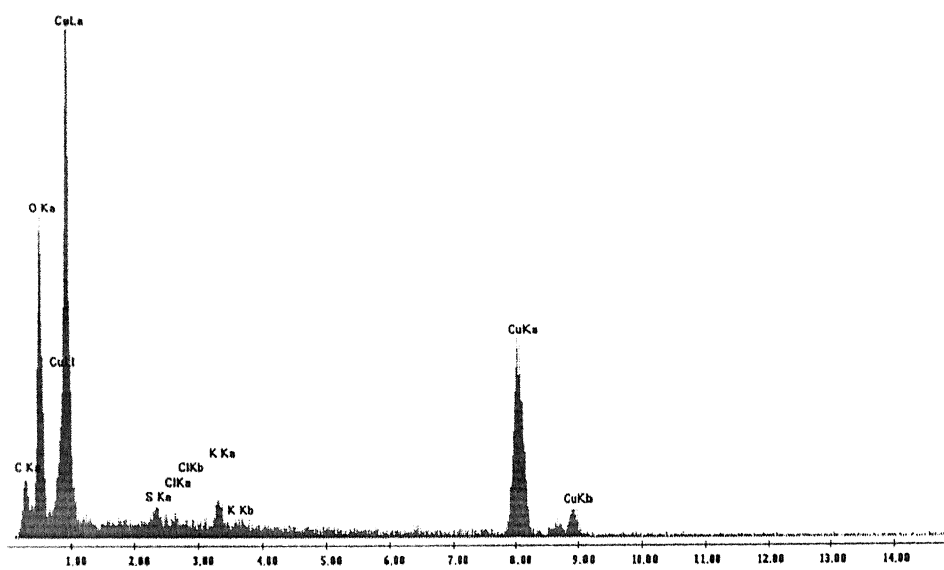


Fig. 68 EDS analysis done at point A in Fig. 67, confirmed it to be a KCl particle.



**Fig. 69** SEM micrograph of copper surface obtained after 432 hours of immersion in soil environment S8, showing that the surface layer was composed of Copper Oxide particles nucleating and agglomerating on the surface.

Table A: EDS Data



**Fig. 70** EDS analysis done at point A in Fig. 69, confirmed that point A was located on Copper Oxide layer.

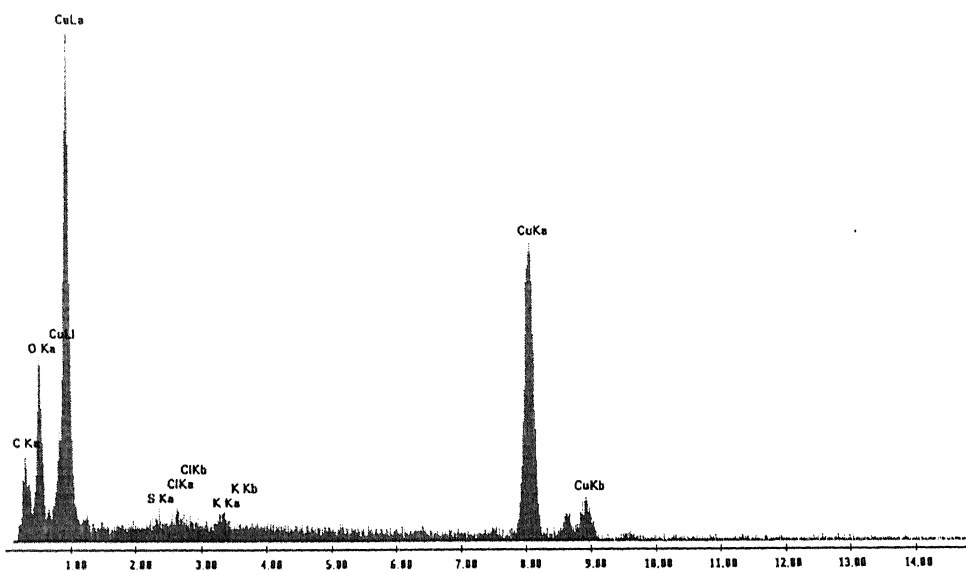


**Fig. 71** EDS analysis done at point B in Fig. 69, confirmed that point B was located on a pore.

## **1000 ppm NH<sub>4</sub>Cl + 20 wt% water + dry soil (S9)**

The surface was covered with a copper oxide layer. At some places the layer was detached and underlying metal was exposed in these areas. The surface layer was porous in nature. Some bright agglomerated particles were also seen at some places in the microstructure (Fig. 72). These bright particles were essentially copper chloride agglomerates (EDS analysis shown in Fig. 73). Figure 74 shows a location where the underlying metal has been exposed (EDS results shown in Fig. 75). Attack has occurred on some preferred crystallographic directions in the metal and also grain boundaries were etched (Fig. 74).

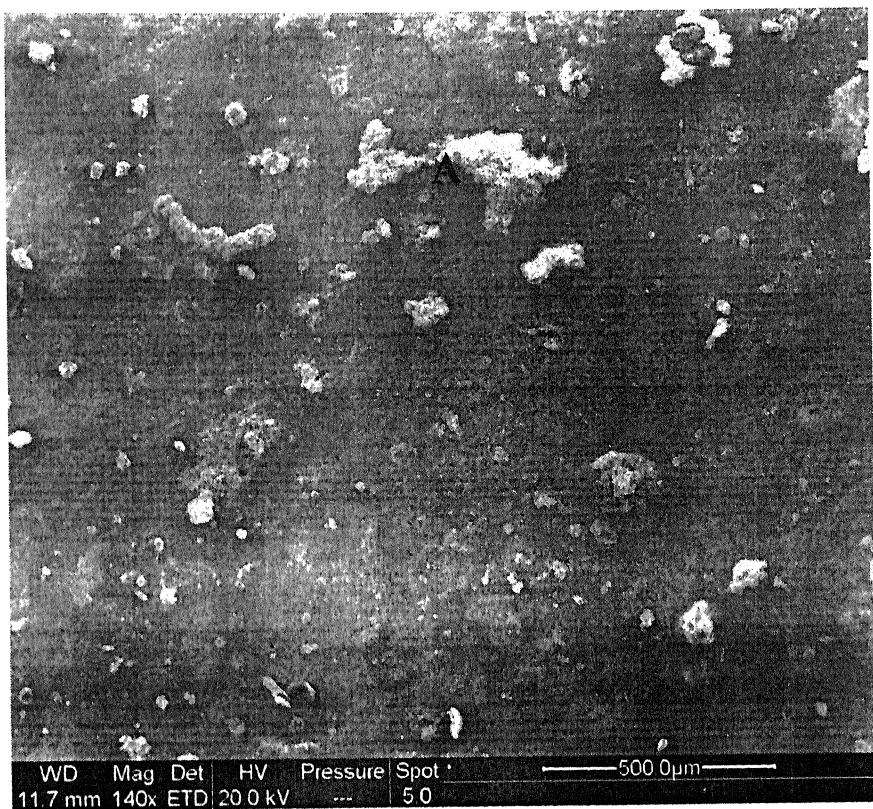


Fig. 72 SEM micrograph of copper surface obtained after 432 hours of immersion in soil environment S9, showing some bright Copper Oxide particles.

value of N = 1000

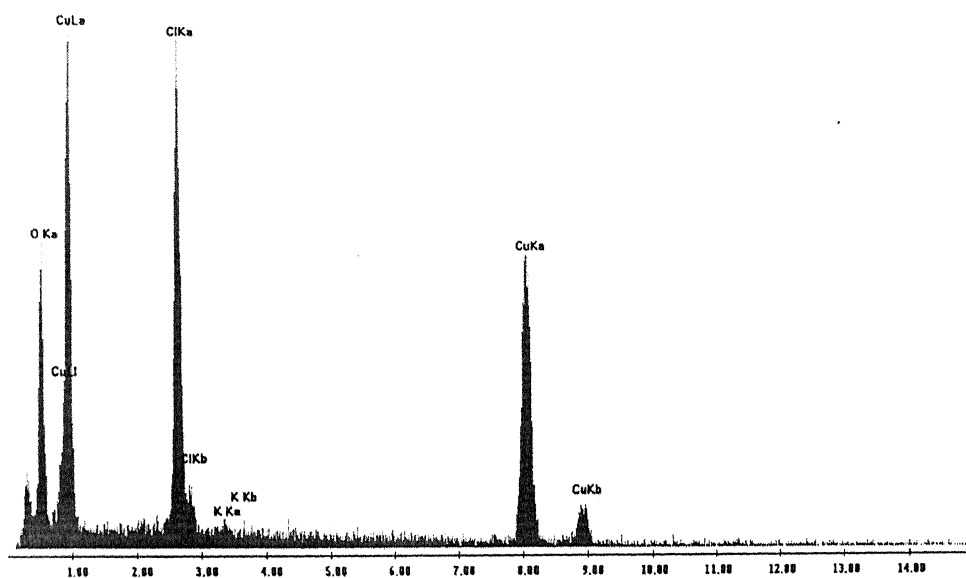


Fig. 73 EDS analysis done at point A in Fig. 72, confirmed that point A was located on a Copper Oxide particle.

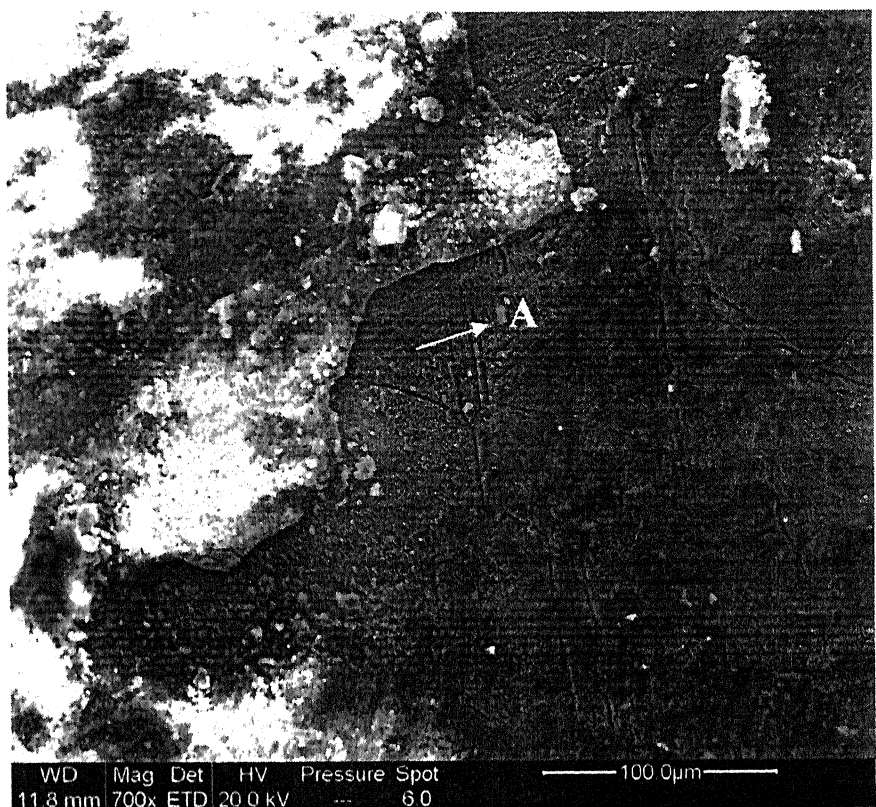


Fig. 74 SEM micrograph of copper surface obtained after 432 hours of immersion in soil environment S9, shows a location where the underlying metal has been exposed

Fig. 74 (continued)

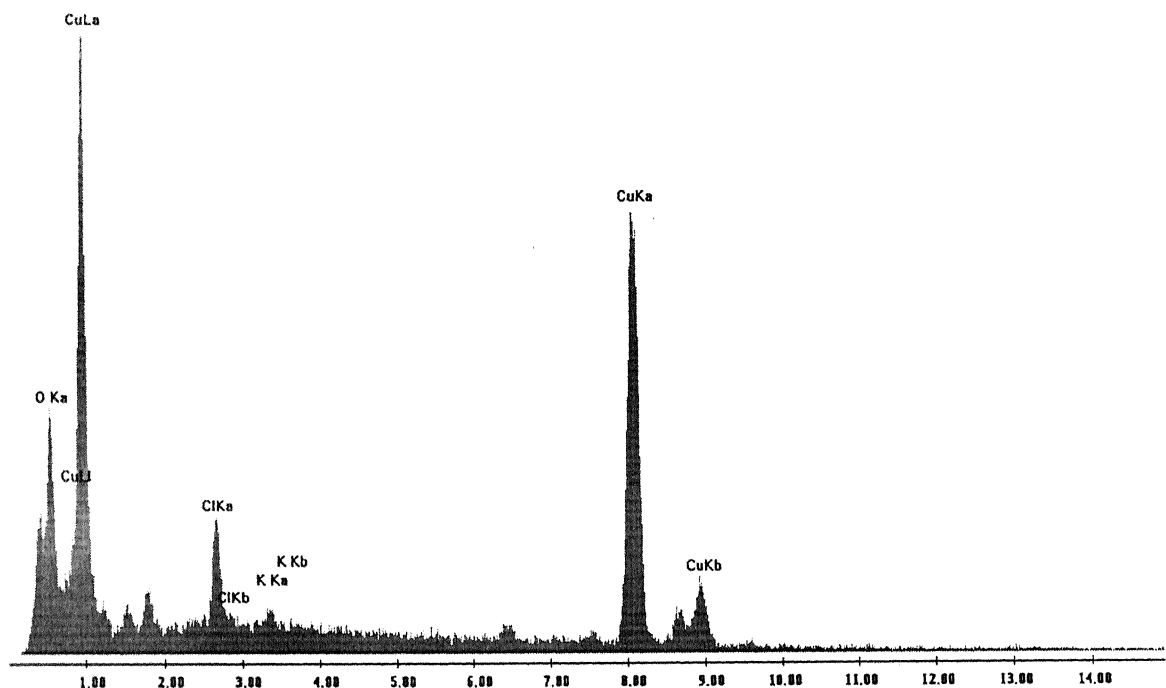


Fig. 75 EDS analysis done at point A in Fig. 74, confirmed that point A was located on the exposed metal.

**3.5 wt% NaCl + 1000 ppm NH<sub>4</sub>Cl + 20 wt% water + dry soil  
(S10)**

In this case, the entire surface was covered with a layer of copper oxide. Some regions appeared bright, while the rest appeared dark (Fig. 76). The locations that appear bright are the layer locations that are peeling off. It has lost contact from the surface, making these regions non-conducting and hence was charged during SEM observations. Moreover, the scale that has peeled off was cracked (Fig. 77). EDS analysis (Fig. 78) at a point A on the scale confirmed that it was copper oxide. EDS analysis (Fig. 79) from the dark region indicated a much lower oxygen content. The bright-appearing copper oxide scale at higher magnifications (Figs. 80, 81 and 82) reveals that the scale was cracked and that the cracks propagated in certain preferred directions. EDS analysis (Fig. 83) at point A in Fig. 82 revealed that the region surrounding the bright scale was essentially of copper oxide layer. Earlier in Fig. 77, pure copper was noticed outside the bright scale. This implies that pure copper and copper oxide were present in the surrounding region of the scale. Pure copper was present at the places where the metal was exposed, due to porosity of the oxide layer. The structure at the interface between the bright and dull regions is shown in Fig. 84. Some fibrous structure (visible at bottom right corner of Fig. 84), appeared to be incorporated into the peeled off layer. Higher magnification view of this fibrous structure (Fig. 85) revealed that these fibers form over the peeled off layer. This fibrous structure was copper oxide, confirmed by EDS analysis (Fig. 86).

There were locations where the copper oxide scale had peeled off (Fig. 87). There were also some locations where single crystals of copper oxide could be identified (Fig. 88). EDS analysis later confirmed it (Fig. 89).

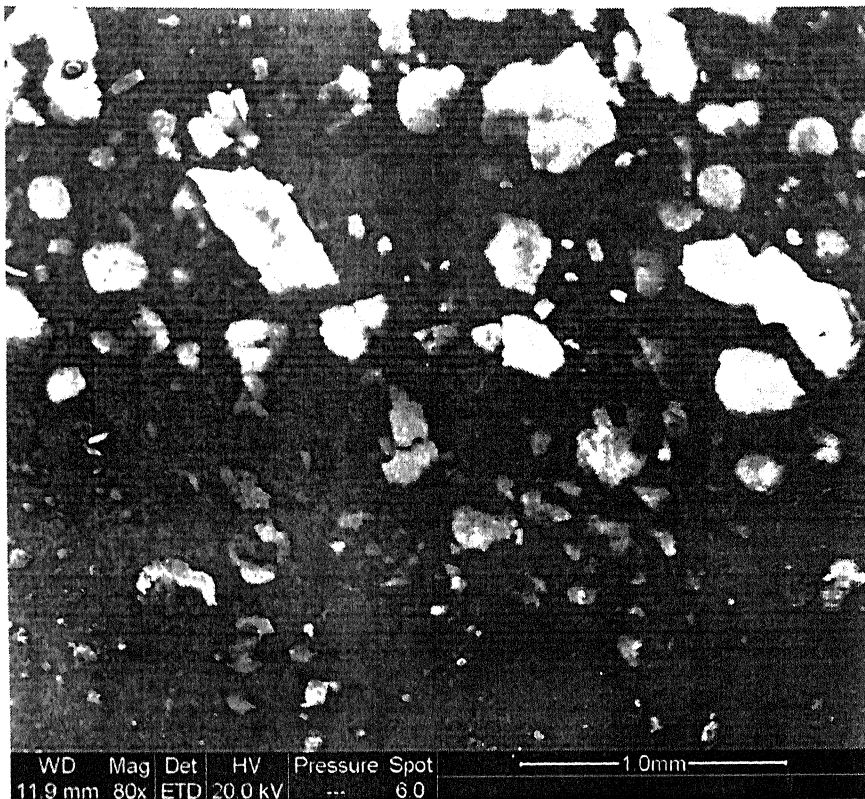


Fig. 76 A typical SEM micrograph of copper surface obtained after 432 hours of immersion in soil environment S10.

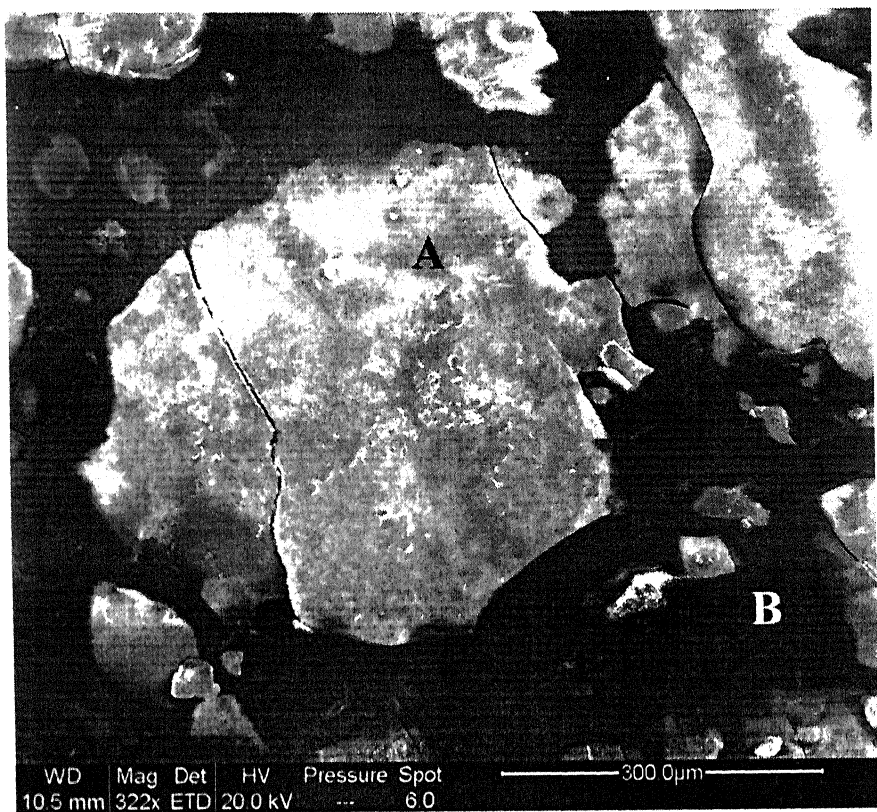


Fig. 77 SEM micrograph of copper surface obtained after 432 hours of immersion in soil environment S10. Bright Copper Oxide scales are peeling off from the surface.

of soil4\_1

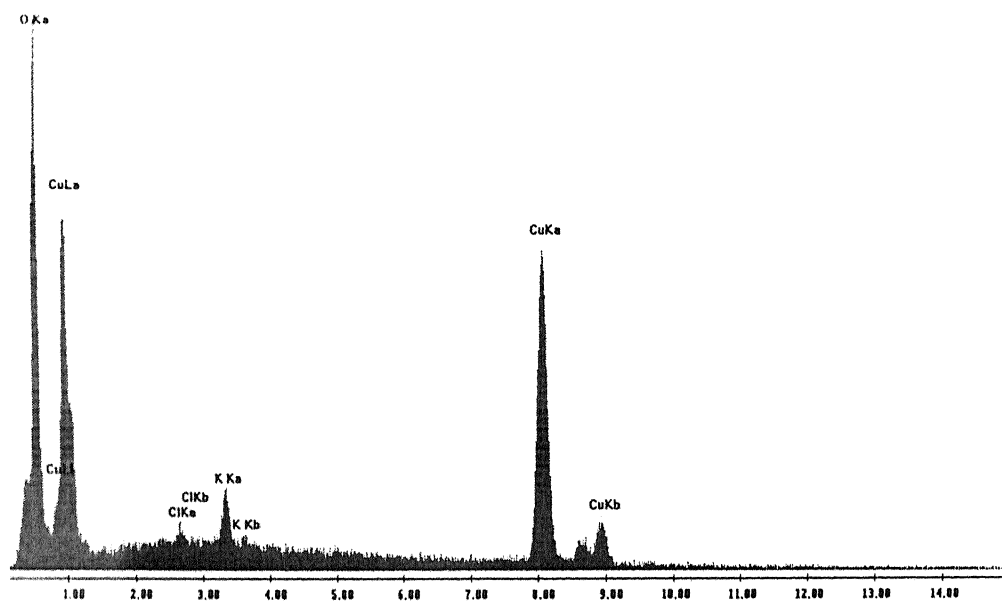
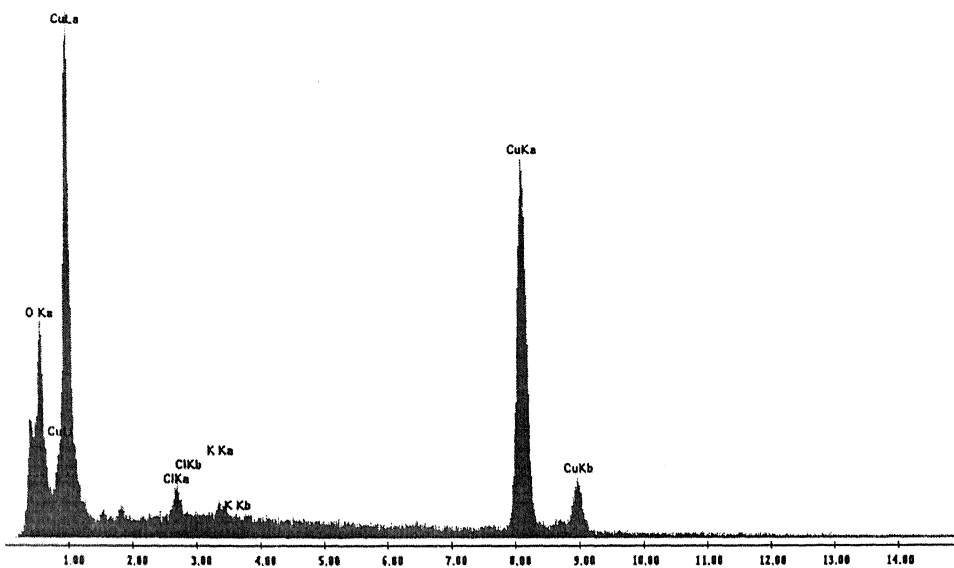


Fig. 78 EDS analysis done at point A in Figure 77, confirmed that point A was located on a Copper Oxide scale.



**Fig. 79** EDS analysis from the dark region of Fig. 77, showing copper with lower oxygen content.



Fig. 80 SEM micrograph of copper surface obtained after 432 hours of immersion in soil environment S10. Copper Oxide scale was peeling off and cracks were present on the scale.

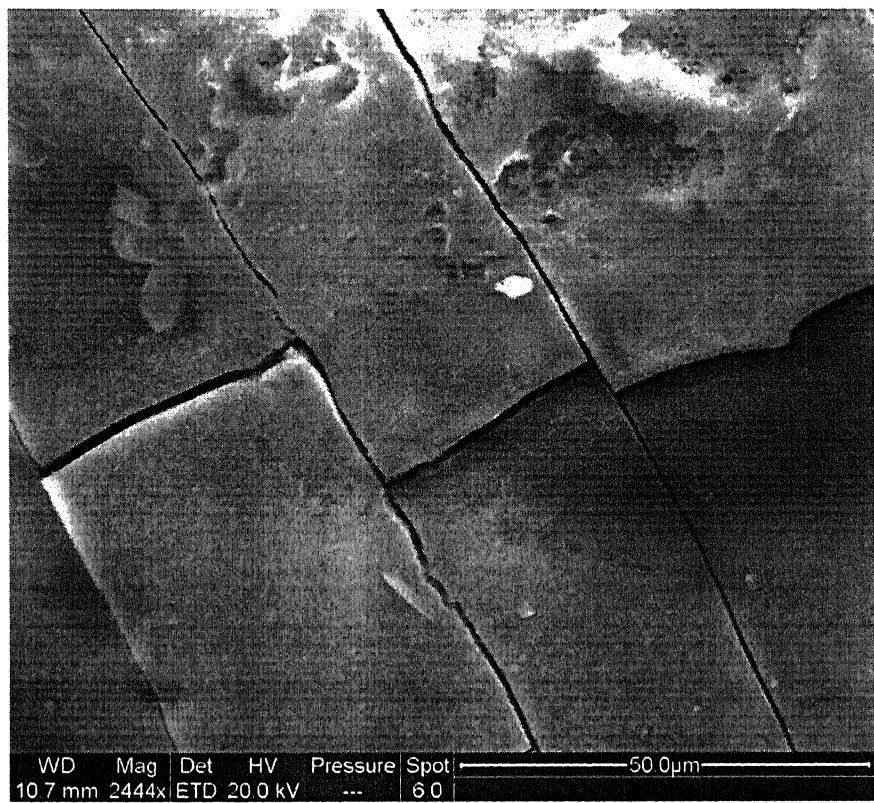


**Fig. 81** SEM micrograph of copper surface obtained after 432 hours of immersion in soil environment S10. A bright copper Oxide scale at higher magnifications is shown.



**Fig. 82** SEM micrograph of copper surface obtained after 432 hours of immersion in soil environment S10. A bright copper Oxide scale at higher magnifications is shown. The region surrounding the scale is composed of Copper Oxide.

Tablet A, soil4\_4

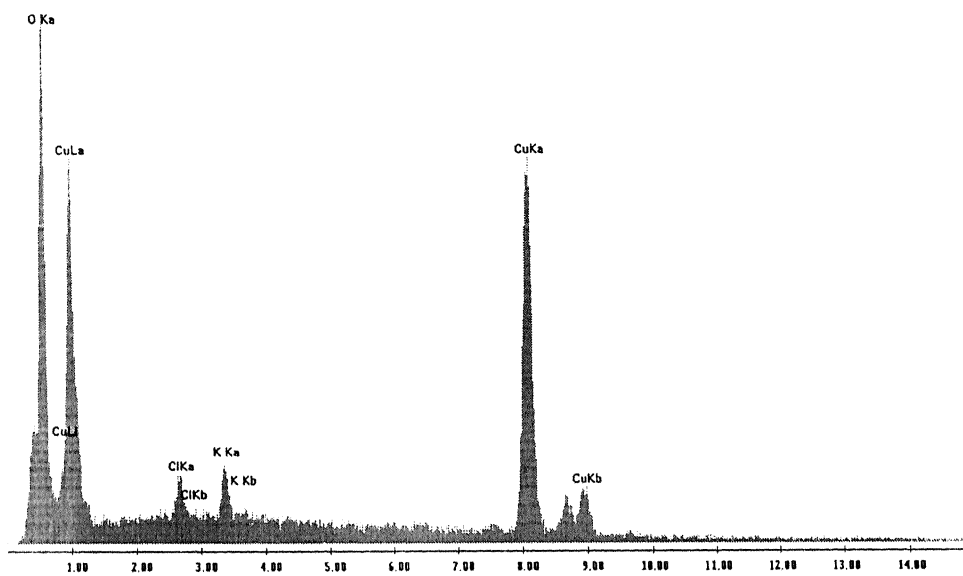
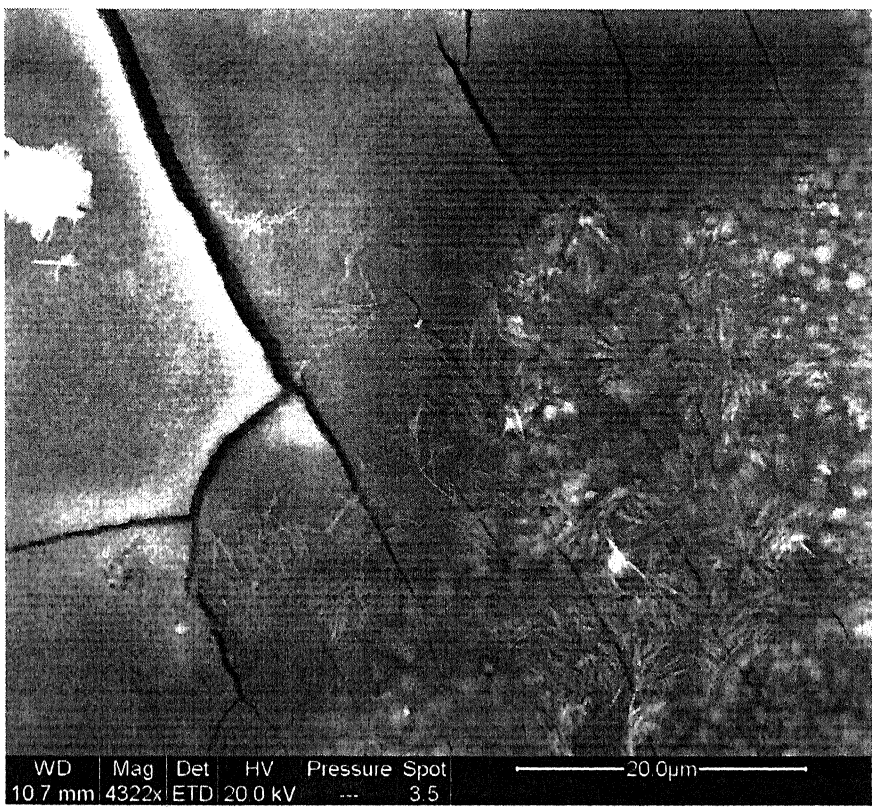


Fig. 83 EDS analysis done at point A in Fig. 82, showing that Copper Oxide is present around the bright scale



**Fig. 84** SEM micrograph of copper surface obtained after 432 hours of immersion in soil environment S10. Some fibrous structure was visible at bottom right corner which appeared to be incorporated into the peeled off layer.



**Fig. 85** SEM micrograph of copper surface obtained after 432 hours of immersion in soil environment S10, showing fibrous Copper Oxide.

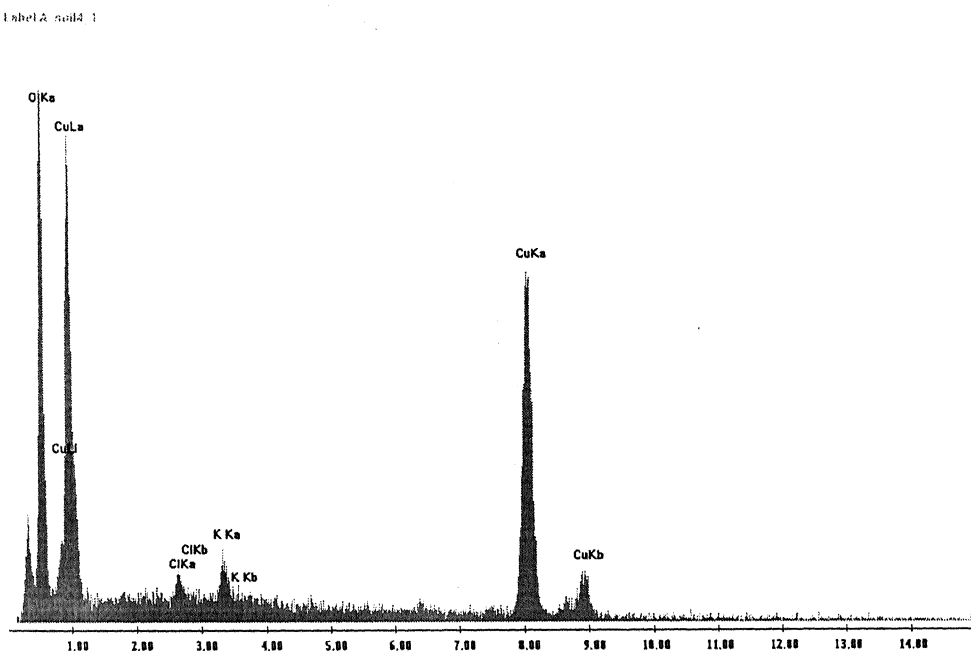
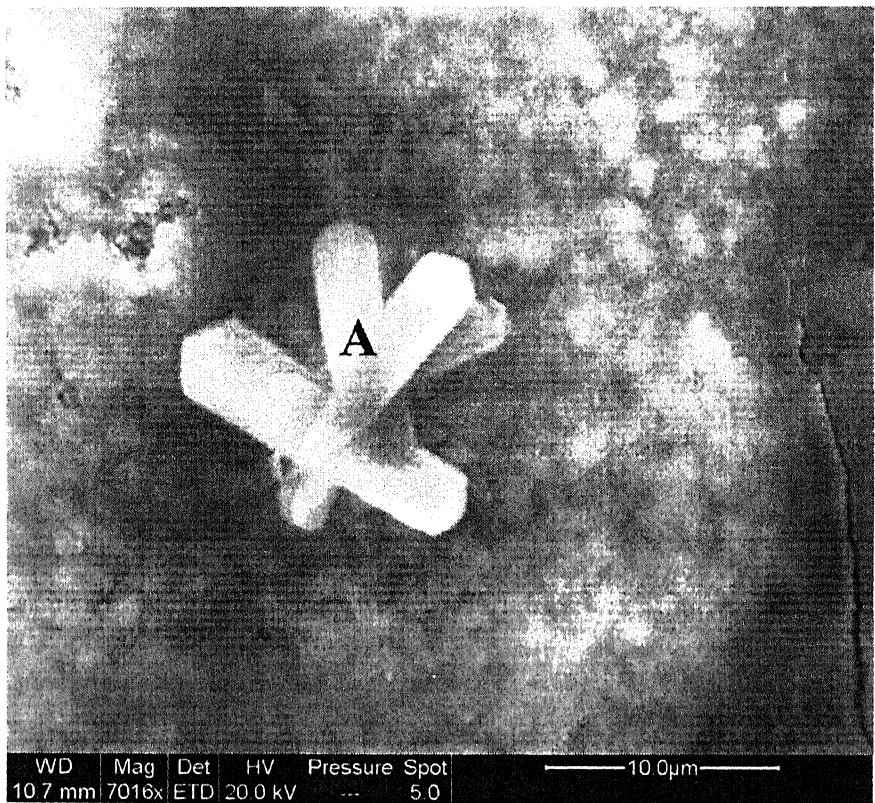


**Fig. 86** EDS analysis done at point 'A' in Fig. 85 showing that fibrous structure was essentially composed of Copper Oxide.



**Fig. 87** SEM micrograph of copper surface obtained after 432 hours of immersion in soil environment S10, showing exposed base metal.



WD	Mag	Det	HV	Pressure	Spot
10.7 mm	7016x	ETD	20.0 kV	...	5.0

— 10.0 μm —

**Fig. 88** SEM micrograph of copper surface obtained after 432 hours of immersion in soil environment S10, showing some Copper Oxide crystals..

Tablet A - point A

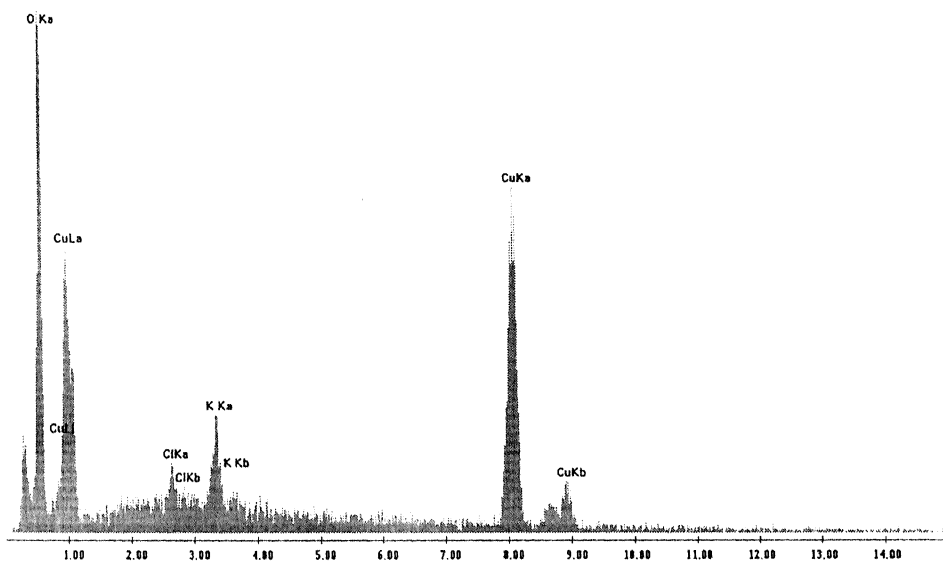


**Fig. 89** EDS analysis done at point A in Fig. 88, confirmed that point A was located on a Copper Oxide crystal.

#### **4.2.3 Comparison**

On comparing the surface films obtained in aqueous solutions, it was found that wherever chloride ion<sup>-</sup> was present in the aqueous environment (as in A1), it resulted in breakage of the surface layer (Fig. 29) after 432 hours of immersion. When there was no Cl<sup>-</sup> (as in A3) or when present in very low concentration (as in A4) the surface layer was thin and moreover not adherent to substrate in aqueous solutions (Fig. 40). Moreover the penetration during corrosive attack was not deep in absence of chloride in aqueous solutions.

The corrosive attack in the soil environments was not homogeneous as it was found in aqueous solutions. The damaging effect of chloride ions was more pronounced in case of aqueous solutions than soil environments. The surface obtained after 432 hours of immersion in solution A1 was more cracked and brittle as compared to surface obtained from soil S6 for the same time of immersion (Figs. 34 and 55).

On comparing microstructures of aqueous solution A1 and soil S6 it was found that morphology of film breakdown in aqueous solutions was different than soil (Figs. 28, 29 and 57). The needle type structure formed in the breakage of surface film obtained from solution A1 (Fig. 30) was not found in surface film obtained from soil environment S6. The nucleation-precipitation morphology of the oxide particles was different in soil than aqueous solutions (Figs. 23 and 54).

On comparing the surface films obtained from aqueous solution A3 and soil environment S8, it was found that in both cases the surface layer partly peeled off from the surface (Figs. 40 and 58). The microstructure presented in Fig. 59 shows that corrosive attack took place along some preferred orientations on the surface obtained from soil S8, whereas it was not noticed in case of solution A3.

The nature of the surface films obtained after immersion in aqueous solution A4 and soil S9 was almost similar and no specific difference could be noticed (Figs .42 and 74).

Figures 44 and 81 suggests that the surface films obtained after 18 days of immersion in solution A5 and corresponding soil S10 did not reveal similar morphology. The surface film formed in soil S10 appeared to peel off (Fig. 76) and was cracked along

some preferred directions (Figs 80 and 81). The surface film obtained from solution A5 (Fig. 51) appeared to be thick and more adherent than obtained from soil S10 (Fig. 77). The whole surface was relatively rough and the surface appeared to have been attacked severely by the corrosive solution in case of solution A5 (Fig. 45). The metal exposed regions were smoother in case of soil S10 (Fig. 87) than from aqueous solution A5 (Fig. 48). The surface obtained from aqueous solution A5 showed that oxide layer growth was by nucleation-precipitation mechanism in this solution (Fig. 51), whereas it grew by nucleation of fibers in soil environment S10 (Fig. 84).

## **4.3 Free corrosion potential**

The nature of stabilization of the free corrosion potential (FCP) provides information about the nature of the film that forms on the surface of materials under free corrosion conditions [74]. If the FCP moves from an active to noble potential during stabilization (i.e. in the positive direction), it suggests thickening of surface film under free corrosion conditions and equilibrium FCP is attained when the dissolution rate equals the growth rate of the film. In case the FCP moves from noble to active potential during stabilization (i.e. in the negative direction), it suggests thinning of surface film under free corrosion conditions and the equilibrium potential is attained when the growth rate equals the film dissolution rate. The film formed on the material when the FCP stabilizes at noble potential indicates that the film may be more protective. Further, in case the FCP stabilizes immediately upon immersion, it implies that the equilibrium conditions are attained relatively fast.

### **4.3.1 Aqueous Environment**

The stabilization of FCP of copper in aqueous solutions would be addressed below. In these discussions, the solutions would be designated as A1 through A5, as indicated in Table 2a.

Generally, the FCP moved towards the noble direction in most of the cases, indicating the formation of surface film on the surface (Fig. 90). This had earlier been confirmed in SEM studies. The FCP remained fairly constant after a few days of immersion in all the cases. The FCP in different solutions are also tabulated in Table 3.

Some features can be noted depending on the ions present in the aqueous solution. In the solutions that contained NaCl, (e.g. A1, A2 and A5) the FCP stabilized at more active potentials compared to the other solutions. It would indicate that the chloride ions from NaCl destabilizes the surface film and renders the surface more active. Among A1, A2 and A5, the FCP was constant throughout the immersion period for A5, whereas the FCP moved from active to noble direction during initial period of immersion in case of

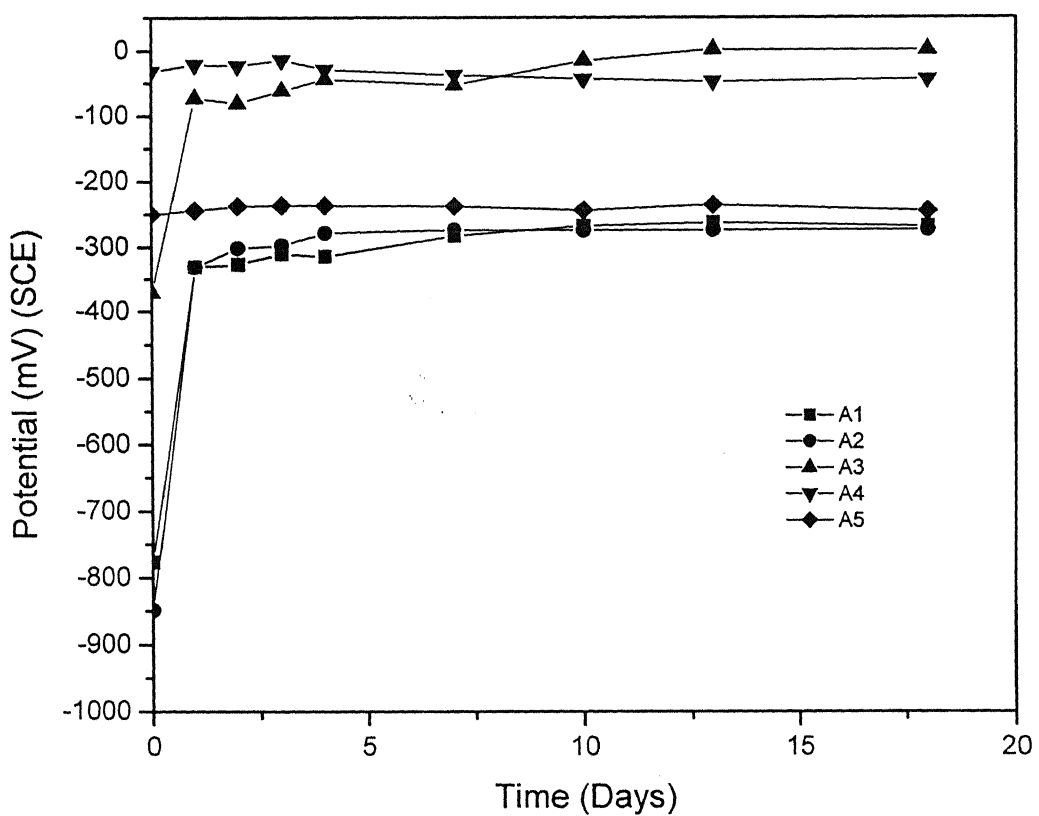


Fig. 90 Variation of free corrosion potential of copper as a function of time for immersion in aqueous solutions of different compositions.

**Table 3** Free corrosion potential (FCP) values in aqueous solutions obtained at different times. All values are reported in mV (SCE).

Time (days)	FCP (Solution A1)	FCP (Solution A2)	FCP (Solution A3)	FCP (Solution A4)	FCP (Solution A5)
0	-776	-849	-371	-32	-250
1	-331	-331	-72.3	-21	-244
2	-327	-301	-80	-23	-237
3	-310	-297	-61	-14	-236
4	-314	-278	-44	-29	-236
7	-282	-273	-52	-37	-237
10	-267	-274	-15	-43	-243
13	-262	-273	2	-47	-235
18	-267	-272	2	-43	-244

A1 and A2. In the case of solutions containing only Na<sub>2</sub>S and NH<sub>4</sub>Cl, the FCP stabilized at much nobler potentials compared to other solutions (Fig. 90). At the end of 432 hours of immersion, the FCP in the case of solution A3 was nobler indicating that sulfide ions were less damaging to the surface compared to chloride ions.

The damaging effect of chloride ions on copper has been extensively studied. Chloride ions stabilize dissolved copper as complex anions, such as CuCl<sub>2</sub><sup>-</sup> and CuCl<sub>3</sub><sup>-2</sup>. The presence of chloride ions therefore enhances copper oxidation [3]. Kruger [8] demonstrated that not only did the presence of water increase the oxidation rate of Cu (to Cu<sub>2</sub>O) but also that Cl<sup>-</sup> had an additional pronounced accelerating effect. The presence of chloride ions can also reduce the stability of the oxide layer (Cu<sub>2</sub>O and CuO) on the copper surface [9]. By incorporation of CuCl ‘islands’ in the surface Cu<sub>2</sub>O film, defects are created, which are believed to be initiation points for pitting. Substitution of monovalent Cl<sup>-</sup> ions for divalent O<sup>2-</sup> in the Cu<sub>2</sub>O lattice enhances the semi conducting properties of the surface film [3]. The Cu<sub>2</sub>O film formed in Cl<sup>-</sup> solutions may, therefore, support O<sub>2</sub> reduction and the anodic Cu dissolution and, therefore, be less protective than Cu<sub>2</sub>O films formed in the absence of Cl<sup>-</sup>.

### **4.3 2 Soil Environment**

The FCP of copper in soil environment would be discussed in this section. In these discussions, the experiments would be designated as S1 through S10 as indicated in Tables 2b and 2c. The first set of experiments was conducted to study the effect of moisture and sodium chloride addition on FCP of copper. The second set of experiments was conducted to understand the effect of pollutants such as sulfide and ammonium salts with and without presence of chloride. All the experiments could not run completely till the end of the decided time, due to loss of electrical contact (S1 and S2). The variation of FCP for these two sets of experiments is provided in Figs. 91 and 92 respectively.

The nature of FCP curves with time in soil environments were almost same with some minor changes depending on the compositions of the environments. The FCP moved towards the noble direction in most of the cases (Figs. 91 and 92), suggesting the

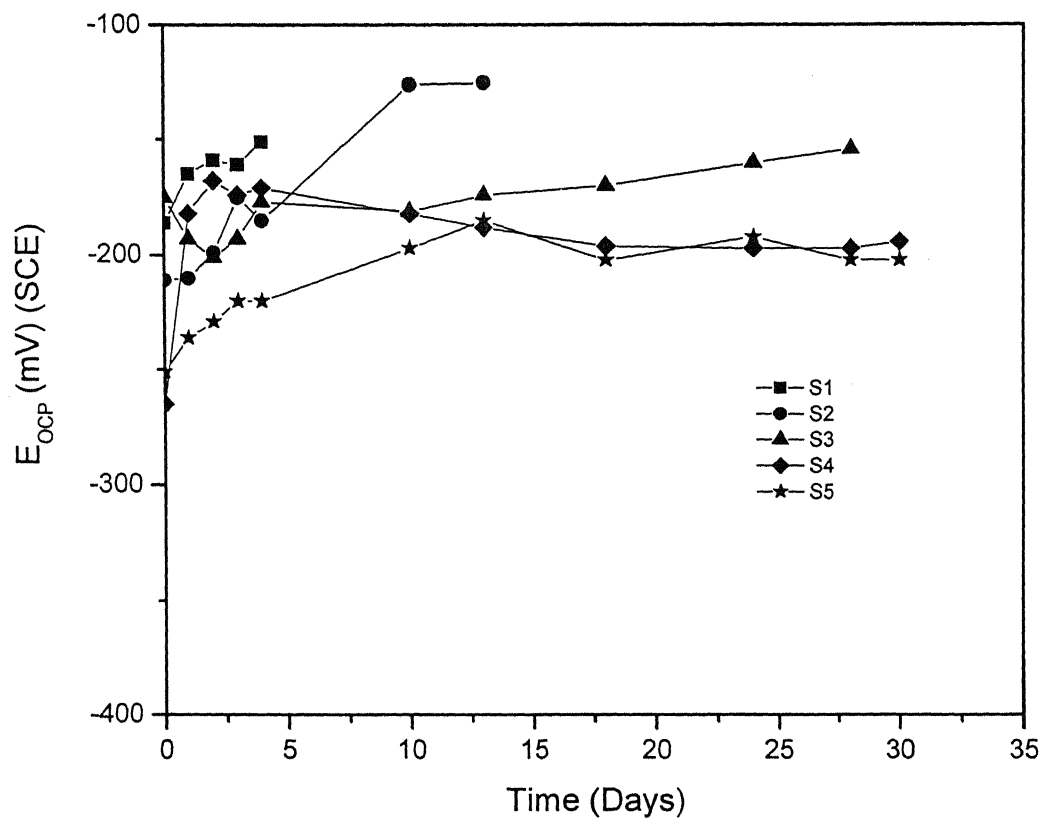


**Fig. 91** Variation of free corrosion potential of copper as a function of time for immersion in soil environment (Set 1).

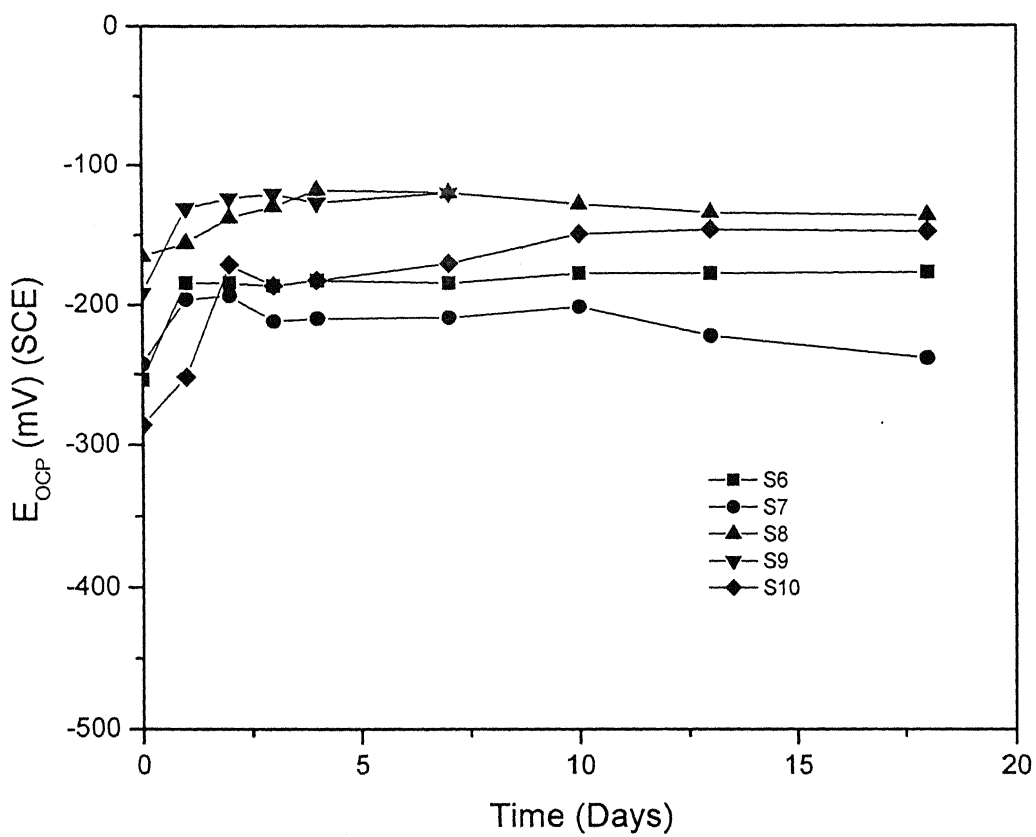


Fig. 92 Variation of free corrosion potential of copper as a function of time for immersion in soil environment (Set 2).

formation of surface film on copper surface. The FCP attained constant values after some days of immersion in soil environment.

In contrast, the FCP attained a steady value relatively faster in aqueous environments, which indicates that electrochemical reaction on the surface reach equilibrium faster in aqueous solutions. The values of FCP in different soil environments are tabulated in Table 4 for set 1 and Table 5 for set 2.

The soil containing low moisture content (S1 and S2) stabilized at relatively noble values compared to S3, which contained the highest moisture (i.e. 20 wt%). This suggested that increasing the moisture content in soil renders the system towards active potentials. However, with prolonged exposure, the situation may be different. The data for S3 indicates that the surface attained FCP almost similar to that for S1 and S2 after prolonged exposure. This would indicate that the formation of surface oxide is almost similar in all the exposure conditions, but the kinetics of film growth may be different.

Previous studies have shown that water accelerates the growth of cuprite film on copper and increases the rate of corrosion [12 & 42]. Figure 91 also suggests that copper in NaCl added soil environments showed more active stabilized potential as compared to other cases. This could be due to damaging effect of chloride ions as earlier mentioned in the previous section. Interestingly, the soil experiment, in which NaCl was added, could run for the full duration of experiment time. NaCl improved the conductivity of soil and hence rate of corrosion also increased in these environments.

The variation of FCP for the second set of experiments conducted in soil environments are presented in Fig. 92 and the data tabulated in Table 5. As noted earlier, the FCP take some time to attain stabilized potentials. The most active potential was attained for copper immersed in 5 wt% NaCl soil and therefore the damaging role of NaCl presence is brought out. In case of soils containing only Na<sub>2</sub>S and NH<sub>4</sub>Cl, the potentials were nobler, with NH<sub>4</sub>Cl addition leading to slightly more noble FCPs.

#### **4.3.3 Comparison**

FCP shifted to nobler directions in aqueous solutions (A3 and A4) in Fig. 90 and in soil (S8 and S9) in Fig. 92 if sodium sulfide or ammonium chloride was added in the

**Table 4** Free corrosion potential (FCP) values in soil environments (Set 1) obtained at different times. All values are reported in mV (SCE).

Time (days)	FCP (Solution S1)	FCP (Solution S2)	FCP (Solution S3)	FCP (Solution S4)	FCP (Solution S5)
0	-186	-211	-175	-265	-251
1	-165	-210	-193	-182	-236
2	-159	-199	-201	-168	-229
3	-161	-175	-193	-174	-220
4	-151	-185	-177	-171	-220
10		-126	-181	-182	-197
13		-125	-174	-188	-185
18			-170	-196	-202
24			-160	-197	-192
28			-154	-197	-202
30				-194	-202

**Table 5** Free corrosion potential (FCP) values in soil environments (Set 2) obtained at different times. All values are reported in mV (SCE).

Time (days)	FCP (Solution S6)	FCP (Solution S7)	FCP (Solution S8)	FCP (Solution S9)	FCP (Solution S10)
0	-254	-243	-165	-191	-286
1	-184	-196	-156	-131	-252
2	-184	-193	-138	-124	-171
3	-186	-212	-130	-121	-186
4	-182	-210	-118	-127	-182
7	-184	-209	-120	-120	-170
10	-177	-201	-128		-149
13	-177	-222	-134		-146
18	-176	-238	-136		-147

respective environments. The stabilized FCP was higher in case of aqueous solutions. It suggested that protective nature of the film was more in aqueous solutions than in soil environments in presence of sulfide or ammonium ions. In aqueous solutions (A3 and A4) the surface films formed were more protective than in soil (S8 and S9).

The damaging effect of NaCl was predominant in aqueous solutions than soil environments. In the environments in which NaCl was added, FCP stabilized at more noble potentials in soil than aqueous solution of same composition. The damaging effect of chloride was more in aqueous solutions than soil due to high conductivity and mobility of chloride ions in aqueous solutions than soil. Similarly the less protective nature of surface films in presence of  $S^{2-}$  and  $NH_4^+$  ions in soil environment could be explained due to low conductivity of soil.

## **4.4 Linear Polarization**

The linear polarization plots obtained after 2 hours and 432 hours of immersion in aqueous and soil environments are presented in Figs. 93 through 96. The polarization resistance  $R_p$  was estimated from these curves and these are tabulated in Tables 6 and 7.

### **4.4.1 Aqueous Solution**

Immersion in solutions A1, A2 and A5 resulted in a decrease, whereas immersion in A3 and A4 resulted in increase in polarization resistance ( $R_p$ ) after 432 hours of immersion in the solutions (Table 6). After 2 hours of immersion in solution, it was found that sample immersed in solution A3 possessed the highest polarization resistance, while that in solution A5 the lowest (Table 6). A higher  $R_p$  value indicates lower corrosion rate. After 2 hours of immersion, the solution containing only  $\text{Na}_2\text{S}$  was beneficial whereas the presence of chloride ions generally lowered the corrosion resistance. With increasing amount of chloride ions (comparing data for A1 and A2), the corrosion resistance decreased. For almost same level of addition of  $\text{Na}_2\text{S}$  and  $\text{NH}_4\text{Cl}$  (comparing data for A1 and A5), the addition of  $\text{Na}_2\text{S}$  was more beneficial. Moreover, taken separately  $\text{Na}_2\text{S}$  appears to increase corrosion resistance compared to  $\text{NH}_4\text{Cl}$  (comparing data for A3 and A4).

After long time immersion, the order of corrosion resistance obtained in different solutions did not change. The drastic increase in corrosion resistance after immersion in  $\text{Na}_2\text{S}$  containing solution (i.e. A3) should be noted. The above results bring out the damaging role of chloride ions while the relatively less severe effect of sulfide ions can also be noted (Table 6). The relative order of polarization resistance after 432 hours was as follows: A3 > A4 > A1 > A2 > A5 (Fig. 94).

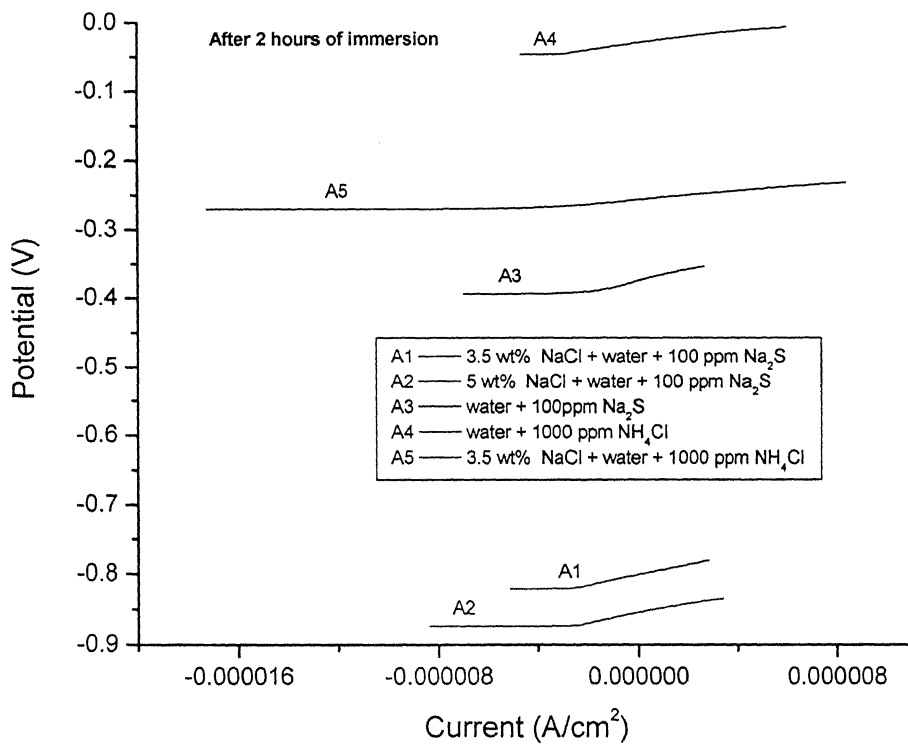


**Fig. 93** Comparison of linear polarization curves obtained in aqueous solutions after 2 hours of immersion.

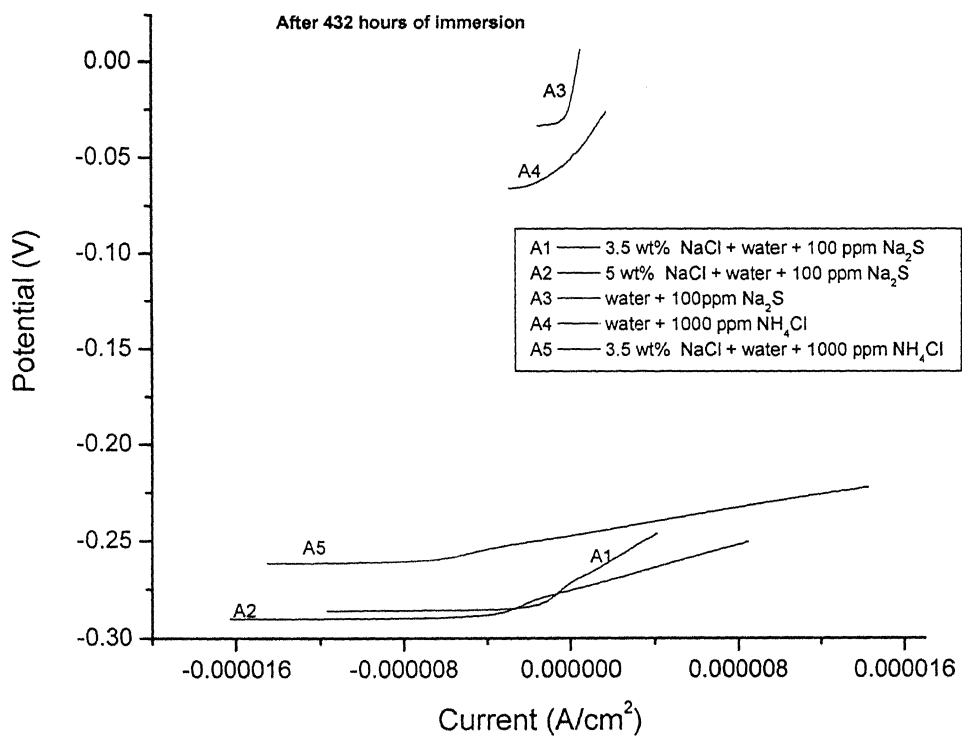


**Fig. 94** Comparison of linear polarization curves obtained in aqueous solutions after 432 hours of immersion.

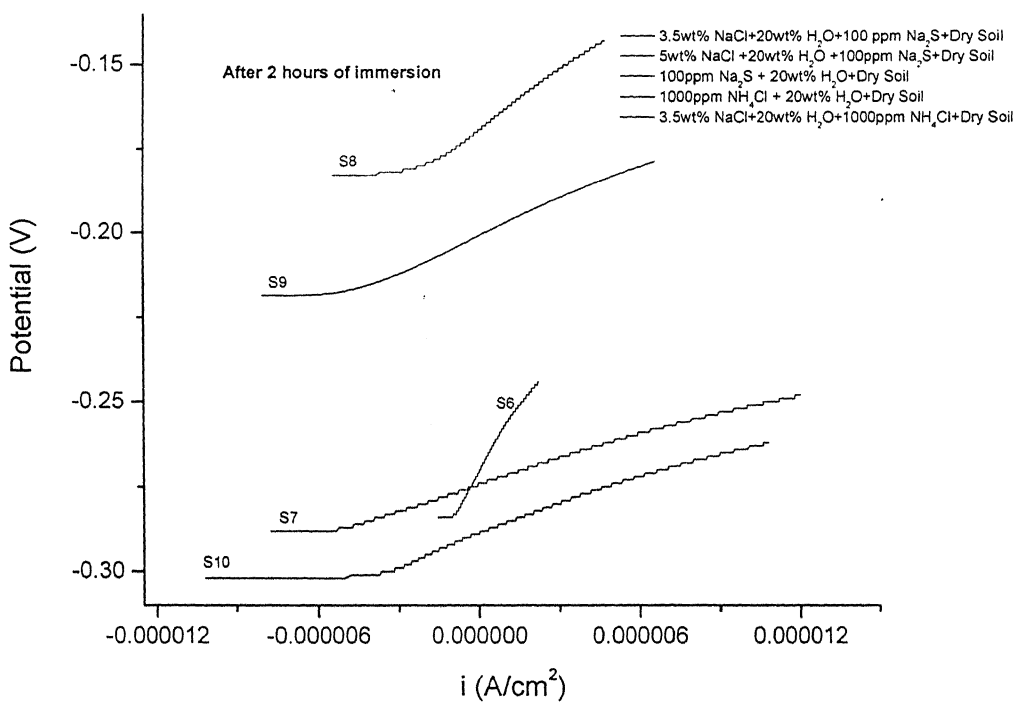


**Fig. 95** Comparison of linear polarization curves obtained in soil environments (Set 2) after 2 hours of immersion.

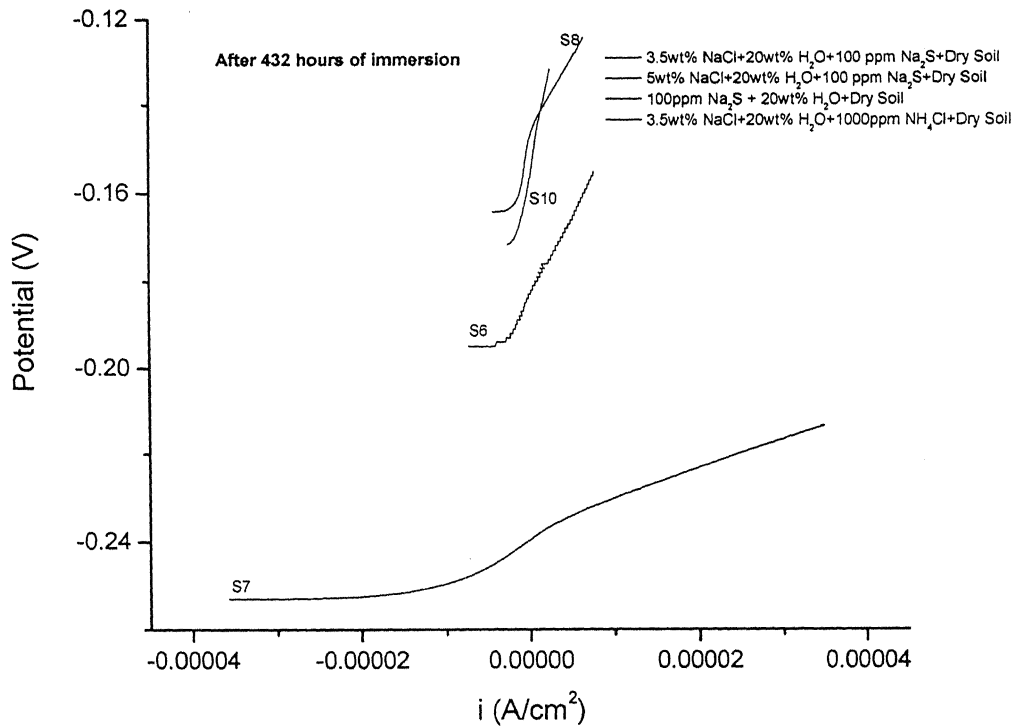


**Fig. 96** Comparison of linear polarization curves obtained in soil environments (Set 2) after 432 hours of immersion.

**Table 6** Polarization resistances ( $R_p$ ) calculated from the linear polarization curves obtained after 2 hours and 432 hours of immersion in the aqueous solutions

Solution Composition	$R_p$ (ohm-cm <sup>2</sup> ) After 2 hours	$R_p$ (ohm-cm <sup>2</sup> ) After 432 hours
3.5 wt% NaCl + 100 ppm Na <sub>2</sub> S + water (A1)	7056	6220
5 wt% NaCl + 100 ppm Na <sub>2</sub> S + water (A2)	6417	2416
100 ppm Na <sub>2</sub> S + water (A3)	10834	56794
1000 ppm NH <sub>4</sub> Cl + water (A4)	4903	16656
3.5 wt% NaCl + 1000 ppm NH <sub>4</sub> Cl + water (A5)	2892	1749

**Table 7** Polarization resistances ( $R_p$ ) calculated from the linear polarization curves obtained after 2 hours and 432 hours of immersion in the soil environments (Set 2)

Solution Composition	$R_p$ (ohm-cm <sup>2</sup> ) After 2 hours	$R_p$ (ohm-cm <sup>2</sup> ) After 432 hours
3.5 wt% NaCl + 100 ppm Na <sub>2</sub> S + water (S6)	13680	3524
5 wt% NaCl + 100 ppm Na <sub>2</sub> S + water (S7)	2505	1430
100 ppm Na <sub>2</sub> S + water (S8)	5467	7069
1000 ppm NH <sub>4</sub> Cl + water (S9)	5588	-
3.5 wt% NaCl + 1000 ppm NH <sub>4</sub> Cl + water (S10)	2910	10869

#### **4.4.2 Soil Environment**

Immersion in soil environment S6 and S7 indicated a decrease whereas immersion in S8 and S10 revealed an increase in polarization resistance ( $R_p$ ) after 432 hours (Table 7). After 2 hours of immersion in soil environments it was found that sample immersed in soil S8 and S9 possessed almost same  $R_p$  value while immersion in S7 possessed the lowest polarization resistance. Presence of chloride ions in soil experiments S6 and S7 lowered the corrosion resistance. Experiment S9 could not run for 18 days as it lost contact after 7<sup>th</sup> day of immersion, therefore linear polarization data for S9 after 18 days of immersion could not be presented in this discussion. With increasing amount of chloride in soil (comparing data for S6 and S7) the polarization resistance decreased as it was also stated while discussing linear polarization data for aqueous solutions. Also  $\text{Na}_2\text{S}$  appeared to increase corrosion resistance after 432 hours of immersion in absence of chloride. The linear polarization data also presented the beneficial effect of sulfide as compared to chloride ions after 432 hours of immersion in the respective soil environments.

#### **4.3.3 Comparison**

The damaging role of chloride ions has already been stated while discussing free corrosion potential [3, 8 & 9]. From the analysis of FCP data and the microstructural characterization it was found that chloride ions appear to damage the surface more severely in case of aqueous solutions. Similar trend has also been revealed in the polarization resistance data.

After 2 hours of immersion, it was found that the sample immersed in aqueous solution A1 revealed lower polarization resistance than sample immersed in soil environment S6. The  $R_p$  values obtained from solution A4 and soil S9 were nearly same after 2 hours of immersion (Tables 6 and 7). Almost similar polarization resistance was obtained from aqueous solution A5 and soil S10 after 2 hours of immersion in the respective solutions. Comparison of linear polarization data for aqueous solution A3 and soil environment S8 indicated beneficial role of sulfide ions in the aqueous solutions,

when chloride was not present. Moreover, protective nature of the surface film was higher in case of aqueous solution A3. The  $R_p$  value was higher in A3 than S8. The unexpected low value of  $R_p$  in soil environment S8 among all other soil environments obtained after 2 hours of immersion could be attributed due to contamination of chloride (KCl) ions from the luggin capillary tube. In aqueous solution A3, the  $R_p$  value was highest after 432 hours and 2 hours of immersion. In the soil environments the contaminations prevailed more or less near the metal surface due to low mobility of ions in soil.

## **4.5 Electrochemical Impedance Spectroscopy**

Electrochemical impedance spectroscopy (EIS) measurements are particularly useful in understanding the nature of surface films. They can also be conducted as a function of immersion time because they do not perturb the system dramatically. It is possible to follow the evolution of the nature of surface film over time. EIS measurements were performed in different aqueous and soil environments. Corrosion processes often involve a slow aqueous diffusion process, which generally have relatively large time constants (on the order of 0.1 to 10 s). Therefore, most impedance studies of corroding systems use frequencies of between a few mHz and 100 kHz [52]. All the EIS experiments were performed in the frequency range of 100 kHz to 10 mHz.

### **4.5.1 Aqueous Solution**

Properties of surface films grown on copper in different aqueous solutions were investigated as a function of immersion time by means of electrochemical impedance spectroscopy. All the impedance experiments were performed after stabilization of free corrosion potential.

The EIS data (Nyquist plots, Bode Magnitude and Bode Phase plots) for pure copper in different aqueous solutions, obtained at open circuit potential (after 2 hours and 432 hours of immersion), are presented in Figs 97 through 102. The EIS data obtained at other times of immersion have all been collected in Appendix A.

The nature of the Nyquist plots (imaginary part of impedance vs. real part of impedance at different frequencies) was not similar for all the solutions. Nyquist plots obtained in all the solutions (Figs 97 and 100) consisted of an arc that would be extrapolated to a semicircle, except in solutions A3, A4 and A5, after 432 hours of immersion, where two arcs could be distinguished. The diameter of the semicircle indirectly indicates the polarization resistance ( $R_p$ ). It could be observed from the Figs. 97 and 100 that after 432 hours of immersion, the diameter of the semicircle decreased for solution A2.

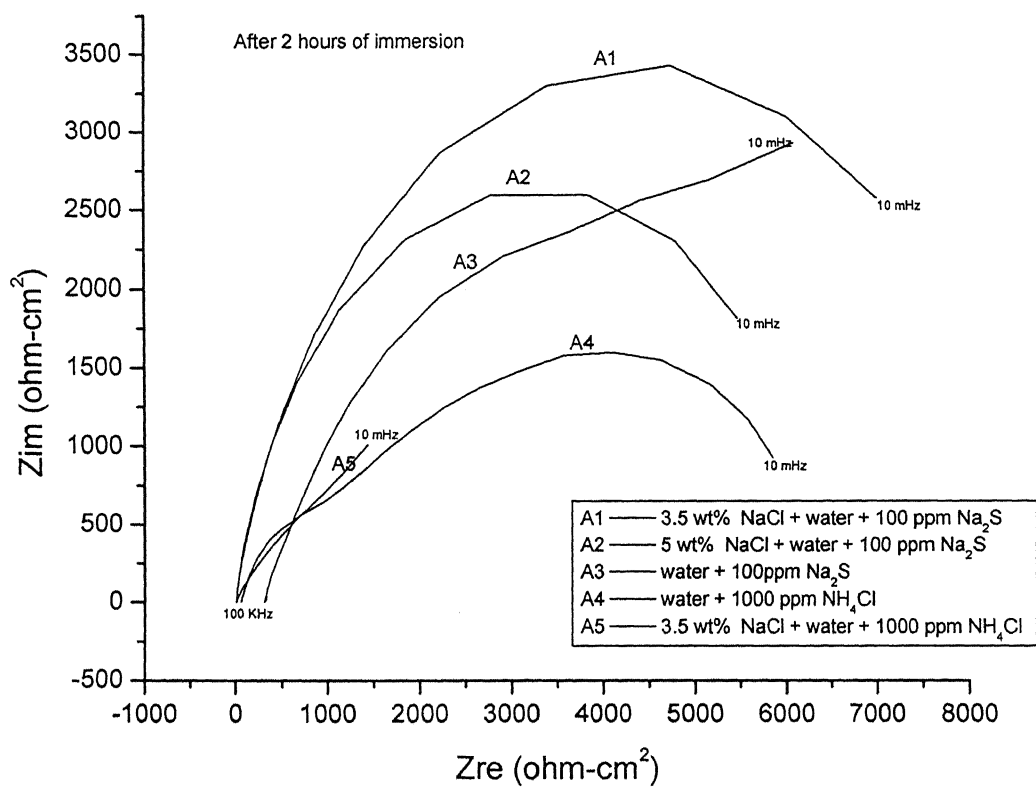


**Fig. 97** Nyquist plots obtained in aqueous solutions after 2 hours of immersion.

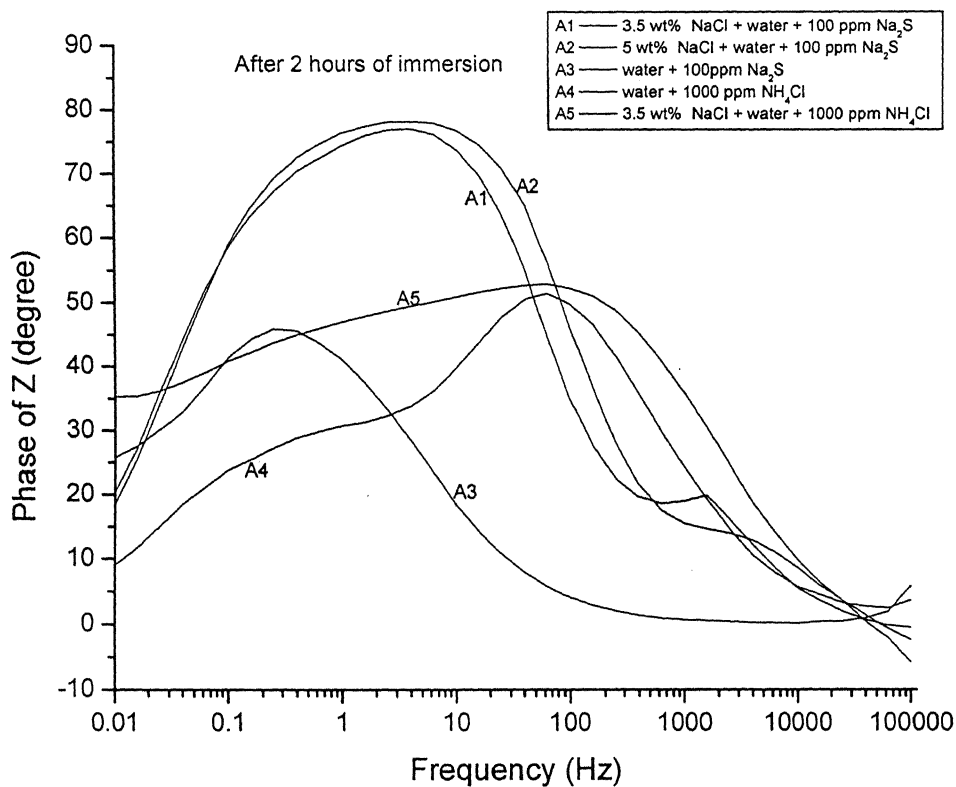


**Fig. 98** Bode phase plots obtained in aqueous solutions after 2 hours of immersion.

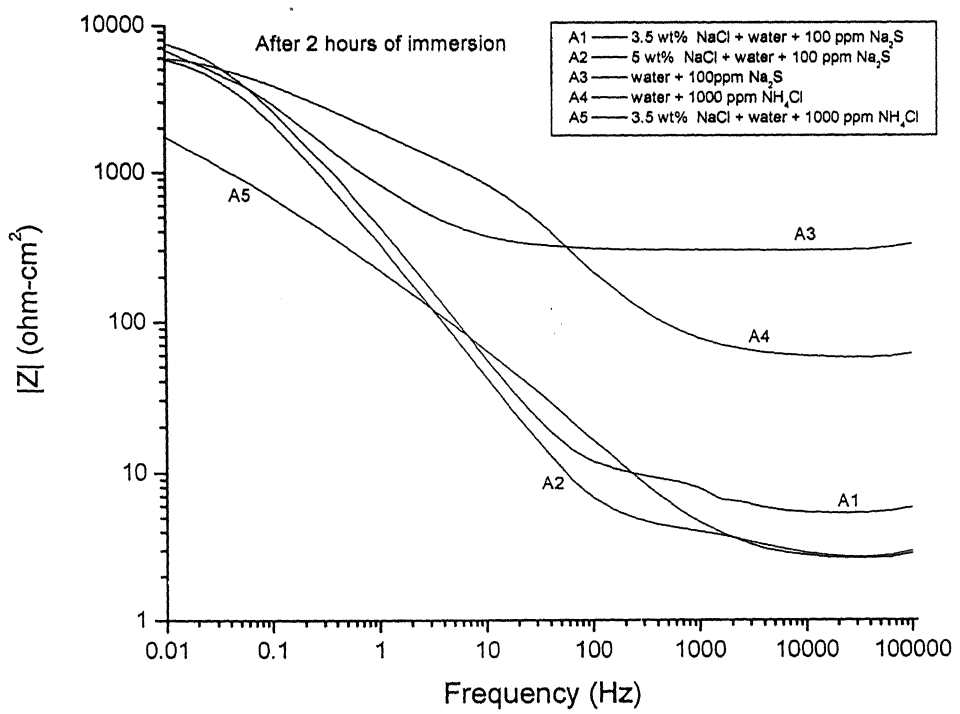


**Fig. 99** Bode magnitude plots obtained in aqueous solutions after 2 hours of immersion.

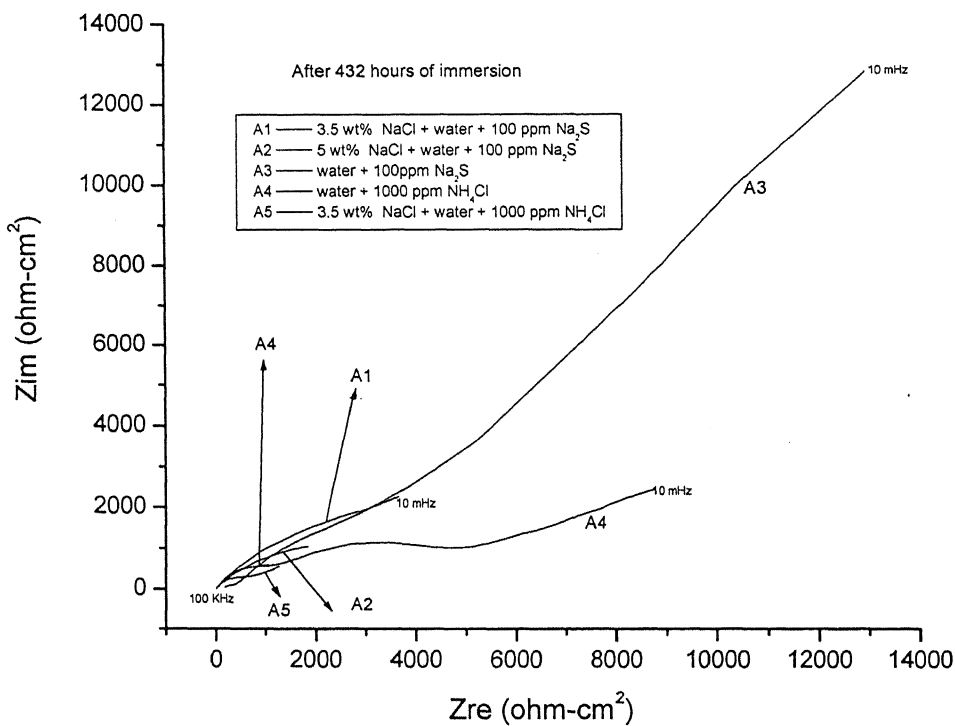


**Fig. 100** Nyquist plots obtained in aqueous solutions after 432 hours of immersion.

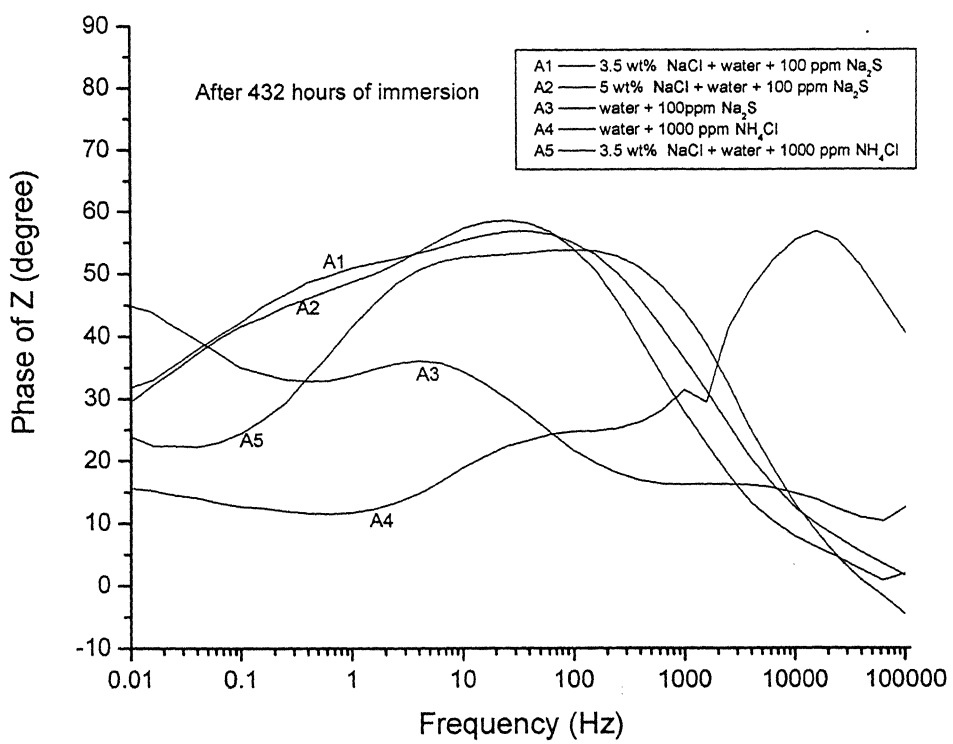
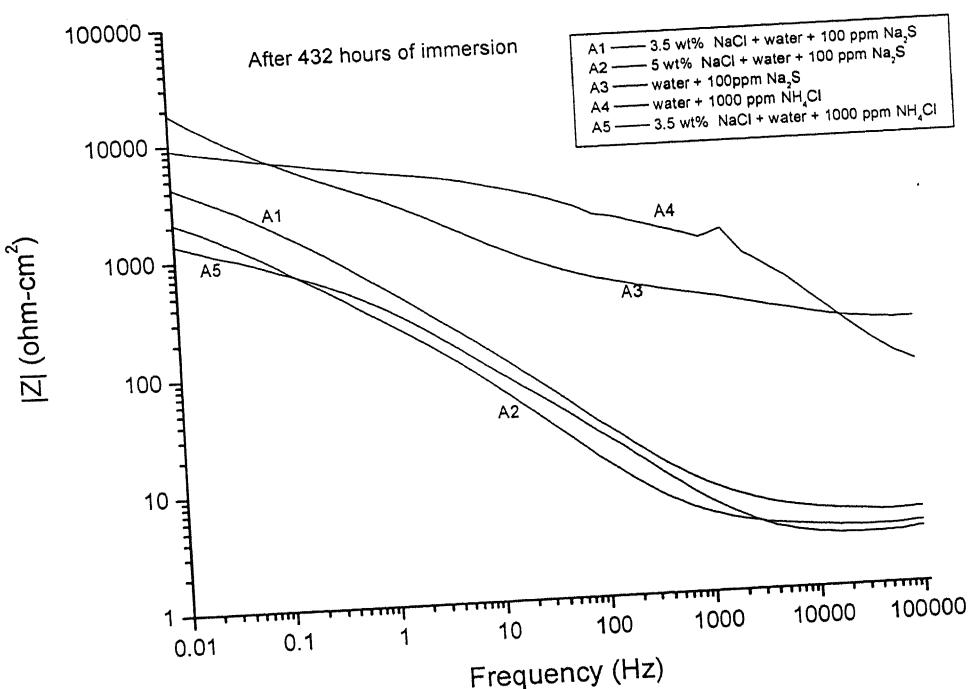


Fig.101 Bode phase plots obtained in aqueous solutions after 432 hours of immersion.



**Fig. 102** Bode magnitude plots obtained in aqueous solutions after 432 hours of immersion.

The decrease in diameter indicates a decrease in corrosion resistance, which is attributed to the damaging effect of chloride. Solution A2 contained highest percentage of chloride. In the case of solution A3, at low frequencies a line making  $45^0$  angle to the X-axis can be noted in the Nyquist plot after 432 hours of immersion. It is a characteristic of Warburg impedance that evolves at lower frequencies indicating that diffusion through the corrosion product layer has become a predominant factor after immersion for 432 hours. The Nyquist plots (Figs. 97 and 100) obtained in solution A4 after 2 hours and 432 hours of immersion showed two arcs joined together. The arc obtained in solution A4 after 432 hours of immersion at low frequencies when extrapolated to a semicircle formed a larger diameter loop than the arc obtained after 2 hours of immersion. This indicates that the corrosion resistance of copper samples put in solution A4 improved after eighteen days of immersion, whereas in solution A2 the corrosion resistance significantly decreased. After 432 hours of immersion in solution A5 the diameter of the semicircular arc at low frequencies decreased, indicating a decrease of corrosion resistance.

The Nyquist plots obtained in all the solutions after 2 hours and 432 hours of immersion compared in Fig 97 and 100, respectively. It indicates that after 2 hours of immersion the surface immersed in solution A3 possessed the lowest corrosion rate while that in solution A5, highest corrosion rate. After 432 hours of immersion the surface immersed in solutions A3 presented lower corrosion rates as compared to solutions containing chloride (A1, A2 and A5).

Comparison of Nyquist plots indicates that the solution containing sulfide ions (A3) was relatively less corrosive compared to the cases where chloride ions were present.

The phase angle,  $\Theta$ , is a sensitive parameter used to indicate the presence of additional time constants in the impedance spectra at the highest and the lowest frequencies. Absolute values of the phase angles with frequency are plotted in the Bode phase angle plots (Figs. 98 and 101). From these Bode phase plots, it can be noted that in most of the cases the phase angle drops towards zero degree at very high frequencies, indicating that the impedance is dominated by solution resistance in this frequency range

(no phase shift between current and potential results due to presence of a resistor in AC circuit).

Capacitive behavior of the surface film for solutions A1 and A2 decreased by a small amount as the phase angle in the middle frequency range drops from nearly  $70^{\circ}$  to  $50^{\circ}$  after 432 hours of immersion (Fig. 101). No large negative phase shift in the low frequency region could be noticed for any of the surfaces immersed in aqueous solutions. Large negative phase shift in the low frequency region after long time immersion is responsible for better capacitive behavior (compact and protective) of the surface film. The overall behavior of all the surface films in this study is assumed to be porous, and the SEM results analyzed in the previous section also confirmed this. The nature of Bode phase plots (Figs. 98 and 101) indicates the porous nature of the film, which is characterized by large phase shift towards zero degrees and very narrow medium frequency capacitive region [56].

At high frequencies, the Warburg impedance is small since diffusing reactants do not have to move very far. At low frequencies the reactants have to diffuse farther, thereby increasing the Warburg impedance. Warburg Impedance ( $Z_w$ ) is given by the following equation

$$Z_w = \sigma\omega^{-1/2}(1-j) \quad (52)$$

where  $\sigma$  ( $\text{ohm s}^{1/2}$ ) is the Warburg impedance coefficient. Diffusion time constants are typically observed at lower frequencies [2]. The Warburg impedance depends on the frequency of the potential perturbation. At high frequencies, the Warburg impedance is small since diffusing reactants do not have to move very far. At low frequencies, the reactants have to diffuse farther, thereby increasing the Warburg impedance. When diffusion is the dominant (rate controlling) process, the  $\log |Z|$  vs.  $\log f$  (frequency) plot will approach a slope of -0.5 and a phase angle ( $\theta$ ) of -45 degrees as  $\omega \rightarrow 0$ . Inevitably, diffusion is not totally dominant, and control of the corrosion process at the base of the pore will be partially controlled by interfacial kinetics. For this situation, the slope of  $\log |Z|$  against  $\log f$  will change with frequency in the range 0 to -0.5, and  $\theta$  will change with frequency over the range 0 to -45 degrees [56]. The Bode phase plot for solution A3 after 432 hours of immersion indicated another time constant emerging in the low frequency range, which approaches towards  $45^{\circ}$  with decreasing frequency (Fig. 101). This feature

indicative of Warburg impedance. A drop of phase angle in the medium frequency range was noticed after 432 hours of immersion in solution A3 suggesting decrease in capacitance of the surface film.

Bode phase plots obtained in all solutions, after 2 hours of immersion (Fig. 98), suggested that solutions A1 and A2 revealed highest negative phase shift in the middle frequency range, indicating that surface layers obtained in these solutions possess higher capacitive behavior after 2 hours of immersion. The aqueous solutions A1 and A2 possessed high chloride content. Chloride accelerates the growth rate of film formation on copper surface, as copper is exposed to chloride containing environment [8]. In solutions A1 and A2, film formation occurs readily after immersion as compared to other solutions, but long term exposure to chloride environment can be deleterious for copper. The damaging effect of chloride ions has been extensively reported in literature. It is believed that chloride ions would affect the properties and stability of the surface films, when exposed to longer times [9]. The presence of chloride ions rapidly can reduce the stability of the oxide layer ( $Cu_2O$  and  $CuO$ ) on the copper surface [9]. By incorporation of  $CuCl$  ‘islands’ in the surface  $Cu_2O$  film, defects are created, which are believed to initiation points for pitting. Substitution of monovalent  $Cl^-$  ions for divalent  $O^{2-}$  in the  $Cu_2O$  lattice enhances the semi conducting properties of the surface film [3]. After 432 hours of immersion, the capacitance of surface films formed in solutions A1 and A2 decreased.

Bode magnitude plots (logarithm of impedance vs. logarithm of frequency) presented in Figs. 99 and 102 shows that the slope of  $\text{Log } |Z|$  vs.  $\text{Log } f$  is close to zero in the very high frequency region indicating that the dominance of solution resistance in this region for most of the cases. In solutions A3 and A4 (after 432 hours of immersion) Bode magnitude plot was not flat in high frequency region, suggesting that this region was not purely resistive for these two solutions. The flat portion of the curve (slope~0), present in high frequency region, marginally shifted its position with immersion. (The solution resistance could also be found from modeling of EIS data with appropriate equivalent circuit). This was due to minor changes in solution resistance ( $R_s$ ) with immersion time in aqueous solutions. For solutions A1, A2 and A5 the solution resistance was less than 5 ohm-cm<sup>2</sup> which was quite low and also did not change drastically with immersion time.

However for solutions A3 and A4, the solution resistance was very high ( $\sim 300$  ohm-cm $^2$  for A3 and  $\sim 50$  ohm-cm $^2$  for A4). These two solutions did not contain NaCl, whereas solution A1, A2 and A5 did. As NaCl is highly conducting salt, this has increased the conductivity of the solutions.

The nature of the Bode magnitude plots was similar after 432 hours of immersion for solutions A1, A2 and A5. The impedance at lowest frequency decreased after 432 hours of immersion for all these three cases. The decrease in impedance at lowest frequency after 432 hours of immersion, for solution A2 was highest ( $\approx 4000$  ohm-cm $^2$ ), as compared to solution A1, (decrease  $\approx 2000$  ohm-cm $^2$ ) and A5 (decrease  $\approx 500$  ohm-cm $^2$ ). It implied that corrosion resistance in solution A2 decreased significantly. This is reasonable because solution A2 contained the highest concentration of NaCl (5 wt%) among all cases. Impedance at lowest frequency after 432 hours of immersion was enhanced for solutions A3 and A4 (increase for A3 was  $\sim 13000$  ohm-cm $^2$  and for A4 it was  $\sim 4000$  ohm-cm $^2$ ). The relative order of total impedance at lowest frequency after 432 hours of immersion was as follows: A3 > A4 > A1 > A2 > A5 (Fig. 102). The total impedance at lowest frequency was highest for A3. In this case (A3), corrosion current (rate) is controlled by mixed (kinetic and diffusion) process.

The equivalent circuit shown in Figs. 103 and 104 was used to fit the above experimental data. In these equivalent circuits,  $R_s$  is solution resistance,  $R_{ct}$  is charge transfer resistance (or polarization resistance),  $Q_f$  is constant phase element (CPE) for film and  $Q_{EDL}$  is constant phase element (CPE) for electrical double layer. Figure 104 shows another circuit element 'W' that corresponds to Warburg Impedance [2]. The CPE considers the fact that experimentally; the barrier film never exhibits the theoretically expected phase shift of  $-90^\circ$  and a slope of -1 for an ideal dielectric. The fitting procedure revealed that better agreement between theoretical and experimental data was obtained if a frequency dependent constant-phase element (CPE) was used instead of pure capacitance. The impedance of a constant phase element is defined in as [52, 55]:

$$Z_{CPE} = [Q(j\omega)^n]^{-1} \quad (53)$$

where Q and n are frequency independent parameters, which usually depend on temperature and  $-1 \leq n \leq 1$  [52].

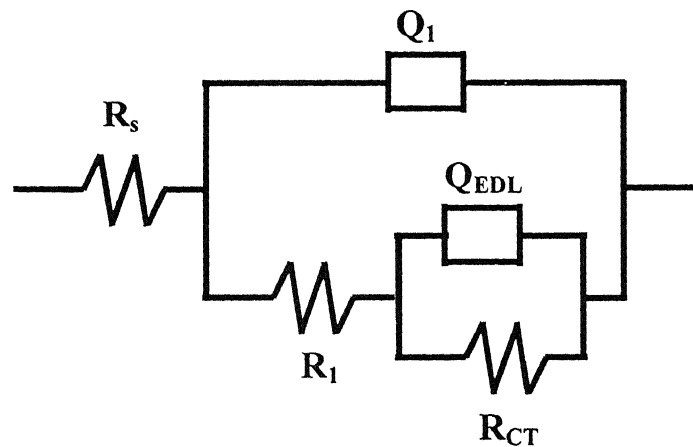


**Fig. 103** Equivalent circuit used for fitting experimental EIS data obtained in aqueous solutions.

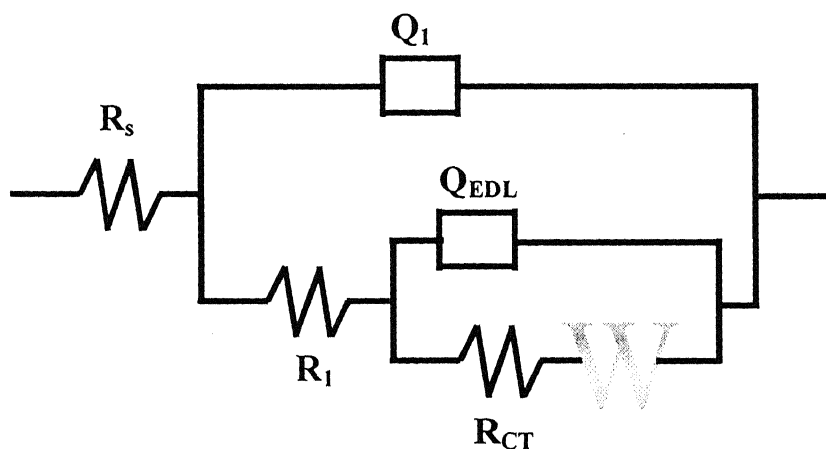


**Fig. 104** Equivalent circuit used for fitting experimental EIS data obtained in aqueous solution A3, when Warburg impedance was also present.

CPE describes an ideal capacitor for  $n = 1$  and an ideal resistor for  $n = 0$ . Generally, the appearance of a CPE is due to the presence of inhomogeneities in the electrode-material system and it can be described in terms of a (nonnormalizable) distribution of relaxation times, or it may arise from non-uniform diffusion whose electrical analog is an inhomogeneously distributed RC transmission line [52].

The theoretically estimated impedance spectra based on fitting the experimental data with the circuit shown in Figs. 103 and 104 have all been presented in Appendix A. The logic for fitting the EIS data to  $R(Q(R(QR)))$  circuit is based on microstructural observation of the surfaces, presented earlier. In all the cases of immersion in aqueous solutions, the nature of the surface indicated the presence of a surface film. Additionally, breaks were noted in the film which would have allowed the solution to come in contact with the metal surface. This justifies the use of  $R(Q(R(QR)))$  circuit to model EIS data.

The values of the circuit parameters, obtained on fitting the experimental data with the circuits shown in Figs. 103 and 104 are tabulated in Table 8. The percentage error is shown within brackets in Table 8. It can be noted from Table 8 that the solution resistance ( $R_s$ ) for solutions A1, A2 and A5 was in the range of 1 to 6 ohms-cm<sup>-2</sup> both on first immersion and after 432 hours of immersion, whereas for solution A4 it varied in between 50 to 90 ohm-cm<sup>2</sup>. The variation of the solution resistance as a function of time has been plotted in Fig. 105 for all the solutions. A relatively high value of solution resistance (in between 150-390 ohm-cm<sup>2</sup>) was obtained for solution A3 (Fig. 105). Moreover, it can be noted there was no appreciable change in the value of solution resistance during 432 hours of immersion for all the cases. The higher solution resistance ( $R_s$ ) in cases where NaCl was not present in the solutions must be noted.

From Table 8, it can also be seen that the values of ' $n_1$ ' were very close to one for solution A5, and therefore  $Z_{CPE}$  can be approximated to be equal to surface film capacitance for this case [55]. The parameter ' $n_1$ ' corresponds to surface roughness of the film [75]. In solution A5, the highest ' $n_1$ ' value indicated that surface obtained after immersion in this solution was less rough than other cases. The variation of ' $n_1$ ' as a function of immersion time is shown in Fig. 106. During immersion for 432 hours in solution A5, it was found that parameter ' $n_1$ ' did not change significantly with time (Fig. 106).

**Table 8(a)** Values of fitting parameters modeled from EIS data obtained in solution A1(3.5 wt% NaCl + 100 ppm Na<sub>2</sub>S + water)

Time (Days)	R <sub>s</sub>	Q <sub>1</sub>	n <sub>1</sub>	R <sub>i</sub>	Q <sub>EDL</sub>	n <sub>EDL</sub>	R <sub>ct</sub>
0	5.282 (1.531)	0.0003173 (7.193)	0.7638 (1.01)	8.203 (8.749)	0.0001674 (12.15)	1 (1.917)	8933 (3.201)
1	1.809 (1.735)	0.0004356 (2.488)	0.7681 (0.5709)	9176 (18.02)	0.001714 (163)	0.8794 (56.75)	4792 (85.15)
2	1.707 (1.707)	0.0003899 (2.54)	0.7755 (0.5601)	9456 (21.3)	0.001119 (156.5)	0.8098 (58.85)	5778 (82.77)
3	1.803 (1.575)	0.0004123 (2.963)	0.7673 (0.6233)	6239 (33.05)	0.0004797 (86.93)	0.6592 (43.62)	1.025E4 (59.4)
4	2.55 (1.423)	0.0003823 (2.596)	0.7646 (0.5715)	7497 (27.69)	0.0004925 (82.52)	0.6753 (40.9)	1.183E4 (58.86)
7	2.402 (1.338)	0.0005451 (4.45)	0.7187 (0.891)	2234 (66.79)	0.0003339 (40.75)	0.4797 (34.77)	1.522E4 (59.77)
10	3.408 (1.849)	0.0007985 (7.716)	0.644 (1.622)	1170 (73.6)	0.0003396 (18.59)	0.5834 (20.85)	9021 (28.34)
13	2.93 (0.8519)	0.0004658 (6.278)	0.6806 (1.04)	374.1 (47.85)	0.0002917 (6.528)	0.4794 (4.229)	1.017E4 (8.072)
18	4.189 (0.912)	0.0003516 (7.095)	0.7118 (1.175)	368.8 (48.26)	0.0004358 (3.205)	0.4202 (6.236)	1.276E4 (17.18)

**Table 8(b)** Values of fitting parameters modeled from EIS data obtained in solution A2(5 wt% NaCl + 100 ppm Na<sub>2</sub>S + water)

Time (Days)	R <sub>s</sub>	Q <sub>1</sub>	n <sub>1</sub>	R <sub>i</sub>	Q <sub>EDL</sub>	n <sub>EDL</sub>	R <sub>ct</sub>
0	2.715 (1.265)	0.0003689 (6.731)	0.7873 (0.8482)	2.849 (7.188)	0.0002368 (9.522)	0.9887 (1.333)	6659 (2.199)
1	3.825 (0.8619)	0.0002513 (81.34)	0.848 (9.109)	1.903 (32.28)	0.001492 (13.81)	0.6615 (1.77)	4343 (2.536)
2	3.656 (0.9349)	0.001372 (4.945)	0.6714 (1.114)	1028 (59.83)	0.0005161 (24.29)	0.5958 (18.84)	4549 (24.34)
3	2.86 (1.139)	0.001411 (6.511)	0.6646 (1.387)	417.4 (37.71)	0.0005699 (15.14)	0.7113 (8.303)	4821 (8.439)
4	2.495 (1.101)	0.001838 (5.915)	0.6224 (1.268)	499.5 (52.05)	0.0002961 (38.31)	0.8107 (14.83)	4936 (5.838)
7	3.579 (0.9434)	0.000595 (14.06)	0.7116 (2.24)	36.59 (16.94)	0.001276 (6.616)	0.5888 (1.153)	4678 (4.93)
10	2.862 (0.8675)	0.0005062 (7.207)	0.731 (1.198)	82.71 (11.63)	0.001285 (2.62)	0.5745 (1.686)	3919 (5.104)
13	3.846 (0.6776)	0.000527 (4.614)	0.7418 (0.8428)	203 (11.36)	0.001106 (1.856)	0.5645 (2.612)	4283 (6.004)
18	3.206 (0.683)	0.000621 (3.617)	0.7423 (0.6945)	346.2 (13.37)	0.001177 (3.765)	0.5337 (4.815)	4140 (9.727)

**Table 8(c)** Values of fitting parameters modeled from EIS data obtained in solution A3  
(100 ppm Na<sub>2</sub>S + water)

Time (Days)	R <sub>s</sub>	Q <sub>1</sub>	n <sub>1</sub>	R <sub>1</sub>	Q <sub>EDL</sub>	n <sub>EDL</sub>	R <sub>ct</sub>	W
0	303 (0.7783)	0.0003995 (3.1)	0.7151 (1.673)	7429 (10.57)	0.007336 (157.5)	1 (48.63)	3194 (114.2)	-
1	365.7 (0.888)	0.0004617 (90.17)	0.7175 (20.76)	210.3 (91.6)	0.0006908 (64.71)	0.7852 (15.86)	1.458E4 (15.72)	-
2	397.4 (0.4724)	0.0003337 (37.89)	0.6764 (7.635)	143.8 (30.12)	0.0005487 (23.83)	0.7887 (5.989)	2.965E4 (19.07)	-
3	276 (1.235)	0.0002115 (94.19)	0.6249 (18.33)	114.9 (46.99)	0.0005501 (37.31)	0.7237 (9.295)	2.804E4 (25.16)	-
4	232.4 (2.512)	0.0001295 (48.35)	0.4725 (11.47)	222.5 (16.36)	0.0004045 (15.17)	0.7078 (4.843)	4.872E4 (56.1)	-
7	192.4 (4.267)	3.421E-5 (56.38)	0.5082 (10.97)	584.9 (27.42)	0.0001107 (19.26)	0.5327 (5.356)	2.915E4 (17.1)	0.0004124 (29.89)
10	164.6 (4.646)	3.263E-5 (59.32)	0.5117 (11.17)	599.7 (30.46)	4.949E-5 (39.65)	0.6465 (9.964)	6014 (17.45)	0.0001605 (8.5)
13	172.2 (6.243)	3.81E-5 (68.63)	0.4798 (13.76)	555.4 (30.65)	4.725E-5 (42.55)	0.6666 (9.437)	7942 (18.14)	0.0001433 (19.5)
18	148.3 (7.172)	2.858E-5 (86.9)	0.5164 (16.09)	391.7 (30.6)	4.186E-5 (47.71)	0.7078 (10.49)	3213 (16.65)	0.0002035 (10.74)

**Table 8(d)** Values of fitting parameters modeled from EIS data obtained in solution A4  
(1000ppm NH<sub>4</sub>Cl +water)

Time (Days)	R <sub>s</sub>	Q <sub>1</sub>	n <sub>1</sub>	R <sub>1</sub>	Q <sub>EDL</sub>	n <sub>EDL</sub>	R <sub>ct</sub>
0	57.83 (0.8099)	3.229E-5 (5.865)	0.7792 (1.051)	1342 (6.273)	0.0002692 (3.612)	0.6042 (3.836)	5505 (4.426)
1	91.87 (4.133)	2.792E-5 (17.94)	0.768 (3.79)	6375 (29.15)	0.0002065 (41.65)	0.6338 (33.38)	1.818E4 (48.8)
2	93.52 (3.624)	3.431E-5 (18.03)	0.7682 (3.84)	4795 (28.39)	0.0002124 (31.85)	0.6467 (25.97)	1.513E4 (35.88)
3	113.3 (4.633)	4.583E-5 (23.75)	0.7311 (5.489)	5028 (37.14)	0.0001674 (28.65)	0.7445 (23.55)	1.894E4 (31.53)
4	154.7 (3.939)	3.611E-5 (13.36)	0.7337 (3.306)	7223 (17.14)	0.0002124 (25.77)	0.8948 (22.57)	1.254E4 (39.65)
7	47.44 16.8	6.102E-7 63.07	0.7668 7.261	302.9 9.412	3.053E-5 6.956	0.6396 2.213	9870 4.422
10	55.08 (12.99)	1.726E-7 (73.69)	0.8768 (7.084)	410.7 (19.67)	5.053E-5 (8.879)	0.4708 (4.698)	1.055E4 (6.961)
13	56.02 (13.71)	1.122E-7 (115.4)	0.9092 (10.1)	317.2 (91.93)	8.253E-5 (12.27)	0.3305 (13.54)	6813 (14.34)
18	52.65 (17.33)	8.212E-8 (125.4)	0.9342 (10.7)	413.9 (148.1)	7.07E-5 (17.99)	0.3086 (22.66)	1.004E4 (25.48)

**Table 8(e)** Values of fitting parameters modeled from EIS data obtained in solution A5  
 (3.5 wt% NaCl + 1000 ppm + NH<sub>4</sub>Cl)

Time (Days)	R <sub>s</sub>	Q <sub>1</sub>	n <sub>1</sub>	R <sub>1</sub>	Q <sub>EDL</sub>	n <sub>EDL</sub>	R <sub>ct</sub>
0	2.66 (1.91)	3.918E-5 (198.3)	0.9722 (17.09)	2.583 (264)	0.001304 (2.844)	0.5444 (6.661)	1823 (11.23)
1	2.66 (1.91)	3.918E-5 (198.3)	0.9722 (17.09)	2.583 (264)	0.001304 (2.844)	0.5444 (6.661)	1823 (11.23)
2	3.165 (2.283)	4.982E-5 (243.5)	0.9517 (22.1)	3.056 (269.9)	0.001223 (4.522)	0.5563 (9.337)	1298 (9.45)
3	3.575 (1.597)	2.954E-5 (162.3)	0.9854 (14.33)	3.132 (147.4)	0.0008849 (2.413)	0.5849 (5.586)	1253 (5.069)
4	4.423 (2.114)	6.131E-5 (182.8)	0.9155 (18.22)	6.658 (200.8)	0.00081 (8.17)	0.561 (9.397)	1256 (5.072)
7	2.895 (2.737)	2.315E-5 (223.3)	1 (19.62)	4.315 (226.5)	0.000736 (4.236)	0.5808 (7.439)	1314 (5.989)
10	6.501 (1.917)	5.925E-5 (167.2)	0.9102 (17.21)	12.41 (261.1)	0.000646 (6.946)	0.5342 (10.63)	1501 (5.050)
13	2.614 (2.096)	2.383E-5 (122.60)	1 (11.10)	6.143 (128.1)	0.0006306 (3.419)	0.5847 (4.418)	1379 (3.839)
18	2.822 (2.444)	2.463E-5 (197.6)	1 (17.44)	4.067 (193.8)	0.0008347 (3.577)	0.5763 (6.184)	1319 (5.735)

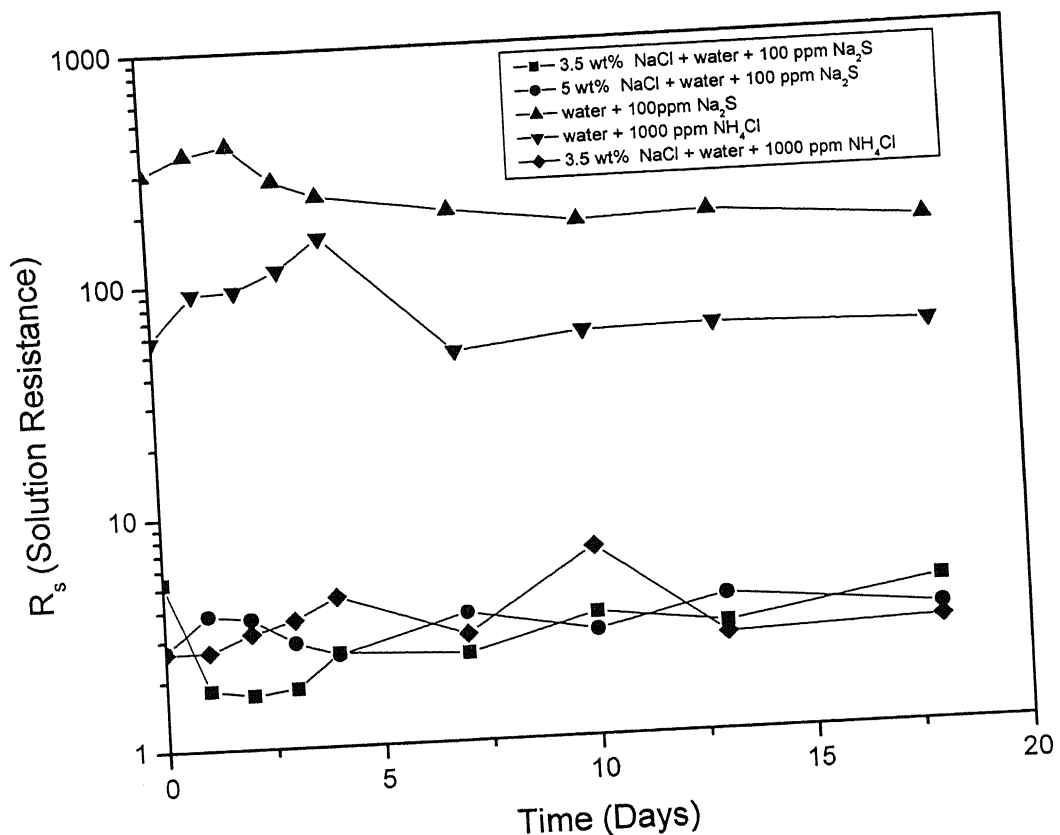


**Fig. 105** Solution resistance ( $R_s$ ) plotted as a function of time obtained after fitting the experimental data in aqueous solutions with the circuits shown in Figs. 103 and 104.

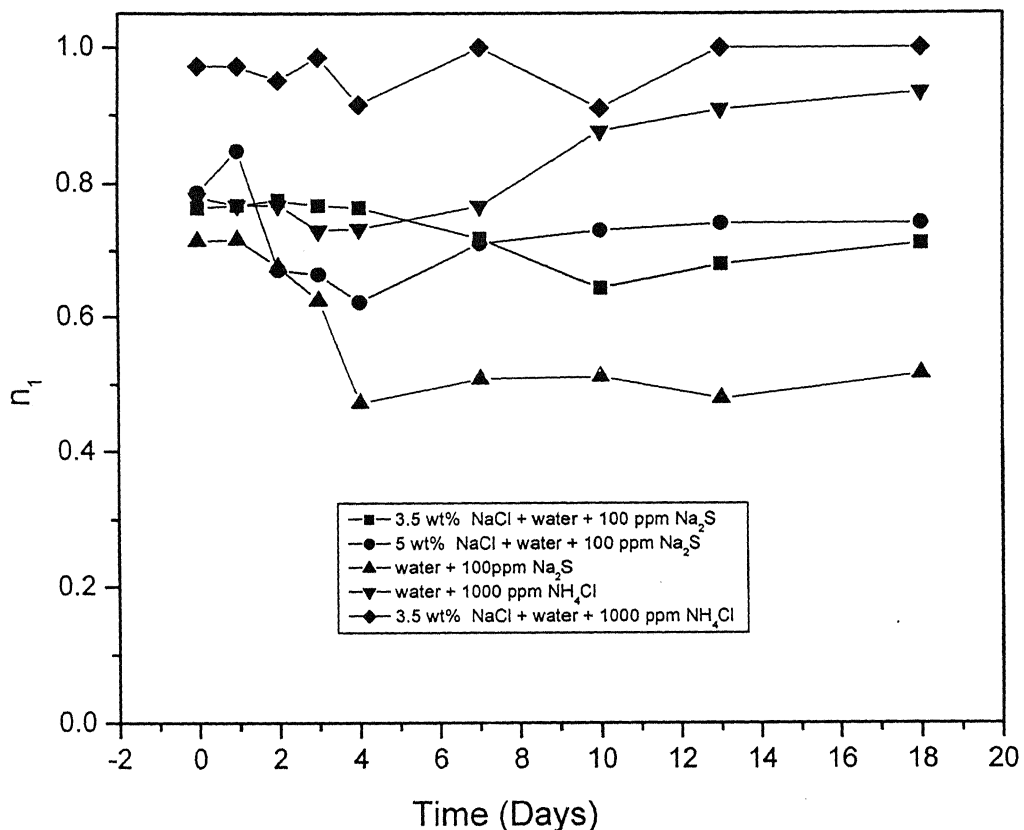


Fig. 106 ' $n_1$ ' (for film) plotted as a function of time obtained after fitting the experimental data in aqueous solutions with the circuits shown in Figs. 103 and 104.

For solution A4, the value of ' $n_1$ ' approached towards one, after 7<sup>th</sup> day of immersion (Fig. 106). This means that in presence of NH<sub>4</sub>Cl the film acquired improved capacitive behavior after 432 hours of immersion. The capacitance of the surface film may be increased as pores are fill up with aqueous solution of high dielectric constant. For solution A3, the value of ' $n_1$ ' was around 0.5 after 7<sup>th</sup> day of immersion (Fig. 106). The value of  $n_1=0.5$ , is an indication of that some diffusion related processes were important in controlling the overall electrochemical corrosion reaction. Solutions A1 and A2 revealed ' $n_1$ ' in between 0.7 to 0.85, which remained fairly constant throughout the experiment (Fig.106).

The improvement in the passive film properties with time was also evident in the values of the capacitance of the passive film ( $Z_{CPE}$ ) for pure copper. The surface film is considered to be a parallel circuit of a resistor due to the ionic conduction in the surface film, and a capacitor due to its dielectric properties [76]. Moreover, the value of capacitance is related to the surface film thickness according to the following relation [77]:

$$C_p = (\epsilon \epsilon_0 A) / d \quad (54)$$

where  $\epsilon$  is the dielectric constant of surface film,  $\epsilon_0$  the permittivity of the free space (8.9E-19 F cm<sup>-1</sup>), A is the area of the surface and  $C_p$  is the capacitance of the surface film. Thus, the decrease in the value of the capacitance with time corresponds to the growth of the surface film, indicating the long term stability of the surface film [77].

From Fig. 106, it was clear that for the surface film formed in solution A5, a nearly pure capacitive behavior was observed because ' $n_1$ ' values were close to 1. The variation of ' $Q_1$ ' as a function of immersion time is shown in Fig. 107. From Equation 54 and Fig. 107 it could be concluded that, in solution A5, the thickness of the film did not change significantly with immersion time. In solution A4, after 7<sup>th</sup> day of immersion ' $n_1$ ' values approached 1 and therefore after 7<sup>th</sup> day, nearly capacitive behavior of the film was obtained. Therefore CPE could be approximated with the capacitance of the film in aqueous solution A4 after 7<sup>th</sup> day of immersion. From Table 8 and Fig. 107 it was seen that CPE decreased after 7<sup>th</sup> day, indicating possible film thickening (Equation 54) after 7 days in solution A4. Solution A1 and A2 possessed ' $n_1$ ' values in between 0.7 to 0.85.

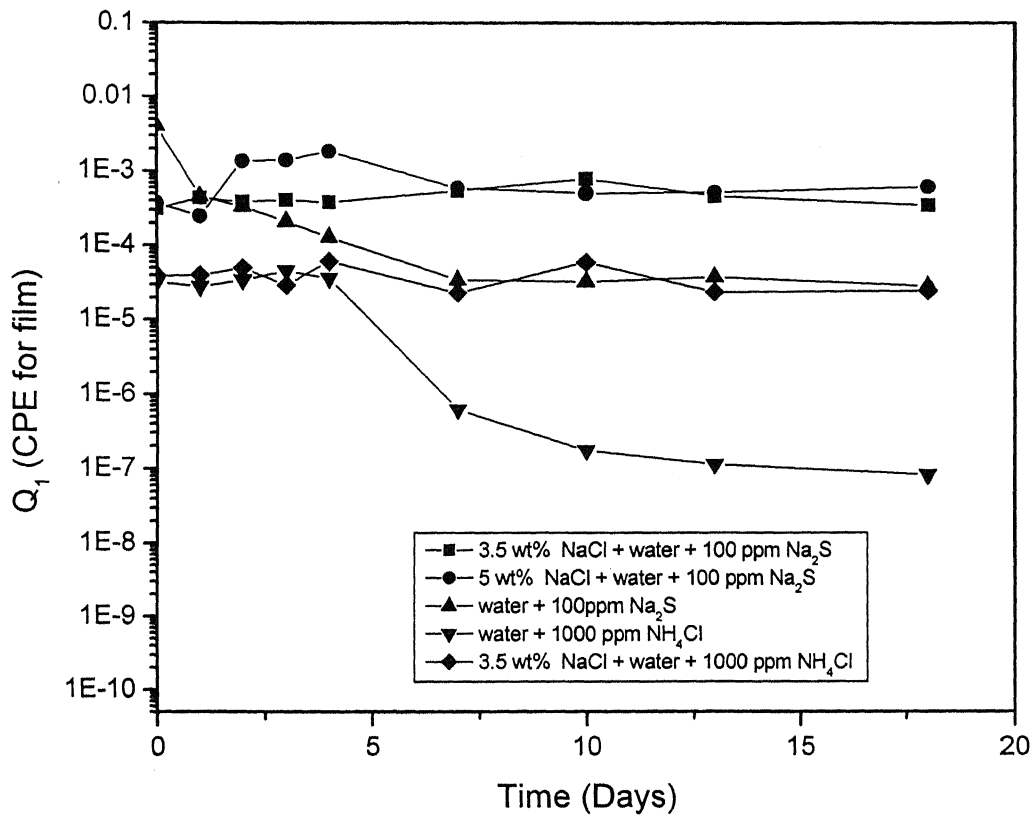


**Fig. 107** Constant phase element ( $Q_1$ ) for surface film plotted as a function of time obtained after fitting the experimental data in aqueous solutions with the circuits shown in Figs. 103 and 104.

The behavior of the film obtained in aqueous solutions A1 and A2, as a capacitor is not as certain as in A4 and A5 but certainly ' $n_1$ ' values were high enough so that a relative comparison for the capacitance of the film could be made. In these two cases (A1 and A2), CPE did not change significantly with time (Fig. 107), therefore thickness of the film did not change with time. In NaCl containing solutions (A1, A2 and A5), film thickness did not change significantly with time. CPE ( $Q_1$ ) of surface films formed in aqueous solutions after 432 hours of immersion varied in the following order:  $A1 \approx A2 > A5 \approx A3 > A4$  (Fig. 107). Due to low  $n_1$  value (equal to 0.5), solution A3 possessed the lowest capacitive nature among all cases, although its CPE is equivalent to CPE of A5. Surface films formed in other solutions (A1, A2, A4 and A5) possessed sufficiently high  $n_1$  value, so that CPE obtained after 432 hours of immersion could be considered to be equal to capacitance of the surface films formed in these solutions. The relative order of capacitance of surface films formed in aqueous solutions after 432 hours of immersion is presented here:  $A1 \approx A2 > A5 > A4 > A3$  (Fig. 107).

It was already discussed that films formed in different solutions were porous in nature, although the extent of porosity was different for different cases. The variation of  $R_1$  as a function of immersion time is shown in Fig. 108. For solution A5,  $R_1$  (porous film resistance) did not change with time, and it was also relatively low compared to the other cases (Fig. 108). In solution A1, A2 and A4,  $R_1$  initially increased after immersion, and then it decreased and attained to a stable value. In solution A3,  $R_1$ , decreased after 2 hours of immersion and approached an equilibrium value after 432 hours.  $R_1$  obtained for films formed in all the solutions, except A5, attained a nearly same value after 432 hours of immersion. Film resistance is a measure of conductivity of ions through the film. It is expected that after some time, electrolyte starts filling in the pores, leading to increase in conductivity of the pores [78]. Solution A5 possessed the highest conductivity of ions through the film, implying that localized corrosion and pitting was maximum in solution A5.

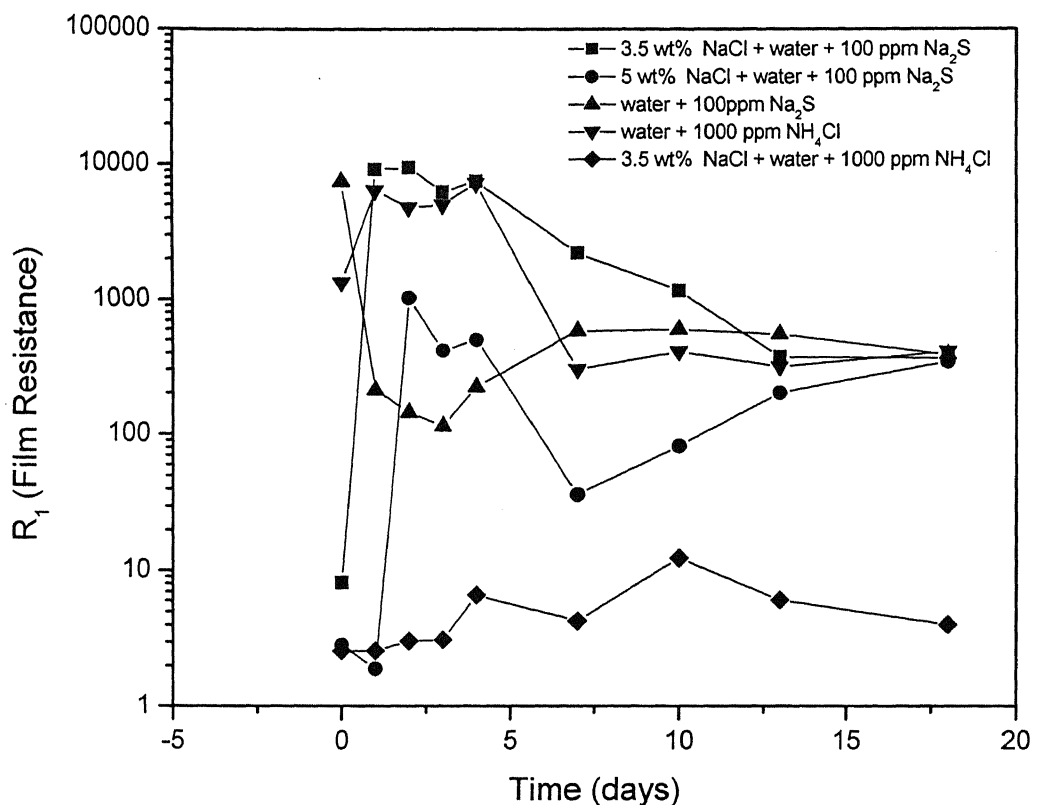


**Fig. 108** Film resistance ( $R_1$ ) plotted as a function of time obtained after fitting the experimental data in aqueous solutions with the circuits shown in Figs. 103 and 104.

The corroded metals represent a general behavior where the double layer on the interface of the metal/electrolyte does not behave as a real condenser. On the metal side of the double layer, electrons control the charge distribution, whereas on the solution side it is controlled by ions. Since the ions are much larger than the electrons, the equivalent ions to the charge on the metal will occupy quite a large volume on the solution side of the double layer. The constant phase element ( $Q_{EDL}$ ) has been defined as differential capacitance by authors.  $Q_{EDL}$  represents all the frequency-dependent electrochemical phenomena, namely double-layer capacitance and the diffusion process [79]. The important factors that cause deviation from the capacitive behavior of electrochemical surfaces are surface roughness, different reaction rates and thickness of the film on the surface. The capacitive nature of rough and porous surfaces in the present study could be understood by studying the variation of CPE as most of the electrochemical surfaces are assumed as imperfect capacitors in nature after long time immersion. The value of the double layer capacitance depends on many variables including electrode potential, temperature, ionic concentrations, types of ions, oxide layers, electrode roughness, impurity adsorption, etc. The variation of ' $n_{EDL}$ ' as a function of immersion time is shown in Fig. 109. In aqueous solutions after 432 hours of immersion the value of parameter ' $n_{EDL}$ ' is far from 1. Capacitive behavior of double layer decreased sharply for most of the cases (Fig. 109) as parameter ' $n_{EDL}$ ' decreased after 432 hours of immersion. This is attributed to the surface roughness of the exposed metal. It also indicated that due to localized attack, exposed metal was very rough. The double layer capacitances of the surface films formed in aqueous solutions after 432 hours of immersion have been compared in Fig. 110 and the order of variation is presented below.

$$A3 \approx A4 > A1 \approx A2 \approx A5$$

It suggested the damaging effect of chloride ions in aqueous solutions (A1, A2 and A5). Solutions A1, A2 and A5 possessed rough metal surfaces, at the regions where chloride ions had penetrated into the metal and opened up the surface oxide layer. It had also been understood and confirmed by SEM (Figs. 28 and 45). Solution A5 possessed almost constant value of parameter ' $n_{EDL}$ ' throughout the immersion period of 432 hours, indicating that capacitive behavior of electric double layer did not change significantly with time for solution A5 (Fig. 109).

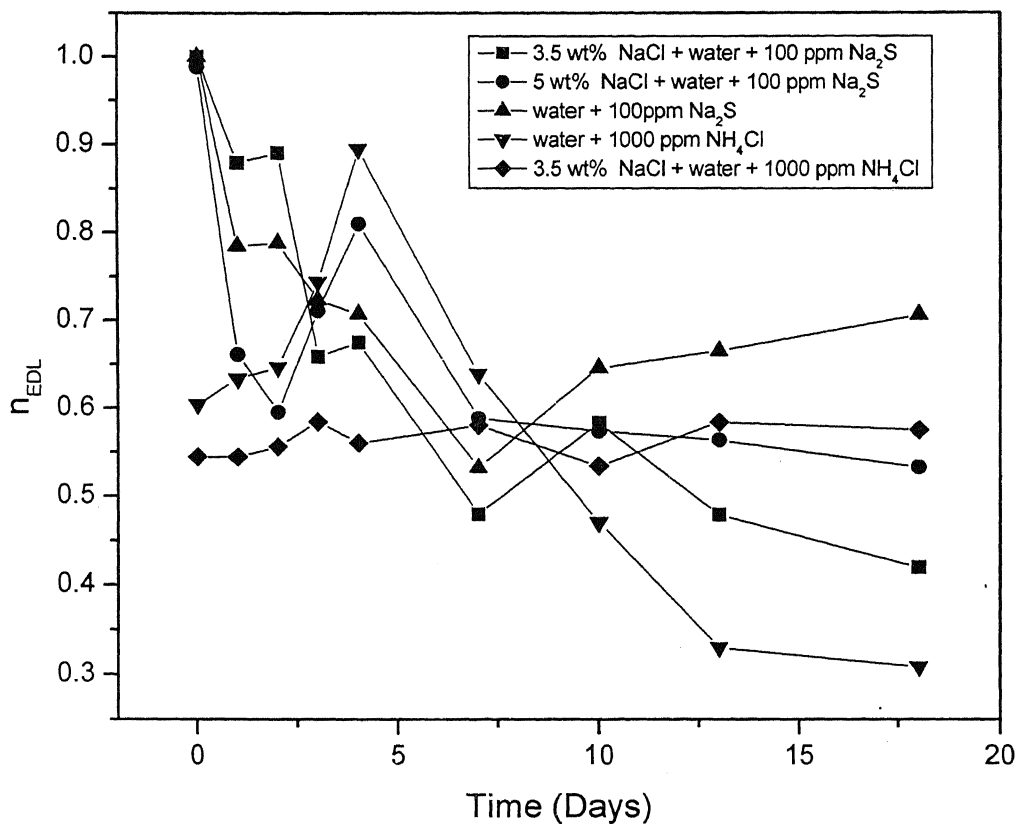


**Fig. 109** ‘ $n_{EDL}$ ’ (for double layer) plotted as a function of time obtained after fitting the experimental data in aqueous solutions with the circuits shown in Figs. 103 and 104.

Charge transfer resistance ( $R_{CT}$ ) occurs only by a single kinetically controlled electrochemical reaction. In this case mixed potential is not there, but rather a single reaction at equilibrium is occurring. If a metal substrate in contact with an electrolyte is considered, the metal molecules can electrolytically dissolve into the electrolyte, according to:



In the forward reaction in Equation 55, electrons enter the metal and metal ions diffuse into the electrolyte. Charge is being transferred. This charge transfer reaction has a certain speed. The speed depends on the kind of reaction, the temperature, the concentration of the reaction products and the potential. Diffusion also can create impedance known as the Warburg impedance. This impedance depends on the frequency of the potential perturbation. At high frequencies the Warburg impedance is small since diffusing reactants do not have to move very far. At low frequencies, the reactants have to diffuse farther, thereby increasing the Warburg impedance. In the mixed, kinetically and diffusion controlled reactions, it has been reported that polarization resistance should contain charge transfer resistance ( $R_{CT}$ ) and diffusive layer impedance ( $Z_w$ ) in series. Mixed kinetic and diffusion controlled process was noticed in solution A3 after 7<sup>th</sup> day of immersion (Table 8c). The variation of  $R_{CT}$  as a function of immersion time is shown in Fig. 111. For the single kinetically controlled reactions, the order of values of  $R_{CT}$  should follow the same trend as obtained from the linear polarization data. Among solutions A1, A2, A4 and A5 the order of variation of  $R_{CT}$  values was as following:

$$A4 \approx A1 > A2 > A5$$

Solution A5 showed minimum  $R_{CT}$  (charge transfer resistance) among all cases and it was fairly constant with time. Nearly similar results were obtained in the polarization resistance data (Table 6).

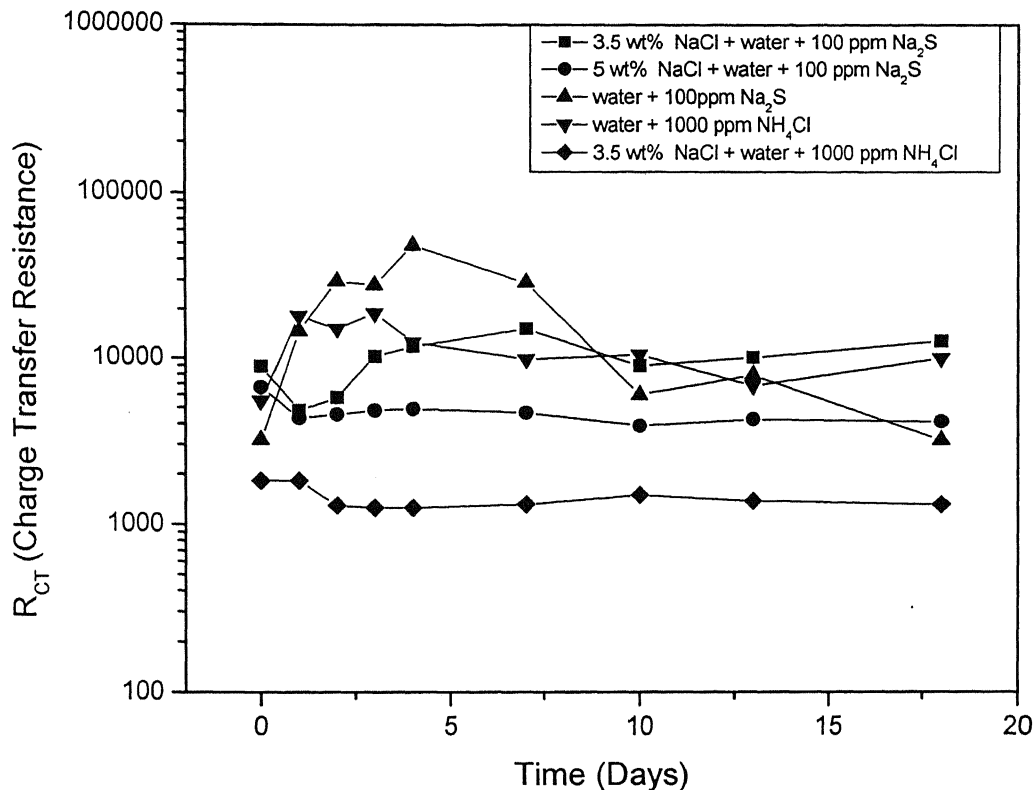


**Fig. 111** Charge transfer resistance ( $R_{CT}$ ) plotted as a function of time obtained after fitting the experimental EIS data in aqueous solutions with the circuits shown in Figure 103 and Figure 104.

#### 4.5.1.1 Damage Function

In order to understand the progression of corrosion damage accumulation on corroded surfaces it is often desirable to use more simplified analysis approaches. In one such approach, a Damage Function (D) is defined as the logarithm of the ratio of the impedance, taken at 0.1 Hz at zero exposure time, to that at some exposure time, t [56], given by:

$$D = \left( \log \frac{Z_0}{Z_t} \right)_{0.1\text{Hz}} \quad (56)$$

In case the corrosion resistance decreases with time, then this would be immediately indicated by the damage function increasing with time. On the other hand, if corrosion resistance increases, then damage function should decrease.

The damage function obtained from the EIS data have been plotted in Fig. 112 as a function of time for immersion of copper in the five different solutions.

The damage function increased as a function of exposure in solutions A1 and A2 thereby indicating the deleterious nature of chloride ions to surface film stability on copper. The damage function decreased in the case of exposure to solutions containing only Na<sub>2</sub>S and NH<sub>4</sub>Cl (i.e. A3 and A4). The lowest damage function after 432 hours of immersion was observed for the case of exposure in solution A3. Therefore the beneficial role of presence of sulfide has been also revealed by damage function analysis. In case of exposure in solution A5, no significant change in damage function could be noted. This condition, incidentally, provided the lowest polarization resistance ( $R_p$ ) from the linear polarization studies, both after 2 hours and 432 hours of immersion. Therefore, the damage function only provides ideas about the relative changes that occur on immersion and do not provide any ideas about the absolute values or absolute corrosion resistance. The poor corrosion resistance observed in solution A5 does continue with time and this is correctly indicated by the linear polarization studies. Nevertheless, the analysis of EIS data using damage function revealed that the surface became less protective on exposure to solution containing chlorides, whereas corrosion tendency decreased on immersion in Na<sub>2</sub>S containing solution. Therefore, the benign role of sulfide ions and the damaging role of chloride ions have been confirmed by damage function analysis.

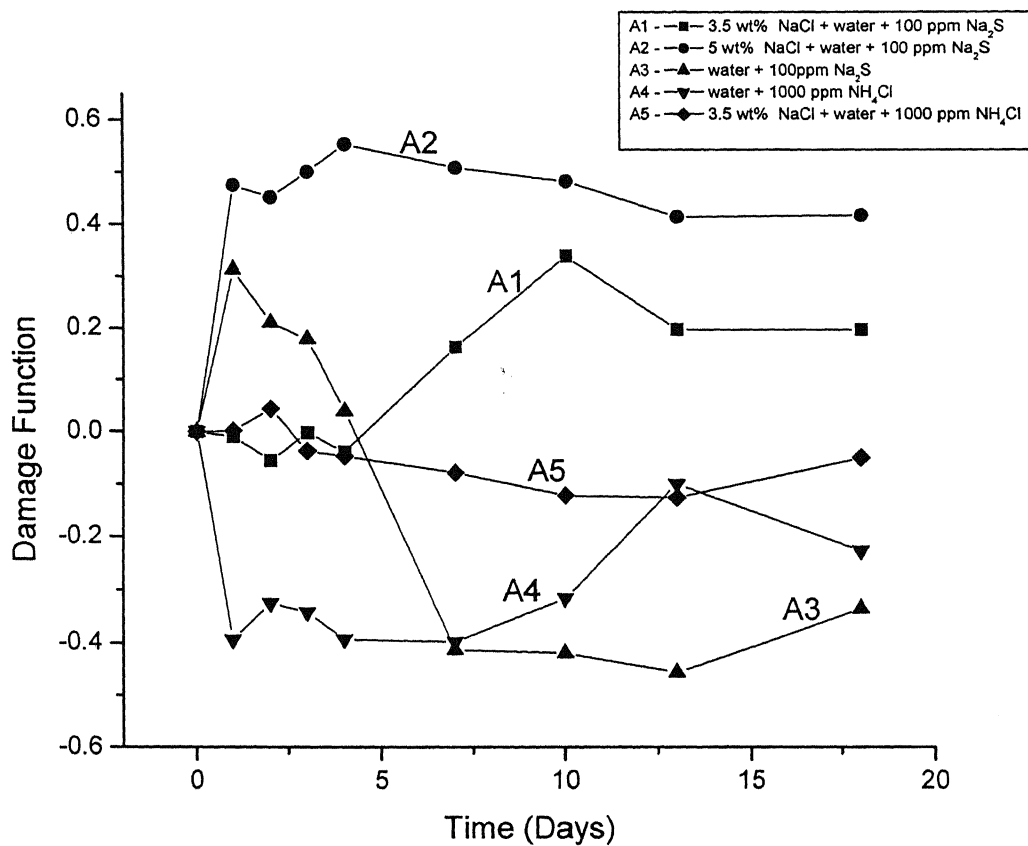


Fig. 112 Damage function plotted as a function of time for all aqueous solutions

#### **4.5.2 Soil Environment**

Electrochemical impedance spectroscopy (EIS) has proven to be a valuable test method for the electrochemical characterization of the protective surface films formed on metals. Stability of surface films formed on pure copper in different soil environments were studied by means of electrochemical impedance spectroscopy. All the impedance experiments were performed after stabilization of free corrosion potential.

The EIS data (Nyquist plots, Bode Magnitude and Phase plots) for pure copper in different soil environments, obtained at open circuit potential (after 2 hours and 432 hours of immersion), are presented in Figs. 113 through 118. The experiment performed in soil environment S9 could not run for 432 hours of immersion as electrical contact with specimen was lost after 168 hours; therefore, EIS data for S9 after 432 hours of immersion is not presented in this discussion.

The nature of the Nyquist plots (imaginary part of impedance vs. real part of impedance at different frequencies) was not similar for all the solutions. Nyquist plots obtained in most of the soil environments (Figs. 113 and 116) consisted of two arcs, which could be extrapolated to semicircles. Different arcs correspond to different time constants in the Nyquist plots. In soil environment S6 after 432 hours of immersion a small arc could be noticed at high frequencies (above 1 kHz) of the spectra whereas Nyquist plot of soil S8 after 2 hours of immersion consisted of a larger diameter arc at low frequencies (below 630 mHz). This feature is illustrated here to understand the different nature of surface films formed in soil environments of different compositions, which depends on the size and diameter of the semicircular arc. The diameter of the semicircle indirectly indicates the polarization resistance ( $R_p$ ). The diameter of the arc in chloride soil environments generally decreased after 432 hours of immersion (S6 and S7), indicating that corrosion resistance decreased (refer Fig. 121, 122). Long term immersion of copper in chloride environments generally results in decrease of the protecting properties of the surface [3, 8, 9, 10, 12]. Interestingly, soil S10 showed an increase in diameter of Nyquist plots after 432 hours of immersion (compare EIS data for S10 after 2 hours and 432 hours), implying that corrosion resistance increased (refer Fig. 120).

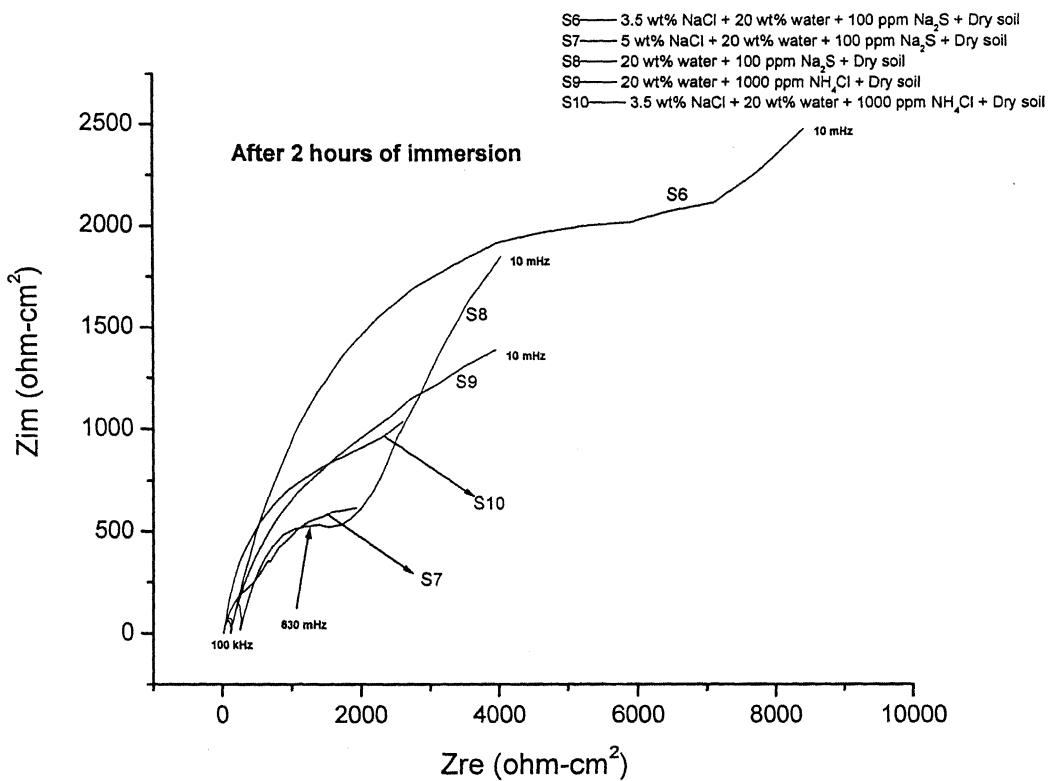


**Fig. 113** Nyquist plots obtained in soil environments after 2 hours of immersion.

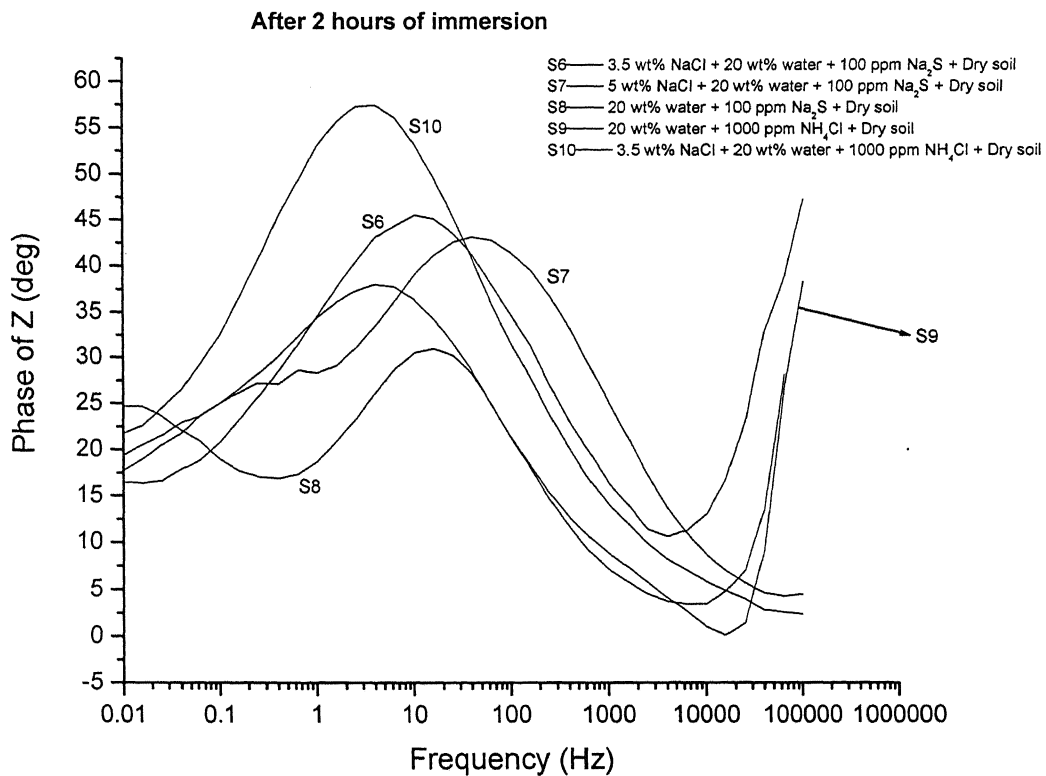


**Fig. 114** Bode phase plots obtained in soil environments after 2 hours of immersion.

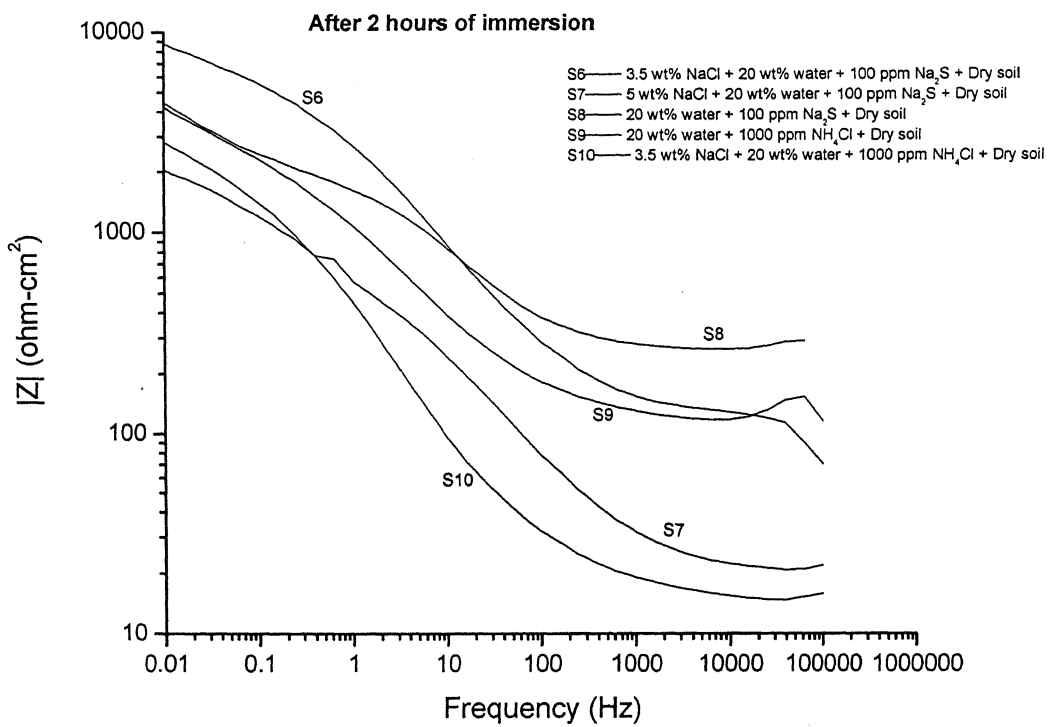


**Fig. 115** Bode magnitude plots obtained in soil environments after 2 hours of immersion.

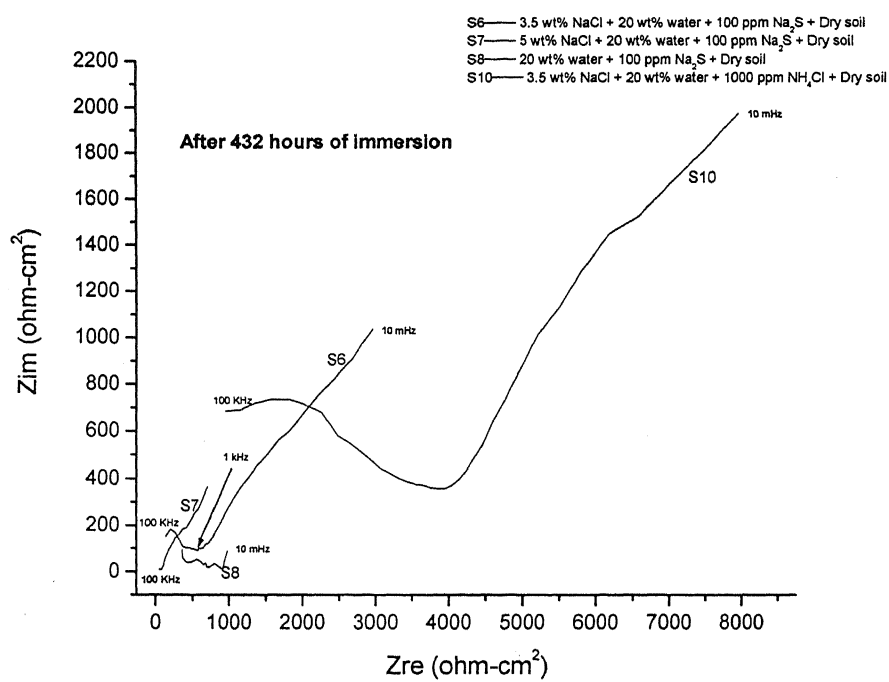


**Fig. 116** Nyquist plots obtained in soil environments after 432 hours of immersion.

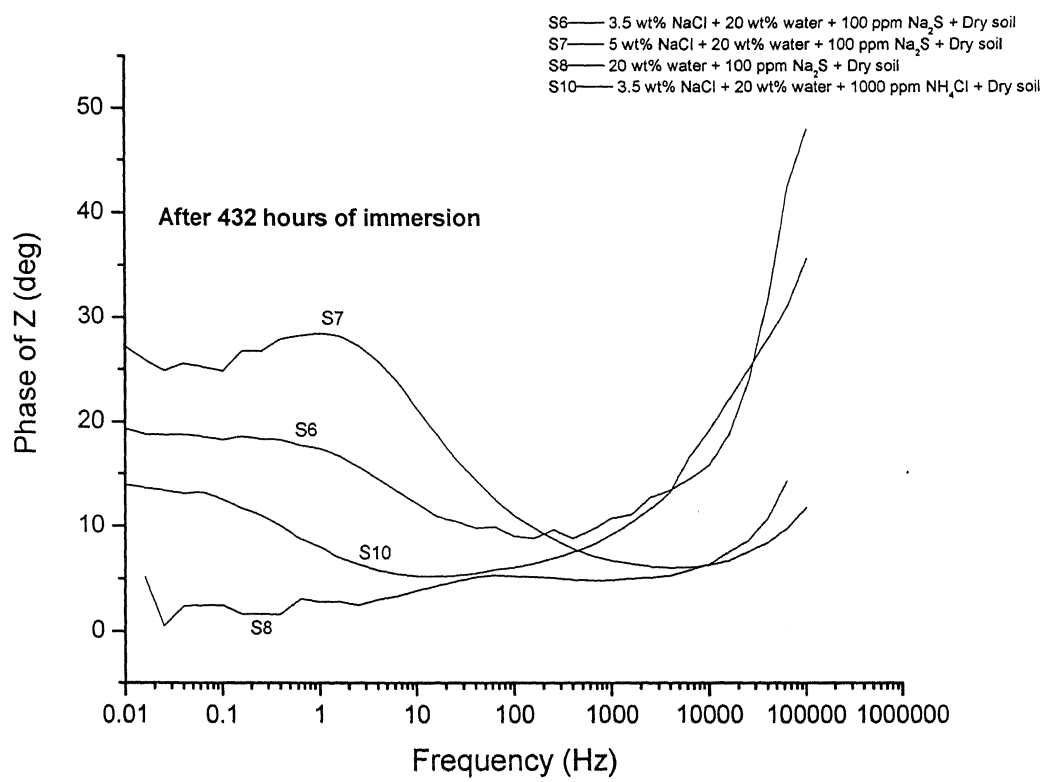


**Fig.117** Bode phase plots obtained in soil environments after 432 hours of immersion.

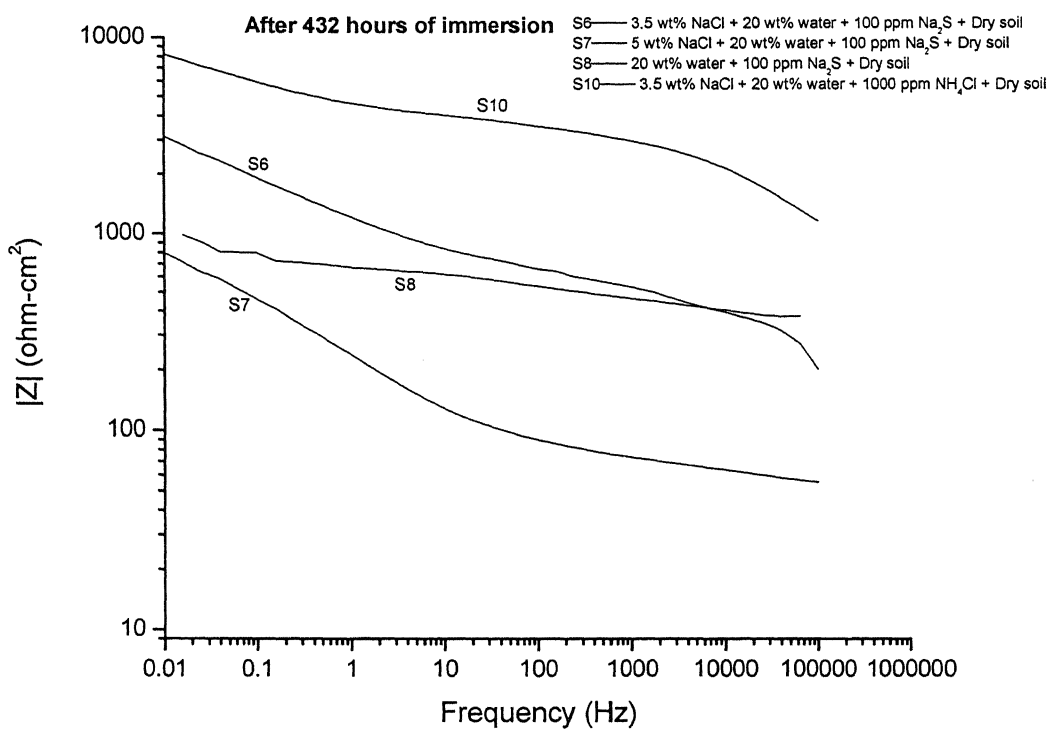


**Fig.118** Bode magnitude plots obtained in soil environments after 432 hours of immersion.

Comparing Nyquist plots for all different compositions in soil environment after 2 hours of immersion, it was found that soil S7 showed the lowest corrosion resistance (Fig. 113). It is reasonable, as soil environment S7 consisted of highest percentage of chloride (5 wt %). The deleterious effect of chloride ions on corrosion properties of copper has been well studied [3, 8, 9, 10, 12]. The unexpected low resistance against corrosion after 432 hours of immersion in soil S8 could be attributed due to contamination of KCl (Fig. 116).

The phase angle,  $\Theta$ , is a sensitive parameter used to indicate the presence of additional time constants in the impedance spectra at the highest and the lowest frequencies. Absolute values of the phase angles with frequency are plotted in the Bode phase angle plots (Figs. 114 and 117). Generally in Bode phase plots, if the phase angle drops towards zero degree at very high frequencies, it indicates the dominance of solution resistance in overall impedance (no phase shift between current and potential results due to presence of a resistor in AC circuit). In most of the soil environments (S6 and S8) at highest frequency (100 kHz), phase angle of zero degrees could not be obtained (Figs. 114 and 117), Rather it appeared part of another peak at high frequencies.

Capacitive behavior of the surface film decreased in most of the cases as the phase angle in the middle frequency range dropped after 432 hours of immersion (Figs. 114 and 117). The key features in the impedance spectra illustrating the influence of the deposit on the corrosion process are to be found at the low-frequency end of the spectra. Large negative phase shift in the low frequency region after long time immersion generally indicates better capacitive behavior (compact and protective) of the surface film. However this feature was not noticed in any of the soil environments. This allows us to conclude that the protecting properties of the surface film formed in most of the soil environments deteriorated with immersion time.

The overall nature of all the surface films formed in soil was generally found to be porous, as the SEM results analyzed in the previous section confirmed. The nature of Bode phase plots (Figs. 114 and 117) indirectly shows the porous nature of the film, which is characterized by large phase shift towards zero degrees and very narrow medium frequency capacitive region [56].

Bode phase plots obtained in all soil environments, after 2 hours of immersion (Fig. 114), suggested that soil environments S6, S7 and S10 revealed high negative phase

shift in the middle frequency range, indicating that surface layers obtained in these environments possessed higher capacitive behavior among other cases after 2 hours of immersion. The soil environments S6, S7 and S10 possessed high chloride content. Chloride accelerates the growth rate of film formation on copper surface, as copper is exposed to chloride containing environment [8]. In soil environments S6, S7 and S10, film formation occurs readily after immersion as compared to other soils. However long term exposure to chloride environment can be deleterious for copper, as it could be seen from the Bode magnitude plots (Figs. 115 and 118) that after 432 hours of immersion the phase shift decreased and the compactness of the surface films had lowered. The damaging effect of chloride ions has been extensively reported in literature [3, 8, 9, 10, 12]. It is believed that chloride ions would affect the properties and stability of the surface films, when exposed to longer times [9].

A common way to rank the performance of surface films is to compute the total impedance by using the magnitude of the impedance at the lowest frequency [56]. A decrease in total impedance was noticed in soil environments S6 and S7. Due to presence of damaging chloride ions the impedance decreased significantly, leading to decrease in corrosion resistance. Chloride ions are expected to deteriorate the properties of the protective surface layer initially formed on copper [3, 8, 9, 10, 12].

The equivalent circuit shown in Fig. 103 was used to fit the above experimental data. In the equivalent circuit,  $R_s$  is solution resistance,  $R_{ct}$  is charge transfer resistance (or polarization resistance),  $Q_f$  is constant phase element (CPE) for film and  $Q_{EDL}$  is constant phase element (CPE) for electrical double layer. The CPE considers the fact that experimentally; the barrier film never exhibits the theoretically expected phase shift of  $-90^\circ$  and a slope of -1 for an ideal dielectric.

The logic for fitting the EIS data to  $R(Q(R(QR)))$  circuit is based on microstructural observation of the surfaces, presented earlier. In all the cases of immersion in soil environments, the nature of the surface indicated the presence of a surface film. Additionally, breaks were noted in the film which would have allowed the

**Table 9(a)** Values of fitting parameters modeled from EIS data obtained in soil environment S6 (3.5 wt% NaCl + 100 ppm Na<sub>2</sub>S + 20 wt% water + dry soil)

Time (days)	R <sub>s</sub>	Q <sub>1</sub>	n <sub>1</sub>	R <sub>i</sub>	Q <sub>EDL</sub>	n <sub>EDL</sub>	R <sub>ct</sub>
0	3.637E-15 (5.947E17)	1.307E-7 (120.5)	0.8296 (13.12)	182.6 (20.61)	0.001444 (8.814)	0.2736 (12.68)	5.134E16 (7.282E14)
1	9.45E-8 (3.146E10)	1.295E-7 (144.7)	0.8193 (16.02)	201.7 (25.47)	0.001257 (10.07)	0.2701 (14.65)	9.299E10 (1.331E9)
2	3.637E-15 (5.947E17)	1.307E-7 (120.5)	0.8296 (13.12)	182.6 (20.61)	0.001444 (8.814)	0.2736 (12.68)	5.134E16 (7.282E14)
3	8.215E-7 (2.153E9)	5.485E-8 (82.64)	0.8814 (8.597)	187.6 (14.02)	0.001232 (5.315)	0.28 (6.992)	1.396E12 (9.833E9)
4	117.8 (1434)	0.0009923 (8355)	0.2216 (2199)	5.391E14 (2.54E20)	1.426E-7 (2.587E33)	0.3133 (1.644E32)	120.9 (1.133E33)
7	173.5 (71.63)	0.0008475 (962.8)	0.2518 (303)	1E20 (4.165E25)	8.29E-10 (2.765E44)	0.0162 (3.16E44)	1653 (2.519E42)
10	137.4 (406.8)	0.000695 (9810)	0.1991 (1997)	1.73E18 (1.516E24)	3.783E-16 (3.849E53)	0.09876 (4.276E53)	0.3285 (7.984E42)
13	3.181E-5 (1.08E8)	5.446E-8 (112.8)	0.8465 (11.9)	289.8 (22.48)	0.0006218 (6.809)	0.2514 (9.91)	1.175E23 (5.809E20)
18	9.999E-8 (3.145E10)	5.208E-8 (77.13)	0.834 (8.401)	373.2 (14.81)	0.0007148 (5.634)	0.2474 (8.738)	8.112E10 (3.934E8)

**Table 9(b)** Values of fitting parameters modeled from EIS data obtained in soil environment S7 (5 wt% NaCl + 100 ppm Na<sub>2</sub>S + 20 wt% water + dry soil)

Time (days)	R <sub>s</sub>	Q <sub>1</sub>	n <sub>1</sub>	R <sub>i</sub>	Q <sub>EDL</sub>	n <sub>EDL</sub>	R <sub>ct</sub>
0	20.21 (1.403)	0.000229 (9.922)	0.64 (2.042)	577.6 (19.98)	0.001063 (11.83)	0.4675 (13.06)	2709 (19.16)
1	48.59 (10.81)	0.00232 (273.8)	0.3583 (64.88)	4.678E15 (1.835E21)	4.612E-11 (3.795E29)	0.09633 (6.384E26)	4.526E7 (1.896E29)
2	65.11 (922.4)	0.002508 (2.609E4)	0.2665 (3578)	2.248E12 (7.357E21)	1.092E-18 (7.283E19)	0.3344 (6.104E18)	2.459E15 (6.725E18)
3	0.01433 (1.469E6)	6.073E-5 (323.2)	0.3442 (179.3)	81.37 (288.5)	0.002492 (11.52)	0.3179 (11.18)	3.206E8 (4.638E6)
4	1.836E-11 (1.393E15)	5.835E-7 (286.6)	0.6556 (114.5)	56.82 (455.4)	0.00314 (4.677)	0.3019 (6.504)	1.827E19 (2.935E17)
7	65.64 (27.74)	0.00248 (8.794)	0.2968 (14.7)	1.482E-7 (6.202E10)	9.327E-8 (3577)	1 (226.7)	3.73E4 (983.4)
10	9.94E-8 (1.021E11)	7.337E-6 (127.3)	0.4793 (45.47)	121.6 (89.38)	0.002195 (3.987)	0.3655 (6.177)	2053 (20.73)
13	76.01 (25.17)	0.002366 (8.691)	0.2928 (14.68)	0.0002288 (2.312E7)	1.451E-7 (1962)	1 (119.4)	1.263E7 (3.145E5)
18	0.0002265 (7.514E7)	2.466E-6 (182.6)	0.5629 (75.33)	64.42 (267.7)	0.002502 (3.883)	0.4031 (4.374)	2027 (18.85)

**Table 9(c)** Values of fitting parameters modeled from EIS data obtained in soil environment S8 (100 ppm Na<sub>2</sub>S + 20 wt% water + dry soil)

Time (Days)	R <sub>s</sub>	Q <sub>1</sub>	n <sub>1</sub>	R <sub>i</sub>	Q <sub>EDL</sub>	n <sub>EDL</sub>	R <sub>ct</sub>
0	270.6 (3.823)	6.884E-5 (38.22)	0.6885 (9.658)	1597 (31.29)	0.001223 (44.36)	0.5404 (47)	1.219E4 (202.9)
1	225 (0.5951)	8.453E-5 (5.426)	0.6948 (1.378)	941.8 (3.399)	0.002136 (5.136)	0.5497 (5.363)	6360 (21.33)
3	30.61 (341.8)	7.872E-9 (364.2)	0.9919 (33.67)	205.9 (67.17)	0.0004665 (13.98)	0.2951 (14.65)	1.831E4 (122.2)
4	63.08 (615.3)	0.0004825 938.55)	0.1701 (66.97)	1E-7 (6.067E11)	5.708E-9 (820)	1 (45.61)	6.609E11 (1.682E10)
7	1.303E-7 (2.647E11)	1.864E-9 (202.3)	1 (24.64)	465.6 (75.79)	0.0002927 (9.299)	0.429 (6.717)	4678 (12.08)
10	1.354E-7 (2.565E11)	1.8E-9 (198.8)	1 (23.84)	500.5 (71.08)	0.000232 (8.841)	0.4439 (6.171)	5779 (11.11)
13	67.03 (24.61)	3.029E-9 (122.9)	1 (8.8620)	500.5 (10.34)	0.0002051 (32.59)	0.4842 (17.27)	4216 (39.04)
18	0.0007119 (3.254E13)	1.272E-12 (7.601E16)	9.428E-6 (7.628E16)	1.582E-7 (1.464E17)	0.0008373 (1848)	0.07937 (1454)	2185 (2.113E8)

**Table 9(d)** Values of fitting parameters modeled from EIS data obtained in soil environment S9 (1000 ppm NH<sub>4</sub>Cl + 20 wt% water + dry soil)

Time (Days)	R <sub>s</sub>	Q <sub>1</sub>	n <sub>1</sub>	R <sub>i</sub>	Q <sub>EDL</sub>	n <sub>EDL</sub>	R <sub>ct</sub>
0	1.01E-7 (1.265E11)	6.851E-9 (256.4)	1 (32.33)	125 (103.8)	0.0003267 (7.718)	0.5569 (3.971)	4691 (9.876)
1	1E-7 (2.572E11)	0.000147 (44.02)	0.1734 (32.62)	1.094E4 (119.4)	8.67E-5 (159)	0.6102 (26.46)	1.892E5 (940)
2	1.054E-7 (9.029E12)	0.0001535 (8031)	0.133 (2749)	4.368E11 (1.472E16)	3.21E-12 (1.261E26)	0.01376 (1.627E26)	1.158E5 (5.551E22)
3	6.652E-5 (4.673E8)	9.621E-9 (179.7)	0.8371 (18.77)	1543 (55.84)	0.0001485 (16.17)	0.1853 (31.6)	1.724E15 (5.941E12)
4	9.995E-8 (2.473E11)	4.113E-8 (136.5)	0.7294 (16.38)	1804 (44.92)	0.0001525 (12.22)	0.1868 (28.26)	9.996E14 (2.951E12)
7	0.000398 (8.75E7)	1.994E-9 (249.8)	0.9495 (21.72)	758.1 (238.6)	9.285E-5 (23.21)	0.1505 (47.85)	1.634E11 (5.363E8)

**Table 9(e)** Values of fitting parameters modeled from EIS data obtained in solution S10  
 (3.5 wt% NaCl + 1000 ppm NH<sub>4</sub>Cl + 20 wt% water + dry soil)

Time (Days)	R <sub>s</sub>	Q <sub>1</sub>	n <sub>1</sub>	R <sub>i</sub>	Q <sub>EDL</sub>	n <sub>EDL</sub>	R <sub>ct</sub>
0	15.79 (2.231)	0.0006154 (4.897)	0.6795 (1.613)	2788 (11.85)	0.01479 (184.9)	1 (60.22)	1082 (118.6)
1	39.01 (4.213)	0.0006228 (8348)	0.594 (363.1)	8868 (1.12E9)	3.734E-15 (9.928E23)	0.5377 (5.721E22)	0.332 (2.993E13)
2	0.0006071 (3.822E7)	5.067E-7 (135.1)	0.5912 (30.56)	422.2 (60.31)	0.0008804 (4.584)	0.2906 (8.585)	3.839E12 (1.965E10)
3	0.0001721 (1.977E8)	9.879E-8 (157.9)	0.7034 (42.34)	241.3 (143.8)	241.3 (143.8)	0.3172 (3.523)	3.03E11 (5.951E8)
4	269.2 (22.89)	0.0007701 (8.952)	0.2722 (15.61)	1E-7 (1.727E11)	3.482E-8 (1682)	1 (104.4)	9.744E9 (8.428E7)
7	9.984E-8 (5.467E11)	4.969E-8 (146.1)	0.707 (34.04)	532 (106.1)	0.0005634 (4.339)	0.2782 (6.64)	2.125E4 (61.61)
10	1.001E-7 (1.882E11)	6.823E-7 (59.93)	0.519 (12.47)	1631 (16.67)	0.0003891 (4.628)	0.2853 (10.43)	9053 (25.13)
13	1E-7 (1.507E11)	8.939E-7 (43.39)	0.4963 (8.829)	2735 (11.21)	0.00045 (6.096)	0.2654 (17.88)	2.172E4 (99.5)
18	1.001E-7 (1.198E11)	6.316E-7 (33.53)	0.5208 (6.367)	3273 (8.083)	0.0003987 (4.838)	0.2638 (14.89)	1.498E11 (4.899E8)

ions to come in contact with the metal surface. This justifies the use of R(Q(R(QR))) circuit to model EIS data.

The values of the circuit parameters, obtained on fitting the experimental data with the circuits shown in Fig. 103 are tabulated in Table 9. The percentage error is shown within brackets in Table 9. In some cases of soil environments the percentage error obtained after fitting was very high, leading to imperfect fit of the model. Therefore the variation of circuit parameters with immersion time is not discussed here.

#### 4.5.3 Comparison

Electrochemical impedance measurements (EIS) are helpful in characterizing the surface films formed on materials during corrosion process. An important advantage of EIS over other laboratory techniques is the possibility of using very small amplitude signals without significantly disturbing the properties being measured. Comparison of EIS data of copper in different environments (aqueous and soil) would provide understanding of effect of environment on corrosion.

On comparing the diameter of the arcs obtained in Nyquist plots (Fig. 119) after 432 hours of immersion in soil environment S8 and aqueous solution A3 it was found that the diameter was less in soil S8 as compared to aqueous solution A3 suggesting that the corrosion resistance was less in soil environment S8 than aqueous solution A3 after 432 hours of immersion. The electrochemical reaction occurred homogeneously on copper surface in aqueous solution A3, whereas due to non-homogeneous mixing of polluting additives (e.g.  $\text{Na}_2\text{S}$ ) in soil environments, the attack was not uniform in this environment. The surface film formed by  $\text{S}^{2-}$  ions in aqueous solutions was more protective than in soil environment.

On comparing the Nyquist plots (obtained after 432 hours immersion) of chloride containing aqueous solutions (A1, A2 & A5) and the soil environments having same chloride content (S6, S7 & S10), it was found that in aqueous solutions the corrosion resistance was lower as compared to respective soil environments (Figs. 120-122). On basis of the above observation it could be said that the damaging effect of chloride ions

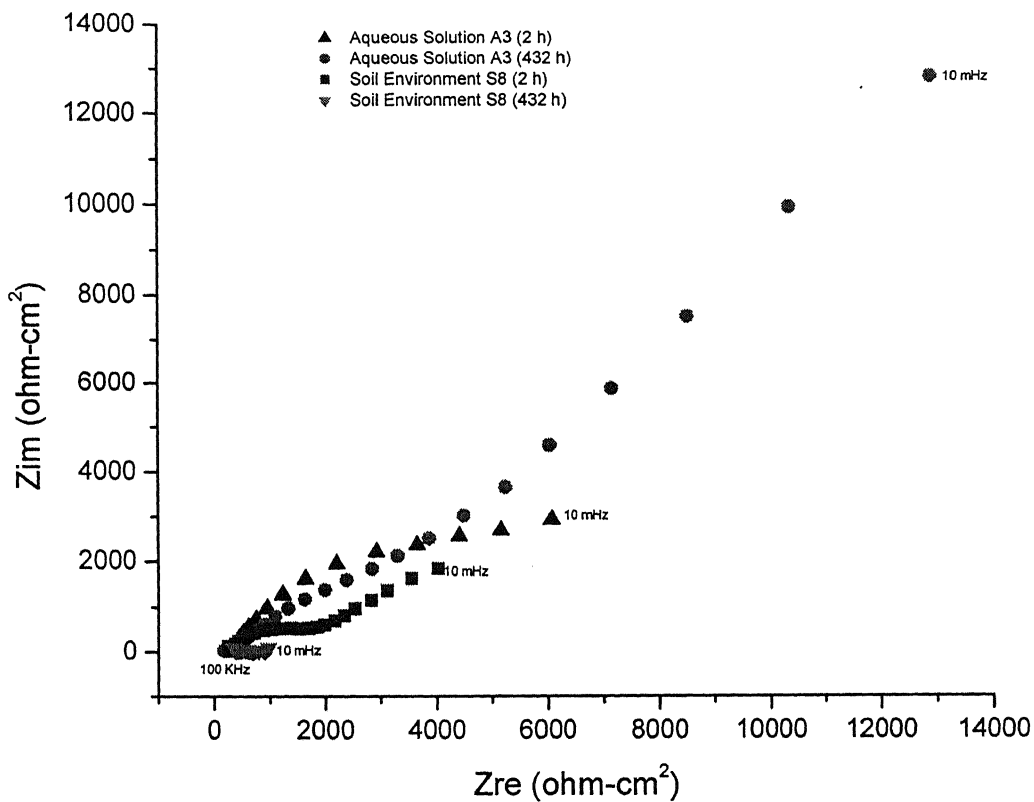


**Fig. 119** Comparison of Nyquist plots obtained after immersion in aqueous solution A3 and soil environment S8.

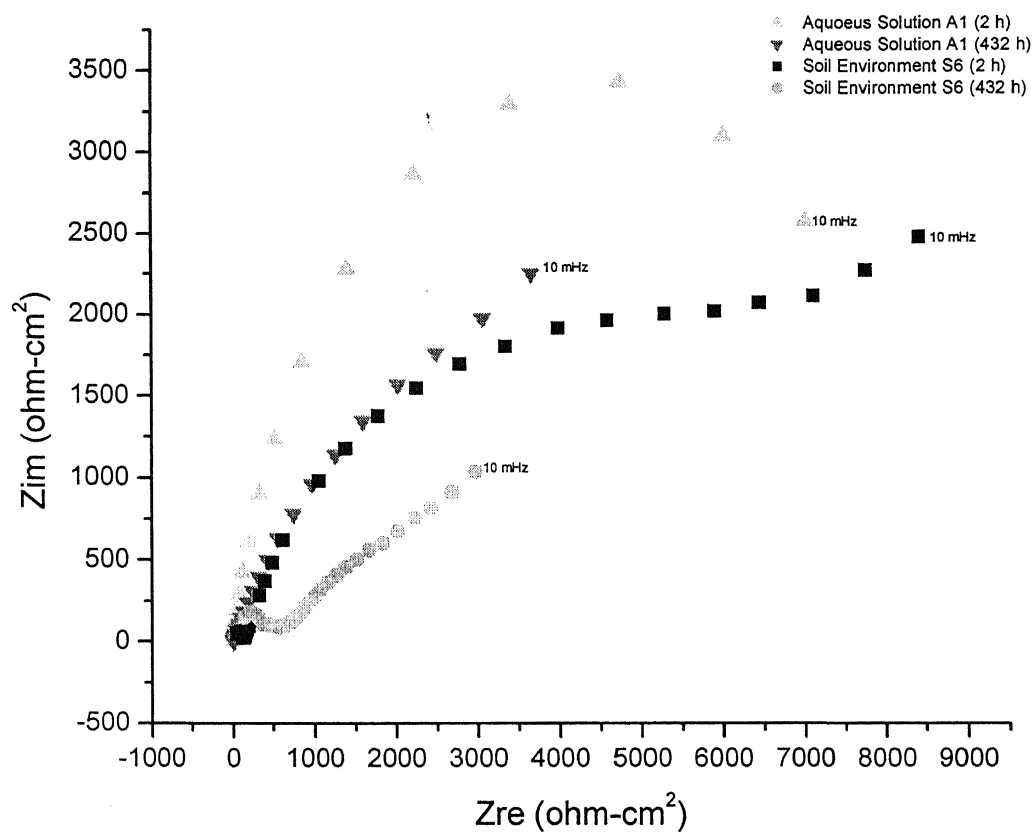


**Fig. 120** Comparison of Nyquist plots obtained after immersion in aqueous solution A1 and soil environment S6.

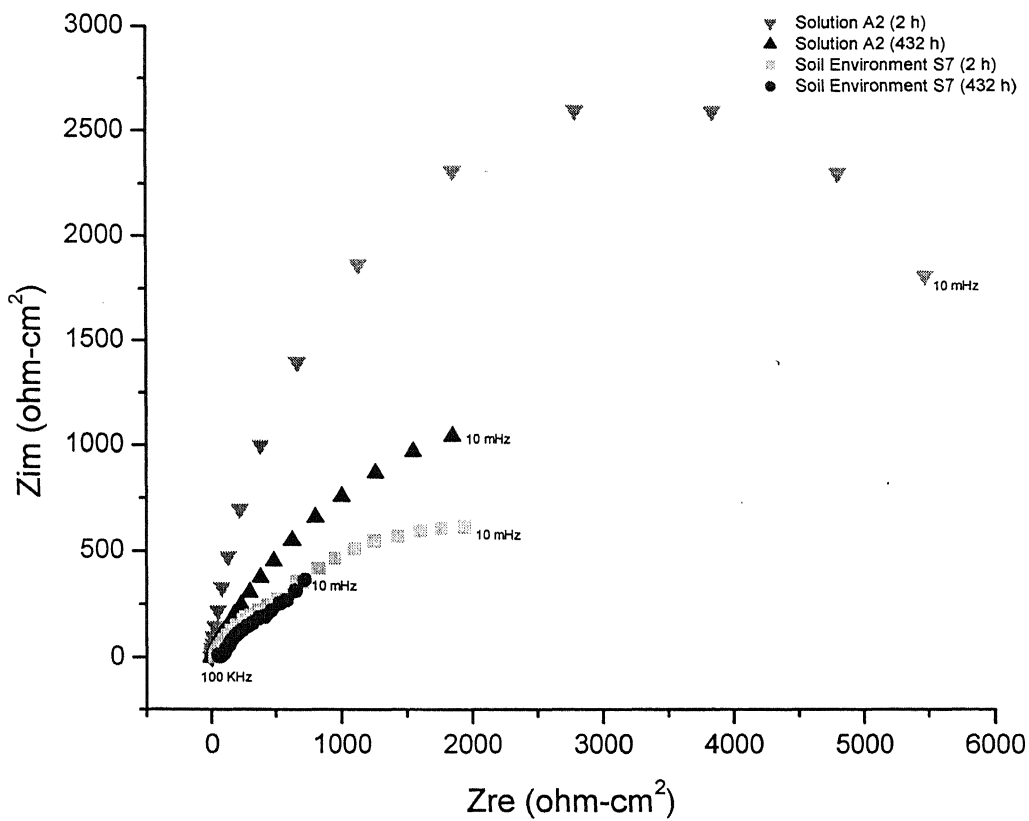


**Fig. 121** Comparison of Nyquist plots obtained after immersion in aqueous solution A2 and soil environment S7.

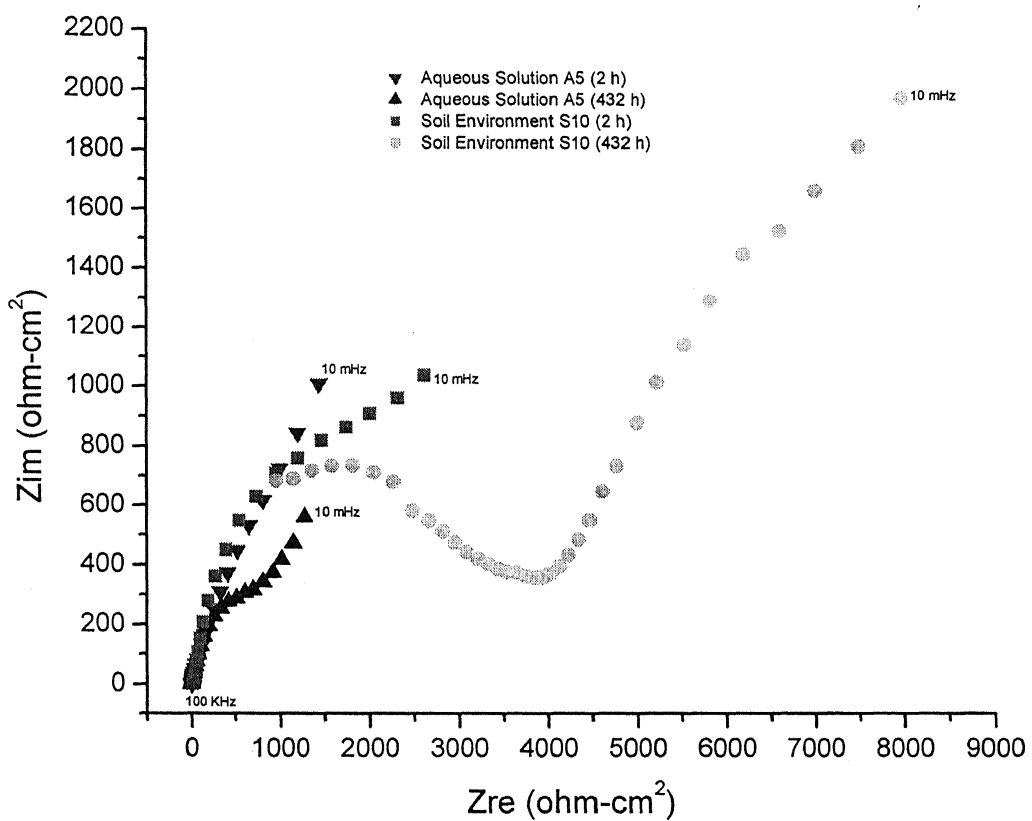


**Fig. 122** Comparison of Nyquist plots obtained after immersion in aqueous solution A5 and soil environment S10.

was predominant in aqueous solutions, which had also been understood from FCP and linear polarization data.

Comparison of Bode phase plots of chloride containing aqueous solutions (A1, A2 and A5) and the soil environments having same chloride content (S6, S7 and S10), it was found that the capacitive behavior of surface films (obtained after 432 hours of immersion) formed in case of aqueous solutions was high as the phase angle was shifted towards  $90^0$  in case of aqueous solutions (Figs. 123-125). Figure 126 suggested that surface film formed after 432 hours of immersion in presence of  $S^{2-}$  ion was more capacitive in case of aqueous solutions than soil environment (compare Bode phase plots of aqueous solution A3 and soil environment S8).

A common way to rank the performance of surface films is to compute the total impedance by using the magnitude of the impedance at the lowest frequency [56]. On comparing the Bode magnitude plots (obtained after 432 hours of immersion) in aqueous and soil environments it was found that soil environment S10 produced higher magnitude of total impedance at lowest frequency than aqueous solution (A5) of same composition (Fig. 127). It indicated that surface film formed in soil S10 was more protective in nature than formed in aqueous solution A5. As already mentioned, the damaging effect of chloride ions in aqueous solutions was more dominant [3, 8, 9, 10, 12]. Therefore it is understood that surface film formed in aqueous solution A5 was less resistant against corrosion as compared to soil S10. As expected soil environments S6 and S7 should also reveal high impedance at lowest frequency than aqueous solutions (A1 and A2) of same composition, but due to contamination of chloride ions from luggin capillary they showed lower impedance as local corrosion was occurring at some places on the surface (Figs. 128 and 129). Aqueous solution A3 (after 432 hours of immersion) revealed higher impedance at lowest frequency than soil environment S8 of same composition. The surface film formed by  $S^{2-}$  ions in aqueous solutions was more protective than in soil environment. Due to low conductivity of soil, availability of  $S^{2-}$  ions near the surface was low. It further affected the film formation process on copper surface in soil environment S8.

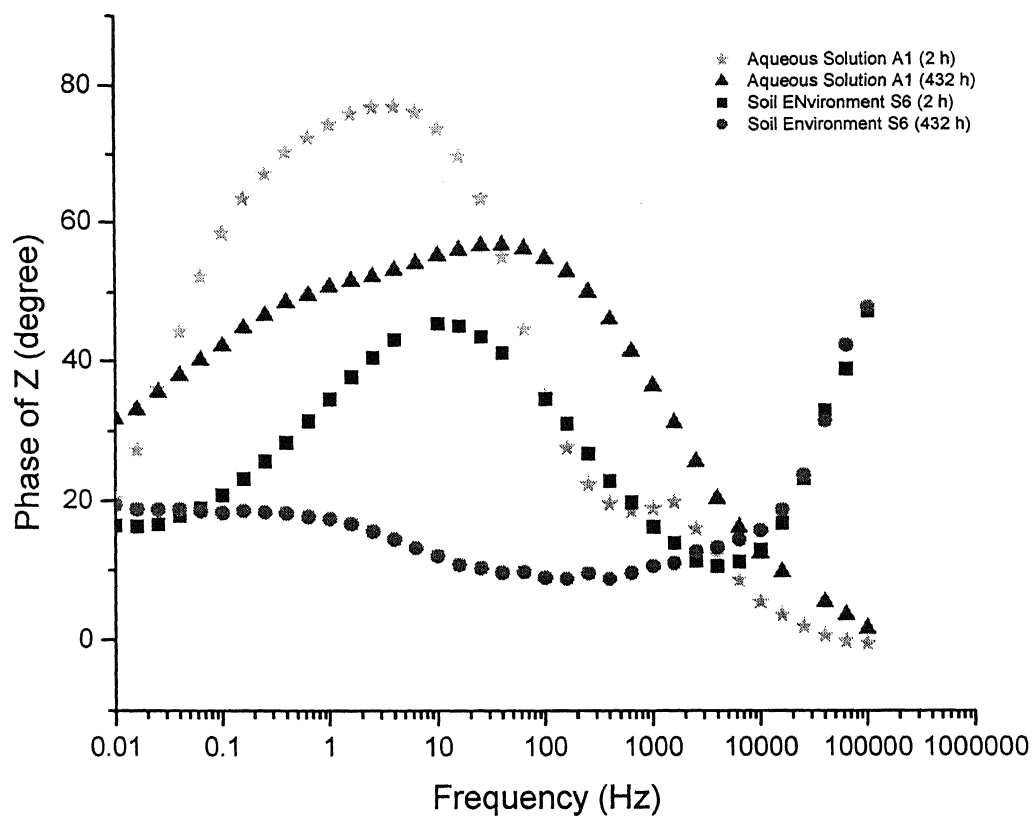


**Fig. 123** Comparison of Bode Phase plots obtained after immersion in aqueous solution A1 and soil environment S6.

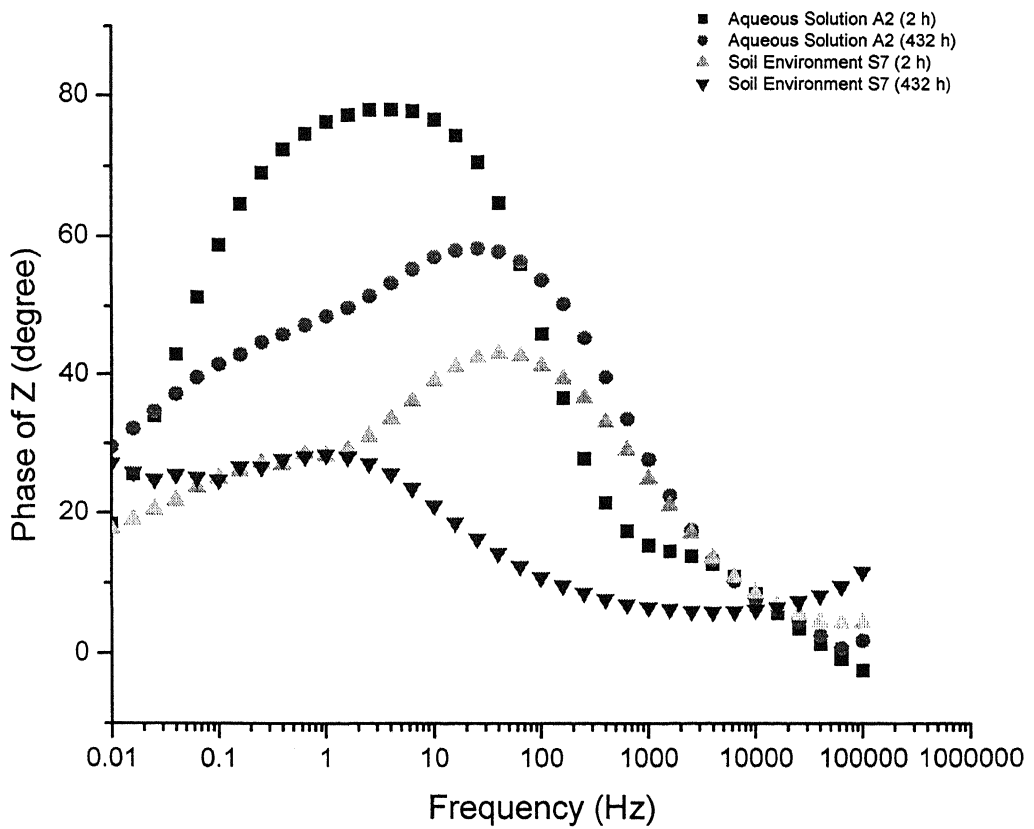


**Fig. 124** Comparison of Bode Phase plots obtained after immersion in aqueous solution A2 and soil environment S7.

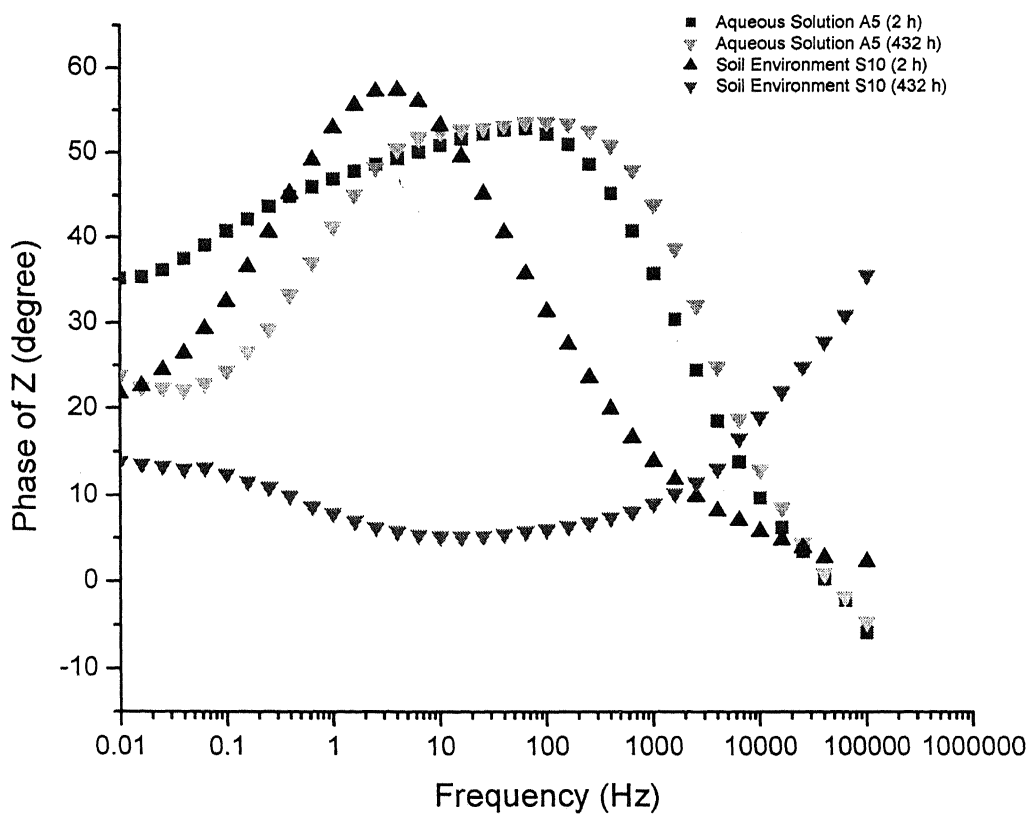
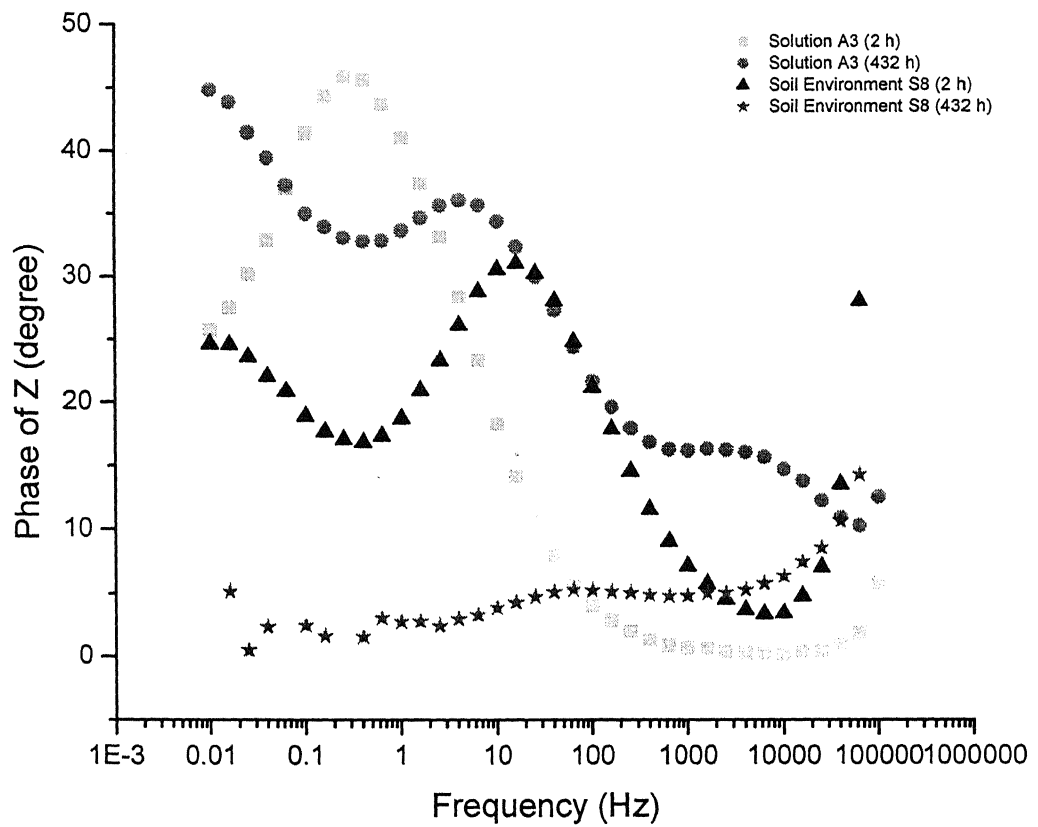
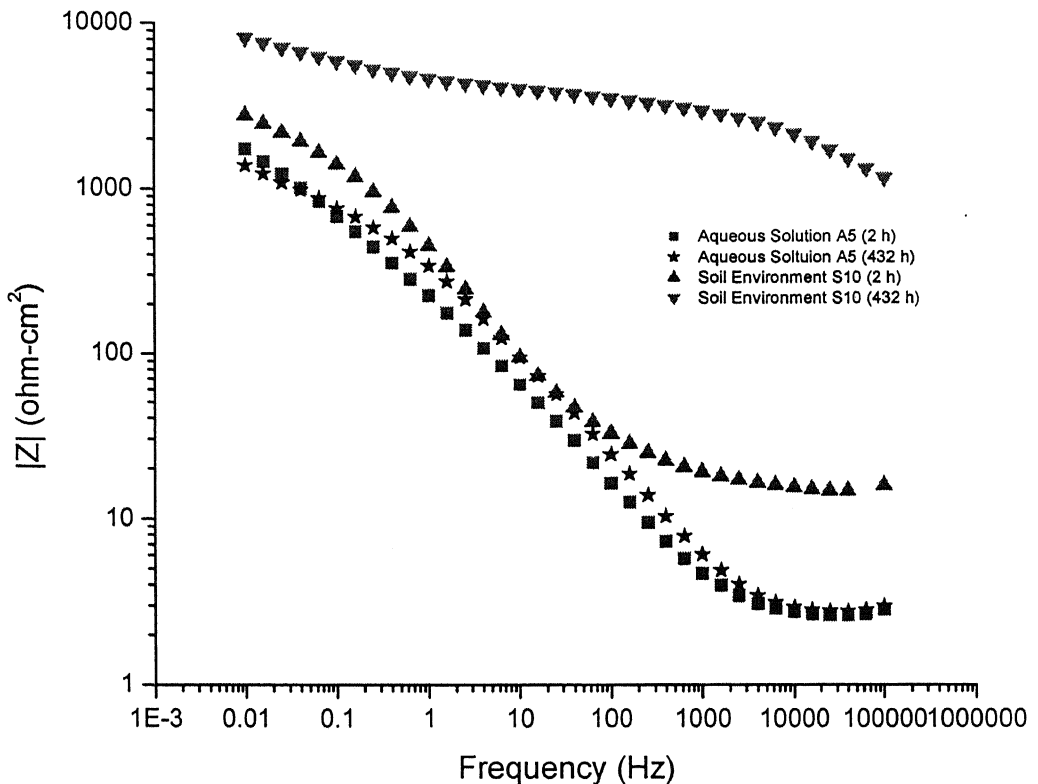


Fig. 125 Comparison of Bode Phase plots obtained after immersion in aqueous solution A5 and soil environment S10.



**Fig. 126** Comparison of Bode Phase plots obtained after immersion in aqueous solution A3 and soil environment S8.



**Fig. 127** Comparison of Bode magnitude plots obtained after immersion in aqueous solution A5 and soil environment S10.

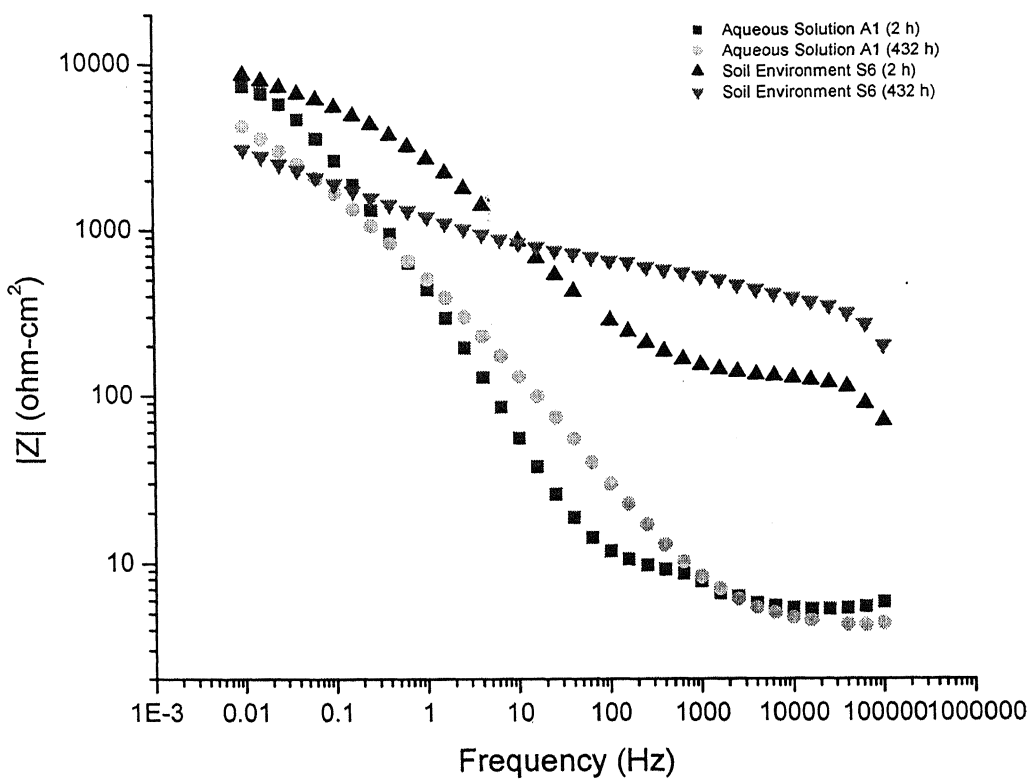


**Fig. 128** Comparison of Bode magnitude plots obtained after immersion in aqueous solution A1 and soil environment S6.

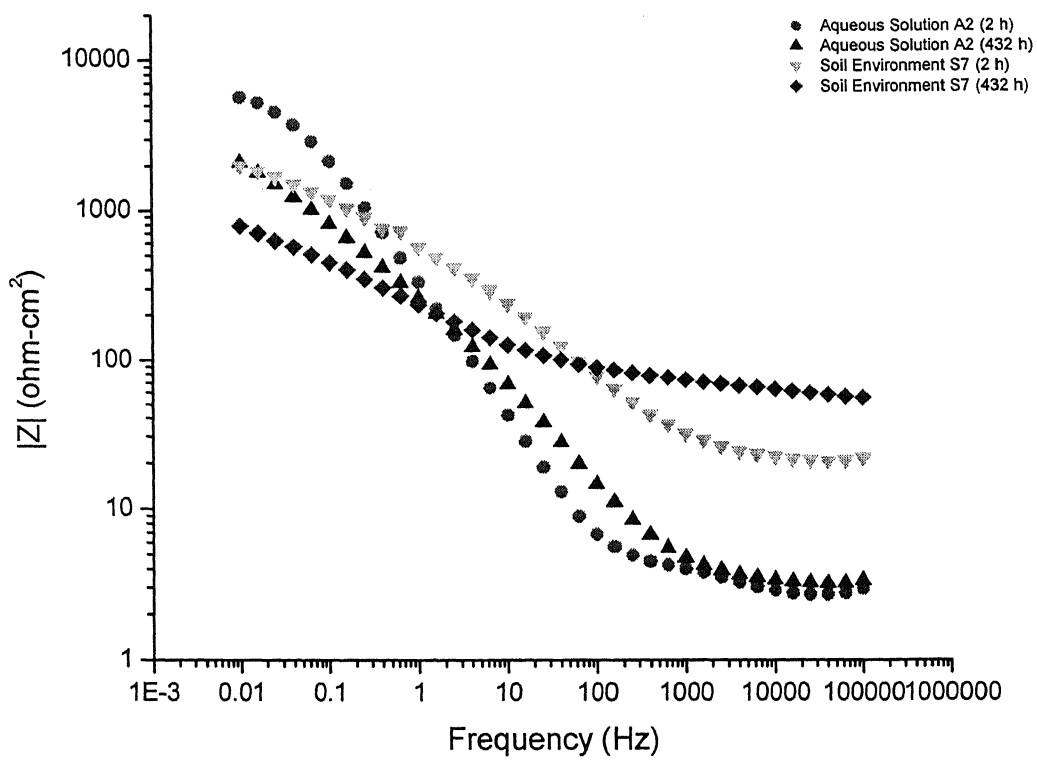


**Fig. 129** Comparison of Bode magnitude plots obtained after immersion in aqueous solution A2 and soil environment S7.

The magnitude of impedance at flat portion of the Bode magnitude plot (slope~0), present in high frequency region provides the value of solution resistance. Generally the NaCl containing soil environments revealed high solution resistance as compared to aqueous solutions of same compositions (Figs. 127-129). NaCl improved the conductivity of soil, therefore the ion mobility increased in presence of NaCl in soil environments. Medium should remain conductive for occurrence of any electrochemical reaction.

### SUMMARY

#### 5.1 Conclusions

The nature of corrosion products on two Chalcolithic archaeological copper samples have been characterized using XRD. The outer regions of the surface film on these coppers were composed primarily of sulphate while the inner region (near the metal-scale interface) was composed of cuprite. Ancient Indian coppers are electrochemically similar to modern copper. As ancient Indian coppers are fairly well preserved in soil conditions, a beneficial effect of studying ancient Indian copper will be the serious consideration of selecting copper as the material of construction of long-term underground storage of nuclear waste. Characterization of surface patina on archaeological copper objects help in understanding long-term corrosion mechanisms and validation of theoretical models for predicting long-term corrosion.

The electrochemical behavior of pure copper in different aqueous and soil environments was studied using linear polarization and electrochemical impedance spectroscopy (EIS) techniques. Linear polarization data was collected after 2 hours and 432 hours of immersion in soil and aqueous environments. Electrochemical impedance spectroscopy studies were conducted both in aqueous and soil environments at free corrosion potential (FCP), for long immersion times. The EIS data was recorded after immersion time of 2, 24, 48, 72, 96, 168, 240, 312 and 432 hours respectively in aqueous and soil environments. The various types of pollutants used in the environment were chloride ( $\text{NaCl}$ ), sulfide ( $\text{Na}_2\text{S}$ ) and ammonium ions ( $\text{NH}_4\text{Cl}$ ). After 432 hours of immersion in aqueous and soil environments the surface of copper samples were carefully observed using SEM to understand the evolution and morphology of the surface films formed on copper in respective environments. All the results were then analyzed in detail. The following are the salient conclusions of the study:

1. On comparing the SEM micrographs obtained from immersion in different environments, it was found that wherever chloride ion was present in the environment, it resulted in breakage of the surface layer after 432 hours of

immersion. When there was no  $\text{Cl}^-$  or when present in very low concentration (as in A4) the surface layer was thin and moreover not adherent to substrate in aqueous solutions. Moreover the penetration during corrosive attack was not deep in absence of chloride in soil and aqueous environments.

SEM studies further suggested that morphology and growth of surface films obtained in aqueous solutions was different than soil environments in most of the cases. The corrosive attack in the soil environments was not homogeneous as was found in aqueous solutions. The damaging effect of chloride ions was more pronounced in case of aqueous solutions than soil environments, as the surface layer obtained after 432 hours of immersion in solution A1 was more cracked and brittle as compared to surface obtained from soil S6 for the same time of immersion.

Local compositional analysis in the SEM confirmed that in most of the cases, the surface film formed was copper oxide. It was porous in nature. Copper chloride was also present locally at some places on the surface of the samples that were immersed in chloride environments.

2. Generally, the free corrosion potential (FCP) moved towards the noble direction in most of the cases, indicating the formation of surface film on the surface. The FCP remained fairly constant after a few days of immersion in all the cases.

In the aqueous solutions that contained NaCl (e.g. A1, A2 and A5), the FCP stabilized at more active potentials compared to the other solutions. It would indicate that the chloride ions from NaCl destabilizes the surface film and renders the surface more active. In the case of solutions containing only  $\text{Na}_2\text{S}$  and  $\text{NH}_4\text{Cl}$ , the FCP stabilized at much nobler potentials compared to other solutions. At the end of 432 hours of immersion, the FCP in the case of solution A3 was nobler indicating that sulfide ions were less damaging to the surface compared to chloride ions in aqueous solutions.

FCP data in soil environments suggested that FCP shifted to active potentials with increasing moisture content in soil. It was also found that copper, in soil environments containing NaCl, showed more active potentials as compared to other soil environments. This could be due to damaging effect of chloride ions. The most active potential was attained for copper immersed in 5 wt% NaCl soil and therefore

the damaging role of NaCl presence was brought out. In case of soils containing only Na<sub>2</sub>S and NH<sub>4</sub>Cl, the potentials were nobler as compared to other soil environments having same moisture (20 wt%) content.

FCP attained a steady value relatively faster in aqueous environments, which indicates that electrochemical reaction on the surface reach equilibrium faster in aqueous solutions than soil environments. The damaging effect of chloride was more in aqueous solutions than soil due to high conductivity and mobility of chloride ions in aqueous solutions than soil. Similarly, the less protective nature of surface films in presence of S<sup>2-</sup> and NH<sub>4</sub><sup>+</sup> ions in soil environment could be explained due to low conductivity of soil.

3. Linear polarization data after 432 hours of immersion in aqueous solutions suggested that solution containing only Na<sub>2</sub>S was beneficial for corrosion resistance whereas the presence of chloride ions generally lowered the corrosion resistance. With increasing amount of chloride ions the corrosion resistance decreased. The drastic increase in corrosion resistance after immersion in Na<sub>2</sub>S containing solution (i.e. A3) should be noted.

Presence of chloride ions in soil experiments (S6 and S7) lowered the corrosion resistance and also with increasing amount of chloride in soil the polarization resistance decreased. Na<sub>2</sub>S appeared to increase corrosion resistance after 432 hours of immersion in absence of chloride. The polarization resistance was lowest for aqueous solution possessing NaCl and NH<sub>4</sub>Cl after long term immersion.

Comparison of linear polarization data for aqueous solution A3 and soil environment S8 indicated beneficial role of sulfide ions in the aqueous solutions, when chloride was not present. Moreover, protective nature of the surface film formed in presence of sulphide ions was higher in case of aqueous solution A3. The damaging role of chloride ions was predominant in aqueous solutions.

4. Comparison of Nyquist plots of aqueous solutions indicated that the solution containing sulfide ions (A3) was relatively less corrosive compared to the cases where chloride ions were present. The nature of Bode phase plots indicated the porous nature of the film for aqueous and soil environments. The capacitive nature of the films was higher in chloride containing aqueous environments. It was revealed

from the Bode magnitude plots that the impedance at lowest frequency decreased with increase of chloride content in aqueous environments.

EIS data was modeled using  $R(Q(R(QR)))$  circuit for all the environments except for aqueous solution A3, where Warburg impedance was also included. Only for this case, the EIS data was modeled using  $R(Q(R(Q(RW))))$  circuit, after 7<sup>th</sup> day of immersion.

Variation of circuit parameters for aqueous solutions with time suggested that among all aqueous solutions, capacitive nature of surface film formed in solution A5 was highest and fairly constant with time. In NaCl containing solutions (A1, A2 and A5), film thickness did not change significantly with time. Film resistance obtained for films formed in all the solutions, except A5, attained a nearly same value after 432 hours of immersion. The film resistance was lowest for the surface film obtained in solution A5. Capacitive behavior of double layer decreased sharply for most of the cases after 432 hours of immersion. This is attributed to the surface roughness of the exposed metal and it also indicated that due to localized attack, exposed metal surface was very rough. Double layer capacitance was lower in chloride containing solutions. It indicated that metal surface was relatively rough in presence of chloride. Charge transfer resistance was low for chloride containing solutions, and among them it was lowest for A5. For solution A5, the properties of the surface film were nearly constant with time, and no drastic change could be noted as the values of the circuit parameters were fairly constant with time.

The variation of Damage Function with time suggested the benign role of sulfide ions and the damaging role of chloride ions in different aqueous solutions.

The diameter of the arc in chloride soil environments generally decreased after 432 hours of immersion (S6 and S7), indicating that corrosion resistance decreased. Capacitive behavior of the surface film decreased in most of the cases as the phase angle in the middle frequency range dropped after long term immersion. The nature of Bode phase plots indirectly shows the porous nature of the film. A decrease in total impedance was noticed from Bode magnitude plots in soil environments S6 and S7. Due to presence of damaging chloride ions in soil

environments S6 and S7 the impedance decreased significantly, leading to decrease in corrosion resistance.

## **5.2 Suggestions for future work**

Some additional work, which may be undertaken in order to resolve certain issues raised in this thesis, are listed below.

1. Soil experiments could be conducted in slurry environments. Moisture content should be maintained constant for long term immersion experiments in slurry.
2. A better mixing mechanism (instead of manual mixing) should be used for mixing additives (NaCl, Na<sub>2</sub>S and NH<sub>4</sub>Cl) in soil.
3. In-situ site testing under the soil should be performed for more practical results and samples should be exposed for longer times (e.g. one or two years).
4. Resistivity of soil should also be taken as a parameter for conducting experiments.
5. Some microorganisms could also be introduced for conducting experiments in soil environment, as microorganisms play a major role for corrosion in soil environments.
6. In order to study the effect of sulfide, different concentrations of sulfide should be used in experiments. In long term immersion experiments sulfide concentration should be maintained constant by adding additional sulfide on a regular basis, as sulfide oxidizes in presence of oxygen. Sulfide concentration could be maintained constant by maintaining the pH of the electrolyte.
7. Surface films formed in different solutions could also be analyzed by other techniques (like Electron spectroscopy for chemical analysis or ESCA, Auger electron spectroscopy or AES etc.) in order to understand the different phases present in the surface film.
8. Linear polarization experiments could be conducted after shorter intervals of immersion in different soil and aqueous environments.

### **5.3 Sources of error**

1. Non-homogeneous mixing of pollutants in soil environment.
2. The concentration of pollutants (e.g. Na<sub>2</sub>S) should be maintained constant, throughout the immersion period, as sulfide oxidizes in presence of oxygen over the period of time.
3. The moisture content in soil environments should also be maintained constant.
4. Low amount of KCl should be used in luggin capillary tubes, otherwise KCl may contaminate the surface.
5. Distance of the reference electrode with working electrode should be maintained constant in different set of experiments.
6. Soil conductivity.

## REFERENCES

---

1. "ASM Specialty Handbook- Copper and Copper Alloys", ASM International, The Materials Information Society, pp.385-418, 446-448.
2. W. S. Trait, "An Introduction to Electrochemical Corrosion Testing for practicing Engineers and Scientists", Pair O Docs Publications, Racine, Wisconsin, pp 44-45, 53-62, 102, 119.
3. L. O. Werme and P. Sellin 2003 in *Proceedings of the international workshop on prediction of long term corrosion behavior in nuclear waste systems* (Cadarache, France: European Federation of Corrosion), pp 395-411.
4. I. Puigdomenech, *et al.*, 'O<sub>2</sub> depletion in granitic media: the REX project', Technical Report TR-01-05 Svensk Kärnbränslehantering AB, Stockholm, Sweden (2001).
5. "Final storage of spent nuclear fuel". Publication KBS3, Swedish Nuclear Fuel Supply Company (1983).
6. J.P. Simpson, "Experiments on container materials for Swiss high-level waste disposal projects", Part 2, Technical Report 84-01, National Cooperative for the Storage of Radioactive Waste (1984).
7. "ASM Handbook, Corrosion" 13, ASM International, The Materials Information Society, p. 512.
8. J. Kruger, *J. Electrochem. Soc.* 108 (1961), p. 503.
9. S. B. Adelaju, Y. Y Duan, "Corrosion resistance of Cu<sub>2</sub>O and CuO on copper surfaces in aqueous media", *Br. Corros. J.* 29 (1994), pp. 309-314.
10. H. Strandberg, L. G. Johansson, *J. Electrochem. Soc.* 145 (1998), p. 1093.
11. Z. Y. Chen, S. Zakipour, D. Persson, and C. Leygraf, *Corrosion* 60, No. 5, pp.479-491
12. R. F. North and M. J. Pryor, "The influence of corrosion product structure on the corrosion rate of Cu- Ni alloys", *Corrosion Science* 10 (1970), pp. 297-331.
13. F. Richards, *Chemical Oceanography*, Academic Press, New York (1965), p. 611.
14. G. L. Baily, *J. Inst. Metal*, 79 (1951), p. 243.

15. R. B. Niederberger, J. P. Gudas and G. J. Danek, Accelerated corrosion of Cu/Ni alloys in polluted waters, *NACE Corrosion Conf./76*, Houston, Texas (1976), Paper No. 76.
16. H. Hack, Susceptibility of 17 machinery alloys for sulfide induced corrosion in sea water. Report A WFAL-TR-BI-4019 Bethesda, MD, U.S.A. (1980).
17. C. Kato, H. Pickering and J. Cartle, *J. Electrochem. Soc.* 131 (1984), p. 1225.
18. B. C. Syrett, "The mechanism of accelerated corrosion of copper-nickel alloys in sulphide-polluted seawater" *Corrosion Science*, 21 (1981), p. 187.
19. S. Glasstone, *Textbook of Physical Chemistry*, D. Van Nostrand, New York (1940), p.1104.
20. M. R. Hoffman, *Environ. Sci. Technol.* 14 (1980), p. 1061.
21. M. Avrahmi and R. M. Golding, *J. chem.. Soc. (A)*, (1968), p. 647.
22. H. E. Ostland and J. Alexander, *J. geophys Res.* 68 (1963), p. 3995.
23. J. F. Bates and J. M. Popplewell, "Corrosion of condenser tube alloy in sulphide contaminated brine", *Corrosion* 31 (1975), p. 269-275.
24. J. N. Al-Hajji and M. R. Reda, "The corrosion of copper-nickel alloys in sulfide-polluted seawater: The effect of sulfide concentration", *Corrosion Science* 34 (1993), No. 1, pp. 163-177.
25. S. R. DE Sanchez and D. J. Schiffrrin, "The flow corrosion mechanism of copper base alloys in sea water in the presence of sulphide contamination", *Corrosion Science* 22 (1982) No. 6, pp. 585-607.
26. Awani P. Patil, "Corrosion behavior of some Cu-Ni-Zn-Mn alloys in seawater", PhD Thesis (2004), VNIT Nagpur.
27. J. P. Gudas and H. P. Hack, *Corrosion* 35, (1979), p. 67.
28. B. C. Syrett, D. D. Macdonald and S. S. Wing, *Corrosion* 35, (1979), p. 409.
29. B. C. Syrett, "Accelerated corrosion of copper in flowing pure water contaminated with oxygen and sulfide", *Corrosion* 33 (1977), pp. 257-262.
30. E. D. Mor and Anna Maria Beccaria, *Br. Corros. J.* 10 (1975), p. 33.
31. D. D. Macdonald, B. C. Syrett and S. S. Wing, *Corrosion* 35 (1979), p. 367.

32. L. E. Eiselstein, B. C. Syrett, S. S. Wing and R. D. Caligiuri, "The accelerated corrosion of Cu-Ni alloys in sulphide-polluted seawater: Mechanism 2", *Corrosion Science* 23 (1983), pp. 223-239.

33. P. Bolmer, *Corrosion* 21 (1965), p. 69.

34. H. Kaesche, *Werkst. Korros.* 21 (1970), p. 185.

35. N. Hackermann and A. Makrides, *Ind. Engng Chem.* 46 (1954), p. 523.

36. Z. A. Iofa, *Zashch. Met.* 6, (1970), p. 491.

37. V. F. Panaseko, Candidates Dissertation, Polytekhn., Inst., Kiev (1972).

38. A. Al-Hashem, J. Carew, *Desalination* 150 (2002), pp. 255-262.

39. T. P. Hoar, J. J. Podesta and G. P. Rothwell, "Reactions of Cu and brasses in ammonical sulphate solutions", *Corrosion Science* 11 (1971), pp. 231-239.

40. J. M. Steigerwald, S. P. Murarka, R. J. Gutmann, D. J. Duquette, *Materials Chemistry and Physics*, 41 (1995), pp. 217-228.

41. T. N. Rhodin, *J. Am. Chem. Soc.* 73 (1951), p. 3143.

42. M. A. Heine and M. J. Pryor, *J. Electrochem. Soc.* 110 (1963), p. 1205.

43. J. Kruger, *J. Electrochem. Soc.* 106 (1959), p. 847.

44. E. Mattson, *Brit. Corros. J.*, 15 (1980), pp 6-13.

45. Pierre R. Roberge, "Handbook of Corrosion Engineering", McGraw Hill Publications, pp 142-155.

46. K. R. Trethewey and J. Chamberlain, *Corrosion for Students of Science and Engineering*, John Wiley & Sons, Inc., New York (1988).

47. D. A. Jones, *Principles and Prevention of Corrosion*, Maxwell Macmillan International Editions, NY (1992), pp. 7, 75-97.

48. M. G. Fontana and N.D. Greene, *Corrosion Engineering*, McGraw-Hill International Book Company, 2<sup>nd</sup> edition (1983).

49. A.V. Oppenheim and A.S. Willsky, "Signals and Systems," Prentice-Hall (1983).

50. J.R. Scully, D.C. Silverman, and M.W. Kendig, "Electrochemical Impedance: Analysis and Interpretation," ASTM (1993).

51. Cottis and Stephen Turgoose, "Electrochemical Impedance and Noise," Robert NACE International, 1440 South Creek Drive, Houston, TX 77084-4906.

52. J. R. Macdonald, "Impedance Spectroscopy- emphasizing solid materials and Systems," John Wiley & Sons, New York.

53. J.A.L. Dobbelaar, "The Use of Impedance Measurements in Corrosion Research; The Corrosion Behavior of Chromium and Iron Chromium Alloys," PhD thesis TU-Delft (1990).

54. C. Gabrielle, "Identification of Electrochemical Processes by Frequency Response Analysis," Solartron Instrumentation Group, (1980).

55. S. Gudic, J. Radosevic, M. Kliskic, "Study of passivation of Al and Al-Sn alloys in borate buffer solutions using electrochemical impedance spectroscopy," *Electrochimica Acta*, 47 (2002), pp. 3009-3016.

56. Robert G. Kelly, John R. Scully, David W. Shoesmith, Rudolph G. Buchheit, "Electrochemical Techniques in Corrosion Science and Engineering", Marcel Dekkar, Inc., pp 223-231, 293, 296-299, 317.

57. D. David, C. Lemaitre and D. Crusset 2003 in *Proceedings of the international workshop on prediction of long term corrosion behavior in nuclear waste systems* (Cadarache, France: European Federation of Corrosion), pp 241-259.

58. R. Balasubramaniam, "Archaeometallurgy of ancient Indian copper", *Trans. Indian Inst. Met.* 57 (2004) 4 (Article in Press).

59. R. Balasubramaniam, *Delhi Iron Pillar: New insights*, Indian Institute of Advanced Study, Shimla (2002).

60. R. Balasubramaniam, "The protective passive film of the Delhi Iron Pillar", *Bulletin of Metals Museum* 34 (2001), p. 64.

61. M. Bojinov, J. Hinttala, P. Kinnunen, T. Laitinen, C. Lilja, K. Mäkelä, and T. Saario, "Approaches chosen to predict the effect of different forms of corrosion on copper in disposal conditions of spent fuel", *ibid.*, pp. 62-72.

62. B. Rosborg, O. Karnland, G. Quirk, and L. Werme, "Measurements of copper corrosion in the LOT project at the Äspö Hard Rock Laboratory", *ibid.*, pp. 412-423.

63. V. N. Misra, V. Shinde, R. K. Mohanty, K. Dalal, A. Mishra, L. Pandey and J. Kharakwal, *Man and Environment* 20 (1995), p. 57.

64. V. N. Misra, V. Shinde, R. K. Mohanty, L. Pandey and J. Kharakwal, *Man and Environment* 32 (1997), p. 35.

65. W. John Williams, "Handbook of Anion Determination", Butterworth & Co. (Publishers) Ltd. (1979), pp. 296-297.

66. Louis Meites, "Handbook of Analytical Chemistry", McGraw-Hill Book Company, Inc., pp. 3-51.

67. Metals Test Methods and Analytical Procedures, "Annual Book of ASTM Standard", ASTM, Philadelphia, USA, 03.02, Section 3 (1999), p. 58.

68. A. Srivastava, and R. Balasubramaniam, "Material characterization of ancient Indian copper", *Bulletin of Material Science* 26 (2003) 6, pp. 593-600.

69. A. Srivastava, R. Balasubramaniam, and V. N. Misra, "Metallurgical investigations on a chalcolithic copper nail from Balathal," *Man and Environment* 28 (2003), p. 33.

70. C. Leygraf and T. Graedel, *Atmospheric corrosion* (New York: Wiley-Interscience) (2000), pp 140–148, 269-280.

71. F. L. LaQue, *Marine Corrosion-causes and Prevention*, John Wiley, New York (1975), p. 146.

72. G. Wranglen, "Review Article on the influence of Sulphide Inclusions on the Corrodibility of Fe and Steel", *Corrosion Science* 9 (1969), p. 585.

73. B. D. Cullity, "Elements of X-Ray Diffraction", Addison-Wesley Publishing Company Inc. (1967), pp 388-396.

74. N.D. Tomashov and G.P. Chernova, "Passivity and Protection of Metals against Corrosion," Plenum Press, USA (1967), pp. 14-28.

75. U. Rammelt and G. Reinhard, "On the applicability of a constant phase element (CPE) to the estimation of roughness of solid metal electrodes", *Electrochimica Acta*, 35, (1990) 6, pp. 1045-1049.

76. G. Moretti, F. Guidi, G. Grion, "Tryptamine as green iron corrosion inhibitor in 0.5 M deaerated sulphuric acid," *Corrosion Science* 46 (2004), pp. 387- 403.

77. J.E.G Gonzalez, J.C. Mirza-Rosca, "Study of the corrosion behavior of titanium and some of its alloys for biomedical and dental implant applications," *J. of Electroanalytical chemistry* 471 (1999), pp. 109- 115.

78. V. Moutarlier, M.P. Gigandet, B. Normand, J. Pagetti, "EIS characterisation of anodic films formed on 2024 aluminium alloy, in sulphuric acid containing molybdate or permanganate species", *Corrosion Science* (2004) (Article in press).

79. İlyas DEHİRİ, "Impedance Measurement of Polyester-Coated galvanized mild Steel in 10xAcid Rainwater After an Accelerated Wet-Dry Test", *Turk J Chem*, 24 (2000), pp. 239-245.

## APPENDIX A

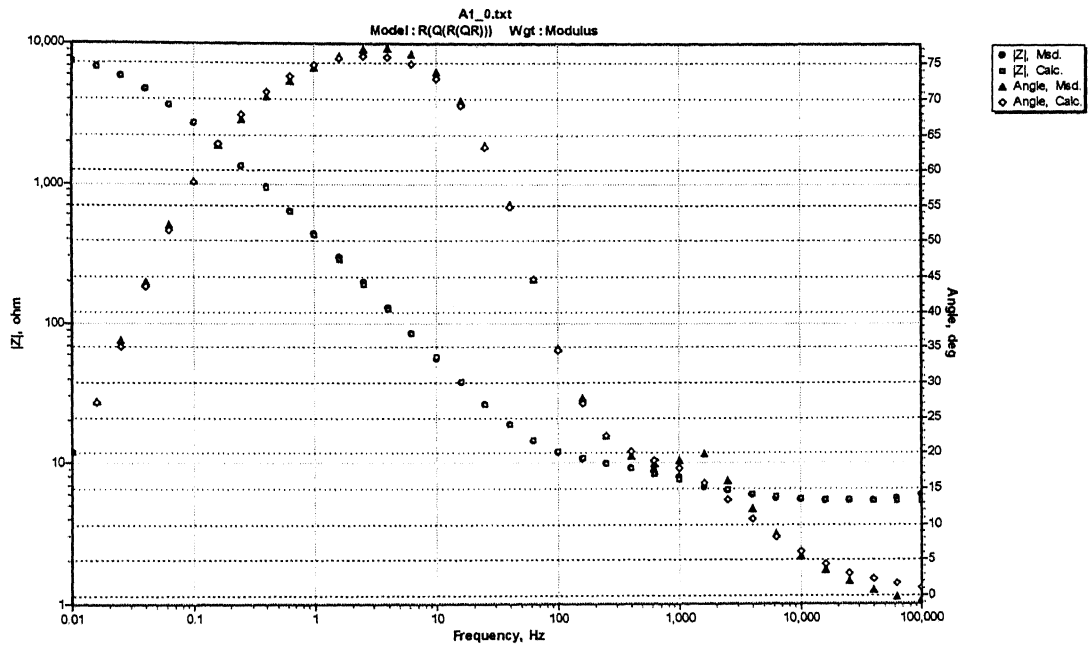


Fig. A-1 Experimental and Simulated Bode Phase and Magnitude plots obtained after 2 hours of immersion in aqueous solution A1.

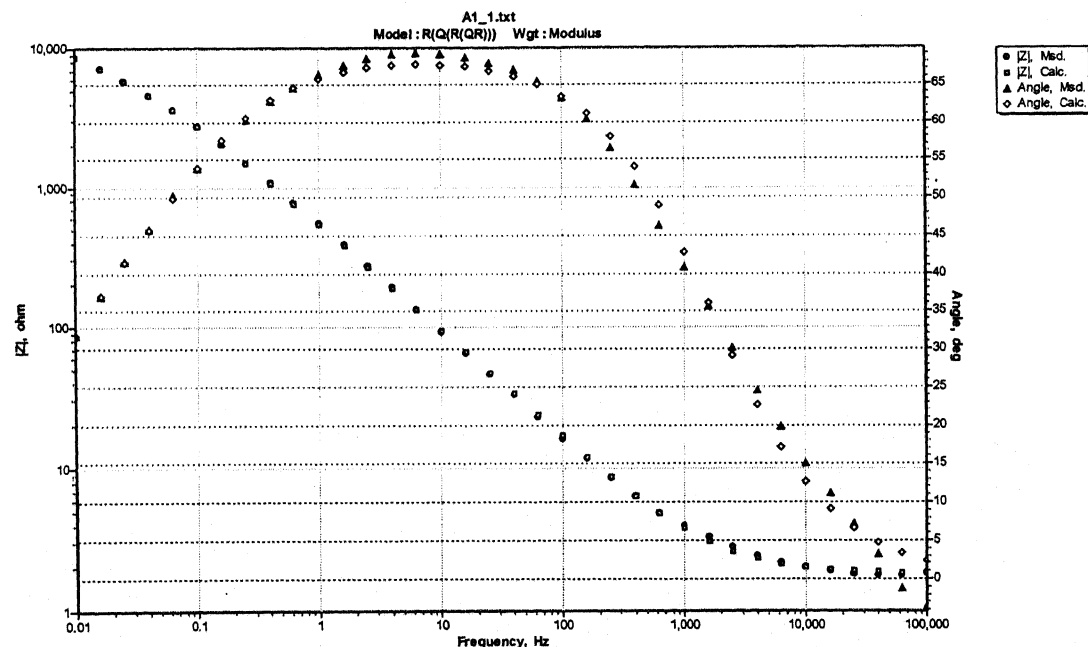


Fig. A-2 Experimental and Simulated Bode Phase and Magnitude plots obtained after 24 hours of immersion in aqueous solution A1.

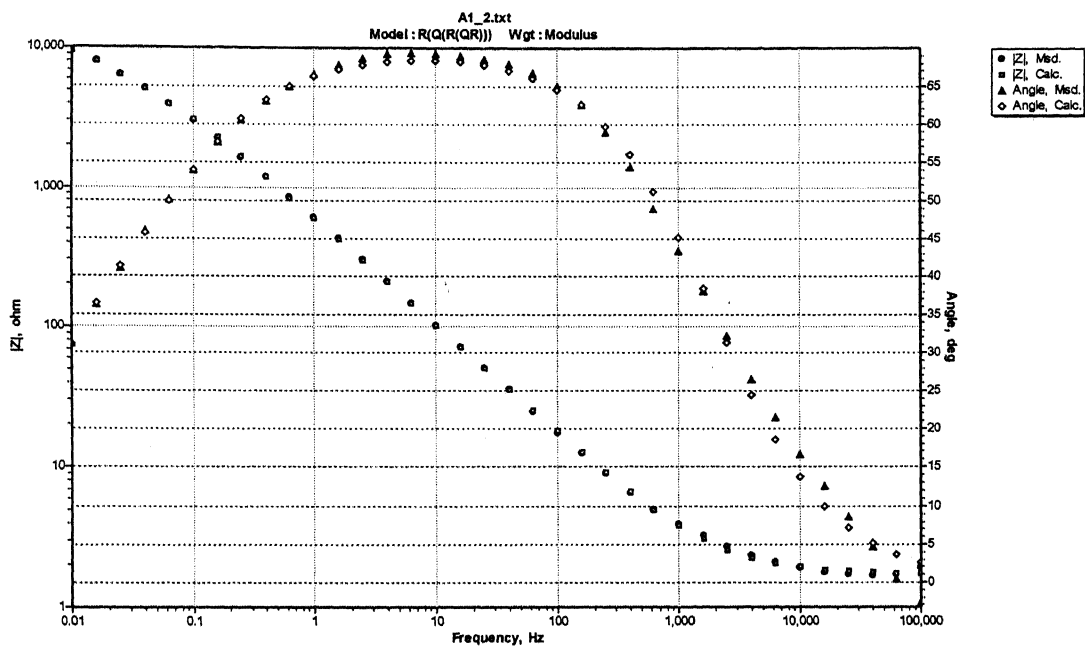


Fig. A-3 Experimental and Simulated Bode Phase and Magnitude plots obtained after 48 hours of immersion in aqueous solution A1.

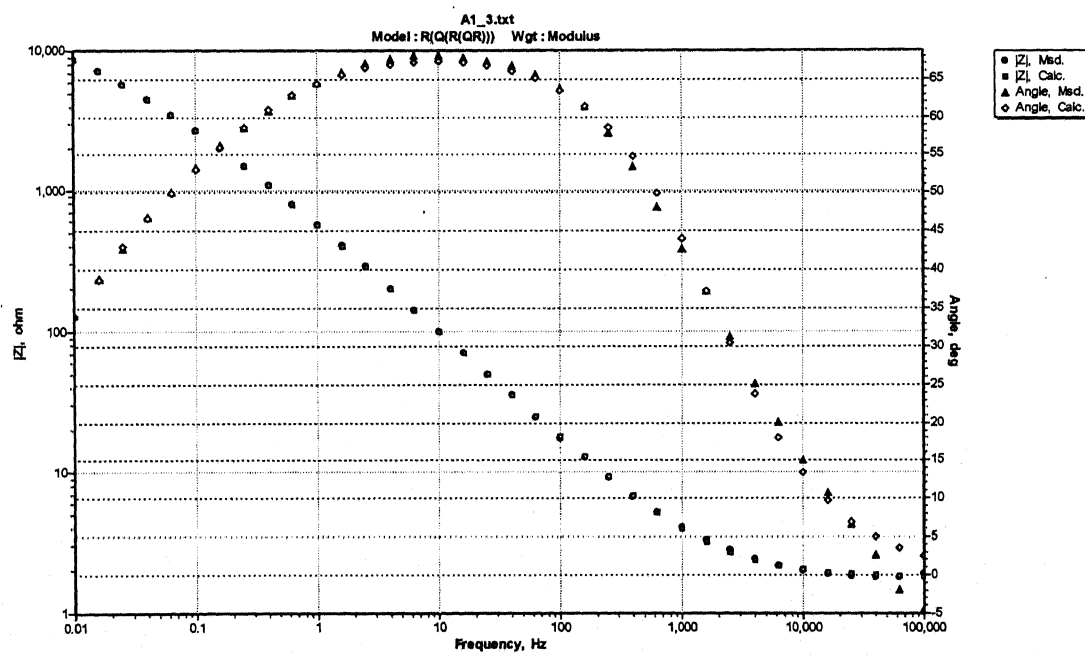


Fig. A-4 Experimental and Simulated Bode Phase and Magnitude plots obtained after 72 hours of immersion in aqueous solution A1.

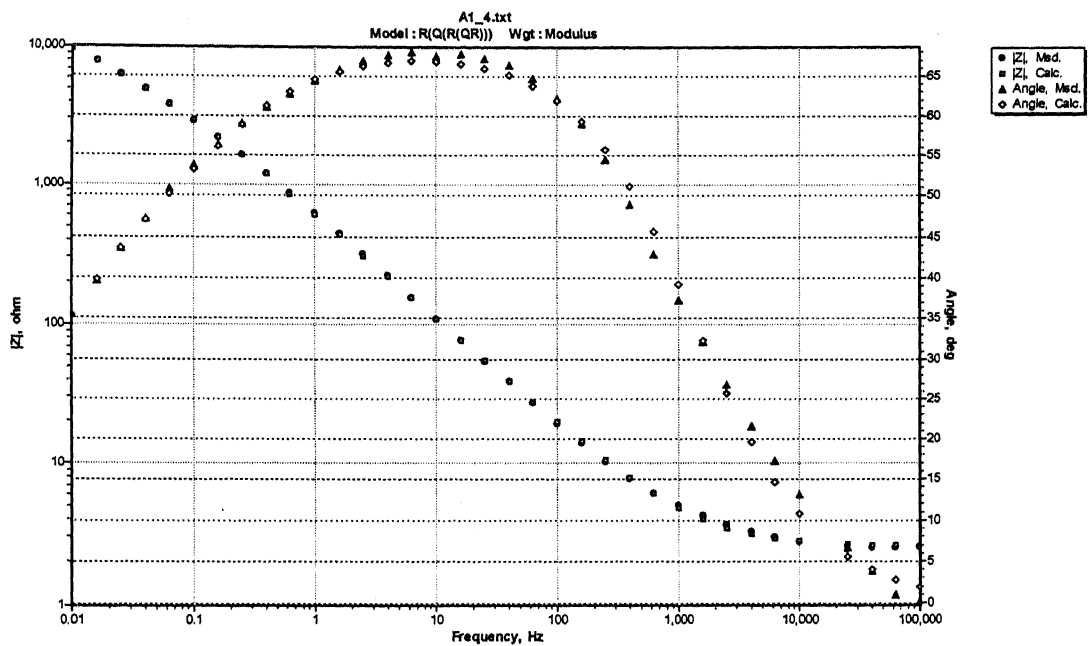


Fig. A-5 Experimental and Simulated Bode Phase and Magnitude plots obtained after 96 hours of immersion in aqueous solution A1.

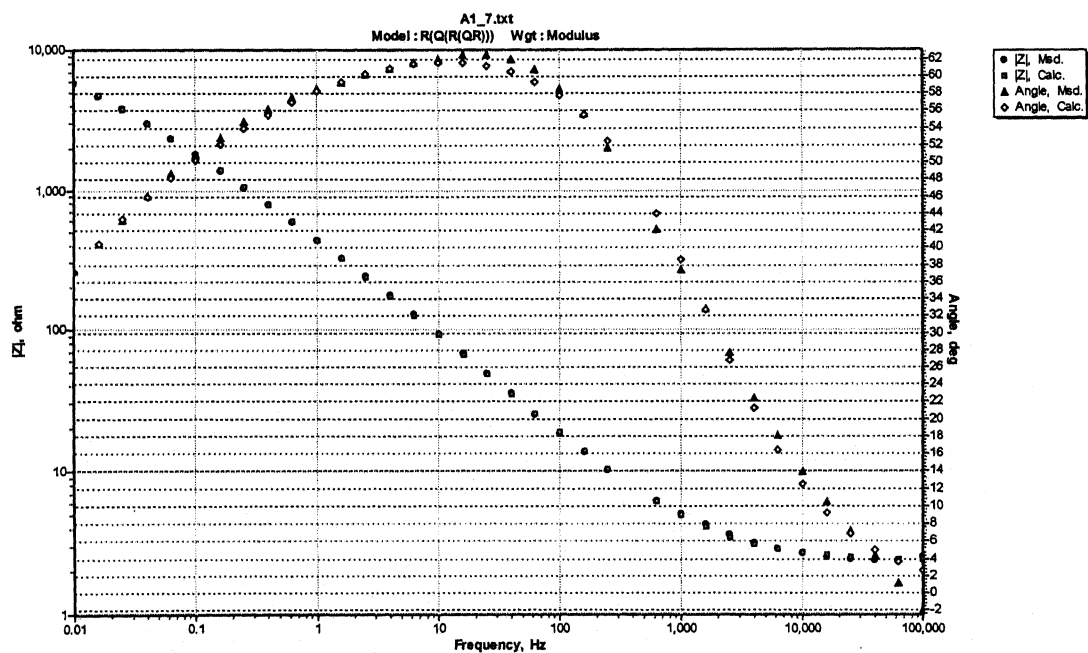


Fig. A-6 Experimental and Simulated Bode Phase and Magnitude plots obtained after 168 hours of immersion in aqueous solution A1.

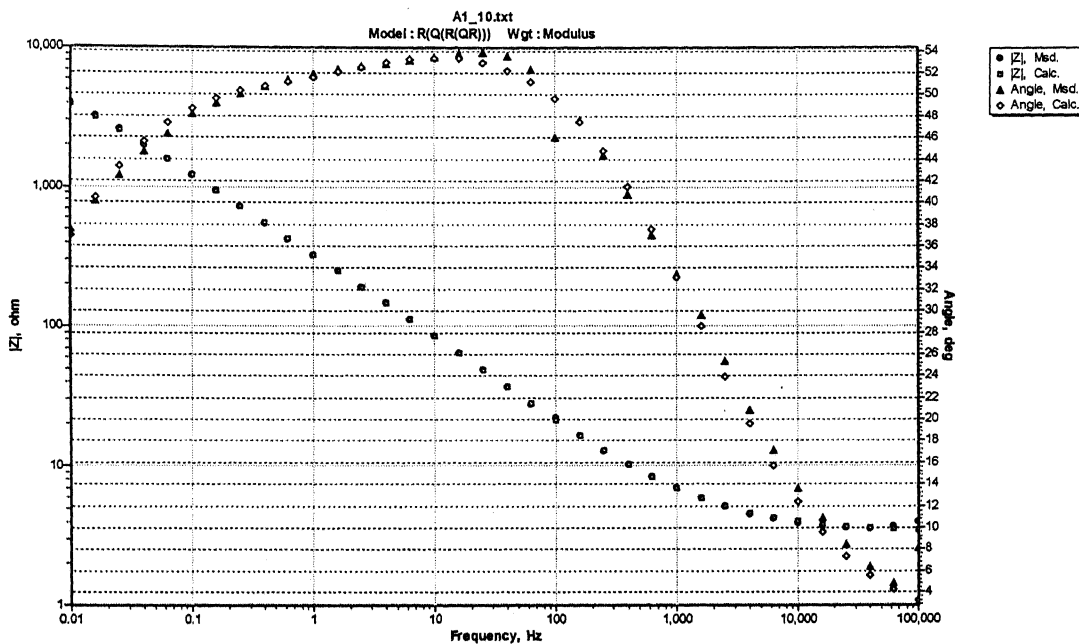


Fig. A-7 Experimental and Simulated Bode Phase and Magnitude plots obtained after 240 hours of immersion in aqueous solution A1.

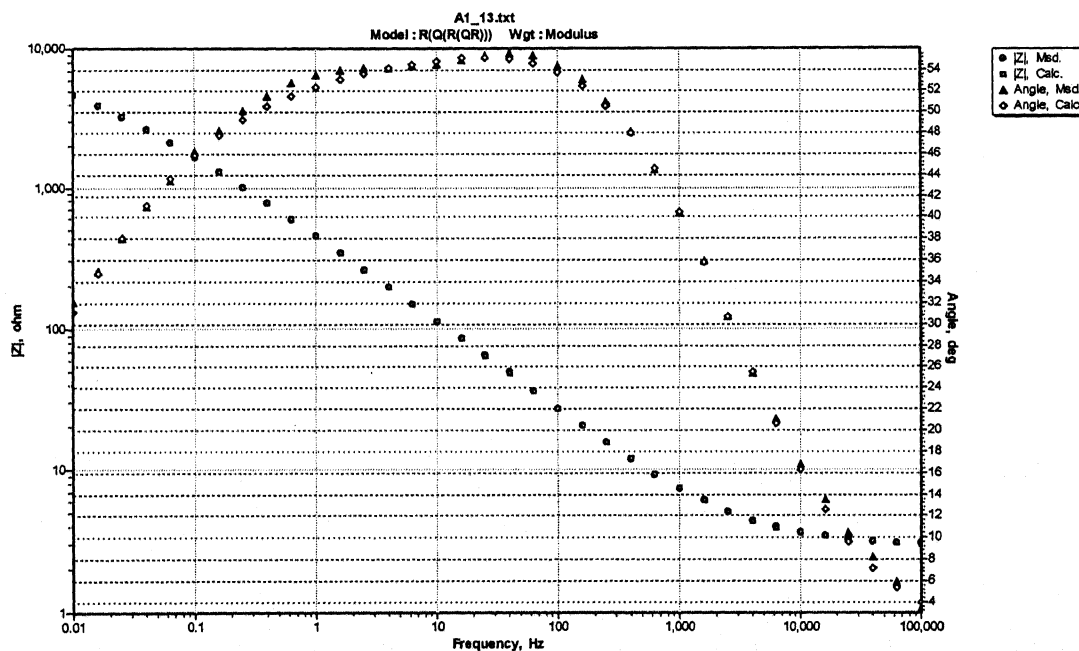


Fig. A-8 Experimental and Simulated Bode Phase and Magnitude plots obtained after 312 hours of immersion in aqueous solution A1.

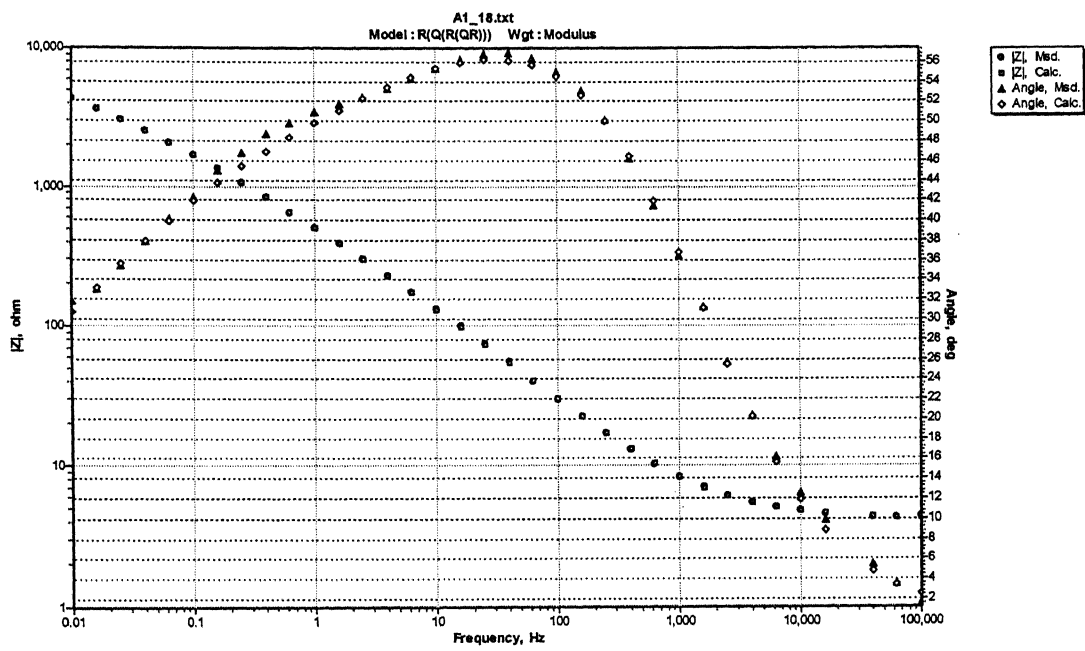


Fig. A-9 Experimental and Simulated Bode Phase and Magnitude plots obtained after 432 hours of immersion in aqueous solution A1.

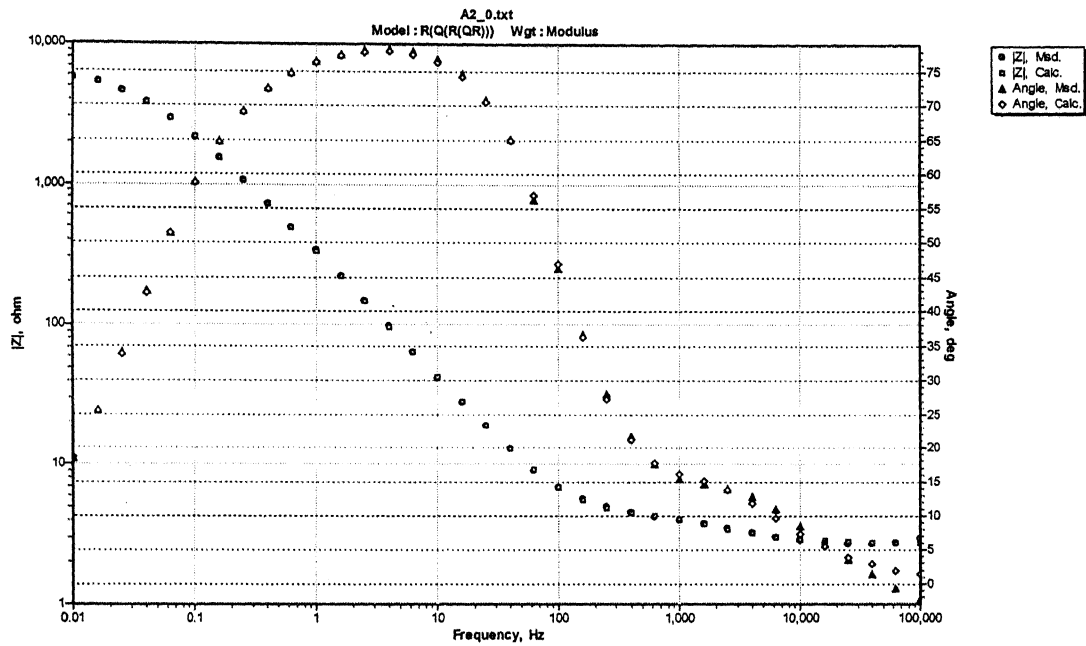


Fig. A-10 Experimental and Simulated Bode Phase and Magnitude plots obtained after 2 hours of immersion in aqueous solution A2.

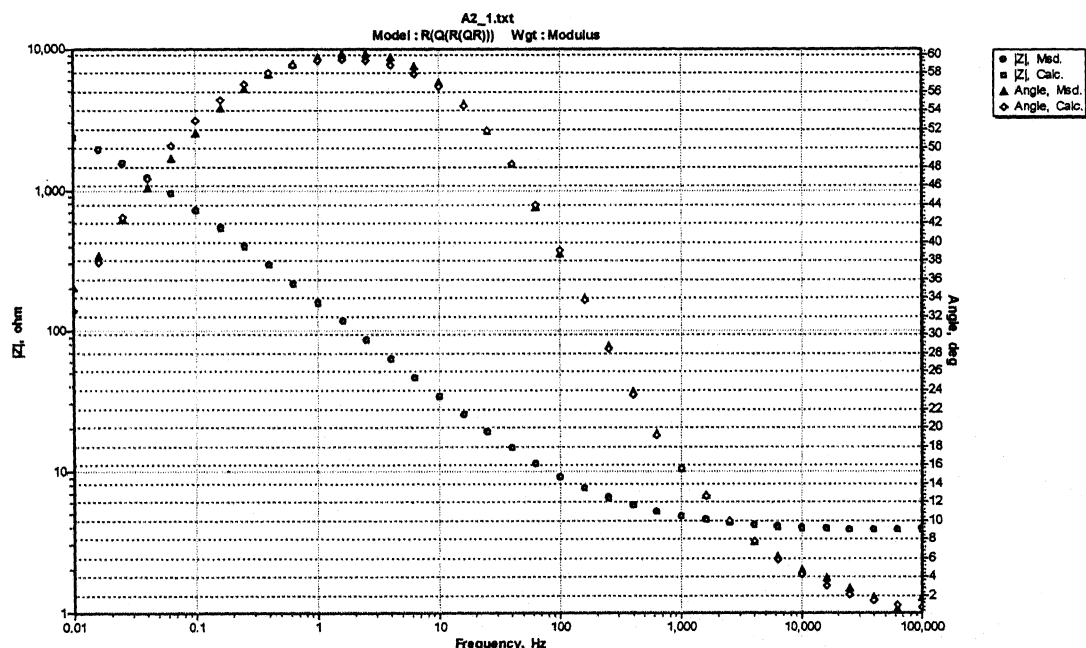


Fig. A-11 Experimental and Simulated Bode Phase and Magnitude plots obtained after 24 hours of immersion in aqueous solution A2.

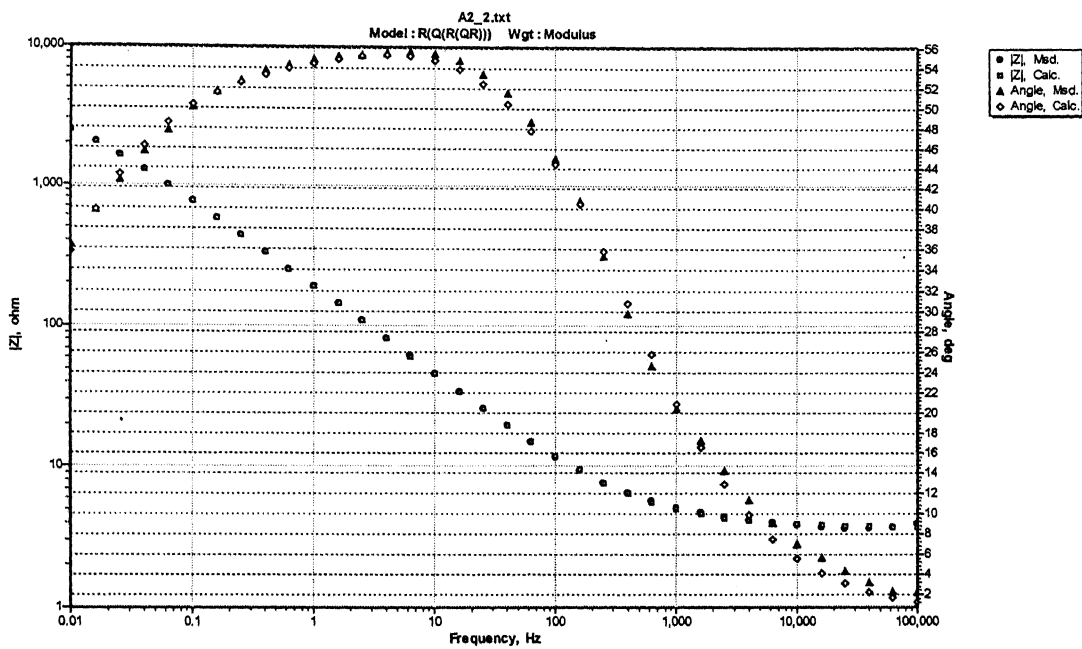


Fig. A-12 Experimental and Simulated Bode Phase and Magnitude plots obtained after 48 hours of immersion in aqueous solution A2.

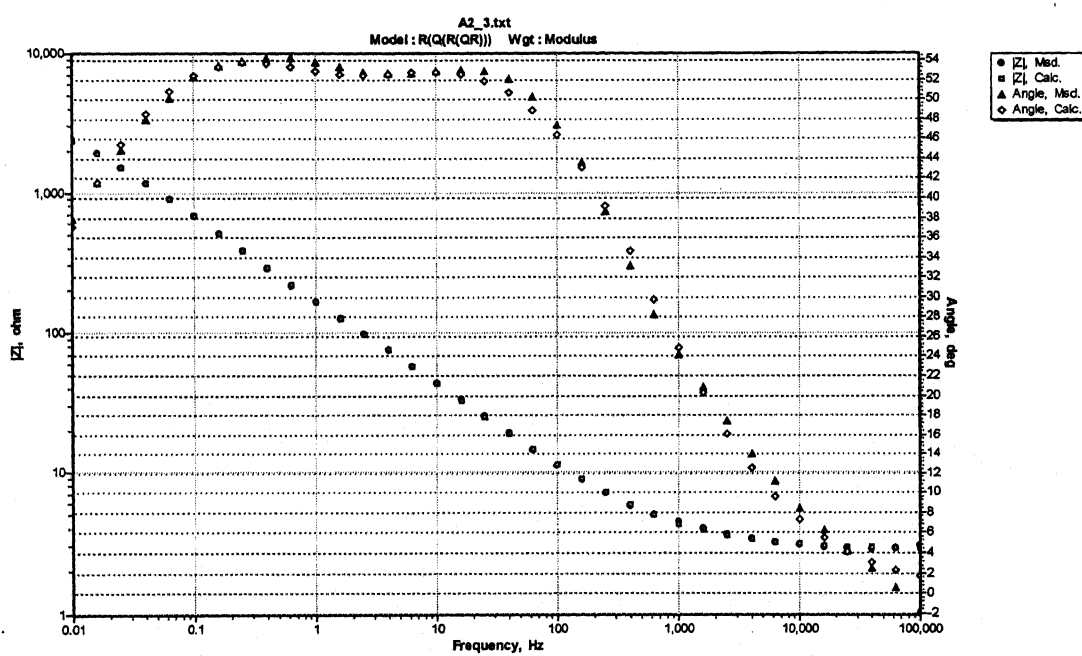


Fig. A-13 Experimental and Simulated Bode Phase and Magnitude plots obtained after 72 hours of immersion in aqueous solution A2.

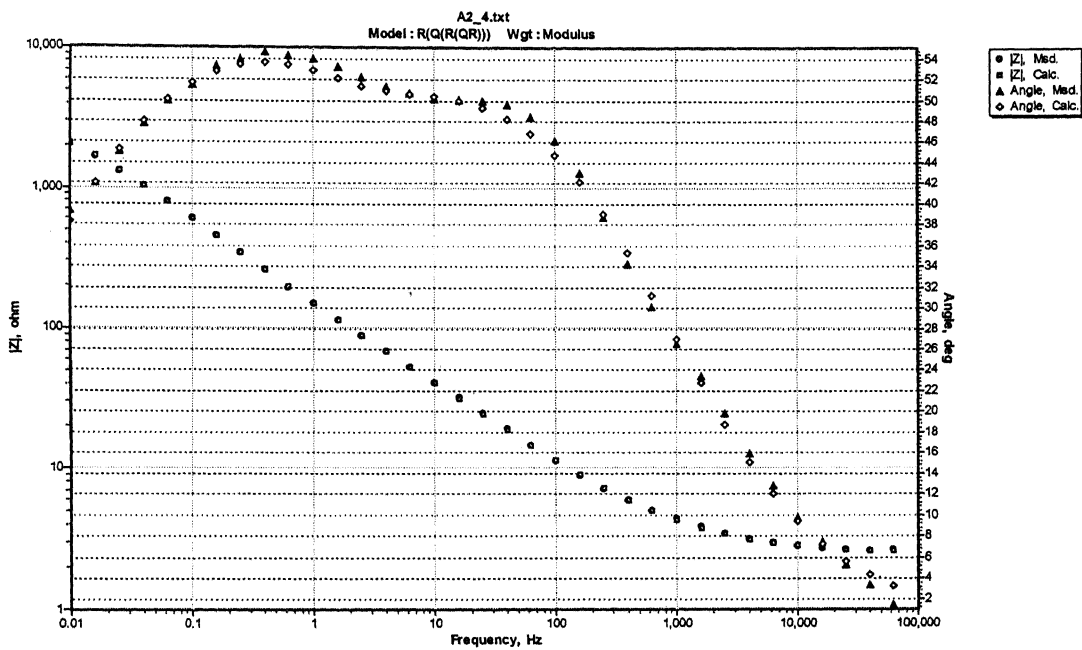


Fig. A-14 Experimental and Simulated Bode Phase and Magnitude plots obtained after 96 hours of immersion in aqueous solution A2.

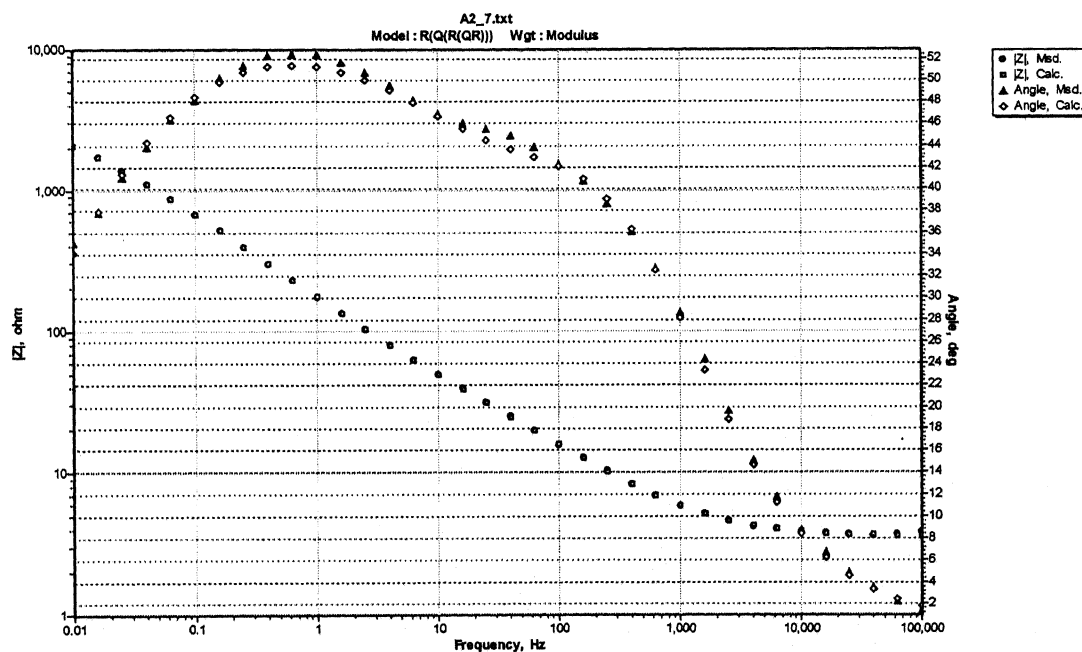


Fig. A-15 Experimental and Simulated Bode Phase and Magnitude plots obtained after 168 hours of immersion in aqueous solution A2.

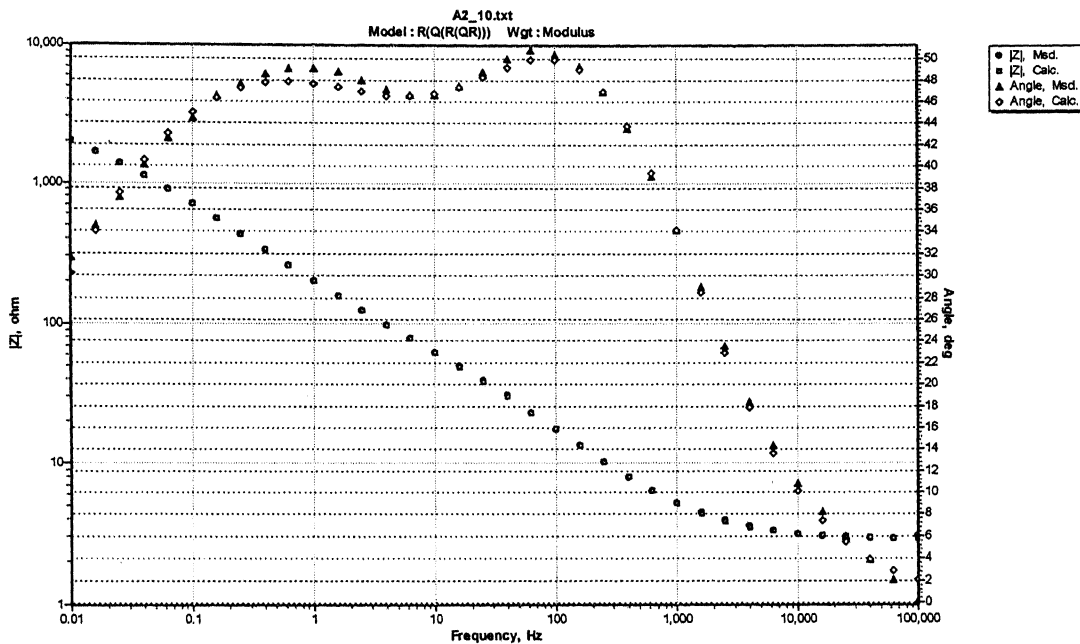


Fig. A-16 Experimental and Simulated Bode Phase and Magnitude plots obtained after 240 hours of immersion in aqueous solution A2.

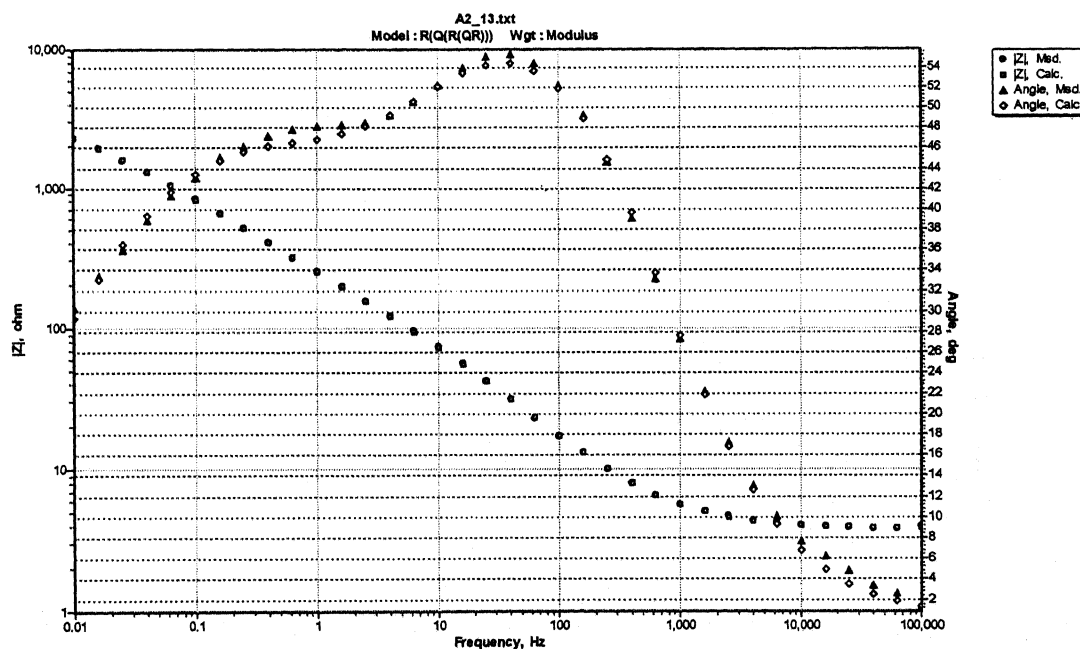


Fig. A-17 Experimental and Simulated Bode Phase and Magnitude plots obtained after 312 hours of immersion in aqueous solution A2.

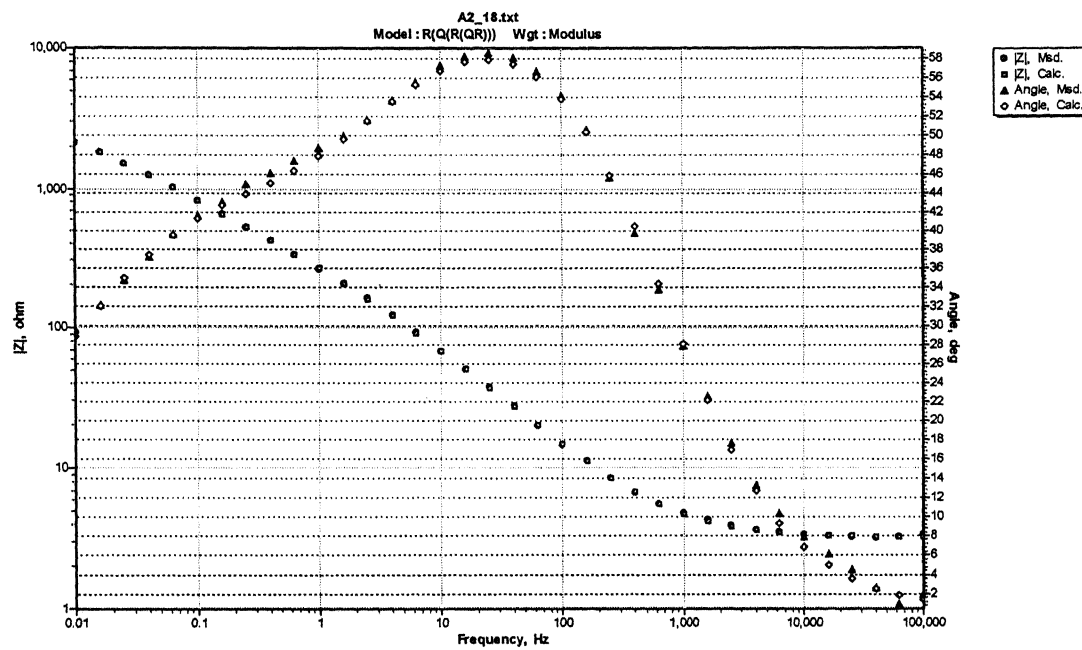


Fig. A-18 Experimental and Simulated Bode Phase and Magnitude plots obtained after 432 hours of immersion in aqueous solution A2.

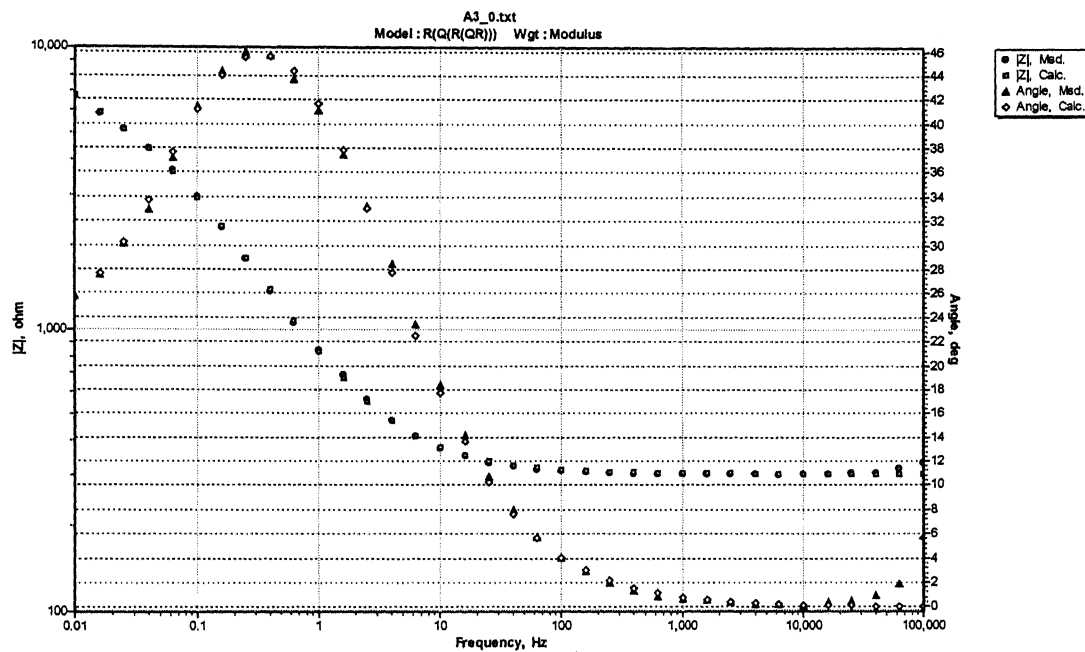


Fig. A-19 Experimental and Simulated Bode Phase and Magnitude plots obtained after 2 hours of immersion in aqueous solution A3.

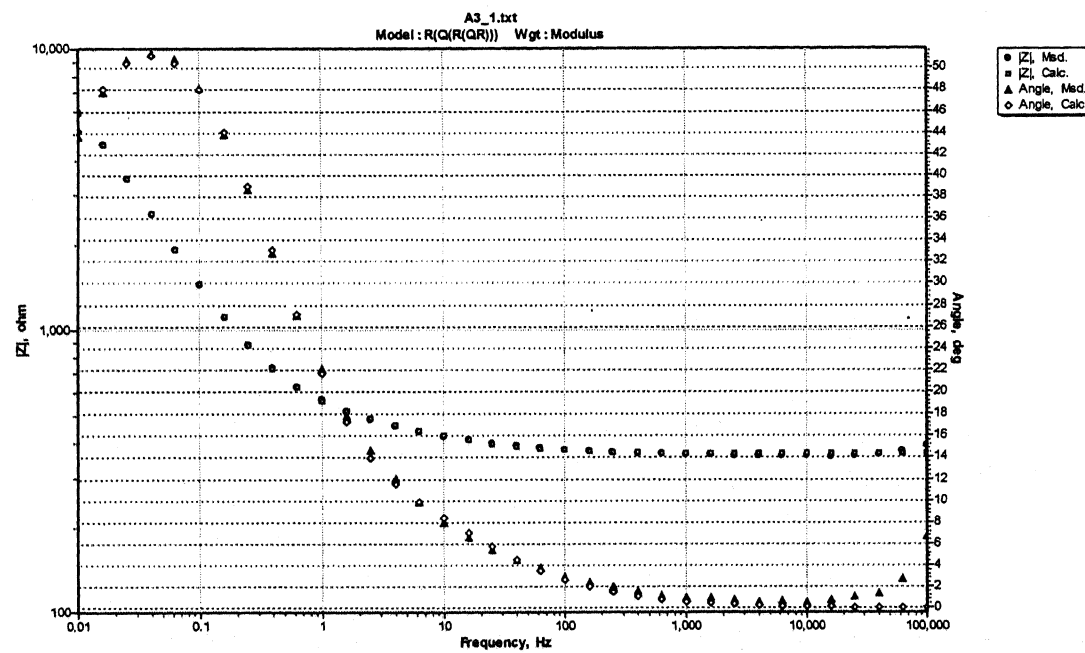


Fig. A-20 Experimental and Simulated Bode Phase and Magnitude plots obtained after 24 hours of immersion in aqueous solution A3.

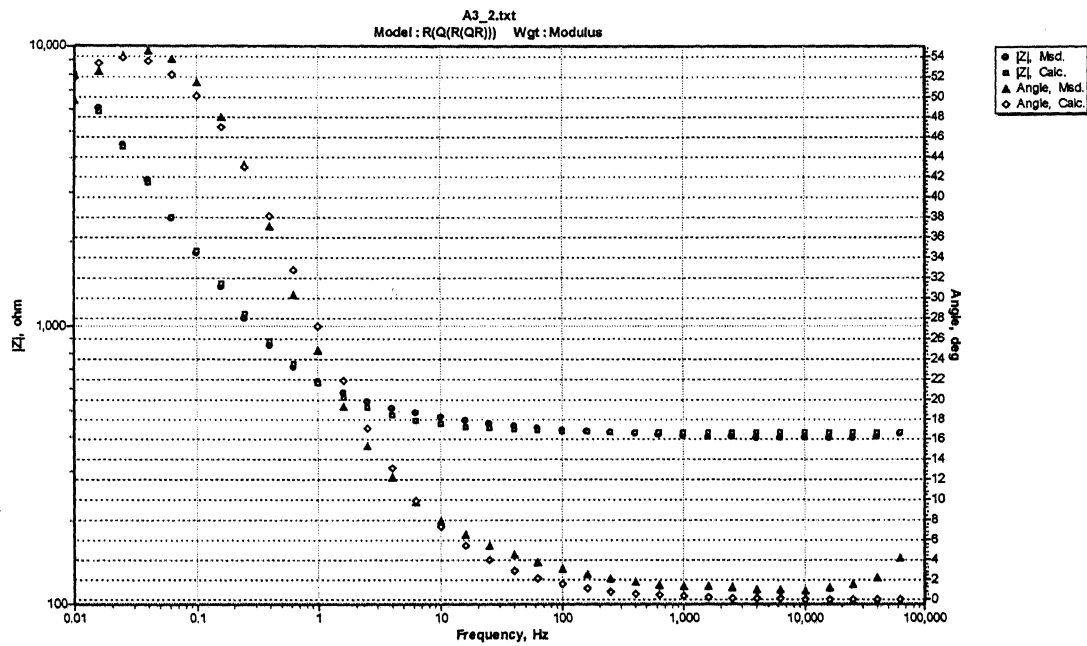


Fig. A-21 Experimental and Simulated Bode Phase and Magnitude plots obtained after 48 hours of immersion in aqueous solution A3.

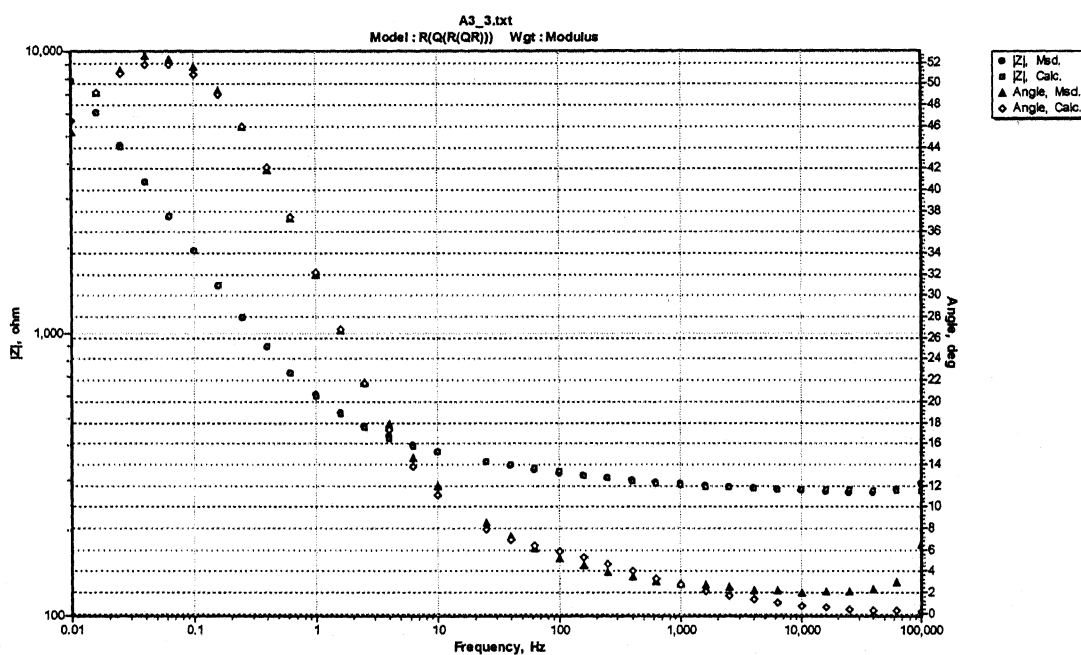


Fig. A-22 Experimental and Simulated Bode Phase and Magnitude plots obtained after 72 hours of immersion in aqueous solution A3.

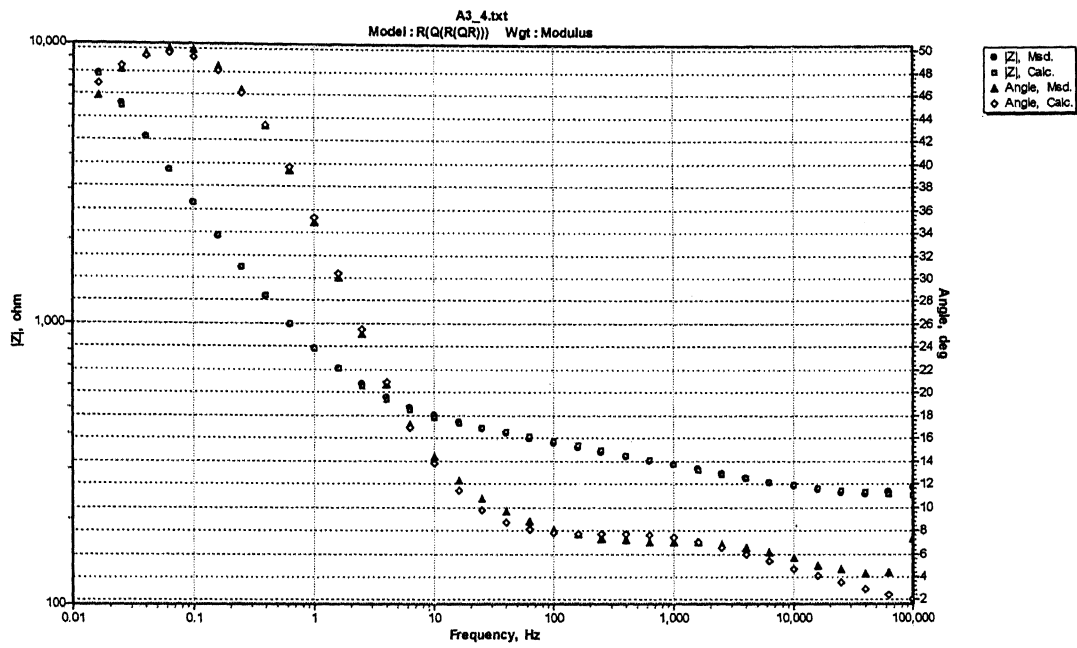


Fig. A-23 Experimental and Simulated Bode Phase and Magnitude plots obtained after 96 hours of immersion in aqueous solution A3.

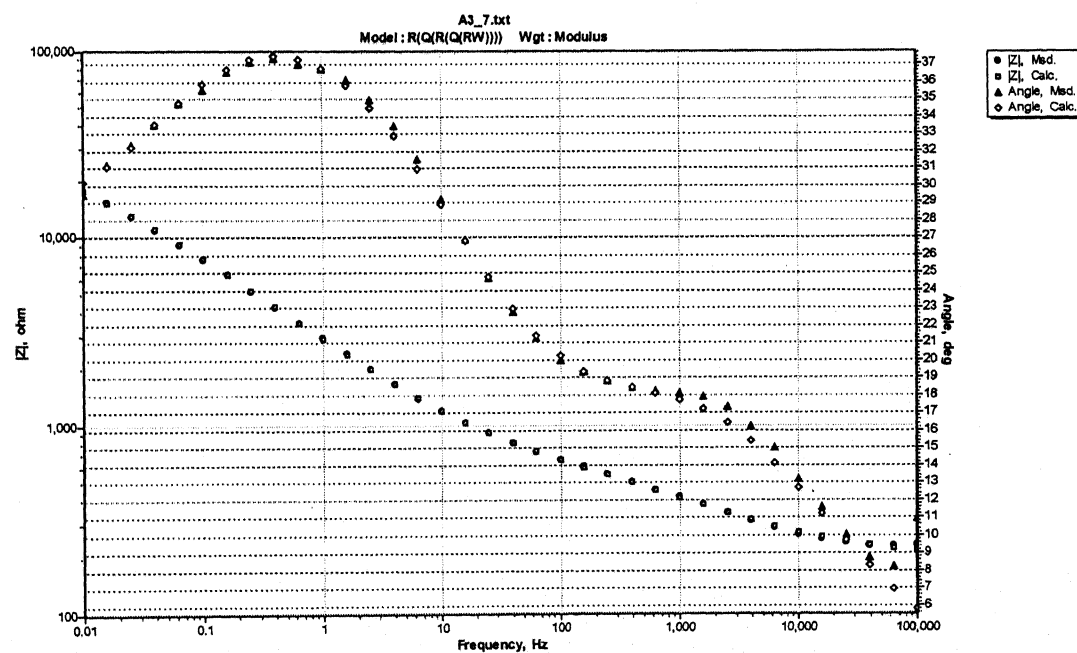


Fig. A-24 Experimental and Simulated Bode Phase and Magnitude plots obtained after 168 hours of immersion in aqueous solution A3.

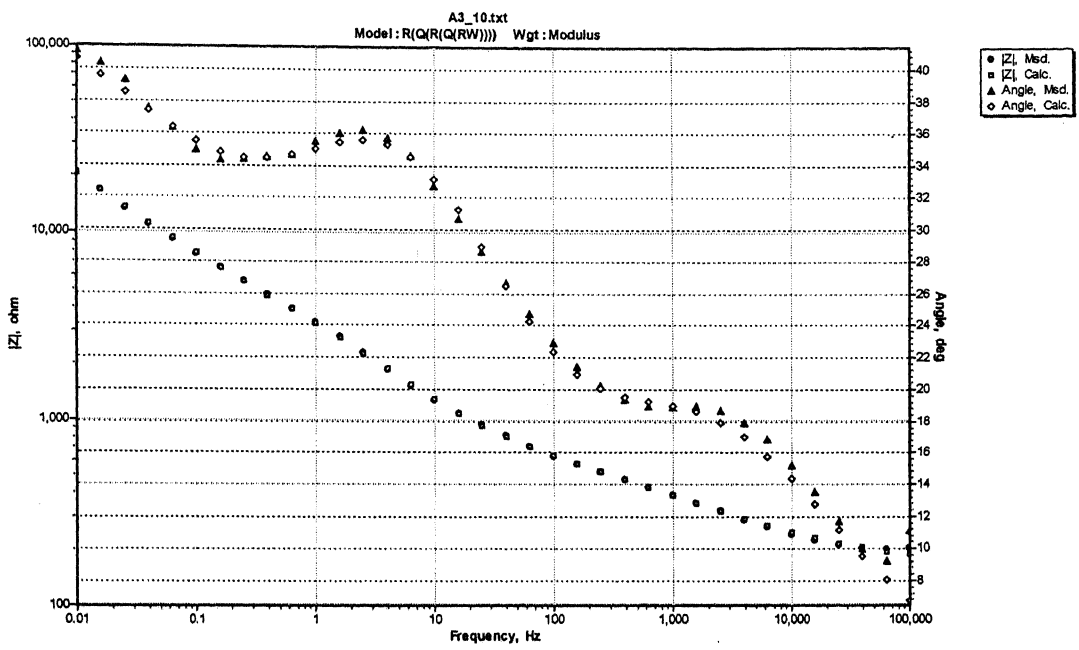


Fig. A-25 Experimental and Simulated Bode Phase and Magnitude plots obtained after 240 hours of immersion in aqueous solution A3.

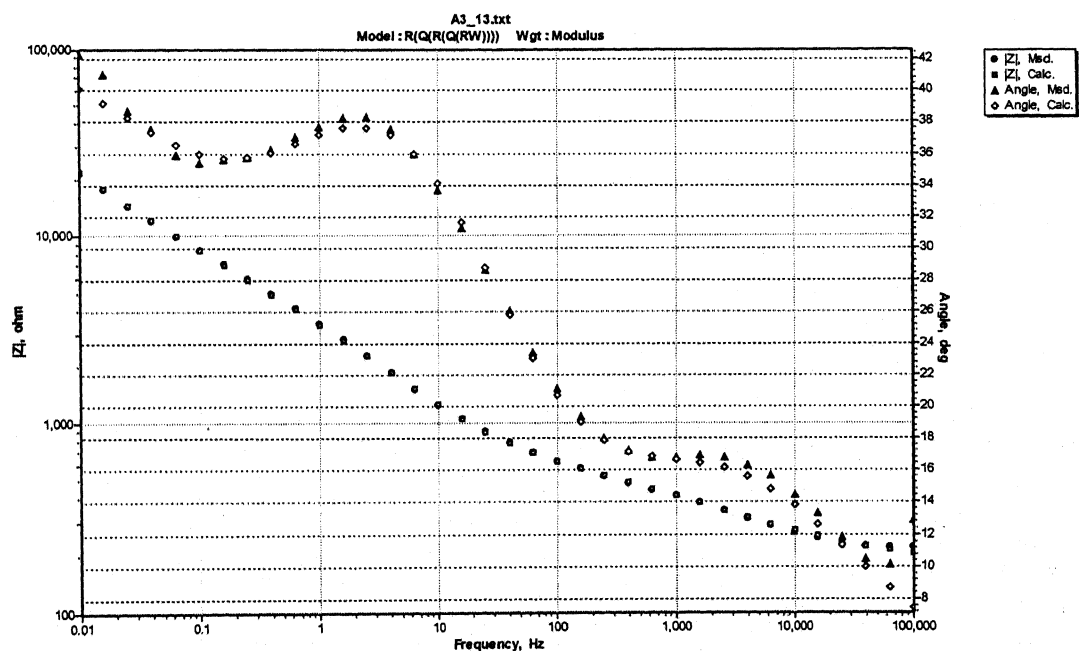


Fig. A-26 Experimental and Simulated Bode Phase and Magnitude plots obtained after 312 hours of immersion in aqueous solution A3.

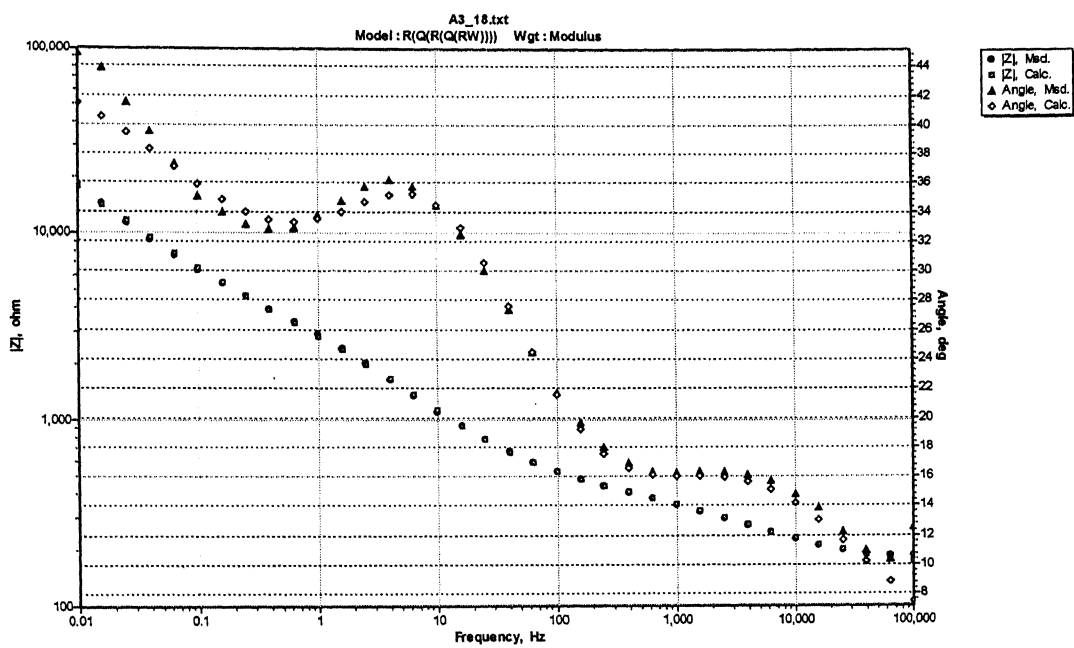


Fig. A-27 Experimental and Simulated Bode Phase and Magnitude plots obtained after 432 hours of immersion in aqueous solution A3.

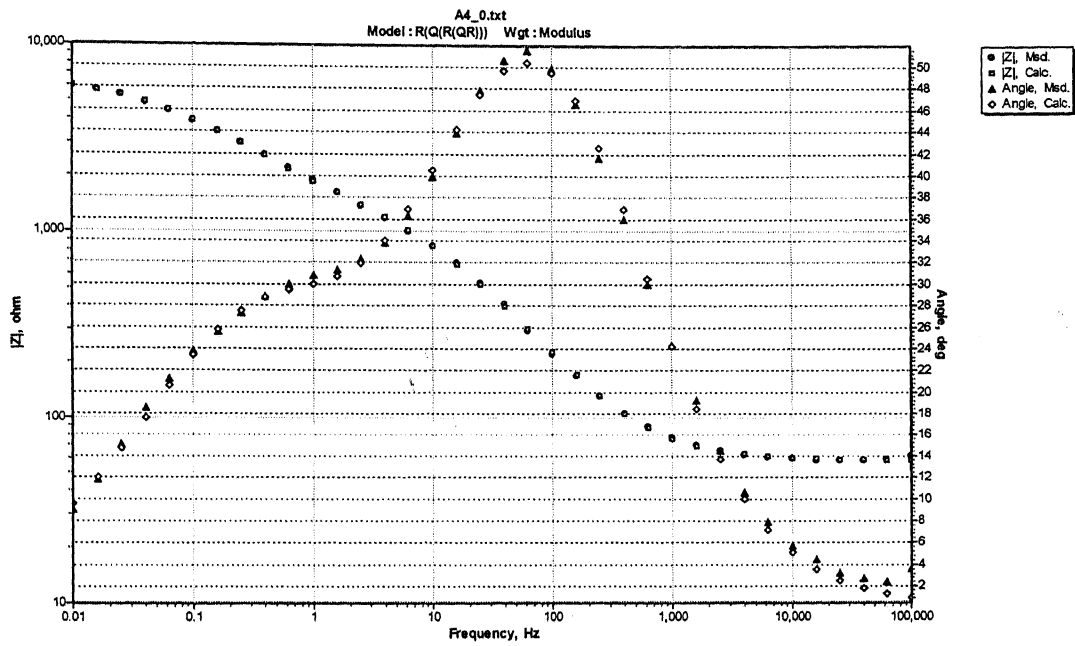


Fig. A-28 Experimental and Simulated Bode Phase and Magnitude plots obtained after 2 hours of immersion in aqueous solution A4.

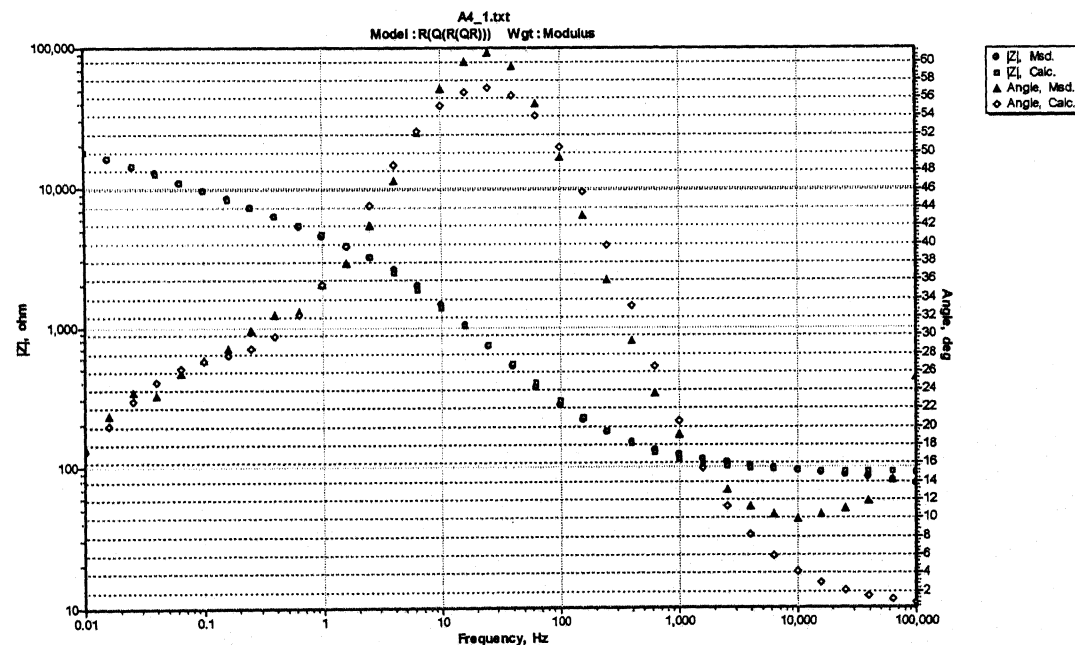


Fig. A-29 Experimental and Simulated Bode Phase and Magnitude plots obtained after 24 hours of immersion in aqueous solution A4.

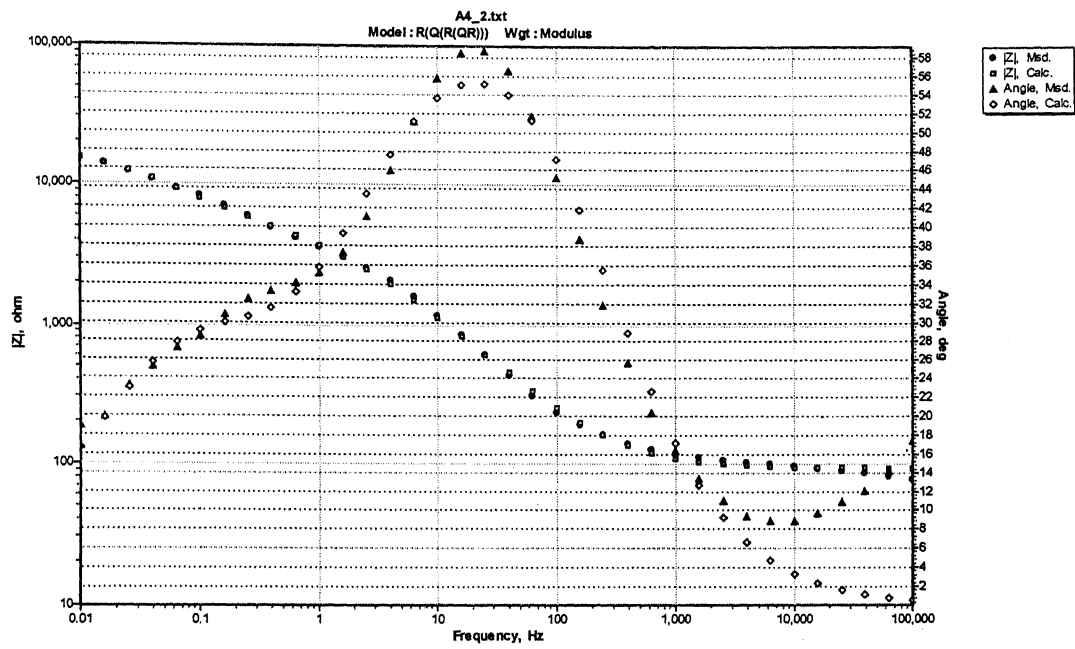


Fig. A-30 Experimental and Simulated Bode Phase and Magnitude plots obtained after 48 hours of immersion in aqueous solution A4.

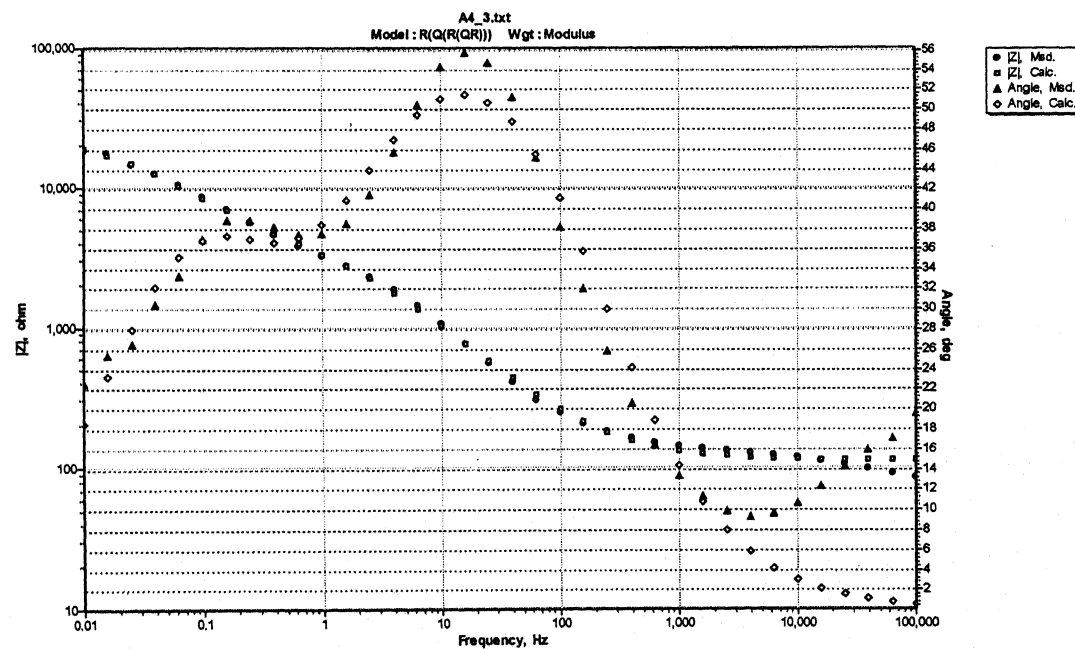


Fig. A-31 Experimental and Simulated Bode Phase and Magnitude plots obtained after 72 hours of immersion in aqueous solution A4.

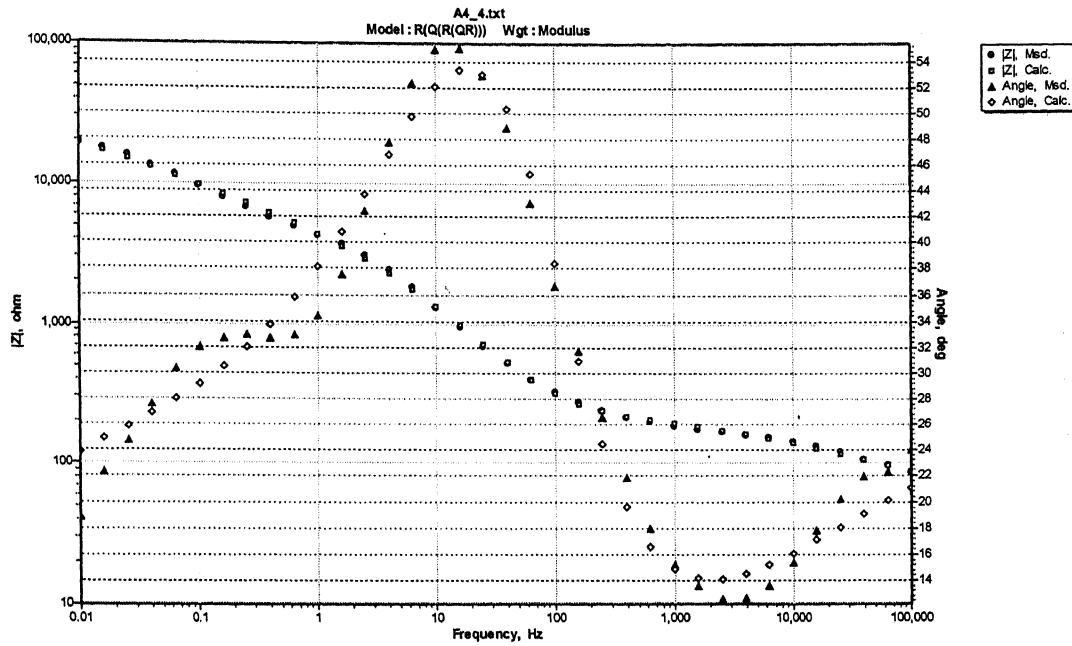


Fig. A-32 Experimental and Simulated Bode Phase and Magnitude plots obtained after 96 hours of immersion in aqueous solution A4.

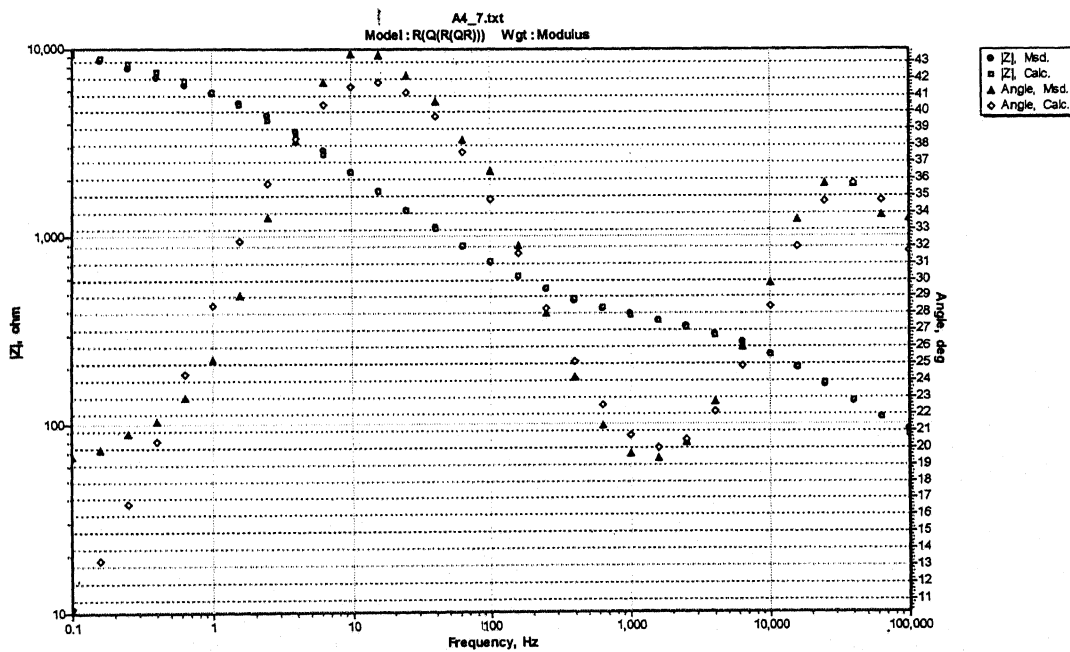


Fig. A-33 Experimental and Simulated Bode Phase and Magnitude plots obtained after 168 hours of immersion in aqueous solution A4.

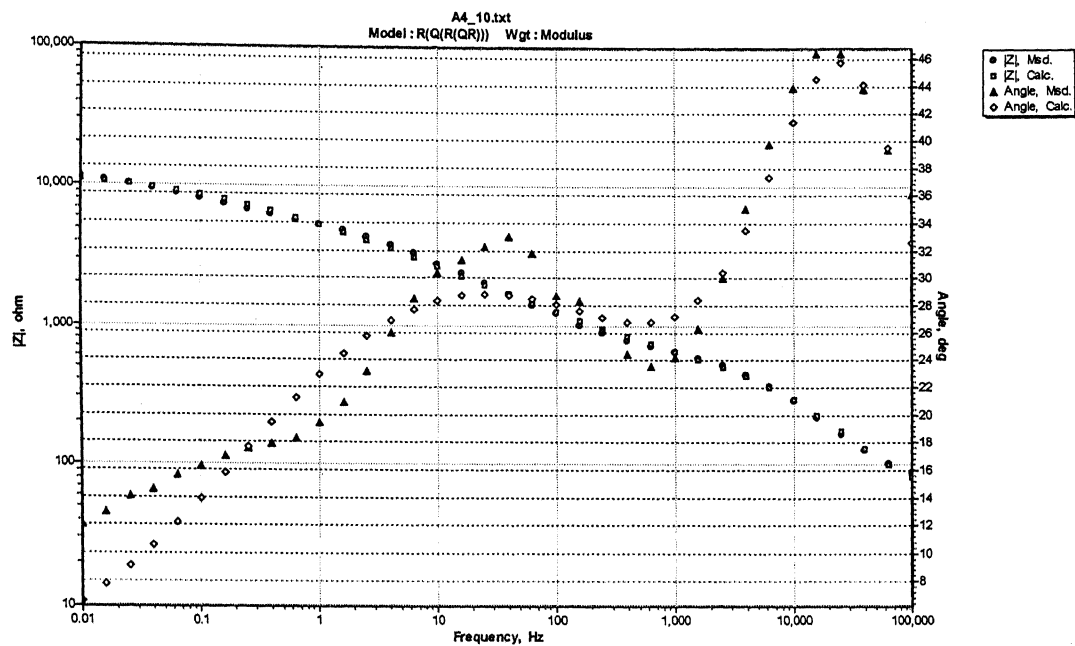


Fig. A-34 Experimental and Simulated Bode Phase and Magnitude plots obtained after 240 hours of immersion in aqueous solution A4.

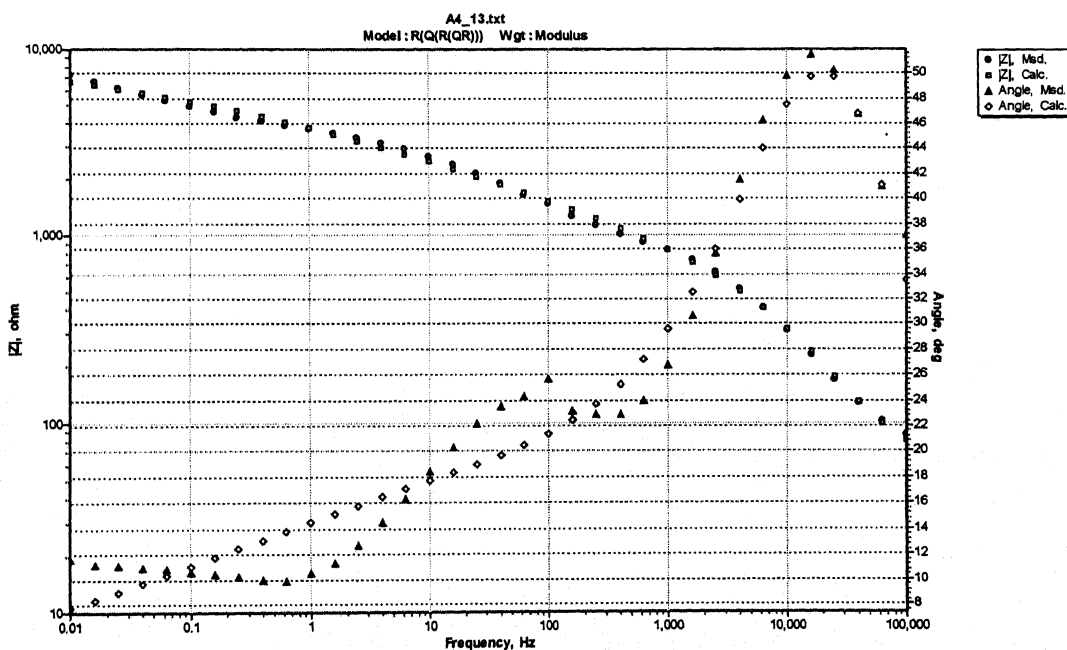


Fig. A-35 Experimental and Simulated Bode Phase and Magnitude plots obtained after 312 hours of immersion in aqueous solution A4.

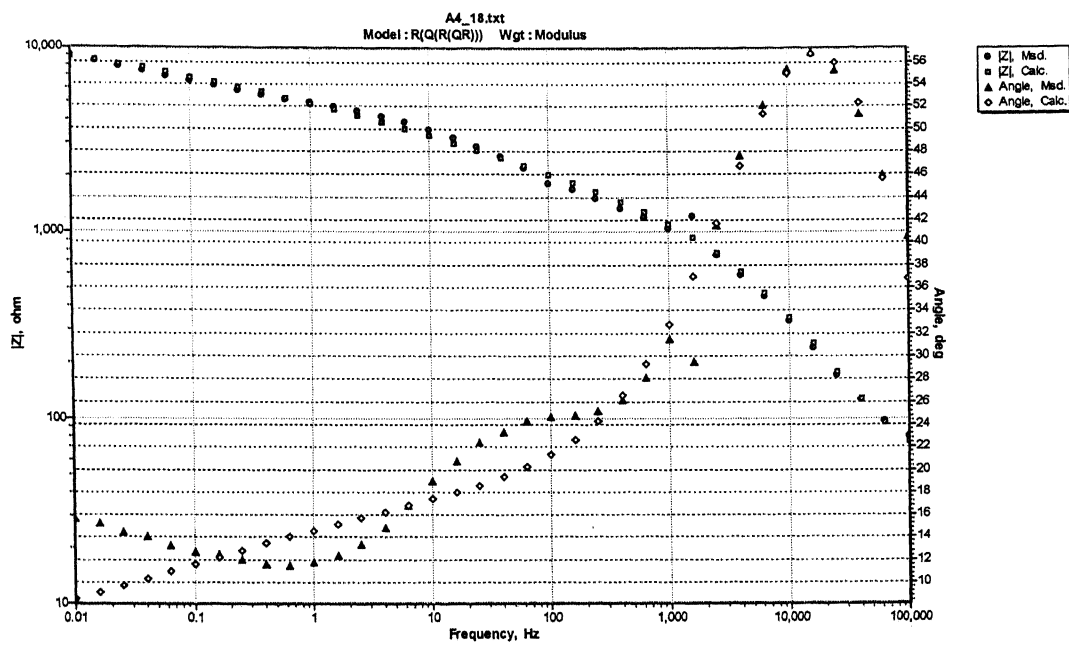


Fig. A-36 Experimental and Simulated Bode Phase and Magnitude plots obtained after 432 hours of immersion in aqueous solution A4.

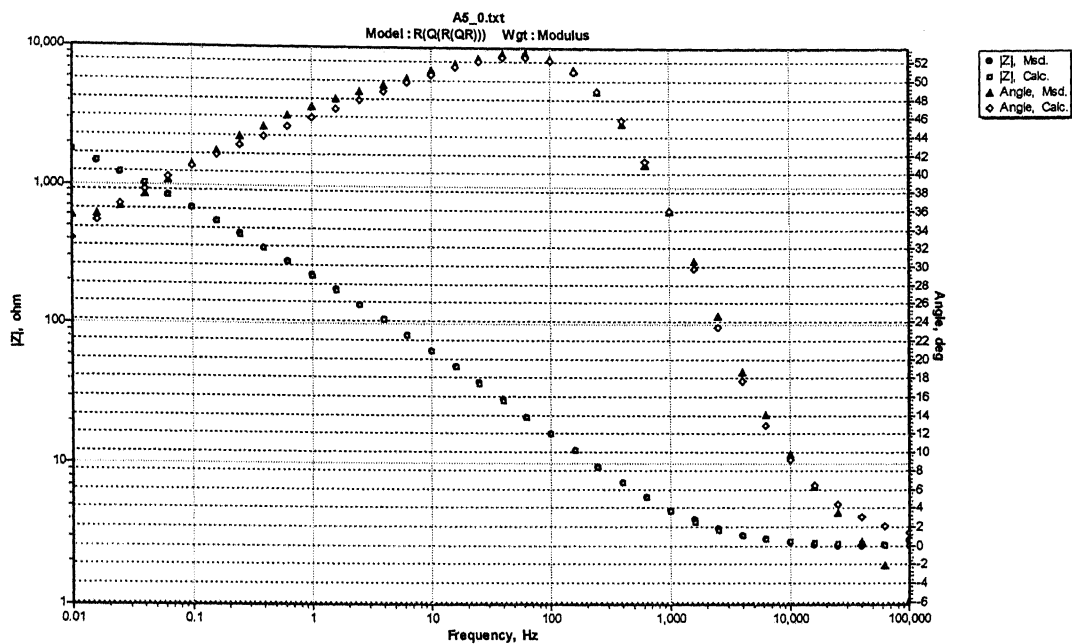


Fig. A-37 Experimental and Simulated Bode Phase and Magnitude plots obtained after 2 hours of immersion in aqueous solution A5.

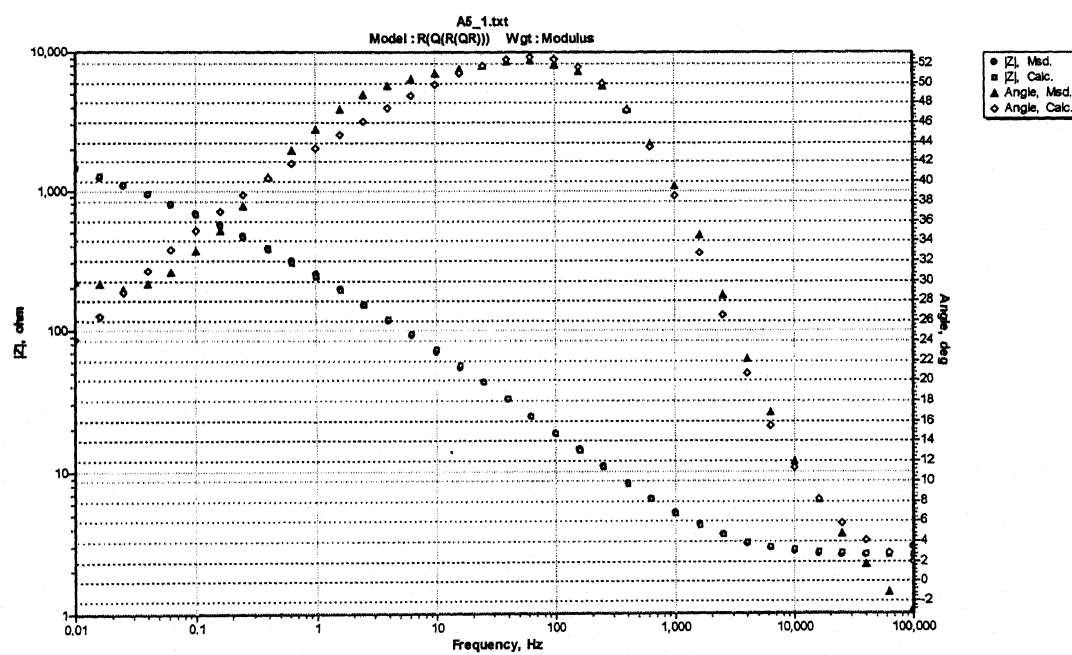


Fig. A-38 Experimental and Simulated Bode Phase and Magnitude plots obtained after 24 hours of immersion in aqueous solution A5.

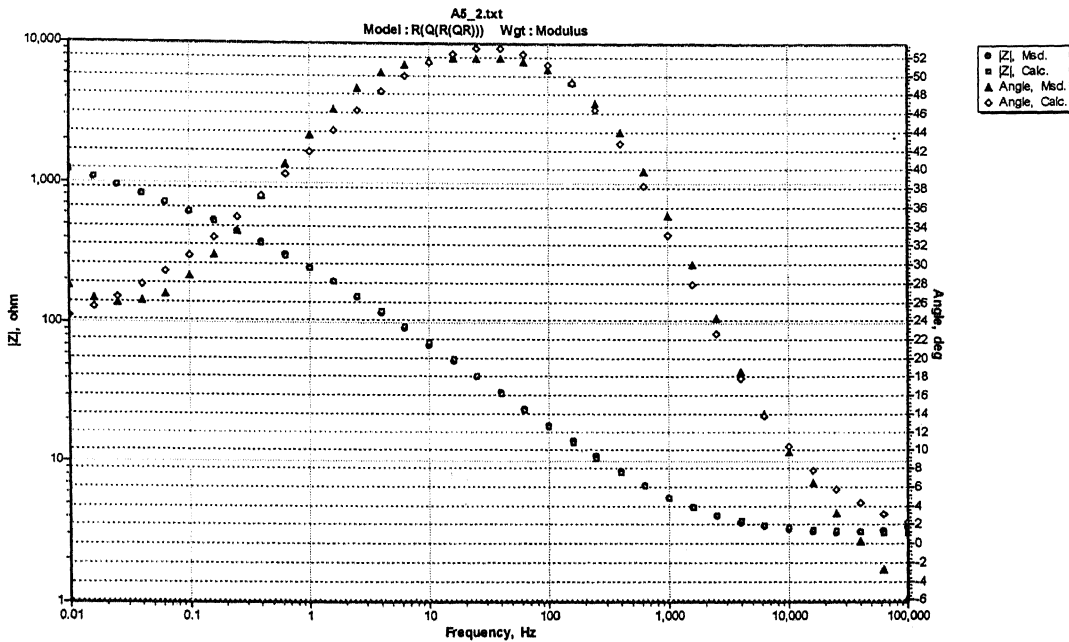


Fig. A-39 Experimental and Simulated Bode Phase and Magnitude plots obtained after 48 hours of immersion in aqueous solution A5.

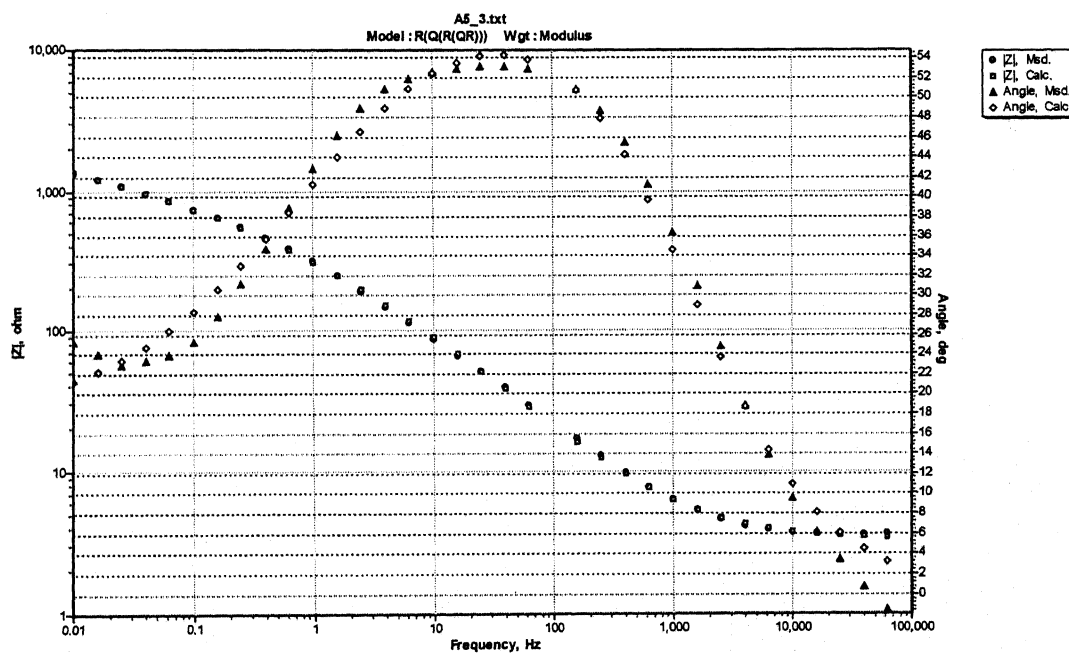


Fig. A-40 Experimental and Simulated Bode Phase and Magnitude plots obtained after 72 hours of immersion in aqueous solution A5.

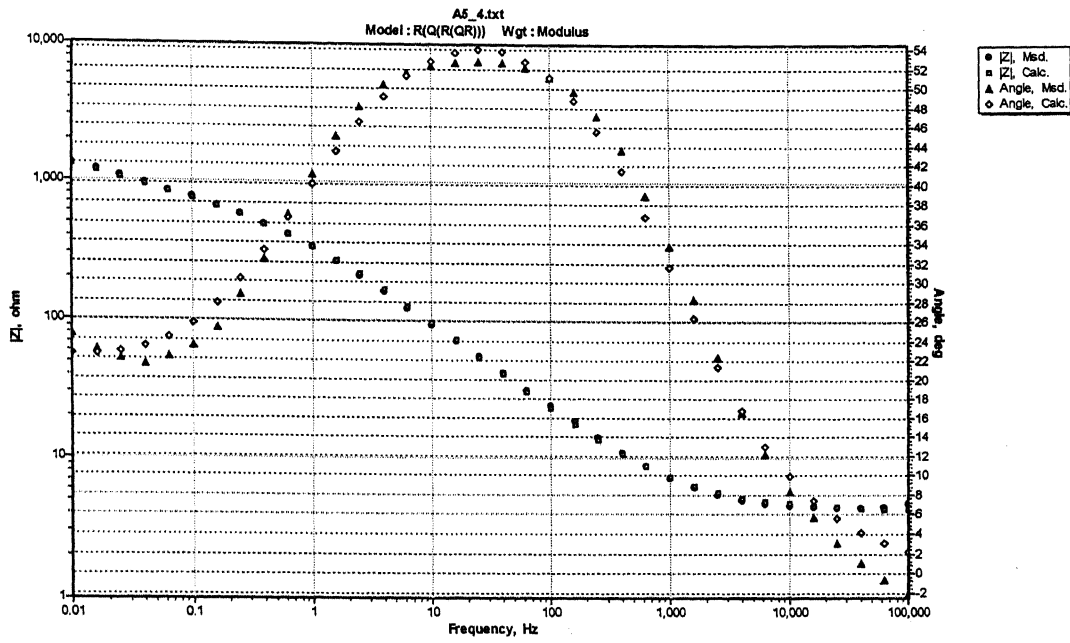


Fig. A-41 Experimental and Simulated Bode Phase and Magnitude plots obtained after 96 hours of immersion in aqueous solution A5.

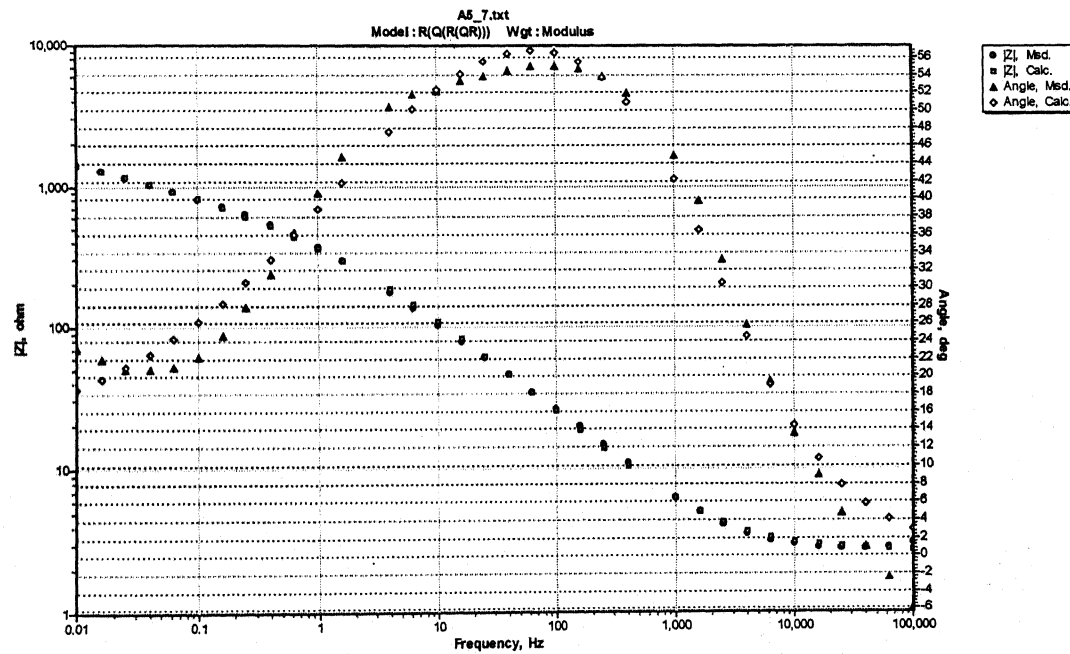


Fig. A-42 Experimental and Simulated Bode Phase and Magnitude plots obtained after 168 hours of immersion in aqueous solution A5.

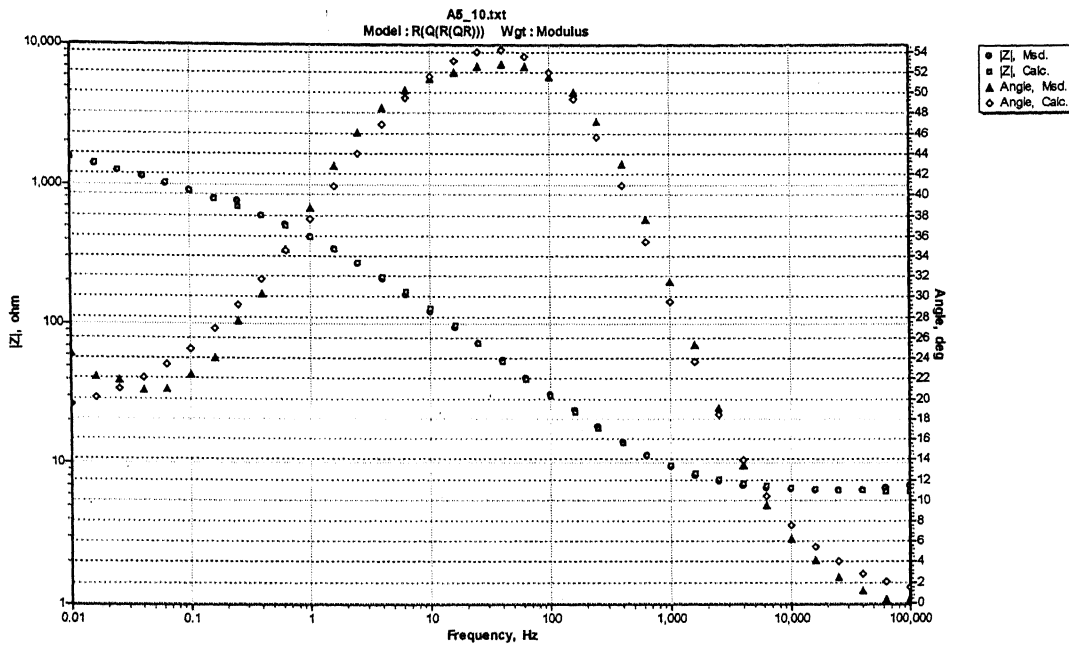


Fig. A-43 Experimental and Simulated Bode Phase and Magnitude plots obtained after 240 hours of immersion in aqueous solution A5.

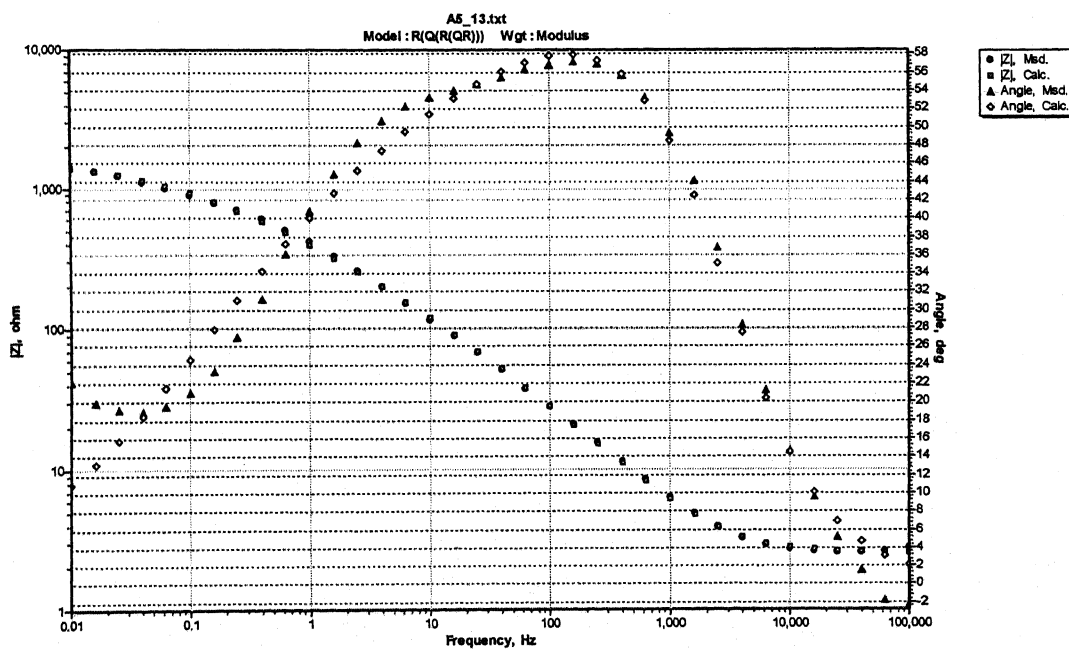


Fig. A-44 Experimental and Simulated Bode Phase and Magnitude plots obtained after 312 hours of immersion in aqueous solution A5.

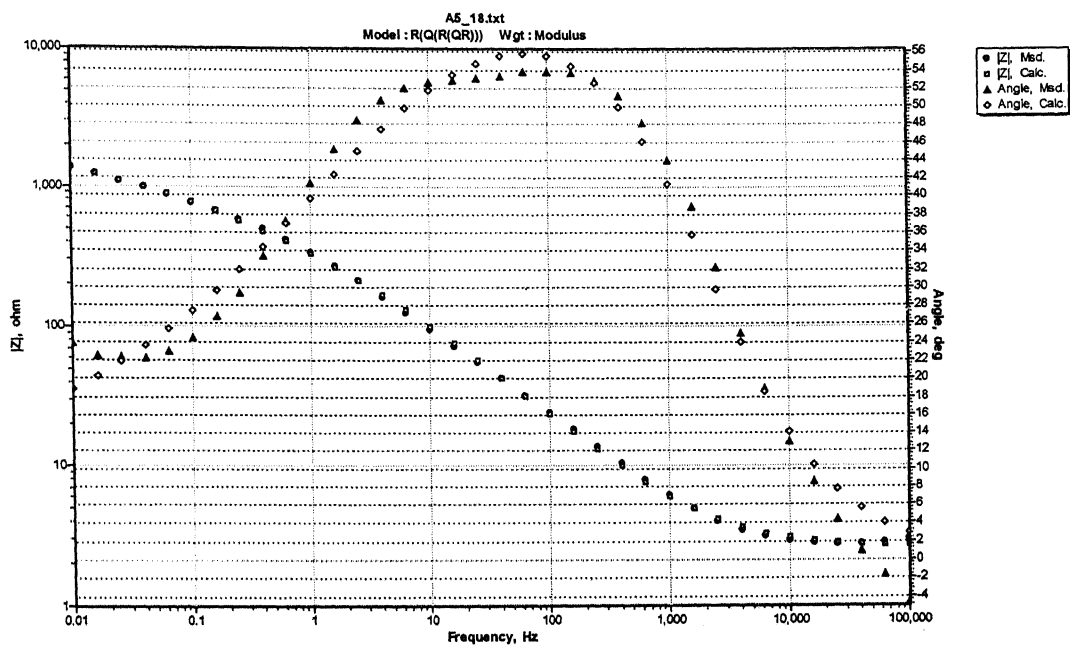


Fig. A-45 Experimental and Simulated Bode Phase and Magnitude plots obtained after 432 hours of immersion in aqueous solution A5.

## APPENDIX B

---

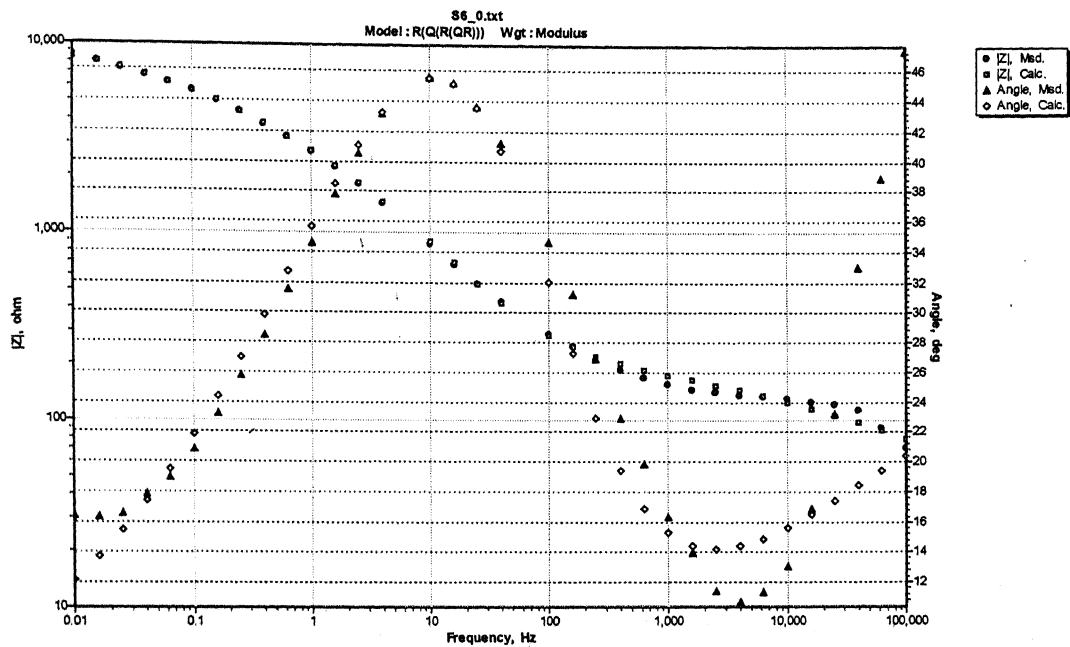


Fig. B-1 Experimental and Simulated Bode Phase and Magnitude plots obtained after 2 hours of immersion in soil environment S6

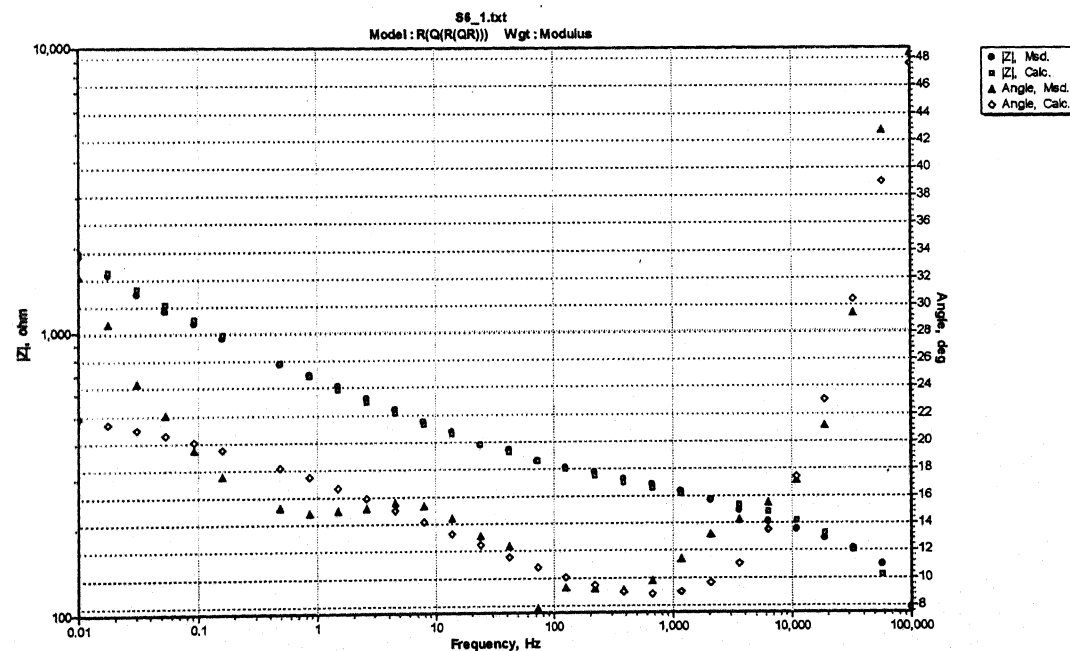


Fig. B-2 Experimental and Simulated Bode Phase and Magnitude plots obtained after 24 hours of immersion in soil environment S6.

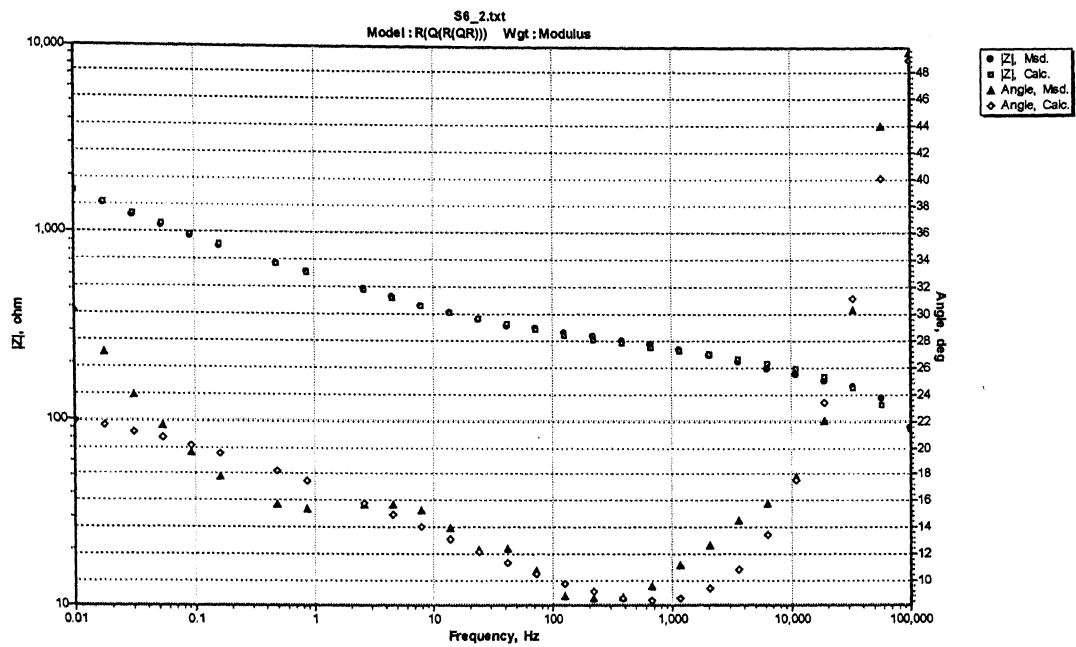


Fig. B-3 Experimental and Simulated Bode Phase and Magnitude plots obtained after 48 hours of immersion in soil environment S6.

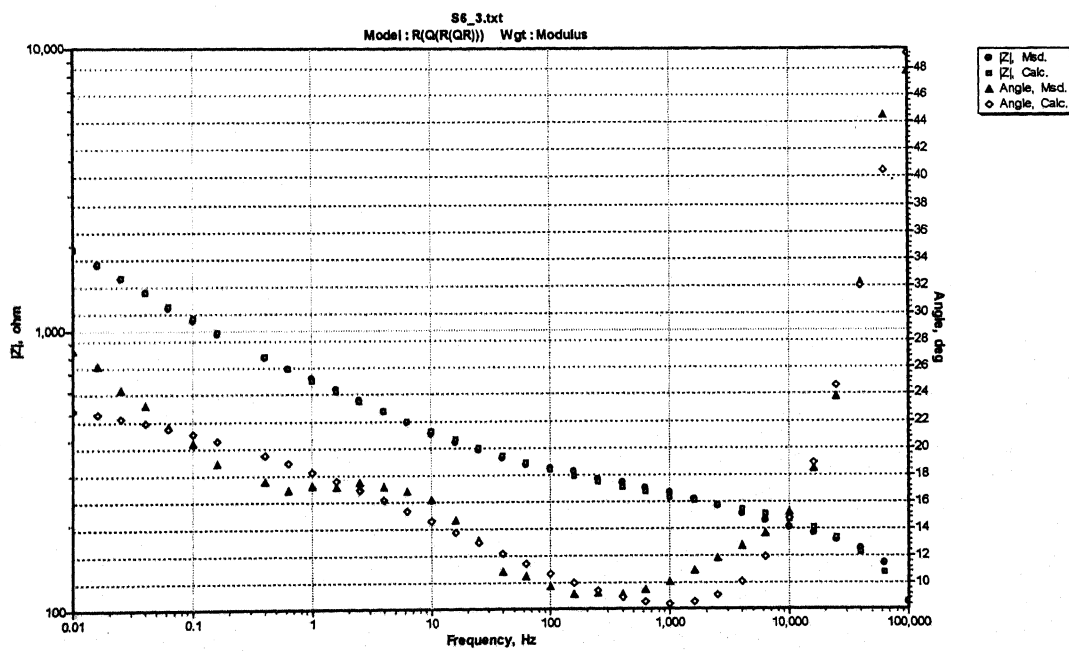


Fig. B-4 Experimental and Simulated Bode Phase and Magnitude plots obtained after 72 hours of immersion in soil environment S6.

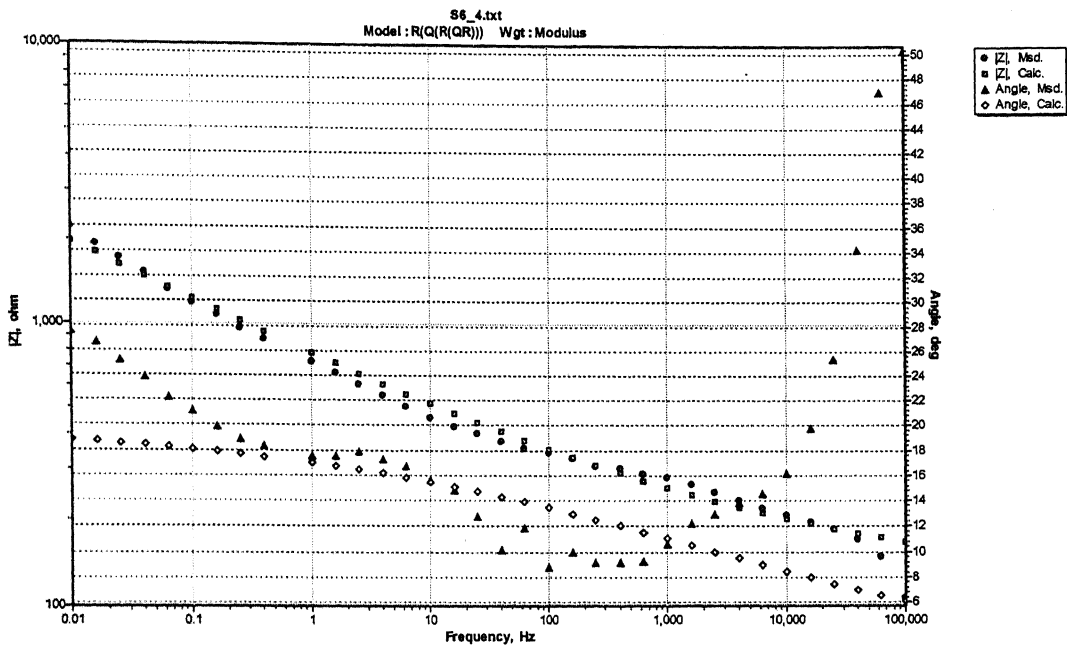


Fig. B-5 Experimental and Simulated Bode Phase and Magnitude plots obtained after 96 hours of immersion in soil environment S6.

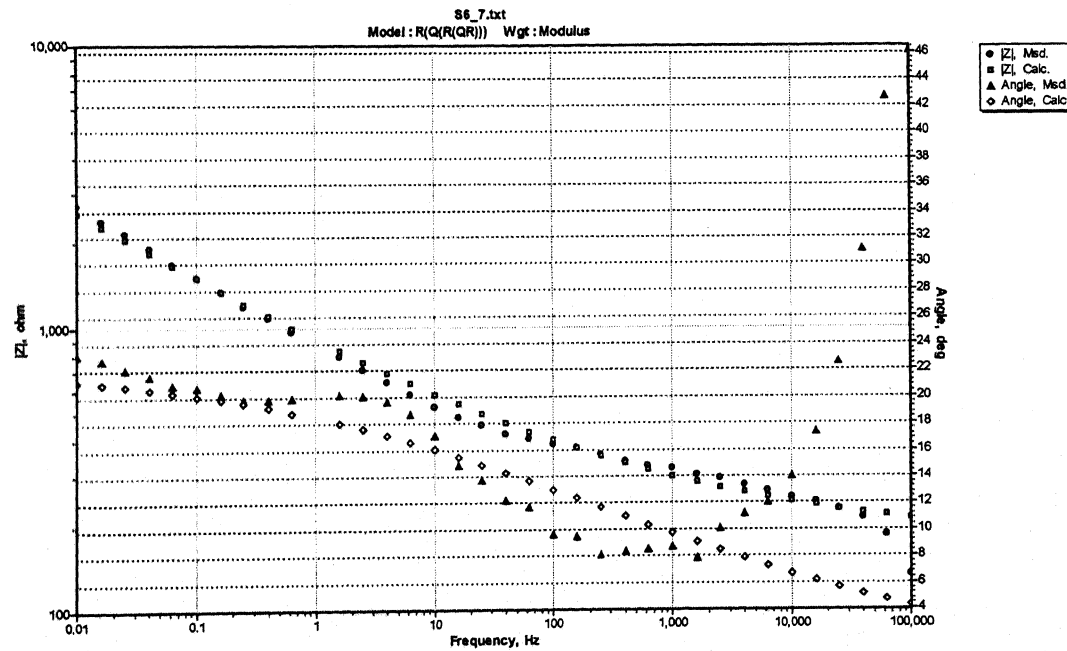


Fig. B-6 Experimental and Simulated Bode Phase and Magnitude plots obtained after 168 hours of immersion in soil environment S6.

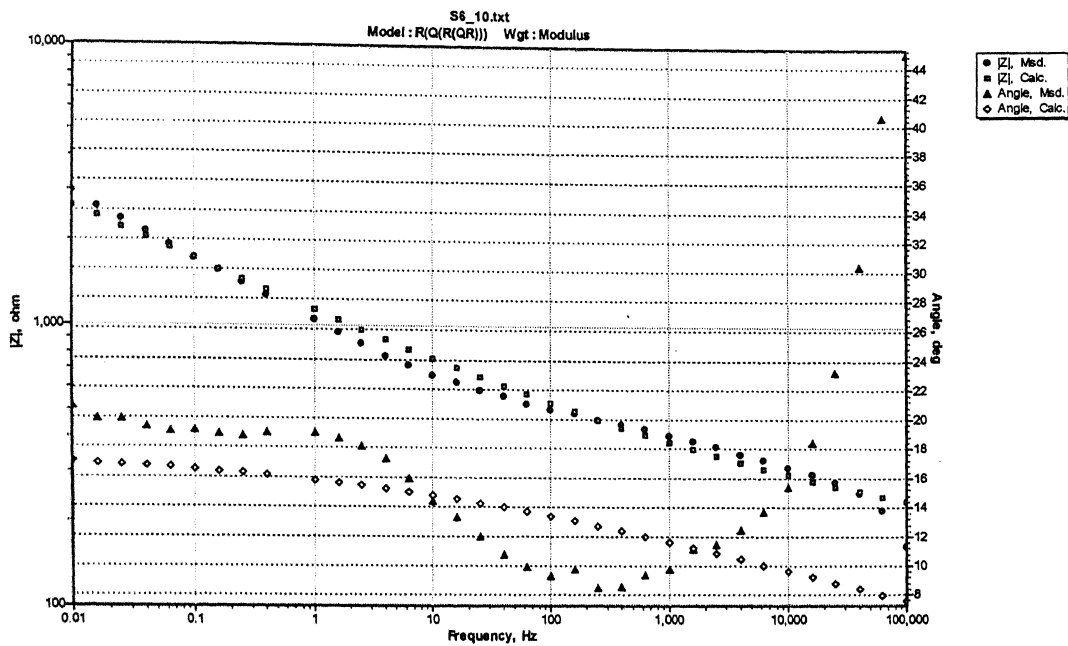


Fig. B-7 Experimental and Simulated Bode Phase and Magnitude plots obtained after 240 hours of immersion in soil environment S6.

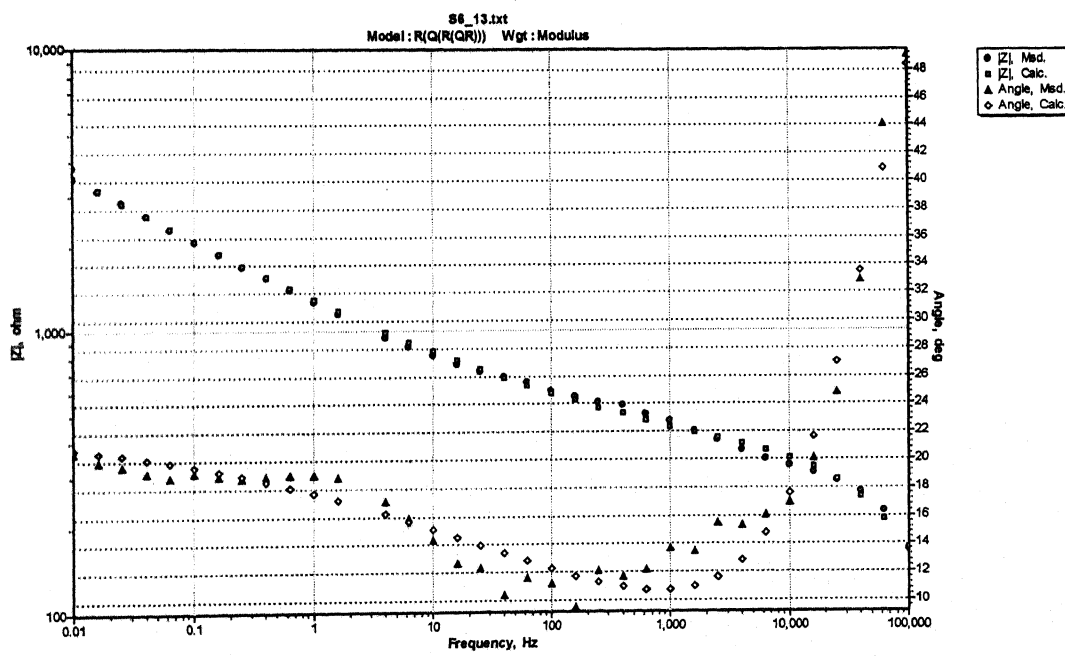


Fig. B-8 Experimental and Simulated Bode Phase and Magnitude plots obtained after 312 hours of immersion in soil environment S6.

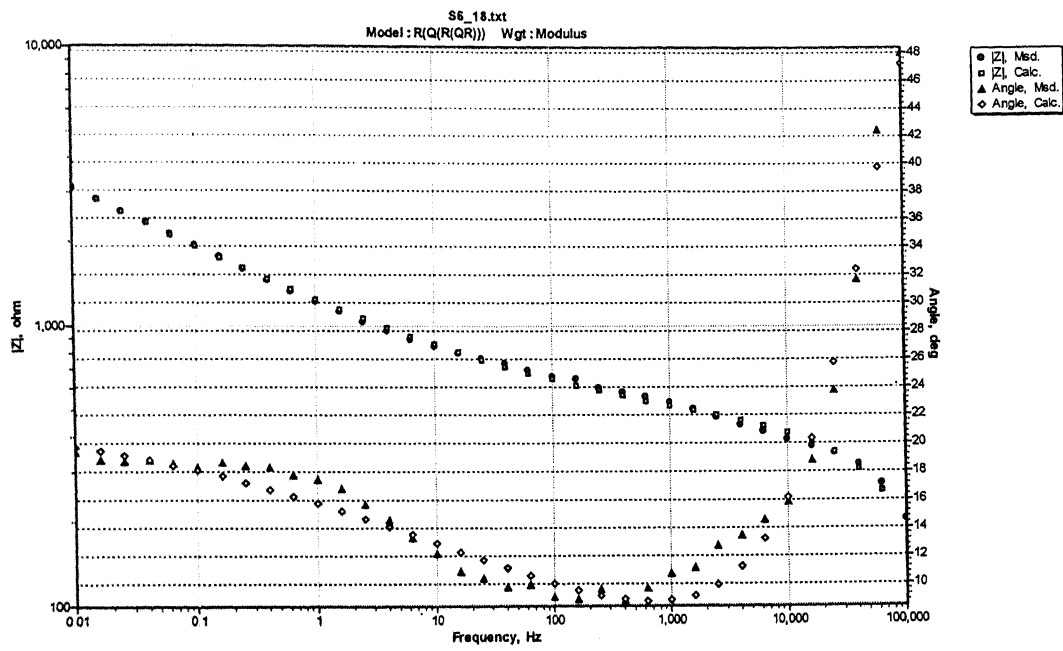


Fig. B-9 Experimental and Simulated Bode Phase and Magnitude plots obtained after 432 hours of immersion in soil environment S6.

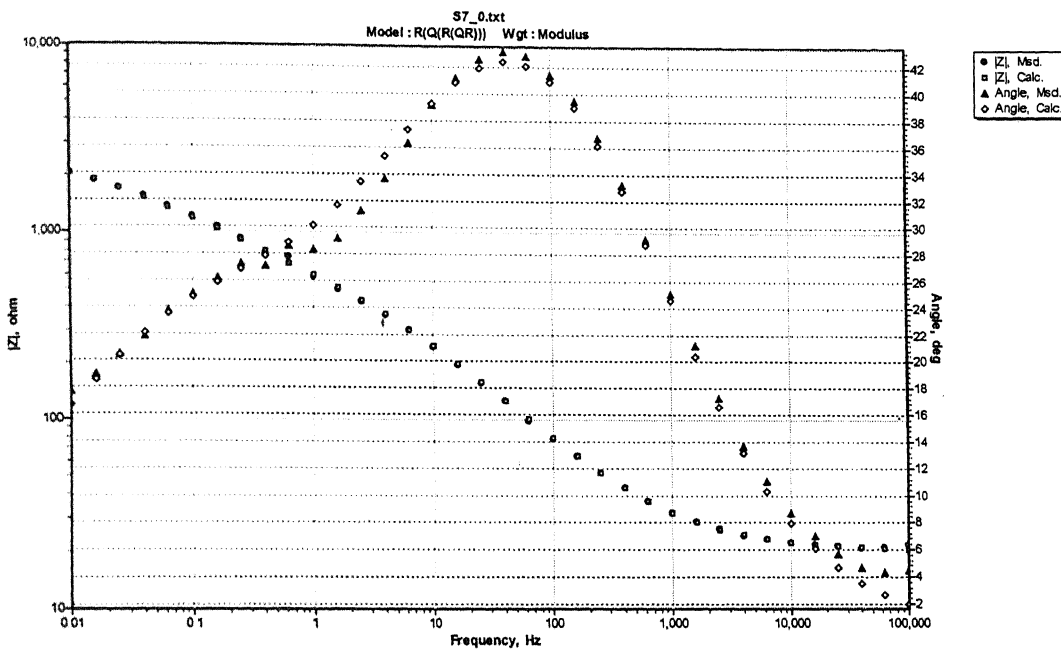


Fig. B-10 Experimental and Simulated Bode Phase and Magnitude plots obtained after 2 hours of immersion in soil environment S7.

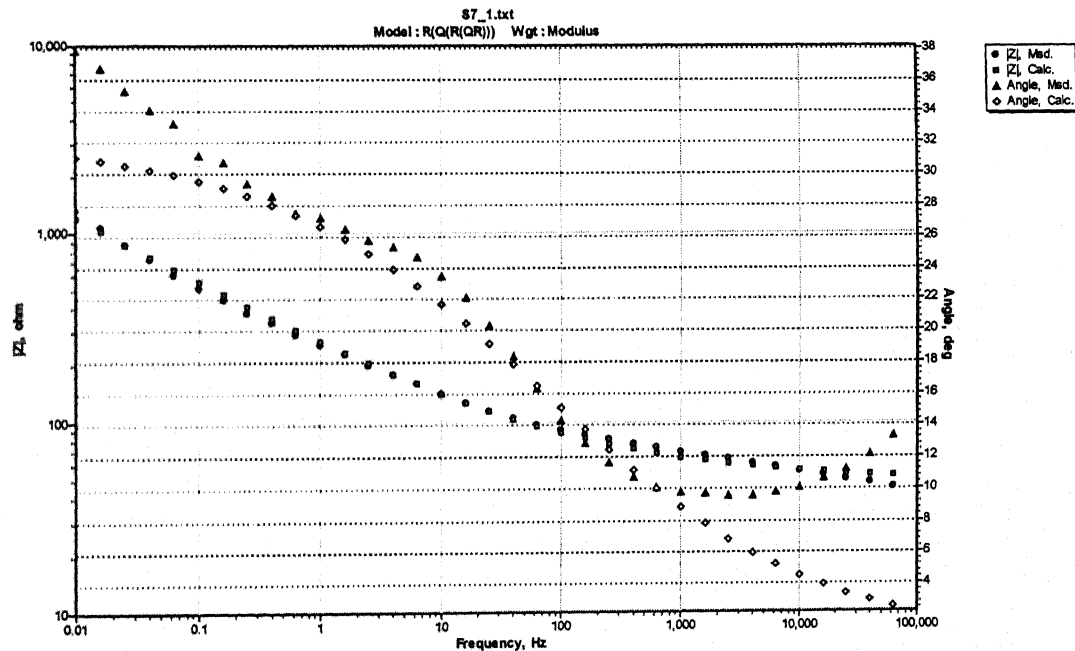


Fig. B-11 Experimental and Simulated Bode Phase and Magnitude plots obtained after 24 hours of immersion in soil environment S7.

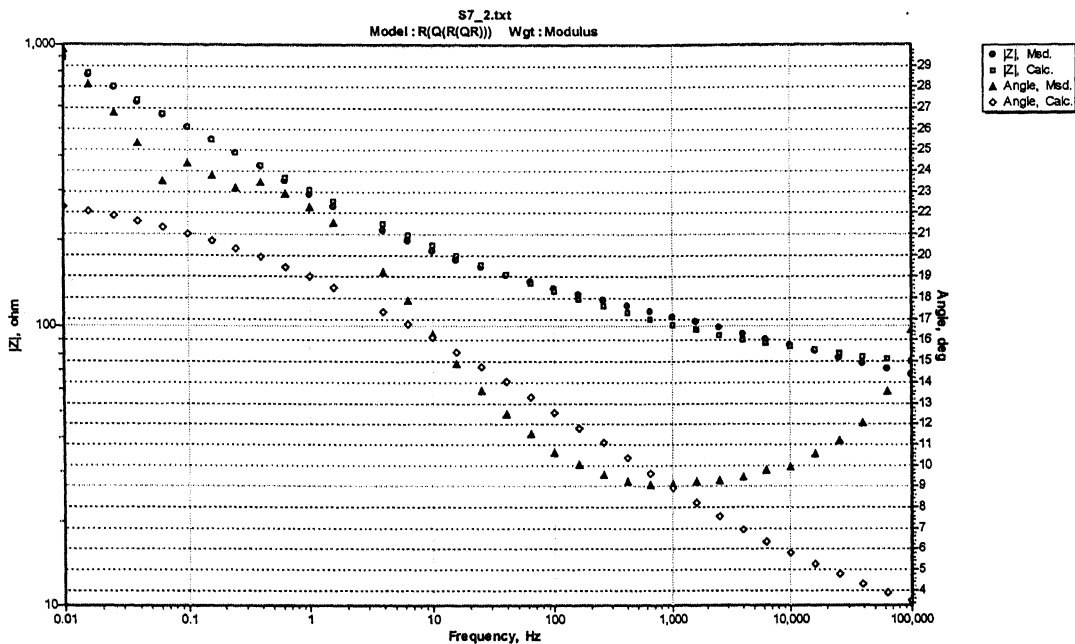


Fig. B-12 Experimental and Simulated Bode Phase and Magnitude plots obtained after 48 hours of immersion in soil environment S7.

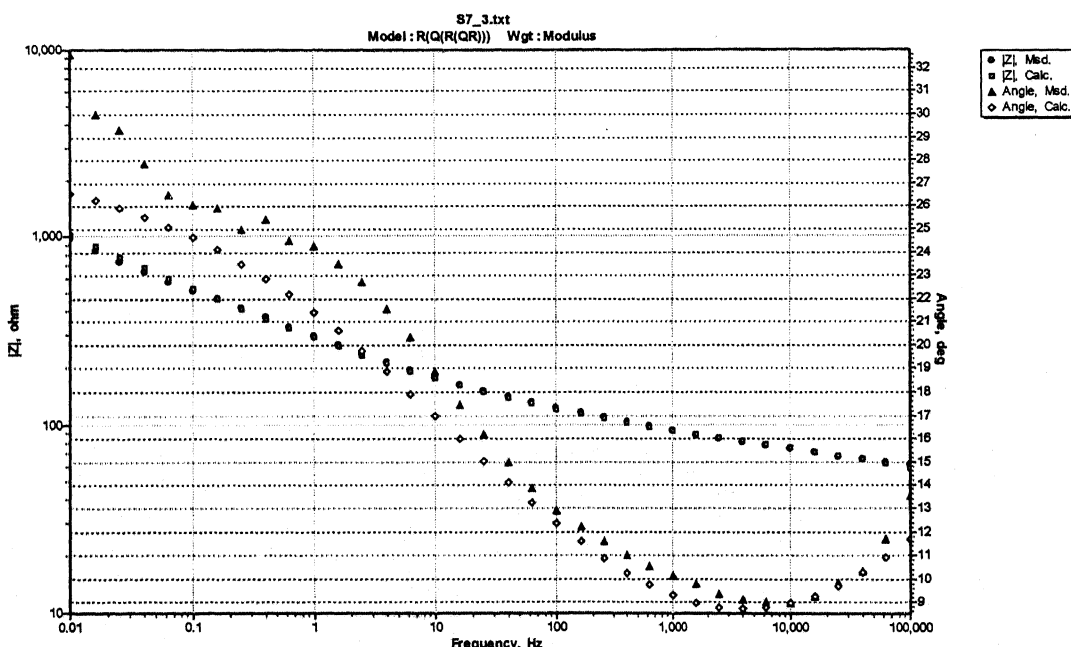


Fig. B-13 Experimental and Simulated Bode Phase and Magnitude plots obtained after 72 hours of immersion in soil environment S7.

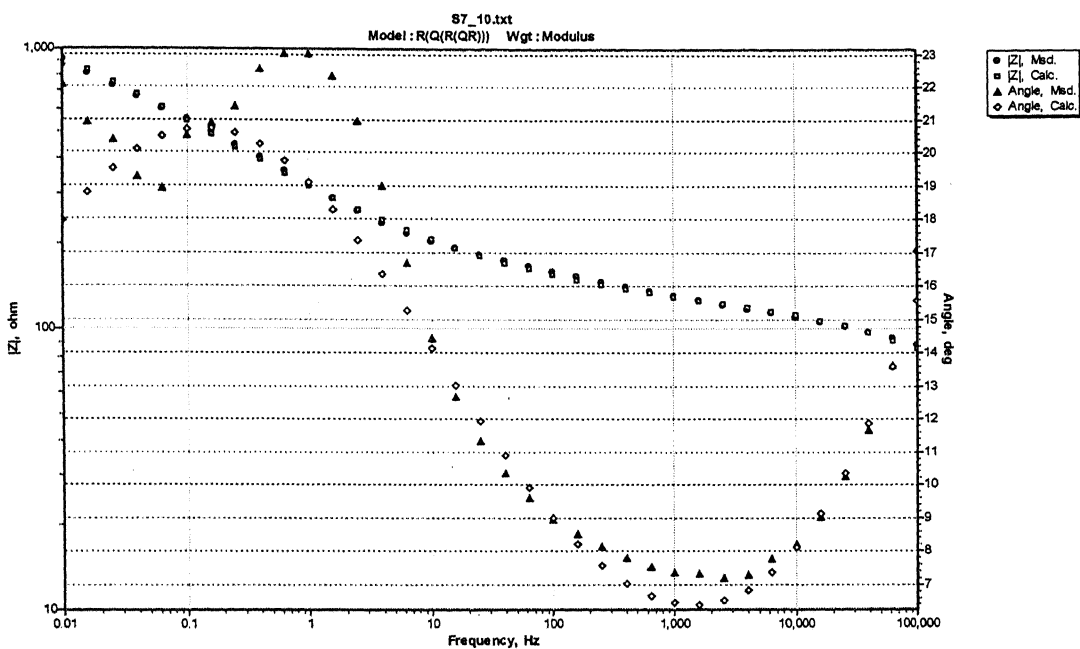


Fig. B-16 Experimental and Simulated Bode Phase and Magnitude plots obtained after 240 hours of immersion in soil environment S7.

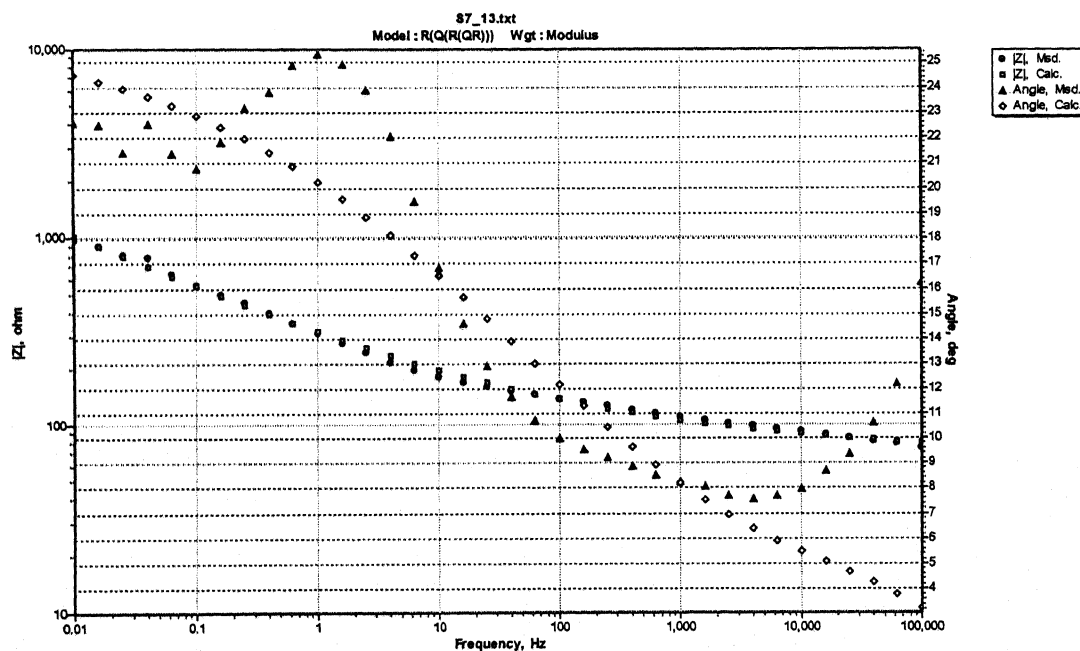


Fig. B-17 Experimental and Simulated Bode Phase and Magnitude plots obtained after 312 hours of immersion in soil environment S7.

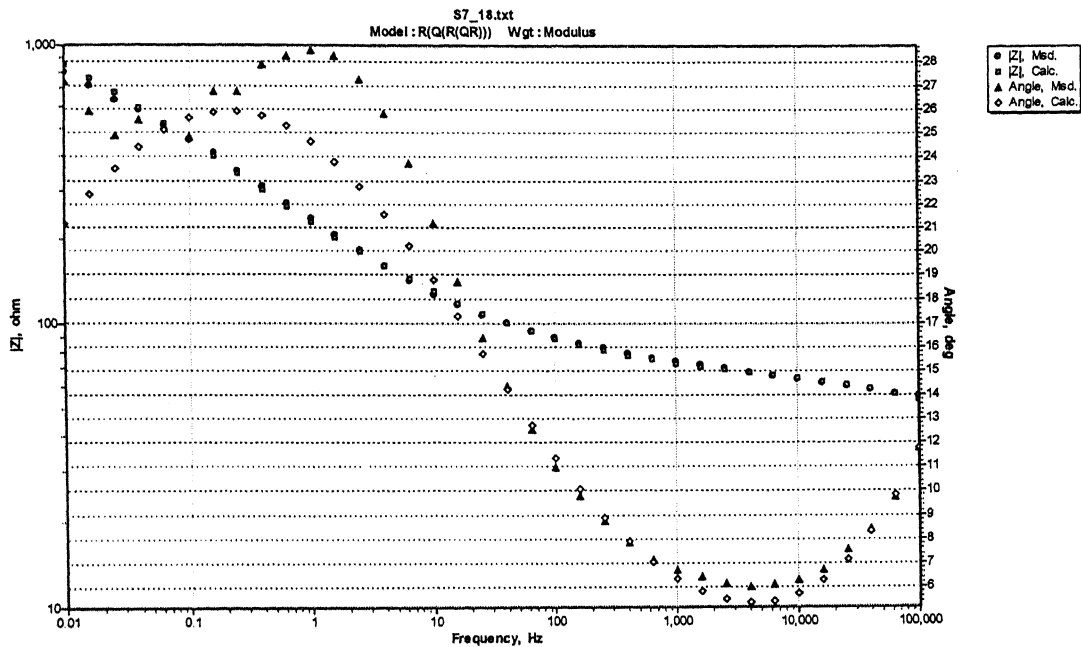


Fig. B-18 Experimental and Simulated Bode Phase and Magnitude plots obtained after 432 hours of immersion in soil environment S7.

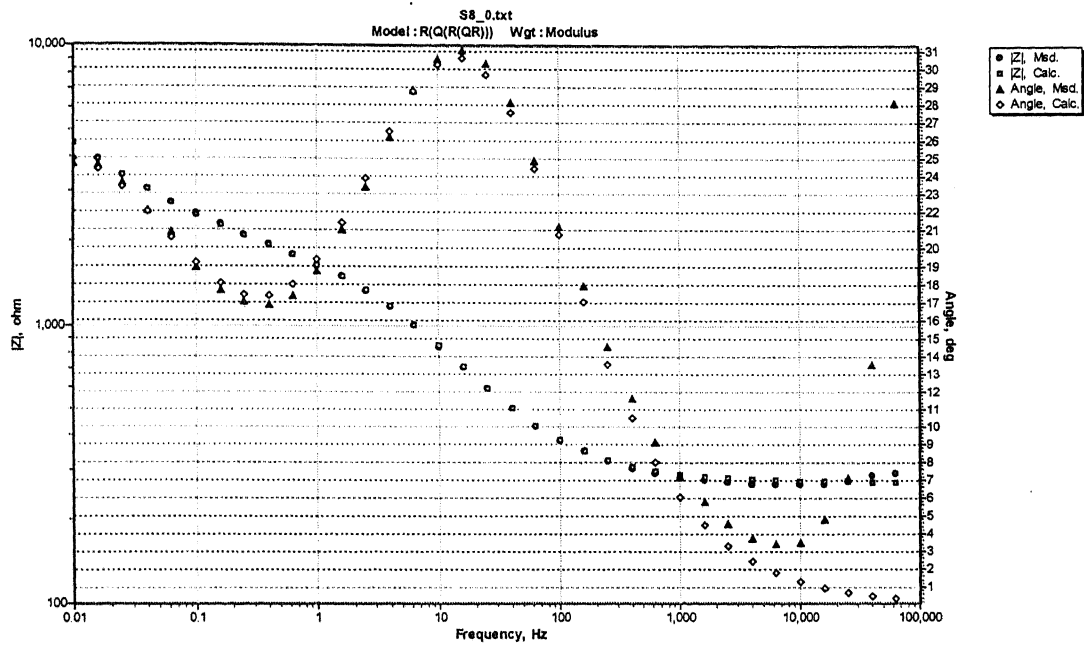


Fig. B-19 Experimental and Simulated Bode Phase and Magnitude plots obtained after 2 hours of immersion in soil environment S8.

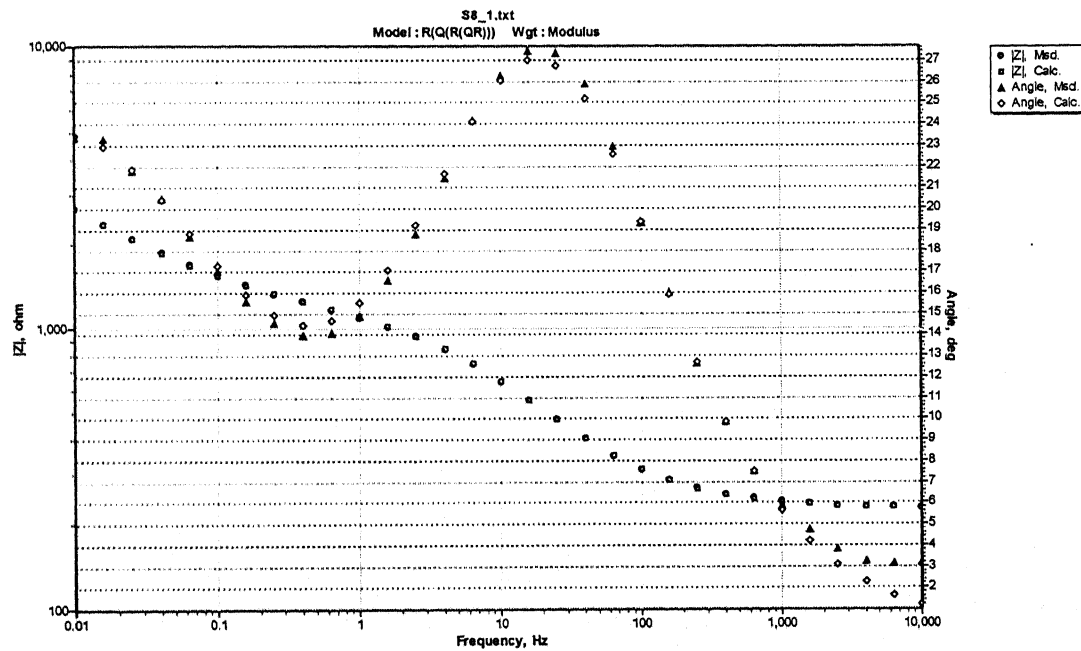


Fig. B-20 Experimental and Simulated Bode Phase and Magnitude plots obtained after 24 hours of immersion in soil environment S8.

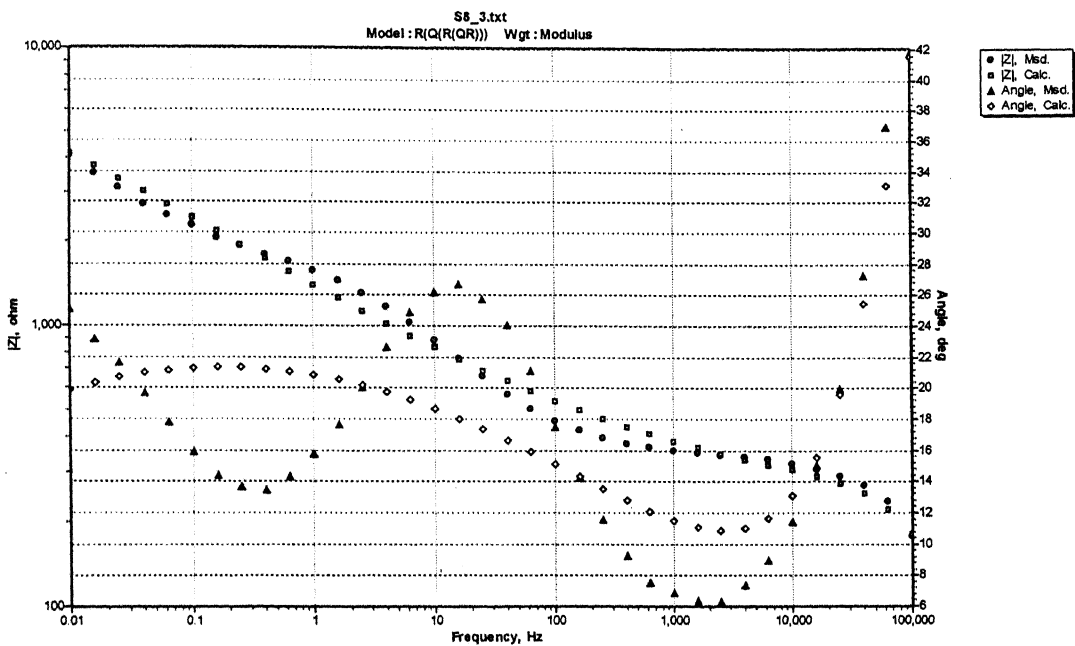


Fig. B-21 Experimental and Simulated Bode Phase and Magnitude plots obtained after 72 hours of immersion in soil environment S8.

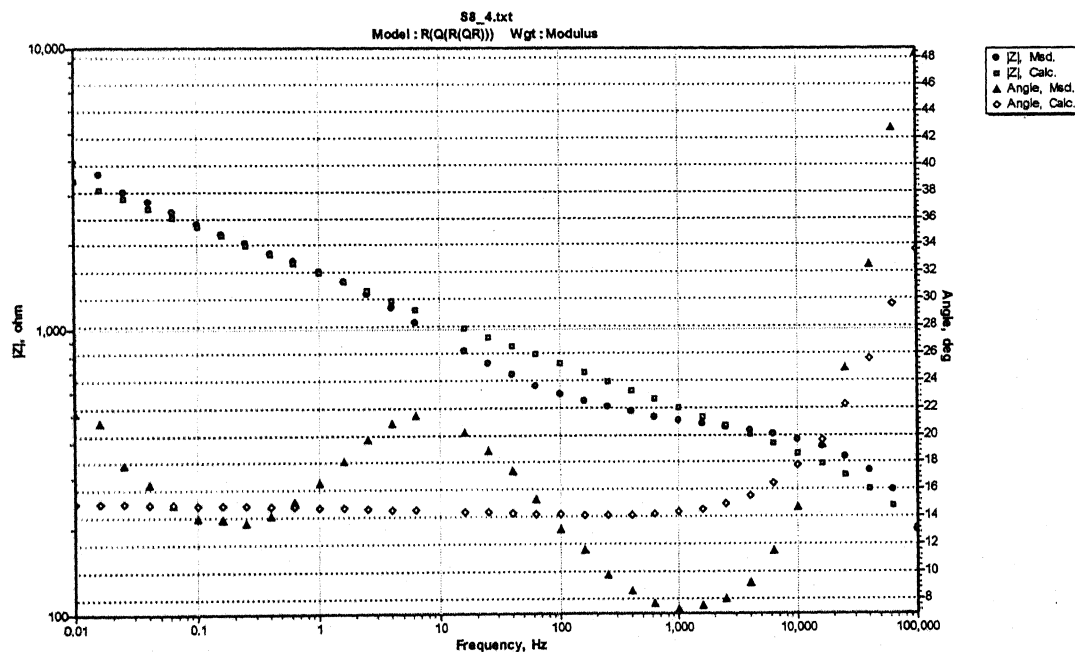


Fig. B-22 Experimental and Simulated Bode Phase and Magnitude plots obtained after 96 hours of immersion in soil environment S8.

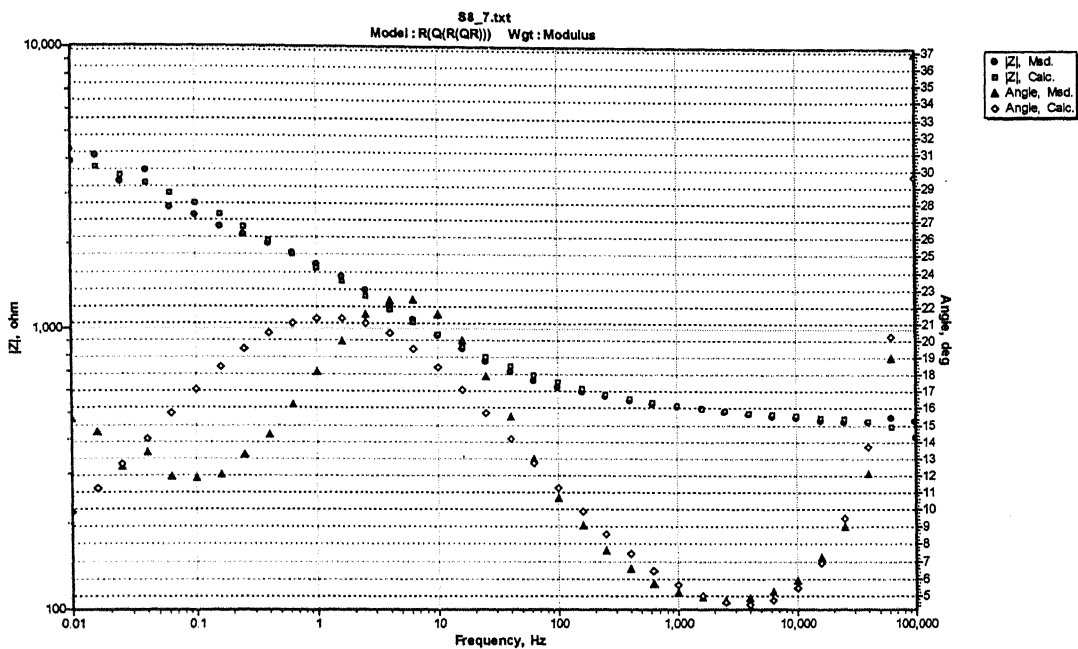


Fig. B-23 Experimental and Simulated Bode Phase and Magnitude plots obtained after 168 hours of immersion in soil environment S8.

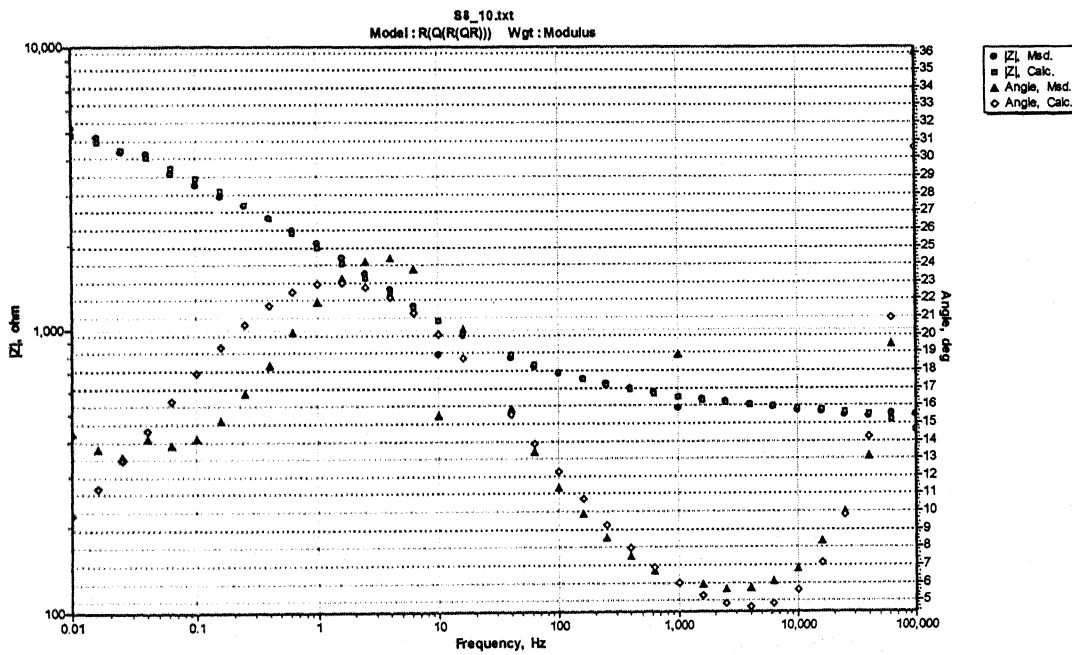


Fig. B-24 Experimental and Simulated Bode Phase and Magnitude plots obtained after 240 hours of immersion in soil environment S8.

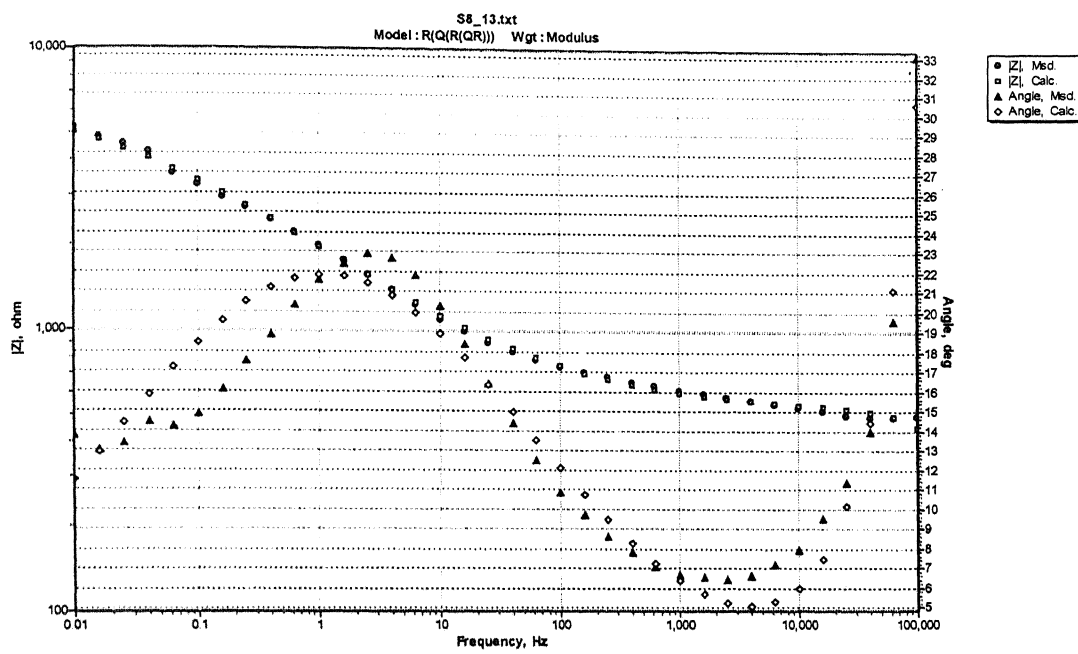


Fig. B-25 Experimental and Simulated Bode Phase and Magnitude plots obtained after 312 hours of immersion in soil environment S8.

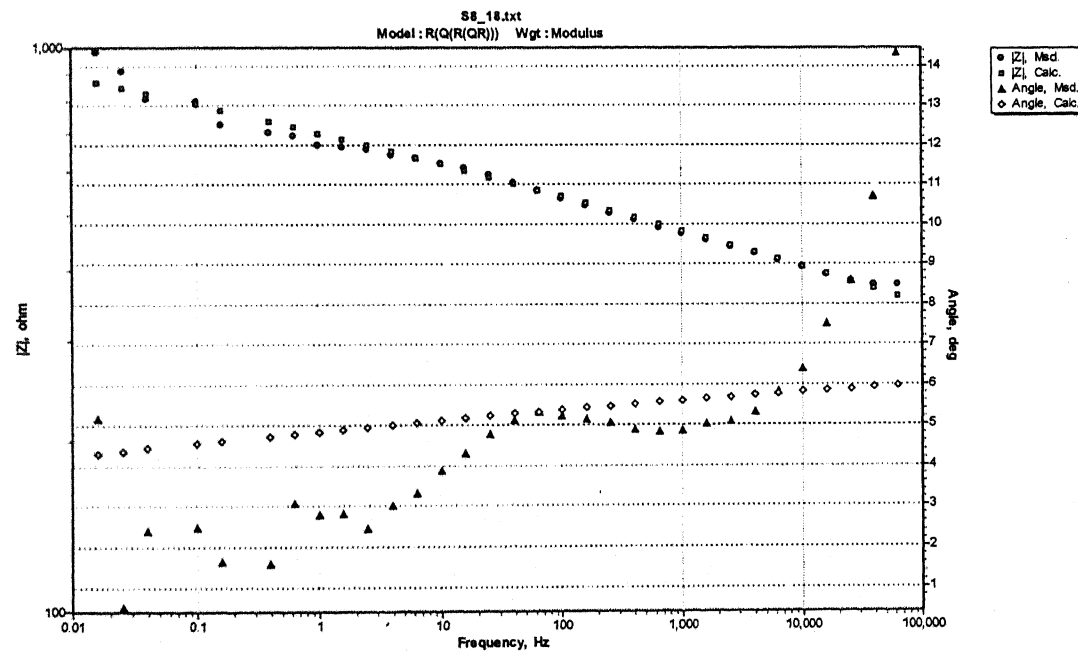


Fig. B-26 Experimental and Simulated Bode Phase and Magnitude plots obtained after 432 hours of immersion in soil environment S8.

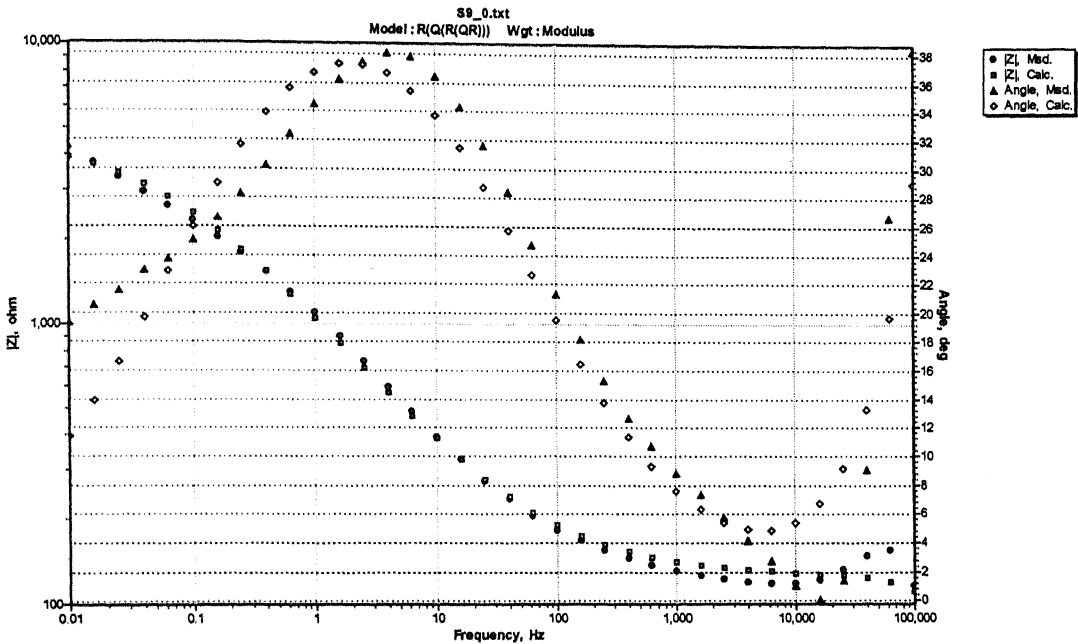


Fig. B-27 Experimental and Simulated Bode Phase and Magnitude plots obtained after 2 hours of immersion in soil environment S9.

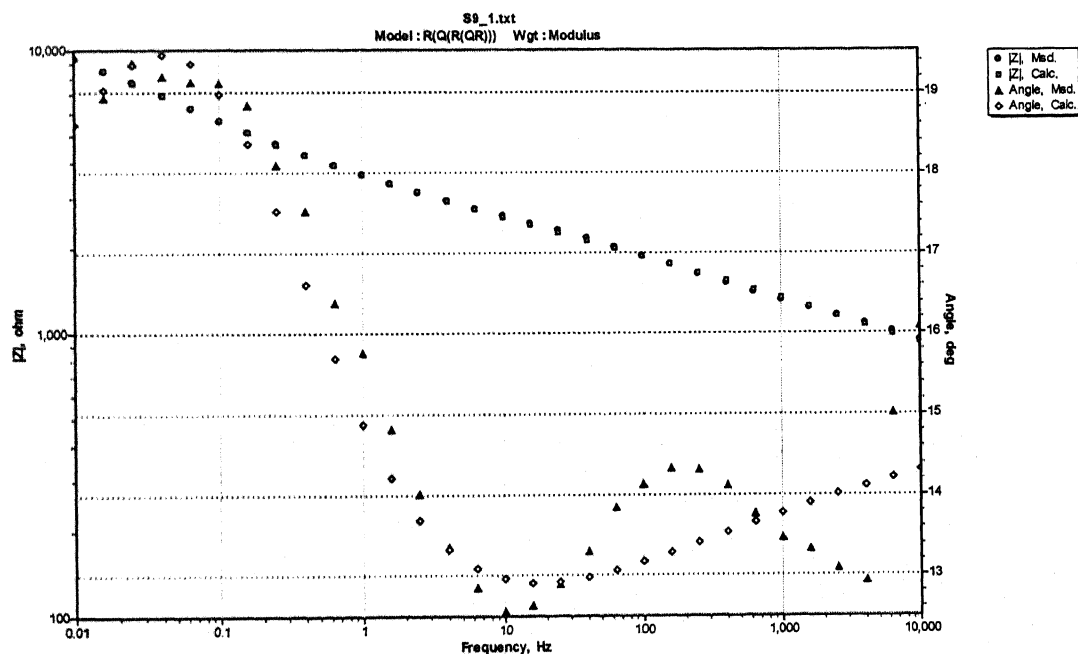


Fig. B-28 Experimental and Simulated Bode Phase and Magnitude plots obtained after 24 hours of immersion in soil environment S9.

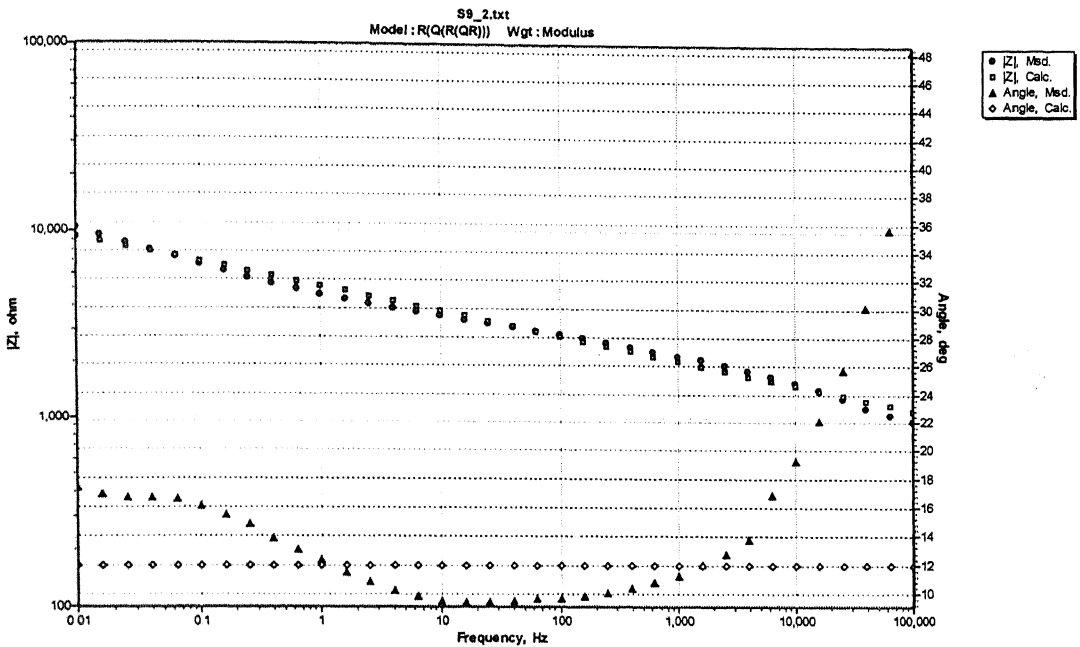


Fig. B-29 Experimental and Simulated Bode Phase and Magnitude plots obtained after 48 hours of immersion in soil environment S9.

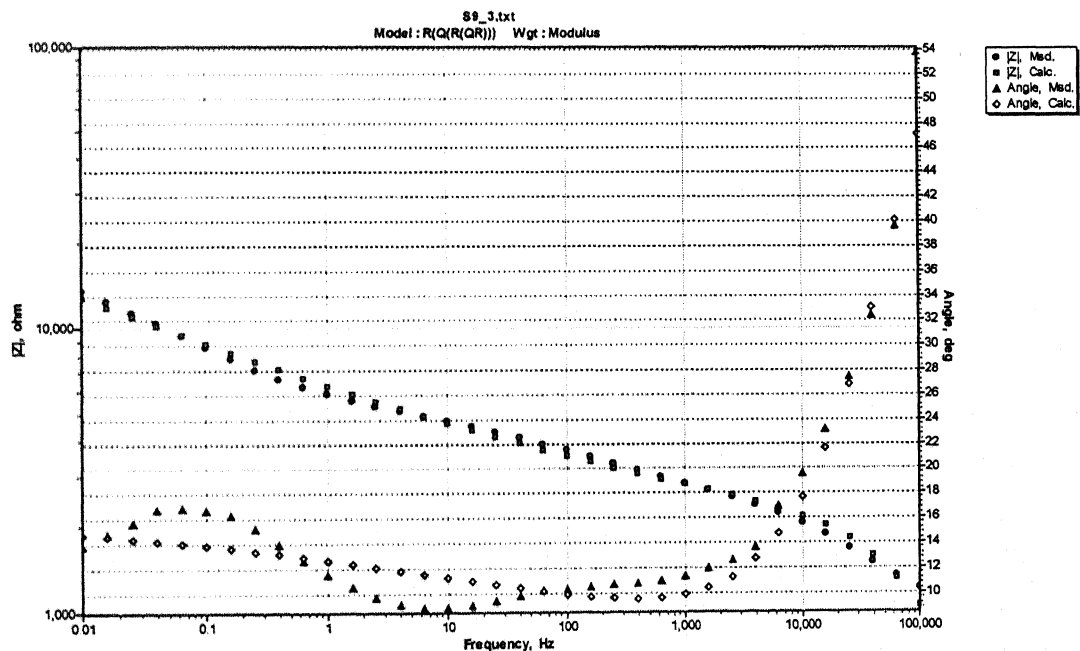


Fig. B-30 Experimental and Simulated Bode Phase and Magnitude plots obtained after 72 hours of immersion in soil environment S9.

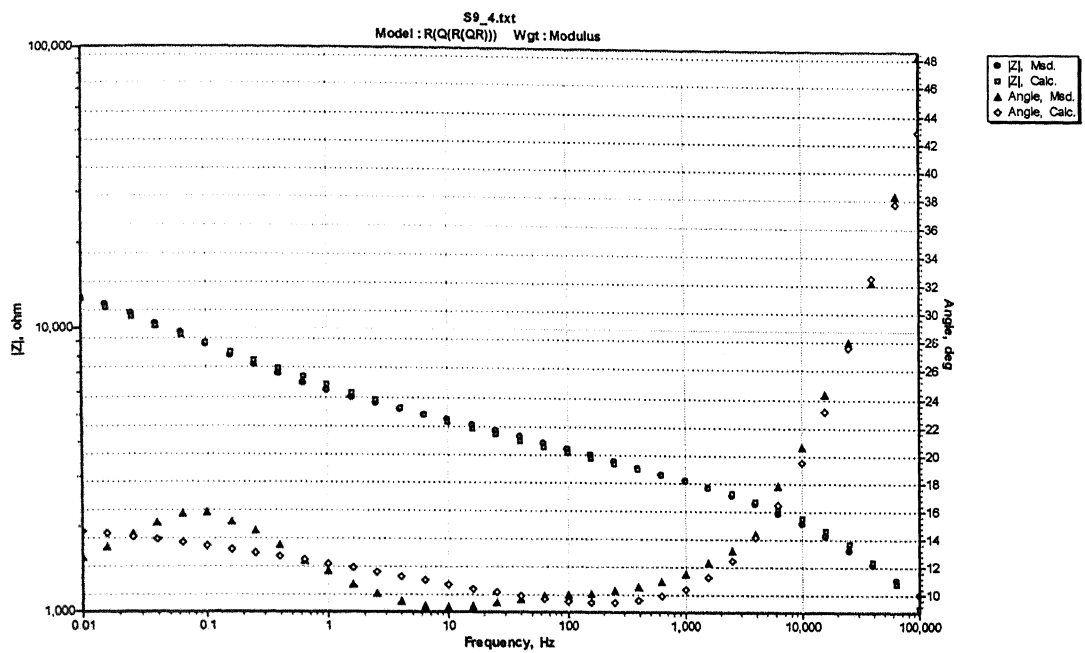


Fig. B-31 Experimental and Simulated Bode Phase and Magnitude plots obtained after 96 hours of immersion in soil environment S9.

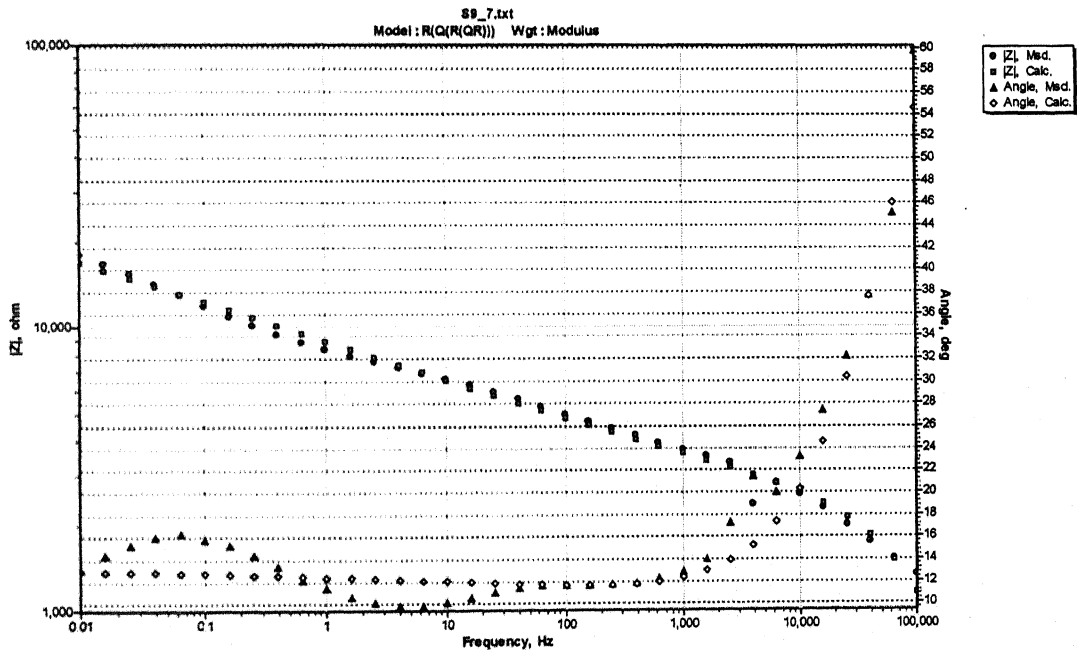


Fig. B-32 Experimental and Simulated Bode Phase and Magnitude plots obtained after 168 hours of immersion in soil environment S9.

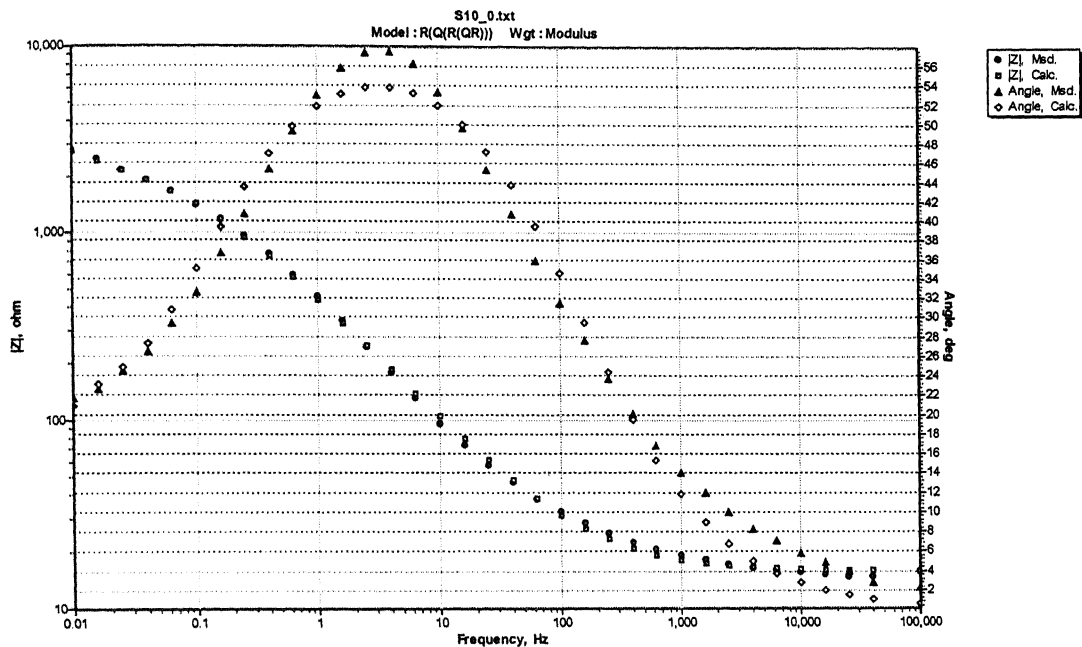


Fig. B-33 Experimental and Simulated Bode Phase and Magnitude plots obtained after 2 hours of immersion in soil environment S10.

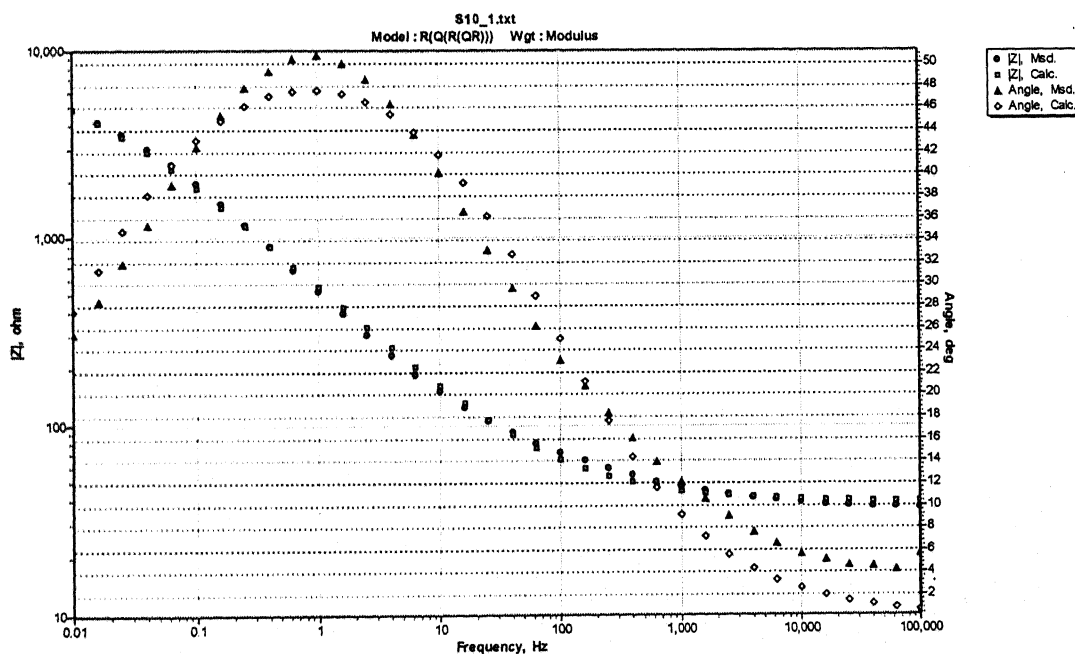


Fig. B-34 Experimental and Simulated Bode Phase and Magnitude plots obtained after 24 hours of immersion in soil environment S10.

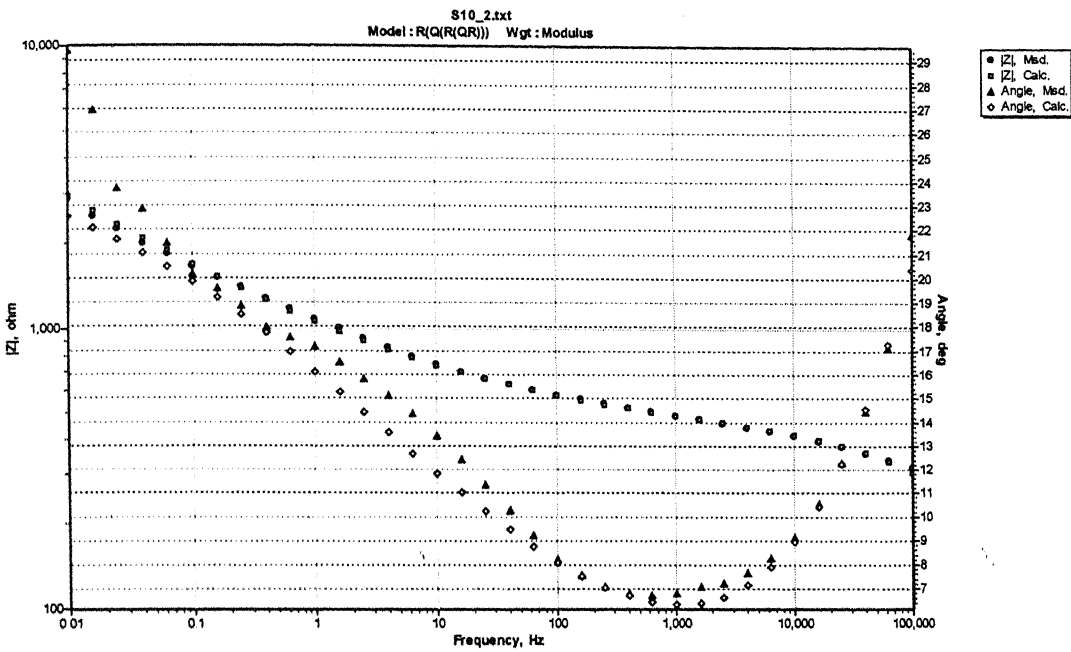


Fig. B-35 Experimental and Simulated Bode Phase and Magnitude plots obtained after 48 hours of immersion in soil environment S10.

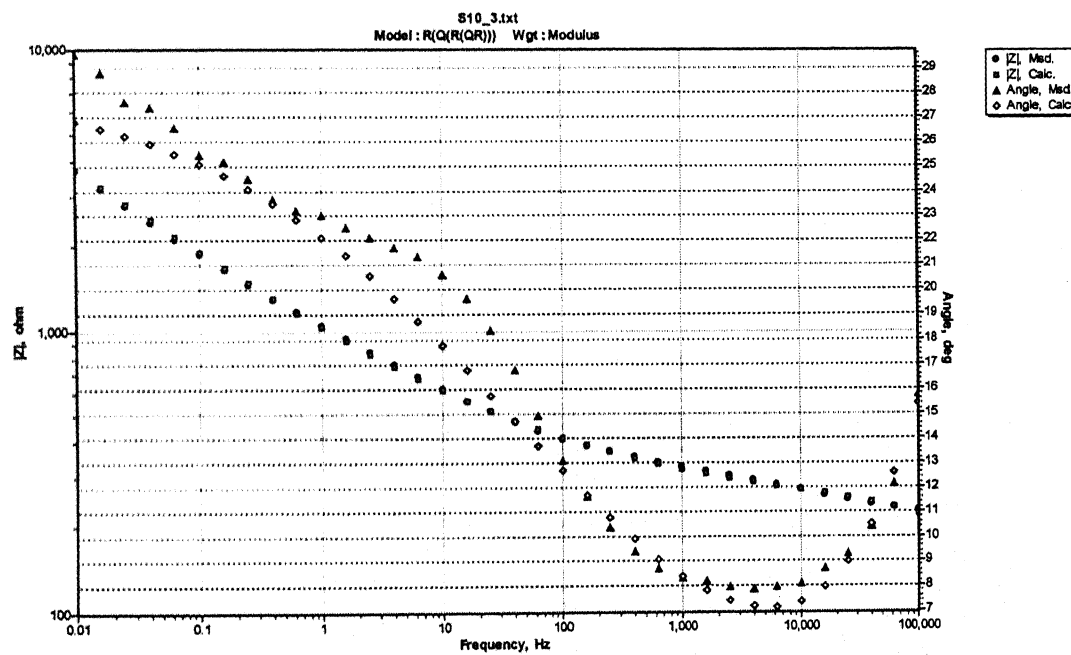


Fig. B-36 Experimental and Simulated Bode Phase and Magnitude plots obtained after 72 hours of immersion in soil environment S10.

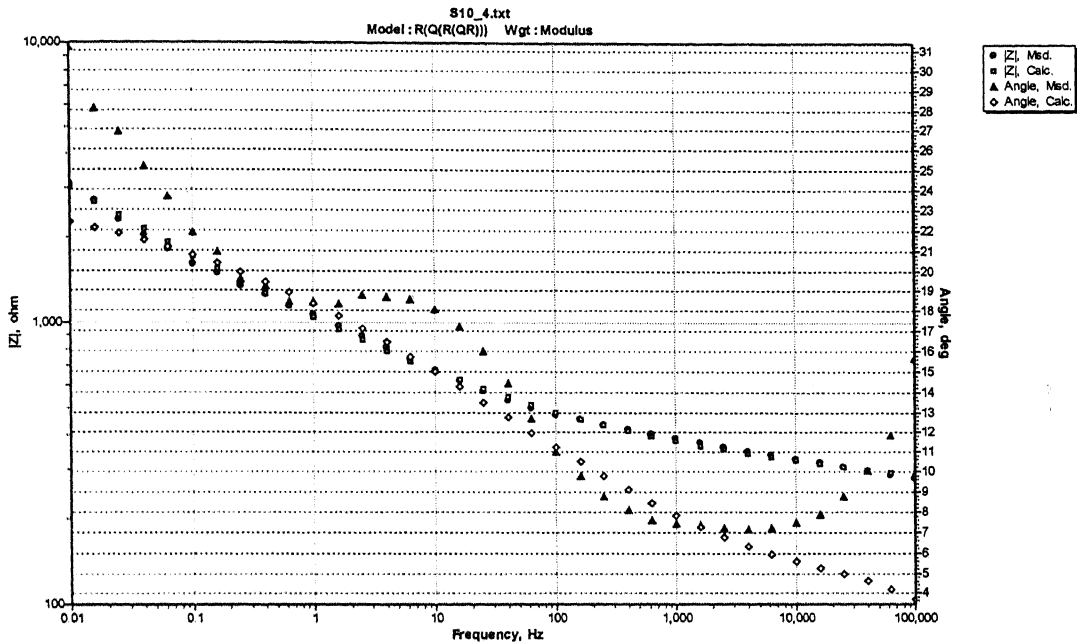


Fig. B-37 Experimental and Simulated Bode Phase and Magnitude plots obtained after 96 hours of immersion in soil environment S10.

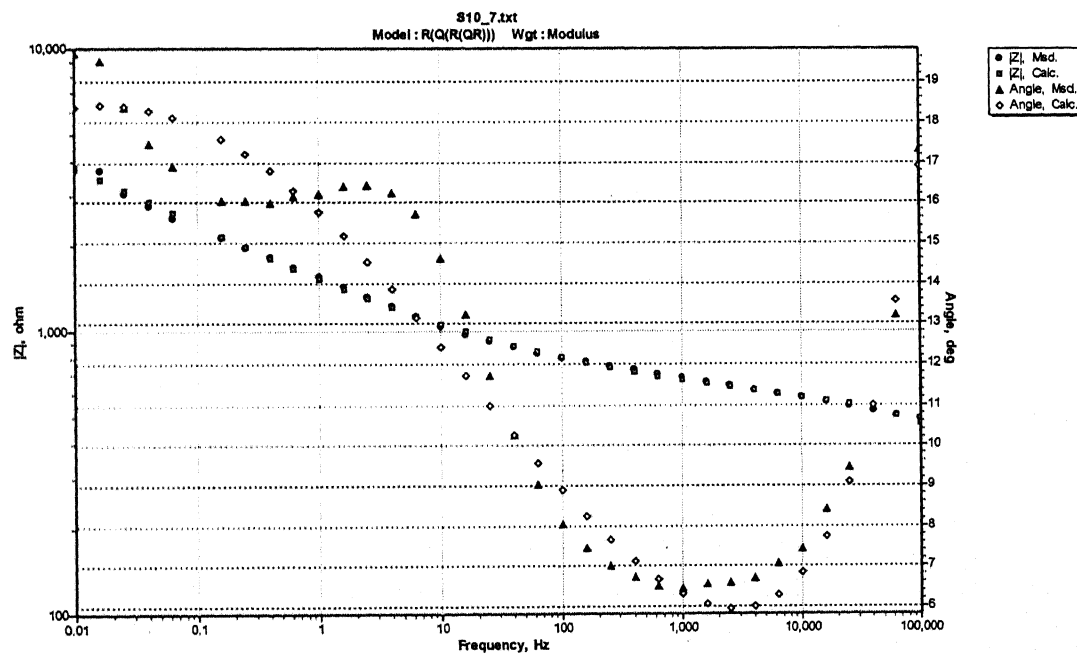


Fig. B-38 Experimental and Simulated Bode Phase and Magnitude plots obtained after 168 hours of immersion in soil environment S10.

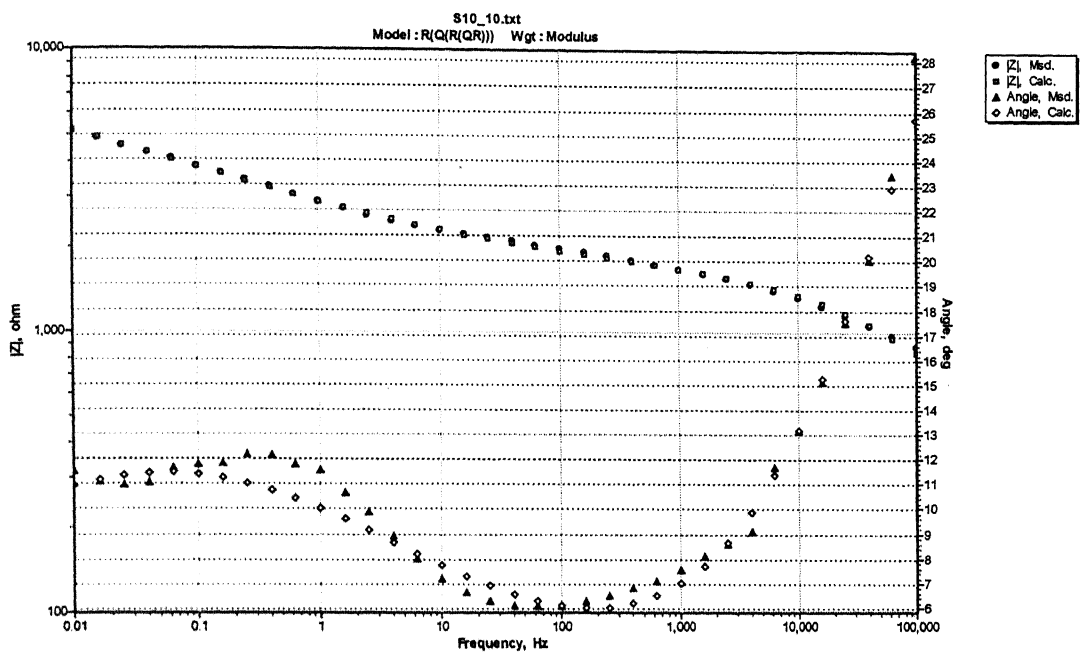


Fig. B-39 Experimental and Simulated Bode Phase and Magnitude plots obtained after 240 hours of immersion in soil environment S10.

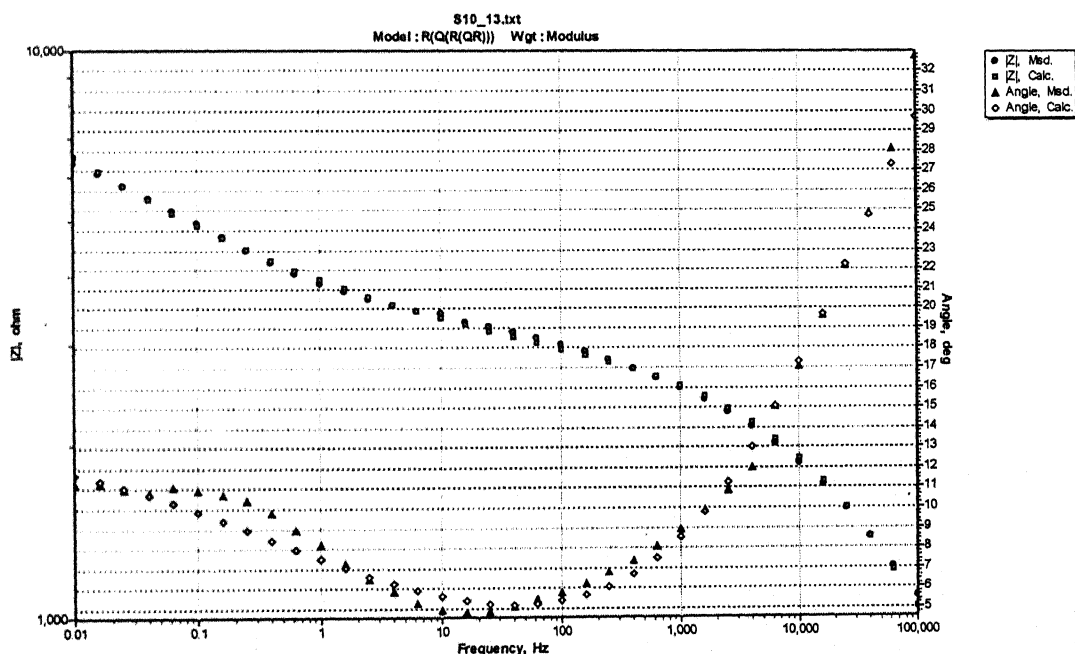


Fig. B-40 Experimental and Simulated Bode Phase and Magnitude plots obtained after 312 hours of immersion in soil environment S10.

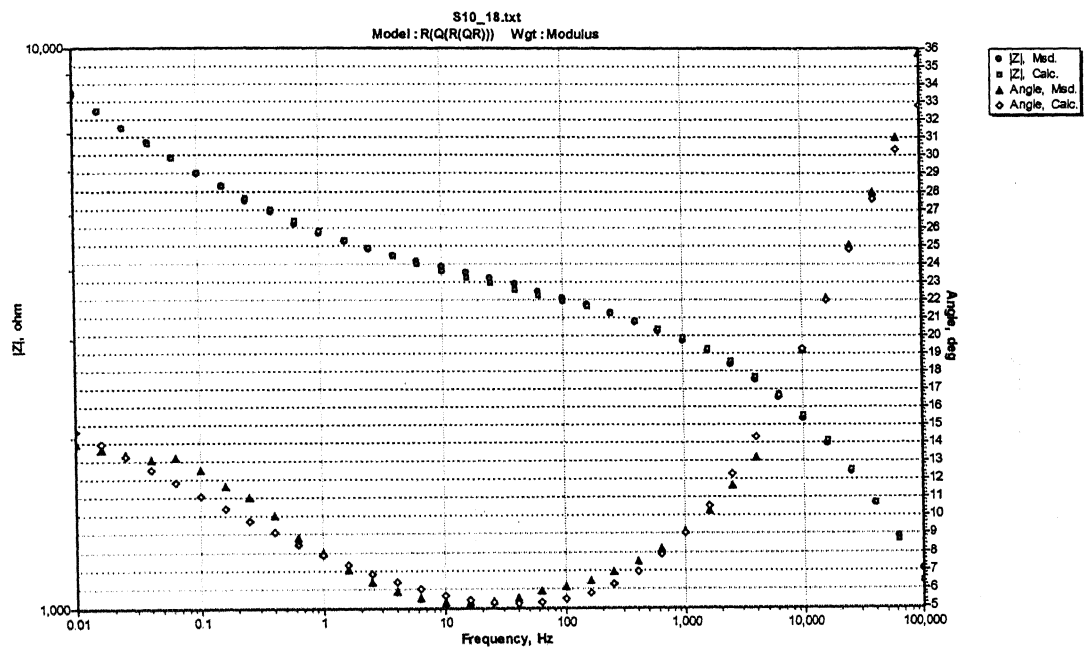


Fig. B-41 Experimental and Simulated Bode Phase and Magnitude plots obtained after 432 hours of immersion in soil environment S10.